Plankton Seasonal Dynamics and Carbon Export in a Warming Ocean

By

Joanna Kirsty Guest

For the degree of

Doctor of Philosophy

Thesis presented to the

University of East Anglia, School of Environmental Sciences

December 2023

Abstract

Anthropogenic climate change is significantly altering marine ecosystems, with profound implications for oceanic carbon dynamics. This thesis investigates the interplay between phytoplankton phenology and carbon export in marine ecosystems, using the PlankTOM12.2 model and a range of observations. The PlankTOM12.2 model's ability to simulate oceanic carbon fluxes was improved by introducing a representation of bacterial biofilms and updating of the parameterisation for the dissolution of calcite based on recent observations. In addition, the phytoplankton seasonality of PlankTOM12.2 model was shown to reproduce chlorophyll seasonality across 5 latitudinal bands, after improvements to the parameterisation of the growth rates of Plankton Functional Types (PFTs). A comprehensive evaluation against observational data from 1998 to 2020 reveals that the PlankTOM12.2 model effectively captures the phenology of phytoplankton on a regional scale but not at the level of the model grid. Opposing trends in initiation and termination drive global increases in duration of the growing period of 5.1-7.8 days per decade between 1998 and 2020. In addition, the model replicates regional variability in observed trends such as the shortening of growing periods in the tropics and lengthening in high-latitude regions. Temperature, mixed layer depth, and primary production were the primary influence on export production and efficiency. While the effects of growing period duration and initiation on export production are often significant, they are non-dominant. However, in the Southern Ocean, the effect of duration and initiation of phytoplankton growth on carbon export is as large as that of mixed layer depth, highlighting the unique environmental dynamics of this region. Under both low- and high- emissions scenarios, primary production decreases by 2100, in line with a decline in phytoplankton biomass; though more variability between regions is observed compared to simpler ecosystem models. Globally, except in the Southern Ocean, particulate organic carbon export production increases despite these declines in primary production. This is driven by increases in export efficiency which increases as primary production declines. This inverse relationship between export efficiency and primary productivity is, at least partially, due to shifts amongst species. The analysis presented here demonstrates that complex ecosystem models are essential for predictions of marine carbon dynamics amidst climate change, underscoring the need for improved model ecosystems and high-resolution observational data for validation. The findings suggest that ecosystem shifts are key drivers in altering phenology and carbon export production, calling for further research to refine our understanding of complex ecosystem interactions.

Contents

List of Tables

List of Figures

3.1. (a-d) Global mean patterns of phytoplankton phenology indices. Data were created from climatologies averaged between 1998 - 2020. Total chlorophyll concentration (mg m^{-3}) were taken from OCCCIv5 (left) and PlankTOM12.2(right). The right hand panels show the latitudinal average of phenological indices from OCCCIv5 (black) and PlankTOM12.2(green) smoothed by 5°. Days greater than 365 are representative of growing periods that span the edges of the calendar year. For example, 400 and 500 represent ~February and ~April, respectively. 65

3.2. (a-c) Indices of magnitude of phytoplankton growth. Data were created from climatologies averaged between 1998 - 2020. Relative maximum amplitude is the relative percentage difference (RPD) between the mean and (b) the average chlorophyll concentration during growing period and (c) the maximum amplitude. Total chlorophyll concentration (mg m-3) were taken from OCCCIv5 (left) and PlankTOM12.2(right). The right hand panels show the latitudinal average of traits from OCCCIv5 (black) and PlankTOM12.2(green) smoothed by 5°. RPDs are calculated as: $REL\Delta b_{a,c} = ((b_{a,c} - b_{chl})/b_{chl}) \times 100$, where b_{chl} is the average yearly chlorophyll concentration, b_c is the average concentration over the growing period and b_a is the maximum amplitude. 66

3.3. Average bias as represented by the mean difference between the NEMO-PlankTOM12.2 model and observations for a) sea surface temperature (SST; °C) and sea surface salinity (SSS; PSU) and mixed layer depth (MLD; metres); and b) initiation (day), timing of maximum (day) and termination date (day), duration (days), maximum amplitude (mg m^{-3}) and average concentration over the growing period (GP; mg m^{-3}). Observations are subtracted from model values. Positive biases are therefore representative of regions where model values are greater than observations. 70

3.4 Relationship between Error in Model estimation of Sea Surface Temperature (ε_{sst}) on Error observed in phenology varies ($\varepsilon_{phenology}$; 1999-2020). Absolute annual mean errors of SST (|ΔSST|) and Phenology indices (|ΔPhenology|) are calculated by |model - observations|. The absolute errors are then regressed by |ΔSST| = a + b|ΔPhenology|, where n=11 and positive values represent where larger |ΔSST| result in larger |ΔPhenology|. Left/right panels show 10° mean latitudinal/longitudinal averages respectively. Points represent the regression coefficient and the error bars show the standard error. Significance is represented with asterisk, where * p < 0.05, ** p < 0.01, *** p < 0.001. Average R^2 values are presented for significant points (p < 0.05). 73

List of Equations

1.1 $$CO_2 + H_2O \longleftrightarrow H_2CO_3 \longleftrightarrow HCO_3^- \longleftrightarrow CO_3^{2-} + 2H^+$$ 10

2.1 $$\beta_{Si} = min\left(rem_{DSI} e \frac{ret_{DSI}}{273.15 + T}, rem_{max,DSI}\right) \eta_O$$ 39

2.2 $$\mu^T = \mu_0 \times Q^{\frac{T}{10}}$$ 39

2.3 $$\mu^T = \mu_{max} \times e^{\left(-1 \cdot \frac{(T - T_{opt})^2}{\Delta T^2}\right)}$$ 40

2.4 $$\lambda^*_{OM} = BAC \cdot M_{opt} f(T) \eta_O \left(\frac{\sum_k p^{BAC}_{OC} OM}{K^{BAC}_{OC} + \sum_k p^{BAC}_{OC} OC}\right)$$ 40

2.5 $$\beta_{CO_3} CAL = M_{CO_3} \cdot (1 - \Omega_{sat})^n$$ 41

3.1 $$REL\Delta b_{a,c} = \left(\frac{b_{a,c} - b_{chl}}{b_{chl}}\right) \times 100$$ 63

3.2 $$\varepsilon^{sst,sss} = a + \beta(\varepsilon^{b_{i-a}})$$
$$where, \quad \varepsilon^{sst,sss,b_{i-a}} = |Y^{mod}_{sst,sss,b_{i-a}} - Y^{obs}_{sst,sss,b_{i-a}}|$$ 64

Table of Abbreviations

Abbrev.	Full Name
BCP	Biological Carbon Pump
CCP	Carbonate Counter Pump
CHL	Chlorophyll
DOC	Dissolved Organic Carbon
EF	Export Efficiency
EP	Export Production
GPP	Gross Primary Production
HNLP	High-Nutrient Low-Productivity
MLD	Mixed Layer Depth
NPP	Net Primary Production
PIC	Particulate Inorganic Carbon
POC_L	Large Particulate Organic Carbon
POC_S	Small Particulate Organic Carbon
SSS	Sea Surface Salinity
SST	Sea Surface Temperature

Acknowledgements

I first want to extend my heartfelt gratitude to my supervisor, Corinne Le Quéré, whose encouragement, guidance and inspiration have been the cornerstone of my success. I am deeply appreciative of the support you have offered, which has been pivotal in helping me overcome challenges and achieve this significant milestone. Your profound influence on both my academic and personal growth is immeasurable.

I would like to thank to Andrew Manning and Stephanie Henson. Your feedback provided valuable insights that helped refine my approach and understanding of my research. Your guidance offered valuable clarity and direction and is greatly appreciated.

I would also like to extend my thanks to the members of the GreenOcean research group, each of whom has contributed significantly to my academic journey. Rebecca Wright, I am grateful not only for your guidance and encouragement but also for your friendship that has enriched this experience. Marie-Fanny Racault, your openness and wisdom have not only guided but also reassured me, offering solace and clarity when most needed. Tereza Jarníková, I extend my heartfelt thanks for your relatable advice, your friendship, and your patience in answering my questions. Erik Buitenhuis, your patience and willingness to share knowledge have been fundamental in my understanding of the PlankTOM model. Anna Sommer, thank you for answering my many questions; your assistance in developing my Python skills was crucial to my success. To Philip Townsend, Nicolas Mayor and David Willis thank you to your continued advice and support throughout my journey.

I would like to express profound gratitude to my Mum and Dad. Your encouragement in my pursuit of higher education, despite not having had the same opportunity, has been a pillar in my journey. Your support, rooted in the desire to see me thrive in a field I am passionate about, has been invaluable. For your unconditional love and encouragement, and for your willingness to listen to my wittering, I am grateful. To my brother, Adrian; your unwavering support and kindness been an anchor during some of the most challenging periods of my life, thank you.

I would also like to extend a special word of thanks to my late mother-in-law, Sarah. Her kindness, generosity, and understanding have been instrumental to my success. Without her support I may not have achieved this dream. Thank you for everything, you have left an indelible mark on my heart.

Finally, I extend my deepest gratitude to my partner, James Merewood, with whom I have shared over a decade of life's journey. I am immeasurably grateful to have found someone who supports me in all aspects of my life. Your unwavering support, constant encouragement, and genuine desire to see me succeed has been the bedrock of my achievements. Your presence and belief in me has been everything – a constant source of strength and inspiration. For all of this and more, I am eternally thankful.

The world was to me a secret which I desired to divine. Curiosity, earnest research to learn the hidden laws of nature, are among the earliest sensations I can remember.

- Mary Shelley, *Frankenstein.*

Chapter 1. Introduction

1.1. Opening Statement

Phytoplankton are among the most diverse and pivotal groups of organisms on Earth, underpinning the entire marine ecosystem. Their role extends from maintaining nutrient balances in the ocean to facilitating carbon sequestration in the deep sea through the biological carbon pump, a process critical for global carbon cycling. Climate change caused by increasing atmospheric CO_2 and other greenhouse gas concentrations is causing rapid changes in the physical and chemical ocean systems. Physical and chemical changes are in turn inducing widespread shifts in biogeography, composition, phenology and abundance of planktonic organisms. Due to their fast life cycles and sensitivity to environmental variations, phytoplankton serve as pivotal indicators of climate change in marine ecosystems.

Extensive research efforts have been channelled to understand how climate change is influencing marine ecosystems and subsequently export production. This includes studies on variations in the timing of phytoplankton growing periods, alterations in primary production rates, shifts in community structures within ecosystems and the effect of community structure on export production. However, a critical gap remains in our understanding: the influence of changing phytoplankton growing periods on carbon export remains largely unexplored. Changes in the phenology and abundance of phytoplankton may lead to a mis-match with organisms in higher trophic levels, fundamentally altering the structure of the marine ecosystem. Furthermore, the latest generation of climate models, while advanced, often lack representation of several key processes essential for accurately modelling the influence of changing ecosystem dynamics on carbon export. These missing elements include temperature/oxygen-dependent bacterial remineralisation, fragmentation, and a detailed representation of zooplankton complexity. These factors are integral in determining the variability of carbon export due to ecosystem changes and seasonal shifts in growing periods. Projections of carbon export in existing models exhibit a substantial range, varying from +2% to -40%. This wide range highlights the uncertainty and challenges in accurately forecasting the impact of climate change on carbon export dynamics.

This thesis aims to shed light on how phytoplankton growing periods impact carbon export using the newly developed, high-complexity ecosystem model PlankTOM12.2 and satellite chlorophyll observations. The PlankTOM12.2 model not only includes many of the crucial processes relevant to carbon export highlighted above, but within this thesis it has been validated for its accuracy in modelling both the export of particulate organic carbon and the seasonal cycles of phytoplankton.

1.2. Phytoplankton, Productivity and Particulate Organic Carbon Export

Phytoplankton are defined as the group of photosynthesising free-floating organisms which spend most or all of their life cycles in the open ocean and drift with the ocean currents (Lürling 2020). There are more than 25'000 known species of phytoplankton spanning eight phyla: Cyanobacteria, Dinophyta (dinoflagellates), Bacillariophyta (diatoms), Haptophyta (coccolithophores), Chlorophyta (green algae), Ochrophyta, Cryptophyta and Euglenophyta (flagellates; Maranon 2007). These species range by four orders of magnitude in size from the smallest cyanobacteria (0.1 μm^3) to the largest (108 μm^{-3}) diatoms (Maranon 2007). Furthermore, phytoplankton support the base of the entire oceanic food-web and despite comprising less than 1% of global biomass contribute ~50% of primary production (Field et al., 1998), because of the very rapid turnover rate of phytoplankton (approximately 1 week). Different species of phytoplankton support specific biogeochemical functions of the ocean, by absorbing atmospheric nitrogen (cyanobacteria and diazotrophs), recycling silica (diatoms), and modulating carbonate chemistry (coccolithophores; Henson et al., 2021).

Gross primary productivity (GPP) in the ocean encompasses the total rate of organic carbon production by autotrophs, primarily driven by phytoplankton. Growth of phytoplankton is tied to their rate of photosynthesis, which depends fundamentally on the availability of both light and nutrients. The process of photosynthesis in phytoplankton, quantified as GPP (Stanley et al., 2010), is typically faster than autotrophic and heterotrophic respiration, leading to a net conversion of carbon dioxide into organic carbon biomass and a release of oxygen. A portion of the GPP is respired by phytoplankton autotrophic respiration, the remaining production is referred to as net primary production (NPP) which is estimated to be 58±7 Pg C yr^{-1} (Buitenhuis et al., 2013b).

Part of the NPP sinks to the deep ocean. This "export" of particulate organic carbon is approximately 10 Pg C out of the euphotic layer each year, regulating atmospheric CO_2 levels on timescales of centuries to millennia (Nowicki et al., 2022). The export of carbon is then respired at depth and transported back to the surface by ocean currents, a full cycle that constitutes the ocean biological carbon pump (BCP), and leads to enhanced storage of carbon in the deep ocean. Without the BCP, atmospheric CO_2 levels would be ~200 ppm higher than they are today (Henson et al., 2022). A substantial portion of the exported organic carbon undergoes recycling within the ocean depths, primarily through the metabolic activities of zooplankton and bacteria, which result in the conversion back to dissolved inorganic carbon (Steinberg and Landry 2017). The efficiency of the BCP varies geographically: up to 30% of NPP is transported out of the euphotic layer in high-latitude regions, contrasting sharply with as low as 1% in low-latitude areas (Henson, et al., 2012). However, due to the complexities of export flux processes the exact fraction of NPP that is exported remains poorly constrained (Henson et al., 2022).

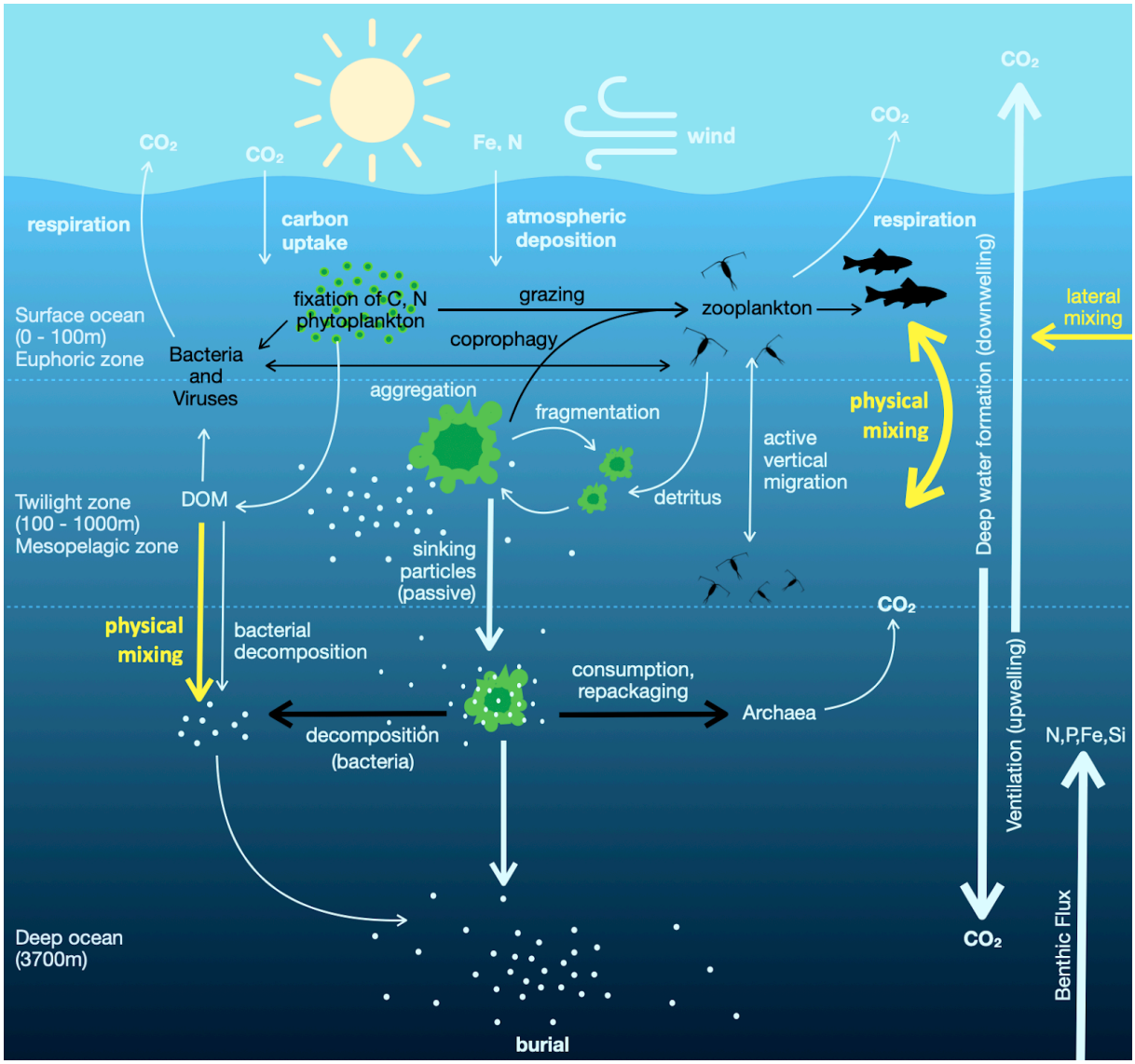

Figure 1.1. The Biological Pump's Role in Carbon Dynamics. Photosynthesis by phytoplankton converts inorganic nutrients and CO_2, releasing Dissolved Organic Matter (DOM). Phytoplankton form Particulate Organic Carbon (POC) and become prey for zooplankton. Larger zooplankton such as copepods produce faecal pellets that, along with other detritus, form sinking aggregates. Bacteria consume and respire part of the DOM. These processes results in ~1% of particles reaching the sea floor, which are eventually released back to the atmosphere via ocean circulation over millennia. Figure modified from Ducklow, et al., (2001).

The depth at which Particulate Organic Carbon (POC) export is quantified can significantly influence the interpretation of carbon sequestration processes. The 100-metre depth definition is commonly used, aligning with a multitude of historical datasets that provide a basis for temporal and spatial comparative analyses in marine studies (Buesseler et al., 2007; Henson et al., 2012). This depth typically lies beneath the euphotic zone across many regions, making it a practical choice for estimating the minimum flux of POC out of the surface ocean where biological production is most active. Its use is primarily justified by the simplicity it offers and the ease of comparison with previous studies, however it does not account for variable oceanographic conditions such as the depth of the

euphotic zone or mixed layer, which can be highly dynamic (Siegel et al., 2016). In contrast, the mixed layer depth (MLD) is another reference point used for measuring POC export, tailored to reflect the specific physical and biological dynamics of the upper ocean. Using the MLD can provide a more ecologically pertinent metric by incorporating the influence of vertical mixing and biological productivity, which are sensitive to regional, seasonal and inter-annual variations (Buesseler et al., 2007; Siegel et al., 2016). For deeper carbon sequestration studies, the 1000-metre depth is increasingly relevant, especially in modelling studies where logistical constraints of deep-water sampling are not a limitation. This depth is significant as it often represents a long-term sequestration of carbon, potentially isolated from the atmosphere for centuries (DeVries et al., 2012; Marsay et al., 2015). This 1000 metre threshold of export production (EP) is used for understanding the efficiency of the biological pump in sequestering carbon deep in the ocean, where it contributes to the attenuation of atmospheric CO_2 levels over geological timescales (DeVries et al., 2012; Kwon et al., 2009). Finally, a recent analysis suggested that the carbon sequestration depth should vary as a function of the overall ventilation of water masses, as these will influence the retention time of carbon in the ocean (Ricour et al., 2023). However the calculation of the sequestration depth itself is subject to major uncertainties and varies across models, which makes it a difficult metric to utilise in practice.

The processes regulating carbon export and its efficiency (the ratio of export to NPP) include: community structure, seasonal dynamics and phenology of phytoplankton, aggregation/ disaggregation processes, grazing, and stratification (Figure 1.1; Ducklow et al., 2001). Sinking speed of organic particles, and hence the associated carbon export flux, is linked to the size, density and morphology of sinking particles (Guidi et al., 2009). Data from underwater video profilers show that the size structure of phytoplankton and integrated chlorophyll concentration in the euphotic zone explain ~68% of the variance of the carbon export flux at 400m (Guidi et al., 2009). However, zooplankton grazing can be regionally important for carbon export; for example, zooplankton faecal pellets contributed up to 94% during the spring bloom of the Californian Current (Turner 2015). In addition, more recent evidence highlights that community structure significantly influences carbon export and its efficiency. Diatoms have long been considered as important contributors to export flux because of their large size and dense shells that lead to fast sinking rates of particles. In comparison, picophytoplankton contribute less EP as they sink slowly and thus the rate of export of these particles relies on subduction of water from the surface, aggregation and consumption by organisms and subsequent excretion as faecal pellets. Furthermore, data from Tara oceans suggest that bacteria and viruses could contribute up to 60% of EP variability in oligotrophic regions (Guidi et al., 2016) despite their small size, highlighting the important role of phytoplankton community structure, in addition to size of phytoplankton, on EP.

In addition, the efficiency of organic carbon export relies on the overlap of the timing of phytoplankton growing periods and the spawn of predators that consume them. High levels of export efficiency (EF) were associated with high faecal pellet concentration (Henson et al., 2019). Carbon EF is therefore likely to change due to shifts in phytoplankton growing period timing and mis-match with higher trophic levels. However, due to the complexities of export flux, described above, processes remain poorly constrained (Henson et al., 2022). The sensitivity of phytoplankton to environmental change, their rapid turnover rate, and their role as the base of the ecosystem make them valuable indicators for studying the effect of ocean warming and associated climate change in the ocean on carbon export (Tagliabue et al., 2023).

Aggregation and disaggregation processes also significantly influence the export of particulate organic carbon (POC) from the euphotic zone to deeper ocean layers. Aggregation involves the coagulation of phytoplankton necromass, zooplankton faecal pellets, carcasses and associated detrital organic matter, which can form into large, rapidly sinking aggregates and form sinking events commonly referred to as marine snow. Larger aggregates have a higher sinking velocity due to their size and density, thus enhancing the vertical transport of POC (Maerz et al., 2020). In addition, the production of Transparent exopolymer particles (TEP) and other forms of gel or mucus production by some microorganisms can enhance the formation of aggregates. These include TEP production by diatoms, bacteria and viruses which increase the stickiness of particles increasing their aggregation rate (Gardes et al., 2011; Guo et al., 2022; Yamada et al., 2018).

Disaggregation, the process by which larger particulate aggregates break down into smaller particles, can occur due to physical disturbances, such as turbulence in the water column, or biological activities, such as grazing by zooplankton and microbial remineralisation. Disaggregation slows down the sinking velocity of particulate matter, potentially reducing the efficiency of POC export to deeper layers. Zooplankton grazing may result in disaggregation of phytoplankton necromass, resulting in reduced export flux (Rohr et al., 2023). Remineralisation by bacteria and grazing by zooplankton are considered crucial controls on EF (Henson et al., 2019).

In contrast to the biological carbon pump (BCP) the carbonate counter pump (CCP) increases the partial pressure of CO_2 (pCO_2) at the surface through the process of carbonate shell formation by calcifying organisms (Frankignoulle et al., 2003), their dissolution at depth and return flow via ocean currents. This process primarily involves marine calcifying planktonic organisms like coccolithophores, pteropods, and foraminifera. Calcifying organisms contributes to a surface-to-depth alkalinity gradient and subsequent CO_2 release back to the atmosphere by producing $CaCO_3$ (calcium carbonate) shells. Recent studies reveal that the CCP's effect varies greatly over different spatial and temporal scales. The efficiency of the CCP is dependent on several factors, including the composition of calcifying species within the plankton community and the relative balance between particulate

inorganic carbon (PIC) and POC export (Manno et al., 2018; Neukermans et al., 2023; Rembauville et al., 2016). For example, calcifying zooplankton like pteropods, ostracods, and foraminifera can promote the sequestration of PIC to the deep ocean, as their shells' large mass enables rapid sinking. In contrast, calcifying phytoplankton such as unicellular coccolithophores, with their calcite platelets, have varied sinking rates depending on their assimilation into larger biological aggregates and faecal pellets (Manno et al., 2018). In addition, a study conducted in the Southern Ocean's Polar Frontal Zone found that in regions with naturally high iron concentrations the excess flux of inorganic carbon surpasses that of organic carbon (Salter et al., 2014). This suggests that the production and flux of carbonate in naturally iron-fertilised waters reduce the overall amount of CO_2 transferred to the deep ocean by a significant percentage, thereby highlighting the strengthened role of the CCP in these environments (Salter et al., 2014).

1.3. Phytoplankton Phenology

Phytoplankton growth is a function of temperature, light availability, nutrient availability, as well as physiological limits intrinsic to the species. The timing of phytoplankton growing periods is modulated by the change in availability of temperature, light and nutrients, due to seasonal and interannual variations in temperature, cloud cover, and MLD, and by grazing pressure (Racault et al., 2012). Phytoplankton phenology is the study of the timings of seasonal variations in ecological indices, such as the initiation date of the growing period, or its duration. The phenology of phytoplankton varies across ocean regions. In regions with high-nutrient concentrations, such as the high-latitudes and some tropical regions, short high-amplitude growing periods are predominant. In comparison, in low-nutrient regions such as the mid-latitude oligotrophic gyres, growing periods are long with low amplitude. In the high-latitudes, two mechanisms have been proposed to explain their initiation: a shallowing of the mixed layer in spring resulting in enhanced light availability and high primary production (Cherkasheva et al., 2014) or/and a deepening of the mixed layer in late winter resulting in reduced grazing (Behrenfeld 2010). In the tropical and subtropical regions where nutrient concentrations tend to be low, long low-intensity growing periods are initiated through deepening of the mixed layer and increased nutrient availability (Racault et al., 2012).

Drivers of phytoplankton growth also vary inter-annually. Climate events such as El Niño cause global and highly variable shifts in phytoplankton phenology (Racault et al., 2017a). For example, during El Niño events, the weakening of the easterly trade winds lead to the displacement of warmer, nutrient-poor waters from the western towards the central Equatorial Pacific, enhancing stratification and delaying the timing of the growing period by up to 40 days (Racault et al., 2017b). In contrast, growing periods tend to occur earlier in the eastern equatorial Pacific, equatorial Indian Ocean and in vast ranges of the Southern Ocean during El Niño events (Racault et al., 2017b). Extreme climatic events such as the El Niño Southern Oscillation are projected to occur more frequently due to climate change (Cai et al., 2015; Cooley et al., 2022). The combination of the observed response of

phytoplankton phenology to climatic events and projected increases in the frequency or intensity of extreme climatic events suggests that there may be important changes to phenology associated with both climate change but also climatic variability.

1.4. Recent and Predicted Changes in Ocean Chemistry

1.4.1. Warming

It is well documented that the climate is warming at an unprecedented rate. It is estimated that the ocean has absorbed 93% of the heat generated by anthropogenic global warming since the 1970s (Wijffels et al., 2016). This heat is distributed throughout the world's oceans and warming is maximum at the surface, but it is also more intense in the Southern and Pacific Oceans (Cheng et al., 2020). The global ocean warmed by 5.4 and 4.0 ZJ per year between 2005 and 2017 in the upper 0-700m and 700-2000m of the ocean, respectively (Bindoff et al., 2019). The Southern Ocean is especially responsive to global warming; an estimated 35-43% of global ocean heat content increase between 1970 and 2017 (0-2000m) occurred within the Southern Ocean (Cheng et al., 2020). This is likely due to internal variability shifting heat from the northern to the Southern Hemisphere (Rathore et al., 2020). The IPCC reports that ocean warming will continue over the 21st century, however by the mid-21st century the scale of warming begins to be scenario dependent (Cooley et al., 2022).

Emissions projections are crucial for exploring future ocean conditions under climate change. The four Representative Concentration Pathway (RCP) scenarios, RCP2.6, RCP4.5, RCP6.0, and RCP8.5, used until the 5th Assessment report of the IPCC, each describe a different trajectory of greenhouse gas concentration and associated radiative forcing levels (with the RCP number indicating the radiative forcing in W/m^2) by the year 2100 (van Vuuren et al., 2011). Following from RCPs, the Shared Socioeconomic Pathways (SSPs) were developed and published in 2017 (Riahi et al., 2017) and used in the IPCC 6th Assessment report. The SSPs are scenarios of societal change that provide both qualitative and quantitative descriptions of alternative future socioeconomic developments. The SSPs consist of five narratives, each with a set of driving forces, and they aim to quantify developments in energy, land-use, and the associated uncertainties for greenhouse gas and air pollutant emissions in a consistent manner (Riahi et al., 2017). Under the RCP 2.6 and 8.5 scenarios, models predict the ocean (0-2000m) will warm by ~0.40°C and ~0.78°C, respectively, by the end of the century (Cheng et al., 2019). However, there is an anticipated reversal in the magnitude of ocean warming between the hemispheres, with a trend towards a higher rate of warming in the Northern Hemisphere compared to the Southern Hemisphere, which is largely attributed to a reduction in the asymmetric cooling influence of aerosols, projected to decrease this century (Shi et al., 2018). CMIP5 models project increases of around 4°C in the Northern Hemisphere and 2.8°C in the Southern Hemisphere from the period of 1975 to 2100 (RCP 8.5; Ruela et al., 2020). Such projections underscore a gradual shift towards warmer conditions in the Northern Hemisphere.

1.4.2. Acidification

Global surface pH has declined from 8.21 to 8.10 since pre-industrial times (Doney et al., 2009), at a rate of between -0.017 to -0.027 pH units per decade since the late 1980s (Canadell et al., 2021). The acidification of the oceans influences the depth at which calcium carbonate ($CaCO_3$) dissolves in the ocean (so called saturation horizon). Like temperature, acidification does not occur uniformly across the ocean basins, and its effect on the saturation horizon of $CaCO_3$ also differs regionally. The $CaCO_3$ saturation horizon is shallowing at a faster rate than the global average in the Southern Ocean because of the large absorption of anthropogenic CO_2 in that region (Petrou 2023). Excess carbon dioxide (CO_2) in the ocean, reacts with water (H_2O] to produce carbonic acid [H_2CO_3] in the following chemical reaction:

$$CO_2 + H_2O \longleftrightarrow H_2CO_3 \longleftrightarrow HCO_3^- \longleftrightarrow CO_3^{2-} + 2H^+ \qquad Equation\ 1.1$$

The weak carbonic acid then breaks into carbonate and hydrogen ions. This excess hydrogen then reacts with carbonate to form bicarbonate. Despite faster rates of CO_2 absorption into the Southern Ocean, the concentration of carbonate ions [CO_3^{2-}] in the surface ocean has declined more in the tropics in comparison, by 29 umol kg^{-1} vs 18 umol kg^{-1}, respectively (Orr et al., 2005). The rate of pH change is also likely to accelerate as the buffering capacity of the ocean is diminished further under rising atmospheric CO_2 levels. Polar and subpolar waters are likely to become undersaturated with respect to carbonate ions within the next 50 years (Orr et al., 2005). Furthermore, certain subtypes of carbonate ions, such as aragonite produced by pteropods, are more sensitive to dissolution and so saturation states of these ions are expected to decrease faster. In the Southern Ocean the saturation state of aragonite is expected to decrease by 50% under RCP8.5 by the end of the century (Orr et al., 2005). However, acidification does not continue to decrease in low-emissions scenarios such as SSP1-1.9 and SSP1-2.6 (Cooley et al., 2022). This highlights the variability of changes in response to different climate emission scenarios.

1.4.3. Deoxygenation

Warming oceans have resulted in wide scale deoxygenation since the 1960s (Bindoff et al., 2019). Solubility reduction due to warming oceans are responsible for ~50% of the deoxygenation observed in the upper 1000 metres (Oschlies et al., 2018). Other changes such as increased bacterial respiration in response to increasing temperatures and nutrient-induced algae blooms also contribute to deoxygenation (Limburg et al., 2020). Despite agreement that ocean oxygen has declined since the 1960s, there is wide disagreement on the scale of the decrease. Schmidtkø, et al., (2017) estimate the global oxygen content has decreased by ~2%, or 4.8 ± 2.1 P mol O_2 in the upper ocean (0-1000m),

since 1960. In contrast, Ito, et al., (2017) estimates that the loss was only 1.46 ± 0.75 P mol O_2 between 1958 and 2015. Similarly to ocean temperature and acidification, loss of ocean oxygen and associated drivers are highly variable across ocean regions. Roughly 25% of oxygen loss has been attributed to the upper 1000m of the Southern Ocean (Helm et al., 2011). Despite the Arctic containing less than 1.2% of the global ocean oxygen content, loss of oxygen in the Arctic (from 1960-2015) accounts for 7.6 ± 3.1% of the global oxygen loss (Schmidtko et al., 2017). However, the largest and most widespread declines have been observed in the subpolar north and tropical regions (Ito et al., 2017). Below 1000m, the Arctic, Equatorial regions, north Pacific and Southern Ocean show the greatest declines, and overall contribute to more than 60% of the total global decline of ocean oxygen (Schmidtko, et al., 2017). In coastal areas the main driver of deoxygenation is anthropogenic eutrophication via runoff and nutrient deposition (Canadell et al., 2021).

Prior simulations with global ocean biogeochemistry models have failed to replicate low-latitude oxygen minimum zones (OMZs; Andrews et al., 2013). It is not surprising therefore that there is large disagreement on the size of the expansion of OMZs in model simulations over this century. Some models predict that OMZs will expand perpetually as a result of increases in N_2O production due to lower oxygen concentrations and stratification under RCP8.5 (Oschlies et al., 2008). Furthermore, Ito et al., 2017 predict that due to rising C : N ratios of sinking organic matter, the global volume of suboxic waters is expected to rise by 50% by the end of the century. In contrast, one model predicts that expanding OMZs will begin to shrink after 2100 (Fu et al., 2018). Continuing development of models and their incorporation of suitable biogeochemical processes will help constrain predictions of OMZs.

1.4.4. Stratification

The upper ocean mixed layer controls in part the transfer of CO_2 to the deep ocean (Bopp et al., 2015), and thus plays an important role in the climate system. Stratification has increased globally by 5.3% between 1960 and 2018, at a rate of 0.90% per decade (Li et al., 2020). Over 90% of this increase in stratification is caused by increases in sea surface temperature (SST), however changes in salinity also have significant regional impacts at high latitudes (Li et al., 2020). Decreases in salinity at high latitudes from the enhancement of the water cycle result in reduced density in the upper ocean and an increase in density stratification; this effect also reduces the strength of vertical mixing (Yamaguchi and Suga 2019). An estimated 6.1% of the global mean stratification observed in recent decades is due to freshening-induced reduced surface ocean density (Yamaguchi and Suga 2019). In addition, freshening-induced stratification is largest in the north Pacific and north Atlantic where 9.2% and 7.2% of the stratification can be attributed to increases in wintertime density stratification (Yamaguchi and Suga 2019). In addition, in the Southern Ocean, changes in salinity contribute more significantly to long-term density alterations than surface warming effects (Yamaguchi and Suga

2019). However, changes in stratification are controlled by complex physical processes which include turbulence from high winds in addition to buoyancy fluxes, which vary among regions.

In the Atlantic Ocean, stratification effects of SST alone should, in theory, induce 1.6 times more stratification than the observed changes (Li et al., 2020). However increases in salinity increase sea surface density and decrease stratification, offsetting the effects of SST rise (Li et al., 2020). Furthermore, Salée et al., (2021) found that the average summertime MLD increases in the Northern Hemisphere despite the strengthening of summer pycnocline stratification. Pycnocline refers to the depth of the ocean where there is a sharp density gradient due to variations in temperature and salinity. The deepening of the mixed layer in these areas is thought to be due to the amplification of surface turbulence, which counteracts the enhanced stability beneath the MLD (Sallee et al., 2021). It is very likely that the stratification in the top few hundred metres of the ocean will rise significantly in the 21st century throughout all ocean basins, owing to increased surface warming and freshening in the near-surface layers at high latitudes (Cooley, et al., 2022).

1.4.5. Nutrients

Nutrients concentrations in the ocean are controlled by ecosystem processes, ocean currents, upwelling, stratification, river influx and dust deposition. Ocean regions are often categorised according to the least available nutrient as availability of this most limiting nutrient will control phytoplankton growth in the region, recognising also interlinkages among nutrients (Tagliabue et al., 2017). In the Southern and sub-Arctic Pacific oceans, iron is generally the limiting nutrient, whereas in the low-productivity tropical regions, nitrogen and phosphorus are generally the limiting nutrients (Bindoff, et al., 2019). The increase of nutrients by atmospheric deposition due to anthropogenic emissions may partly oppose the effects of stratification which upwelling and nutrient supply. For example, nitrogen levels increased in the north Pacific (1988-2011) increased the N : P ratio and induced a shift towards phosphorus limitation (Bindoff, et al., 2019). This increase is driven primarily by atmospheric deposition, which has more than doubled in the past 100 years globally (Kim et al., 2014). Furthermore, increases in iron concentrations in high-nutrient low-productivity (HNLP) regions characterised by iron limitation has occurred due to increased deposition, as well as ocean circulation and mixing changes (Nishioka et al., 2021). Regionally, atmospheric deposition of nutrients increased ocean productivity, especially in low-nutrient low-latitude regions. Ocean productivity increases of 3% globally and up to 25% regionally can be attributed to increases in deposition (Ren et al., 2017). However, whilst previous studies have predominantly focused on dust as the main source of iron in ocean biogeochemical cycles, Tagliabue, et al., (2017) have highlighted a more complex picture. They reveal that the ocean iron cycle involves a variety of biological, chemical, and physical processes that contribute to iron's cycling and distribution. These processes include the subduction and spreading of iron signals across different water mass density layers, affecting local phenomena interpretation (Tagliabue, et al., 2017).

1.5. Recent and Predicted Changes in Ocean Ecosystems

1.5.1. Impacts of Physical Ocean Changes on Phytoplankton

The synergistic and varied effects of climate change across ocean regions combined with the diversity of phytoplankton sensitivity, mean that wide scale changes in phytoplankton communities are likely to be varied across ocean regions. Projections of NPP and EP this century do reflect some diversity of responses, but there appears to be a consensus based on existing models on the direction of change towards decreasing export flux under RCP8.5 by 2100 (Figure 1.2). 90% of models agree within the

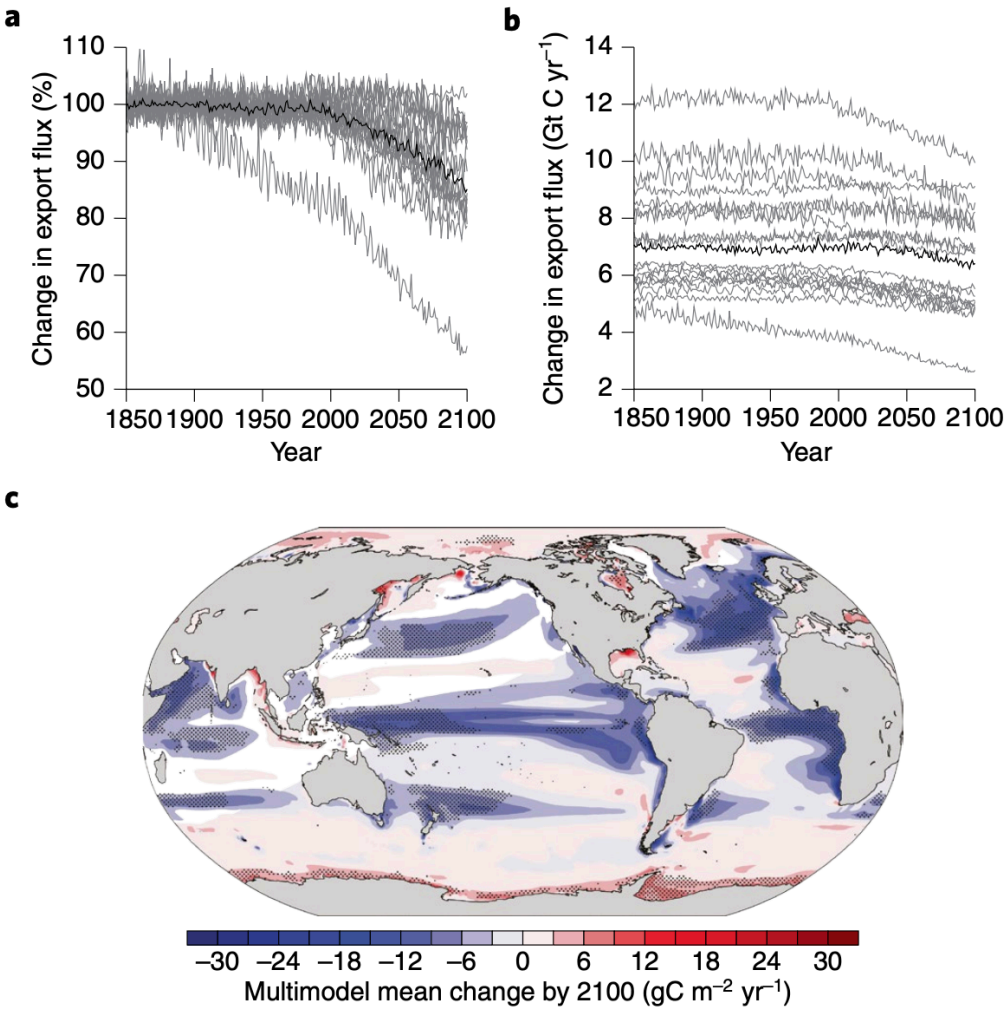

Figure 1.2. Figure reproduced from Henson, et al., (2022). This figure shows the impact of climate change on export flux, using data from 19 coupled climate models under the high-emission SSP5–8.5 scenario from the CMIP6 archive. It shows time series for both the a) percentage and b) absolute changes in globally averaged export flux, with changes calculated relative to the 1850–1900 mean for each model. The multi-model mean is represented by a thick black line. Additionally, the figure includes in c) a multimodel mean of the change in export flux between 2080–2100 and 1850–1900, with hatching marking areas where at least 90% of the models (17 out of 19) agree on the change's direction.

hatched areas (Figure 1.2) that decreases in export are likely in the low and mid- latitudes, whilst agreement in increases are apparently in the Southern Ocean. However, global declines in export flux range significantly between -41 and 1.8% (Henson, et al., 2022), and models include relatively simple representations of ocean ecosystems.

Ocean warming has already had direct impacts on ocean ecosystems. Temperature changes influence most growth and loss rates by phytoplankton and zooplankton. The overall ecosystem changes in response to a change in temperature is thus complex. Declining phytoplankton concentrations, as well as expansion of low-chlorophyll areas, have been observed in the equatorial zone between 1998 and 2006 (Polovina et al., 2008). Shifts in range boundaries have been observed in a wide range of species, from phytoplankton and zooplankton, to fish and mammals (Bindoff, et al., 2019). Furthermore, thermal niches of phytoplankton are usually wider in the tropics than in high-latitudes, suggesting increasing SSTs alone may be sufficient to induce a shift in the composition of existing phytoplankton communities (Anderson et al., 2021). Most models project a shift towards smaller phytoplankton under future ocean conditions (medium confidence; Canadell et al., 2021). Increasing ocean temperatures have also resulted in deoxygenation, stratification and changes in nutrient supply, which act both synergistically and opposing temperature changes.

Decreases in carbonate ion availability due to ocean acidification have resulted in shell dissolution of pteropods and other shell building organisms, such as coccolithophores, molluscs, echinoderms, corals and coralline algae (Doney et al., 2009). Pteropods which form tests (shells) of aragonite, a particularly soluble form of calcite, may be especially vulnerable to changing ocean pH (Bednaršek et al., 2012). Comparatively, coccolithophores may be more resilient to ocean acidification as their ability to utilise both bicarbonate ions and carbonate ions to build shells may limit the impact of reduced carbonate ion availability (Krumhardt et al., 2019; Ries et al., 2009). In addition, as coccolithophores construct their shells intracellularly, they may be able to buffer the impacts of dissolution during shell production (Brownlee et al., 2021). These trends in decreasing ocean pH and effects on ecosystems are likely to continue as long as atmospheric CO_2 concentration continues to rise. Studies project that the Southern Ocean will become corrosive to calcifying organisms by 2100 under RCP8.5 (Bindoff et al., 2019). Whilst the counter carbonate pump increases CO_2 in the upper ocean, the sinking of high density carbonate shells may serve as a ballast thereby increasing EP and EF (Neukermans et al., 2023). Therefore, understanding how dissolution of calcifying organisms may affect export under climate change is important for understanding carbon export.

Large scale deoxygenation is likely to have significant impacts on ocean ecosystems living in low-oxygen areas (including extensive parts of the tropics and many coastal areas), particularly when considering synergistic interactions with other ocean changes. Despite acidification and temperature being the focus of coral extinction studies, mass coral bleaching events have also been recorded following acute anoxic events (Hughes et al., 2020). In addition, during anoxic events pteropods

migrate to cooler waters to reduce metabolic rates and conserve energy, a behaviour that's likely to become less effective due to increasing SSTs (Bednaršek et al., 2016). Suppression of reproduction and growth caused by warming alongside anoxic events, combined with shell dissolution as a result of acidification, is likely to have significant population level consequences on pteropods (Manno et al., 2017). High productivity due to nutrient influx can also result in intense anoxic events (Bristow et al., 2017), highlighting the synergistic effects of climate change on the ocean.

This changing distribution of nutrients is likely to have major impacts on the growth and distribution of phytoplankton by the end of the century. Global primary production declined by >6% between 1981 and 2002, and by 2.1% between 1998 and 2015 (Gregg et al., 2003; Gregg and Rousseaux 2019). This decrease is linked to a reduction in surface MLD by 2.4% per decade and a decline in nitrate concentrations by 3.2% per decade (Gregg and Rousseaux 2019). Whilst ocean stratification does reduce the vertical supply of nutrients to the surface, it may also act to alleviate seasonal light limitation in the high-latitudes (Canadell et al., 2021). As a consequence, changes in nutrient concentrations are not regionally consistent across the global ocean. Locally the increase of nutrients by atmospheric deposition may oppose the nutrient limiting effects of stratification. For example, in the south China Sea elevated nitrogen levels between 1988 and 2011, driven primarily by atmospheric deposition, induced a shift towards phosphorus limitation (Kim et al., 2014). Furthermore, the magnitude of changes in primary production rates are likely to increase under climate change and strengthening stratification. Global prediction models anticipate a 6% decrease in primary production by 2090 (Kwiatkowski et al., 2020; Misumi et al., 2014). This decline is largely driven by changes such as increased thermal stratification and reduced upwelling intensity, especially in permanently stratified tropical oceans. However, in HNLP regions primary production is expected to increase by 11% (Misumi et al., 2014). Increased iron supply is responsible for 50% of the expected 11% rise in primary production in HNLP regions (Misumi et al., 2014). Increases in iron supply and reduction in iron limitation in HNLP regions may offset some of the decrease in NPP and EF due to climate change in other ocean regions.

1.5.2. Biogeographic Shifts

Large scale biogeographic shifts have already occurred and are expected to intensify under increasing atmospheric CO_2 concentrations. A meta-analysis revealed that marine species (80% ectotherms) move polewards by ~6 km yr^{-1} (Lenoir et al., 2020; Canadell et al. 2021). Stuart-Smith, et al., (2015) found that 33% of marine ecoregions analysed exceeded the upper limits of the thermal niches of 100% of species by 2125, under RCP8.5. This is important as species are more likely to experience range shifts and phenological changes than to evolve to their changing environment in-situ (Ji et al., 2010). An analysis by Barton, et al., (2016) which assessed 87 north Atlantic diatom and dinoflagellate species, predicted that community structure will change basin-wide by 16% in 2051-2100 compared to 1951-2000 under RCP8.5. They found that 74% of analysed taxa move polewards at a median

range of 12.9 km decade^{-1} under RCP8.5 between whilst 90% of taxa shift eastward (median range 42.7 km dec^{-1}) (Barton, et al., 2016). In addition, taxa that live in more southerly north Atlantic waters are more likely to experience larger shifts in geographic ranges. For example, dinoflagellates, often found in warmer, more stratified waters with lower nutrients, are predicted to have a greater northward expansion than diatoms (Barton et al., 2016).

Polar communities are likely to experience invasions concurrently with equatorial communities experiencing local extirpation due to the predicted movement of equatorial species polewards to escape warming waters. Beaugrand, et al., (2015b) assessed the future vulnerability of plankton species by comparing future distribution predictions (2081-2100) of four RCPs in 5 ocean general circulation models to a historic reference period (2006-2013). They found that ~94% of the global ocean experienced biodiversity changes of greater than 5%, under RCP8.5 (Beaugrand, et al., 2015b). The rate of biodiversity change is predicted to exceed changes recorded between the Mid-Pliocene (5.3 to 2.58 million years ago) and today in ~70% of the ocean under RCP8.5 (Beaugrand, et al., 2015b). Such extreme shifts in planktonic organism ranges and biodiversity have never been observed over such a short time frame in the earth's history. These shifts in response to ocean warming are expected to have major impacts on ecosystem services and provisions. In particular, those who rely on ocean services and historical ocean knowledge to provide traditional foods may be particularly vulnerable to ocean changes (Bindoff et al., 2019). In addition, whilst some studies have demonstrated that organisms may have the capacity to respond to environmental changes through adaptation, historical records show that adaptation is not always sufficient to mitigate impacts and that biogeographic range changes and phenological shifts are most likely to result from environmental changes (Bindoff et al., 2019; Ji et al., 2010).

1.5.3. Changes in Phenology

In response to both the physical, chemical and biodiversity trends in recent decades, the timing of seasonal activity (phenology) of marine organisms has shifted (Bindoff et al., 2019; Canadell et al., 2021). A meta-analysis of observed shifts in phenology caused by warming of the ocean demonstrate that shifts in ocean ecosystems are the same or more extreme than those observed in the terrestrial ecosystem in recent decades (post-1990; medium length = 19 years; Poloczanska et al., 2013). Spring growing periods appear to be advancing by between 2.8-4.4 days per decade, and in high latitudes this observed change in the spring temperature timings is greater than that on land (Hoegh-Guldberg et al., 2018; Poloczanska et al., 2013). In contrast, autumn and winter blooming species were shown to be delayed by 6.5-8.4 days per decade (Hoegh-Guldberg et al., 2018; Poloczanska et al., 2013). Globally, blooms were found to start earlier in all regions except the north Atlantic and tropical Indian oceans between 1998 and 2015 (Friedland et al., 2018). The duration of primary bloom became longer in all regions other than the north Atlantic, increasing by an average of 23 days in Oligotrophic regions (Friedland et al., 2018). Whilst duration increased globally, the magnitude and intensity of the

bloom decreased in the tropics and increased in the high-latitudes (Friedland et al., 2018). In contrast, Racault et al., (2012) identified mostly negative trends in duration. However the time period used in this analysis began with two strong El Niño years which likely altered the trends. In comparison, the relationship between increases in SST and duration anomalies between 1998 and 2007 (Racault, et al., 2012) is remarkably similar to the trends seen between 1998 and 2015 in Friedland, *et al.,* (2018). This suggests that current phytoplankton assemblages have predictable responses to SST. Both studies agree that duration is likely to increase in the poles and decrease at low-latitudes due to warming temperatures.

Trends in phenology are not only evident globally, but also from localised studies. In the Arctic, earlier ice melts resulted in earlier growing period initiation and later termination of open ocean blooms, increasing annual net primary production by 30% between 1998 and 2012 (Ardyna and Arrigo 2020). Prior to 2012 chlorophyll concentrations were relatively constant (0.27 % yr^{-1}), however between 2012 and 2018 concentrations increased at a rate 16 times faster than between 1998 and 2012, despite the rate of increase in bloom duration decreasing (Ardyna and Arrigo, 2020). Conversely, in the Barents sea shallower MLD was found to trigger earlier growing periods with higher amplitude that terminate *earlier* due to lack of nutrient upwelling (Silva et al., 2021). Furthermore, Regions north of 50°N in the north Atlantic, Gulf of Alaska and south Chukchi Sea saw a significant increase in the proportion of double growing periods within a year between 2003 and 2020 (Zhao et al., 2022). Zhao et al., (2022) suggest that double growing periods in high-latitudes will become more prevalent in future oceans potentially caused by changes in the ecological succession in calcifiers and other groups. In contrast, in the northern Red Sea, warming temperatures resulted in growing periods initiated ~1-4 weeks later and bloom duration became ~4 weeks shorter between 1998 and 2015 (Gittings et al., 2018). Due to the higher level of stratification observed under warmer temperatures, Gittings, *et al.,* (2018) hypothesise that the increase in SST resulted in slower nutrient transfer to the surface due to less vertical mixing in the winter. Finally, in the Southern Ocean phytoplankton exhibited increased amplitude and reduced seasonal variability, alongside delayed initiation, advanced termination, and a shortened duration of growth periods between 1998 to 2022 (Thomalla et al., 2023b). By 2100, under the scenarios SSP1-2.6 and SSP5-8.5, approximately 18.8% and 38.9% of the ocean, respectively, are likely to experience a shift of more than 20 days in the beginning of the phytoplankton growth period, with this estimation carrying a low degree of confidence (Canadell et al., 2021).

Large-scale changes in marine phenology are expected in the future under a warming climate, but projected changes differ based on model representation of trophic interactions. At high latitudes, the spring bloom advanced by 50-100 days by 2100 under RCP8.5 in a model simulation (HadGEM2-ES forcing NEMO-MEDUSA-2.0 model; Henson et al., 2018). In subpolar regions, the initiation dates became later towards the end of the century (Henson, et al., 2018), consistent with the observed expansion and intensification of oligotrophic conditions (Henson, et al., 2018). Another study

identified that all of the ocean underwent an advance in bloom initiation, except the tropical Pacific between 1990 and 2100 under RCP8.5 using a 30-member large ensemble simulation with GFDL-ESM2M (Yamaguchi et al., 2022). However, both studies lack sufficient phytoplankton and zooplankton complexity. The MEDUSA-2.0 biogeochemical model represents a medium complexity ecosystem with two phytoplankton and two zooplankton plankton function types (PFTs; Henson et al., 2018). Whereas the ESM2M biogeochemical component (TOPAZ2) represents three phytoplankton groups and one allometric zooplankton group (Yamaguchi et al., 2022). Sufficient representation of phytoplankton and zooplankton groups is important to accurately represent ecosystem phenology and associated processes.

Increasing representation of zooplankton from one to three zooplankton functional types in a global model induced faster nutrient recycling that sustained higher concentrations of chlorophyll over summer and autumn (Karakuş et al., 2021). Furthermore, in the Southern Ocean the additional top-down control exerted by zooplankton delayed the initiation of the spring bloom by three weeks and controlled the magnitude of the growing period (Karakuş et al., 2021). In a separate model study, shifts in phytoplankton growing period timing were found to be in part a result of increased zooplankton predation, despite only representing one allometric zooplankton in the model system (Yamaguchi et al., 2022). In addition, increasing zooplankton complexity in a model system resulted in a 25% increase in NPP and a 10% decrease in EP (Karakuş et al., 2021). In contrast, mis-matches between trophic levels, referred to as decoupling, can result in high-EF in low-productivity regions as large-aggregates are not subject to grazing and disaggregation (Henson et al., 2019). This highlights the importance of zooplankton representation in a model system. Large scale changes in phenology are likely to be varied across phytoplankton and zooplankton, representing a potential for large-scale disruptions in ecosystem structure.

1.6. Implications of Changes in Ocean Ecosystems for Trophic Mismatches and Carbon Export

As the base of the marine food web, phytoplankton fundamentally support all life in the ocean. Changes in phenology and primary production are likely to have severe consequences for species of higher trophic levels. Trophic mismatch between primary and tertiary production has already occurred due to changes in the timing of phytoplankton growing period and amplitude (Edwards and Richardson 2004). For example, delayed growing periods have led to reduced fish stock recruitment due to reduced food supply for larvae (Asch et al., 2019). In addition, in the Beaufort Sea delayed ice melts have been found to result in mismatch between herbivorous copepods and microalgae (Dezutter et al., 2019). Effects of physical or chemical ocean changes on zooplankton are also likely to be exacerbated by a decrease in food supply. In Sitka Sound, Alaska, seasonal shifts in phytoplankton exacerbated effects of increased energetic demands due to warmer winters in pinto abalone (Kroeker et al., 2020). In the Baltic Sea demands of naturally low phytoplankton biomass during

winters combined with ocean warming results in strong declines in growth in mussels (Melzner et al., 2020). In the Strait of Georgia, periods of early growth correlated with an increased abundance of crustaceans, yet this was characterised by a lower overall biomass, predominantly comprising smaller taxa (Suchy et al., 2022). Canadell, et al., (2022) suggests that increased severity of changes in the timing of the growing period increases the risk of temporal mismatch between phytoplankton growing periods and fish spawning periods. Due to the importance of ecosystem structure on the BCP, it is likely that changes in communities will induce changes in the EP and EF.

Long-term trends in phenology and primary production, as well as future model projections, suggest that increasing temperatures, stratification and nutrient limitation may lower carbon EF (Bindoff et al., 2019; Bopp et al., 2015). Multi-model averages project a decline of integrated primary production by ~3% between 2080 and 2099 relative to 1870-1988 under RCP5-8.5 (Bopp et al., 2013). This decline is mostly expected at low-latitudes due to nutrient limitation driven by stratification, with increases in primary production expected in high-latitude regions due to increases in light availability (Bindoff et al., 2019). However, models strongly disagree on the direction of change, with one standard deviation from the multi-model mean ranging from -6% to 12% (Kwiatkowski et al., 2020). Most models don't include sufficient zooplankton complexity to represent the effect of top-down control by grazing on phytoplankton populations, which controls the duration of the growing period alongside nutrient availability. Furthermore, models that allow for shifts in phytoplankton community structure show larger declines in EP than in primary production due to the trend towards small body size in warmer temperatures (Fu et al., 2016). Increasing phytoplankton and zooplankton community representation in models is likely to alter future projections of export flux significantly (Tréguer et al., 2017).

1.7. Modelling Ocean Ecosystems

1.7.1. NPZD

NPZD models are simple ecosystem models that simulate the interactions between four components: Nutrients, Phytoplankton, Zooplankton and Detritus. The nutrient component of the model normally consists of dissolved inorganic nitrogen (Heinle and Slawig 2013; Priester et al., 2017). Priester, *et al.,* (2017) developed an NPZD model (nitrogen, phytoplankton, zooplankton, detritus) using an optimal control approach and successfully able to reproduce plankton distributions in Iron limited HNLC regions from observed distributions. However, the plankton distribution is only representing one group of phytoplankton and one of zooplankton. This is problematic because different taxa of phytoplankton and zooplankton react differently to climate-induced changes in the ocean (Barton et al., 2016; Beaugrand et al., 2015b; Bindoff et al., 2019; Dutkiewicz et al., 2015). Therefore, whilst NPZD models may be able to predict general ecosystem changes, they are unsuitable for assessing complex ecosystem community changes, as there is no competition for nutrients between groups, an interaction that has been observed in real ecosystems. Furthermore, NPZD models are usually

assessed in transects (Priester et al., 2017) or used to assess a specific region (Arellano and Rivas 2019; Dorantes-Gilardi and Rivas 2019; Song et al., 2016), and no longer at a global scale.

1.7.2. ECCO-Darwin Model

In addition to process models, data assimilation has been used to produce hybrid models that are nudged towards observations. ECCO-Darwin (ED) is one of the most recently developed Global OBMs (GOBMs) that uniquely employs a data assimilation technique to combine observational and model output data to create an optimal estimate (Carroll et al., 2020). The model consists of a physical component (1 degree) coupled to a biogeochemical component with 39 “prognostic variables'' which are distributed by the ECCO physical fields (Carroll et al., 2020). ED includes seven Plankton Functional Types, consisting of five phytoplankton (diatoms, other large eukaryotes, the cyanobacteria *Synechlorococcus,* and low-light and high-light adapted cyanobacteria *Prochlorococcus*) in addition to two zooplankton functional types, one which consumes mostly large eukaryotes and the other which consumes mostly small pico-phytoplankton (Carroll et al., 2020). Chemical cycles represented in the ECCO-Darwin model include the carbon cycle, alongside nitrogen, phosphorus, iron, silica, oxygen and alkalinity, however there are no feedback loops present between this biogeochemistry and the model circulation (Carroll et al., 2020). The Global Carbon Project estimates the global ocean CO_2 sink at -2.24 ± 0.76 PgC yr^{-1} (1995-2017), aligning with the ED model, which also mirrors patterns in equatorial Pacific surface ocean pCO_2 and high latitude uptake (Carroll et al., 2020). However, ED's Southern Ocean CO_2 sink is significantly larger than other models, potentially due to inaccuracies in winter mixed layer dynamics, raising concerns about ED's effectiveness in Southern Ocean analysis (Keppler and Landschutzer 2019).

ED is a complex model which accurately represents the majority of chemical systems in the ocean, however the model has low ecosystem complexity with three of its five phytoplankton groups representing cyanobacteria (Carroll et al., 2020). In addition, the ED model only represents two zooplankton functional types. This is problematic because analysis by Le Quéré et al., (2016b) suggests that grazing by zooplankton controls summer Southern Ocean Chlorophyll; this may limit the ED models ability to accurately represent summer phytoplankton concentrations.

1.7.3. The PlankTOM12 Model

Dynamic Green Ocean Models (DGOMs) have been proposed as a pragmatic way to represent multiple groups of species using observed vital growth and loss rate (Hood et al., 2006; Le Quere et al., 2005). DGOMs were created in an attempt to capture the complexity and interactions within ecosystems that were omitted in previous generations of models, in the context of a changing climate and ocean environment. The development of DGOMs was inspired by terrestrial modelling effects using Dynamical Global Vegetation Models (DGVMs), which group diversity within Plant Functional Types. DGOMs group organisms into PFTs. Le Quéré, et al., (2005) argued that a PFT should be

represented for groups of organisms which: a) contribute significantly to biogeochemical processes in the ocean; b) have distinct and coherent physiological, environmental or nutrient requirements which control their growth; c) have 'distinct' effects on the other PFTs (e.g. mortality by grazing); and d) are important to at least some of the ocean. DGOMs have enhanced detailed assessments of the biological carbon pump (Hauck and Volker 2015), the contribution of micro- and meso-zooplankton to biogeochemical fluxes (Buitenhuis et al., 2006; Buitenhuis, et al., 2010), the importance of ecosystem structure in biogeochemical dynamics (Manizza et al., 2010), the contribution of pteropods to shallow $CaCO_3$ export (Buitenhuis et al., 2019), and most recently, the contribution of gelatinous zooplankton in regulating marine ecosystems (Wright et al., 2021) alongside comprehensive analyses of carbon uptake kinetics (Heinze et al., 2015; Le Quéré et al., 2010).

DGOMs represent an approach in global ecosystem modelling to categorise and simulate the functional diversity of plankton communities. However, even these advanced models often neglect key plankton traits such as size within PFTs, physiological plasticity, acclimation, and evolutionary adaptation, which are evident in natural environments. Physiological plasticity enables plankton to adjust their physiological traits in response to varying environmental conditions, including changes in temperature, light, and nutrient availability (Allen and Polimene 2011; Morley et al., 2024). For instance, studies have shown that certain species of diatoms can alter their cellular chlorophyll content and photosynthetic capacity in response to varying light conditions (Fisher et al., 2020; Zhou et al., 2021). This goes beyond existing model parameterisations such as that included in the PlankTOM model, which accounts for chlorophyll-light-iron interactions among PFTs, but not within PFTs. Additionally, coccolithophores have demonstrated the ability to modify their calcification rates under different CO_2 concentrations, which is a critical response to ocean acidification (Feng et al., 2018; Meyer and Riebesell 2015). Despite its prevalence in natural settings, DGOMs typically employ fixed trait values within PFTs, which may create discrepancies in responses to environmental change. This limitation could lead to inaccuracies in model predictions, particularly under scenarios of rapid environmental change, such as ocean warming and acidification (Allen and Polimene 2011).

In addition to physiological plasticity, acclimation represents another important process often overlooked in DGOMs models. Acclimation involves short-term physiological adjustments that allow plankton to optimise their metabolic processes under different environmental conditions (Schaum and Collins 2014). Evidence of acclimation is observed in various plankton species, which demonstrate changes in metabolic rates and photosynthetic efficiency in response to shifts in temperature and nutrient levels (Fernandez-Gonzalez et al., 2020; Winder and Sommer 2012). For example, diatoms have been observed to acclimate to changes in temperature and light availability, maintaining their productivity even in low light conditions (Fisher and Halsey 2016; Gleich et al., 2020; Torres et al., 2013). By not incorporating these adjustments, DGOMs models may misrepresent plankton productivity and survival, especially during periods of abrupt environmental shifts.

Furthermore, evolutionary processes, which drive long-term genetic adaptations within plankton populations, are typically excluded from these models due to modelling complexity. This oversight is particularly concerning in the context of climate change, where evolutionary adaptations could significantly alter plankton community composition and ecosystem functioning (Ward et al., 2019). Studies have shown that evolutionary adaptations in plankton can occur over relatively short timescales (<15 years Irwin, et al., (2015)), influencing traits such as thermal tolerance and nutrient utilisation (Andersson et al., 2023; Collins et al., 2014; Thomas et al., 2012). For instance, the coccolithophore Emiliania huxleyi, has shown rapid evolutionary responses to increased CO_2 levels, resulting in altered calcification processes (Lohbeck et al., 2012). Neglecting these evolutionary dynamics could result in biases in predicting the range shifts and population declines in phytoplankton in future warming conditions. Incorporating physiological plasticity, acclimation, and evolution into PFT-based models may be an important next step for improving the accuracy of predictions regarding plankton responses to environmental variability, thereby enhancing our understanding of marine ecosystem resilience and functioning in a changing climate.

While evolutionary adaptations may provide significant resilience to environmental changes, there is evidence that the rate of environmental change may outpace plankton's ability to adapt. This limitation in evolutionary capacity is often manifested in the tendency of phytoplankton species to undergo range shifts rather than evolve new physiological traits. Poloczanska et al., (2013) observed that phytoplankton, are adjusting their geographical distributions in response to warming waters, emphasising the trend of range shifts over evolutionary adaptations. Furthermore, Beaugrand (2009) found that calanoid copepods are responding to rising SSTs by migrating northward at a rate of approximately 23.16 km per year. Moreover, the existing genetic diversity within phytoplankton populations may not always provide the necessary variation for adaptation to new environmental conditions. Genetic limitations can constrain adaptive responses, especially in environments where changes occur abruptly and on a scale that outstrips the available genetic diversity (Thomas et al., 2012). This can result in populations that are more likely to experience range shifts as a response to environmental stressors rather than evolve adaptively. Evolutionary responses to climate change are also often limited by the rate at which suitable mutations arise, which can be too slow compared to the rapid changes in climate (Chevin et al., 2010). This results in a reliance on existing genetic variance within populations for adaptation, which may not always be sufficient. Current models that do not include evolutionary adaptations may overestimate the effects of climate change on range and phenological shifts. However, this approach effectively represents a worst-case scenario where no phytoplankton evolve in response to changing conditions, providing a crucial perspective for assessing potential ecological outcomes.

This thesis uses the PlankTOM12 model, which represents 12 PFTs. These PFTs include six phytoplankton, namely: picophytoplankton, N_2-fixers, coccolithophores, mixed-phytoplankton, diatoms, and *Phaeocystis*. PlankTOM12 also includes bacteria and five types of zooplankton, namely:

protozooplankton, pteropods, mesozooplankton, crustaceous macrozooplankton, and gelatinous zooplankton (Le Quéré, et al., 2016; Buitenhuis, et al., 2019; Wright et al., 2022). PlankTOM12 is described in Chapter 2.2. The latest model version, PlankTOM12.2, includes over 50% of the specific mechanisms controlling the export flux outlined by Henson, et al., (2022), namely: fragmentation, phytoplankton size effect on sinking, temperature dependent remineralisation, oxygen dependent remineralisation, as well as mineral ballasting. Missing mechanisms include: zooplankton and fish vertical migration, particle stickiness (including TEP) and variable stoichiometry in sinking particles. However, no currently published models reproduce vertical migration or particle stickiness and only one model represents variable stoichiometry. PlankTOM12.2 therefore should not only provide a more complete representation of the dynamical processes that exist within marine ecosystems than models with less functional types or size classes, but also makes a great tool for understanding changes in phytoplankton phenology and export flux in a warming ocean.

1.8. PhD Objective

The main goal of this thesis is to assess the impact of climate change on phytoplankton phenology and its implication for the export of carbon to depth this century. To achieve this goal, the PlankTOM12 model had to be improved in two ways (Chapter 2). First, the fluxes of organic and inorganic carbon needed to be better parameterised and validated to ensure that the observed attenuation of sinking organic carbon flux to depth, and its associated ballast from calcium carbonate and silicate, were reproduced. Second, the mean phenology of phytoplankton in the PlankTOM12 model needed to be improved significantly. These improvements resulted in the production and publication of the PlankTOM12.2 manual (Buitenhuis et al., 2023; https://doi.org/10.5281/zenodo.8388158). PlankTOM12.2 was then been used to assess the impact of a warming ocean on phytoplankton phenology in past decades (Chapter 3) and the implications of changes in duration and initiation date on carbon export (Chapter 4), and to project the implications of a warming ocean on carbon export when incorporating ecosystem dynamics as represented in this model (Chapter 5).

This thesis aims to:

1. Evaluate the accuracy of the PlankTOM12.2 model in simulating particulate organic, inorganic carbon, and silica fluxes (Chapter 2).
2. Assess the replication of phytoplankton phenology and its trends over the past two decades by PlankTOM12 (Chapter 3).
3. Investigate the effects of changes in phytoplankton phenology on carbon export between 1999 and 2020 (Chapter 4).
4. Explore the response of phytoplankton phenology, ecosystem dynamics, and export under various climate scenarios by 2100 (Chapter 5).

Chapter 2. Model Development and Evaluation

Abstract

In this chapter I introduce PlankTOM12.2, a newly developed version of the PlankTOM model series that is designed to improve the representation of bacterial remineralisation of particulate organic carbon (POC), dissolution of particulate inorganic carbon (PIC) and silica, and seasonality of phytoplankton. I introduced simulations of bacterial biofilms, updated POC dissolution rates, and identified discrepancies in silica export rates and phytoplankton phenology that led to improvements by others. Silica export rates and phytoplankton phenology were improved using a 3-parameter growth model and improved temperature-dissolution curve of silica. These updates to PlankTOM12.2 are shown to deliver major improvements in the representation of PIC, POC and silica export fluxes, as well as the seasonality of surface chlorophyll. The seasonality improvements are particularly relevant for the Southern Ocean, where previous model iterations exhibited a 6-month delay in phytoplankton bloom timing. Remaining weaknesses in the PlankTOM12.2 model include low concentrations of coccolithophore and pteropod in high-latitudes, and low concentration of bacterial biomass. Despite these limitations, improvements made to seasonality and particulate export fluxes within PlankTOM12.2 highlight this model version as a suitable tool to assess changes in phenology of phytoplankton and its impact on POC, PIC and silica export fluxes.

2.1. Introduction

Due to anthropogenic emissions of greenhouse gases, the oceans are experiencing rapid warming, with potential consequences for biogeochemical cycles, notably carbon export to depth. This chapter focuses on the critical need to enhance our modelling capabilities to accurately quantify and predict the ocean's role in sequestering atmospheric CO_2, a process integral to understanding the impacts of climate change. The efficacy of the ocean as a carbon sink is contingent upon the stability of the dynamics of the ecosystem and POC flux. Export efficiency, the ratio of export production (EP) to net primary production (NPP), is controlled by the entire ecosystem community (Laufkötter et al., 2016; Rii et al., 2008). Low export efficiency (EF) is associated with a high concentration of macrozooplankton and bacteria whereas high EF is mediated by a high concentration of aggregates or high faecal pellets (Henson et al., 2019). In addition, dynamic phytoplankton community models show reductions in EF driven by community shifts to smaller phytoplankton class sizes (Fu et al., 2016). However, predictions of changes to export and EF in the face of climate change are uncertain.

Global export flux predictions range from -41% to +1.8% and models disagree on the direction of change in 84% of the global ocean (Henson et al., 2022). This lack of consensus highlights the need for continuous improvements in the modelling of the drivers of NPP and EP to help explain these complex processes. In their 2022 study, Henson et al., highlighted several critical factors that are often inadequately represented in current models concerning the export of POC. These include the fragmentation of particulate matter, the temperature-dependent bacterial remineralisation, the influence of phytoplankton size on sinking rates, oxygen-dependent remineralisation processes, and the role of mineral ballasting (Henson et al., 2022). The PlankTOM12 model, as introduced in Chapter 1.7.3, notably incorporates the above essential processes of carbon export (over half of those outlined by Henson, et al., 2022). Nevertheless, there were four distinct areas within the PlankTOM12 model that required improvements. Addressing these concerns is imperative to enhance the model's capacity for accurate assessments of the response of carbon export to changing ecosystems.

In this Chapter, the PlankTOM12 model developments focus on accurately simulating the processes governing the export of both organic and inorganic carbon, including the role of bacterial biofilms in the remineralisation of POC (section 2.1.1). The incorporation of biofilm-associated bacterial processes in the model aims to improve both the representation of bacterial types in the model, from only plankton-bacteria, and the representation of POC flux. Furthermore, this chapter addresses the refinement of PIC dissolution rates in relation to saturation states (section 2.1.2). By integrating updated dissolution rates based on recent studies (Naviaux et al., 2019), the model now offers a more realistic estimation of PIC export, a critical component of the carbonate counter pump. This is particularly significant in the context of organisms like pteropods and coccolithophores, which play a central role in the marine carbonate cycle and are represented explicitly in the PlankTOM12 model (Buitenhuis et al., 2019). Additionally, the chapter delves into the improved representation of

phytoplankton seasonality achieved through the implementation of a 3-parameter growth model (section 2.1.3). This improvement is important for capturing the complex seasonal dynamics of phytoplankton, which are pivotal in the ocean's carbon uptake and export processes. The nuanced representation of export and seasonal dynamics is expected to yield more accurate predictions of the ocean's response to ongoing climate change.

The aim of this chapter is to describe improvements to the seasonality of phytoplankton and the export fluxes of POC, PIC and of silica in the PlankTOM12 model, and to evaluate the suitability of the resulting PlankTOM12.2 for characterising trends in seasonality and export fluxes in the recent past and in the future. To achieve this, I have:

1. Introduced a representation of biofilm-associated bacteria in POC dissolution in the PlankTOM12.1 model.
2. Updated the equations of PIC dissolution used in the PlankTOM12.1 model.
3. Assessed the effect of improved Plankton Functional Type (PFT) growth rate parameterisations on phytoplankton phenology.
4. Conducted a validation of the combined PlankTOM12.2 model developments with respect to seasonality of phytoplankton and associated export fluxes.

2.1.1. Bacterial Remineralisation of Organic Carbon

Detritivorous bacteria play an important role in remineralising POC in the surface and mesopelagic (100-1000 metres) ocean. Global patterns of POC decay with depth follow a power-law curve called the Martin-Curve, where remineralisation rapidly declines from the surface layer approaching zero at ~1000m (Armstrong McKay et al., 2021). However, POC remineralisation rates vary greatly between regions. In deep polar stations (>2000m), remineralisation between 100-800m was found to exceed surface export of organic carbon (Jacquet et al., 2015). In these regions the efficiency of bacterial remineralisation, the proficiency of bacteria in transforming organic matter into inorganic compounds, controls the extent of deep carbon export. Furthermore, the efficiency of bacterial remineralisation is influenced by physical export pathways (Dall'Olmo et al., 2016; Le Moigne 2019; Taucher et al., 2014), temperature-dependent respiration (Boscolo-Galazzo et al., 2018; John et al., 2014), size of POC (Benner and Amon 2015) and ecosystem community structure (Henson et al., 2019). A comparison between export proxies from the Eocene and early Holocene periods found that higher rates of respiration and nutrient recycling in the Eocene prevented carbon export sediment burial, concluding that increasing respiration in a warming ocean may act as a positive feedback loop that maintains high pCO_2 (Olivarez Lyle and Lyle 2006). This finding suggests that mesopelagic bacterial concentration fundamentally controls the rate of particulate organic carbon export and should be carefully considered in the model ecosystem (Griffith et al., 2021).

Marine bacteria exhibit three primary lifestyles: plankton, biofilm-associated, and intracellular bacterial symbionts (Lu et al., 2023). Bacteria in the plankton lifestyle are simply present in the open water, whereas biofilm-associated bacteria form colonies of phytoplankton on surfaces in the ocean, including marine organisms. Biofilm-associated bacteria are estimated to account for between 10-40% of the total bacterial abundance in the ocean ecosystem (Flemming and Wuertz 2019; Lu et al., 2023). For example, Rhodobacteraceae have been found on diatoms, dinoflagellates and coccolithophores whilst Cytophaga- have been observed to be dominant on marine macro-aggregates (Riemann et al., 2000; Simon et al., 2017). Intracellular bacteria that live within ocean organisms are often symbiotic, providing some benefit to the host cell. For example, the heterocyst-forming cyanobacteria *Richelia intracellularis* provides its host, the diatom species *Hemiaulus hauckii*, with fixed nitrogen that it creates from atmospheric N_2 in the heterocyst (Flores et al., 2022). Biofilm-associated bacteria can also be symbiotic, and can even switch between symbiotic and pathogenic life styles depending on the species and environment. For example, *P. inhibens* exhibits selective pathogenicity towards specific *E. huxleyi* strains, particularly the calcifying and haploid flagellated types (Bramucci et al., 2018). The selective pathogenicity towards calcifying *E. huxleyi* strains could have significant implications for carbon export, as these calcifying cells contribute to the formation of calcite plates, a key component in the marine carbon sink (Bramucci et al., 2018).

The estimated large abundance of biofilm-associated bacteria combined with their pathogenic behaviour towards phytoplankton highlights the importance of biofilm-associated bacteria in the remineralisation of organic carbon. In PlankTOM12.1 (described in Chapter 1), planktonic marine bacteria are represented as a PFT, however concentrations of bacteria are low in comparison to observations (Buitenhuis et al., 2013b). I introduce a simple simulation of biofilm-associated bacterial remineralisation, with the aim of improving bacterial remineralisation in the mesopelagic layer of the PlankTOM12 model.

2.1.2. Plankton Calcification and Carbonate Export

Absorption of carbon dioxide into the ocean results in the production of carbonic acid, which dissociates into hydrogen and bicarbonate ions (Chapter 1, Equation 1.1; (Heinze et al., 2015)). As the ocean becomes more acidic, excess hydrogen ions are produced and bond with carbonate ions (Leung et al., 2022). This reduction represents a decrease in the availability of the building blocks used for calcification which is dominated in the open ocean by pteropods, coccolithophores and foraminiferans (Hofmann et al., 2010). These calcifying organisms control the carbonate counter pump, representing the production and sinking of inorganic carbon in the form of calcium carbonate (Neukermans et al., 2023). Roughly 50% of sinking calcite dissolves by 1000m and the remineralised elements are subsequently redistributed through ocean currents (Neukermans et al., 2023). Whilst coccolithophores were previously thought to be the primary contributor to this ocean carbonate pump, pteropods have been identified as equally important. Despite producing the majority of PIC at

the surface, coccolithophore shells sink slowly on their own, and require aggregation into larger aggregates to sink efficiently (Manno et al., 2018). Conservative PlankTOM12 estimates demonstrate that pteropods are less abundant than coccolithophores but contribute an estimated 38% of shallow (100m) export (Buitenhuis et al., 2019). pteropods may be especially important in high-latitude regions as they are a primary food source in polar food chains, including for zooplankton (Bednarsek et al., 2014; Lischka et al., 2011; Manno et al., 2017). For example, in the Arctic Ocean pteropods contribute 66-96% of the standing stocks of particulate inorganic carbon below 100 metres (Anglada-Ortiz et al., 2021). Together pteropods and Coccolithophores contribute the majority of carbonate export (estimated ~75%) in the global ocean (Buitenhuis et al., 2019).

Furthermore, whilst the calcification of organisms like pteropods and coccolithophores increases CO_2 in the upper ocean, the sinking of their high-density carbonate shells serves as ballast, potentially enhancing the efficiency of the organic carbon pump, as highlighted by Neukermans, et al., (2023). This ballasting effect, predominantly due to PIC mainly composed of calcium carbonate, is essential for the sequestration of carbon in the deep ocean. Klaas and Archer (2002) found that up to 83% of global POC fluxes to the seafloor are associated with calcium carbonate, highlighting its substantial role in the deep-sea organic carbon fluxes. Additionally, Cael et al., (submitted) revealed significant regional variations in opal ballasting, influenced by factors such as upper ocean silica availability and diatom frustule thickness. These findings illustrate the complex interplay between PIC, opal, and regional biogeochemical conditions in facilitating the transport of organic carbon to the ocean's deeper layers.

The efficiency of the carbonate pump may be altered due to ocean acidification, as calcifying organisms may be sensitive to the loss of carbonate ion availability (Kroeker et al., 2010). In fact, the saturation state of CO^{2-}_3 is predicted to decrease by up to 50% by 2250 relative to pre-industrial values under the SRES A1B scenario (~ RCP6.0; Heinze 2004). Pteropods may be especially vulnerable to this loss as they form highly-soluble, thin and delicate shells from aragonite using CO^{2-}_3 ions (Bednaršek et al., 2012). In addition, life cycles of calcifying organisms are likely to be impacted by increased acidity; for example, larval pteropod mortality increased by >38% when exposed to pH conditions predicted under RCP8.5 (Gardner et al., 2018). Moreover, migration towards mid-latitudes in order to escape acidified high-latitude regions may be restricted due to the strict temperature limitations of pteropods (Bednaršek et al., 2016). In contrast, coccolithophores use bicarbonate (HCO_2^-) and calcium ions to create crystalline calcite scales called coccoliths (Krumhardt et al., 2019). The ability to utilise bicarbonate in calcite precipitation may buffer the effects of ocean acidification on coccolithophore populations as carbonate concentrations decrease (Ries et al., 2009). Furthermore, coccolithophores may be able to buffer against the effects of acidification as the process of creating coccoliths is done intracellularly in isolation from surrounding seawater (Brownlee et al., 2021). In addition, increasing photosynthesis due to alleviation of carbon limitation may increase the concentration of coccolithophores despite reductions in calcification (Krumhardt et al.,

2019). Thus changes in pteropod and coccolithophore concentrations are challenging but essential to parameterise within model systems to constrain future impacts of ocean acidification on the carbonate pump.

To accurately assess changes to the carbonate pump as a result of climate change, the factors that control removal and dissolution of sinking pteropods and coccolithophores must be well constrained in models. The amount of calcite that reaches depth is controlled by multiple factors, including grazing by zooplankton, the particle density and the rate of dissolution. The rate of dissolution is controlled by its relationship with the saturation state which is poorly constrained (Naviaux et al., 2019). Previous model estimates of dissolution rate were based on laboratory experiments. Recent studies show that dissolution rates are ~4 times slower in-situ than previous estimates from laboratory studies (Naviaux et al., 2019; Subhas et al., 2017). I identified that these dissolution rates are tenfold slower at any given saturation state compared to the rates applied in PlankTOM12.1 (Naviaux et al., 2019; Subhas et al., 2017). The overestimation of dissolution in PlankTOM12.1 could lead to a significant underestimation of carbonate export in response to ocean acidification in the model. I improved the representation of the carbonate pump by updating the PIC dissolution equations used as part of the PlankTOM12.2 model developments (described in full in 2.2.4).

2.1.3. Phytoplankton Phenology & Associated Changes

Phytoplankton phenology is regionally variable across the global ocean. Short, high-amplitude blooms characterise high-latitude regions, whereas low-latitude growing periods are long with low amplitudes (Friedland et al., 2018; Racault et al., 2012). These cycles of phytoplankton growth are closely linked with the change in seasons. In the high-latitudes, growth of phytoplankton is triggered by either dilution of grazers at the end of the winter due to deepening mixed layer depth (MLD) or/ and increasing light availability due to shallowing of the mixed layer in the spring. In low-nutrient low-latitude regions, growth is initiated by nutrient influx due to deepening mixed layers. The phenology of phytoplankton is changing rapidly in response to seasonal changes and ocean warming (Chapter 3).

The timing of phytoplankton seasonality has been shown to play an important role in carbon export annual and inter-annual variability. In one study, the presence of seasonality was shown to improve the efficiency of the organic carbon pump by 145% in models (de Melo Virissimo et al., 2022). In addition, the EF alters markedly throughout the year in areas with strong seasonal cycles (Lacour et al., 2023). In the north Atlantic and Southern Ocean, EF is usually highest during the start of the bloom phase, where the growth of phytoplankton outpaces that of its grazers (Lacour et al., 2023). Despite previous studies suggesting that phytoplankton community change and NPP are the main drivers of carbon export (Fu et al., 2016; Lutz et al., 2007), the entire community structure can alter the EF of the bloom. Non-synergistic change in timings between trophic levels, referred to as decoupling, can result in high-EF in low-productivity regions (Henson et al., 2022). For example in the

Californian Current, it was found that during the spring bloom zooplankton faecal pellets contributed up to 94% of the total export, compared to just 1.9% during the fall (Turner 2015). Modelling phytoplankton phenology and community composition accurately is crucial to ensuring that associated changes in export flux seasonal variability are represented realistically.

2.2. Model Developments

This section presents the model improvements that have been made following my evaluation of the PlankTOM12.1 model used as a starting point for this thesis, and my identification of some shortcomings, particularly in the chlorophyll seasonal cycle. Some of these improvements have been made by others, some by myself as part of this thesis. The resulting PlankTOM12.2 is here validated and will be used in Chapters 3-5.

2.2.1. Model Overview

The PlankTOM12.1 model used as a starting point for this thesis has been developed from the PlankTOM10 model, which included six phytoplankton including coccolithophores, three size classes of zooplankton, and pico-heterotrophs (*Bacteria* + *Archaea*). These functional groupings are referred to as PFTs. PlankTOM12.1 incorporated two additional zooplankton functional types: calcifying pteropods, which calcify to produce aragonite shells, and gelatinous zooplankton (Cnidaria; Figure.2.1.). A full description of PlankTOM10 is available in (Le Quéré et al., 2016b). The addition of gelatinous zooplankton is described in Wright, et al., (2021) and the addition of pteropods and the aragonite cycle are described in Buitenhuis et al., (2019). The latest PlankTOM12 model since its last publication in Friedlingstein et al., (2022), beyond those developed within this thesis, include the addition of a sediment pool, updates to silica remineralisation, the introduction of a 3-parameter growth rate formulation, and salinity restoring at the ocean surface (described in: 2.2.2).

PlankTOM12 represents 39 biogeochemical tracers, including complete marine cycles of carbon, phosphorus, silicon, alkalinity, and oxygen. Nitrogen and iron cycles are represented as simplified cycles. Nutrients enter the ocean through river fluxes and are cycled through marine ecosystems by PFTs growth and loss processes including primary production, respiration, zooplankton grazing, messy eating, faecal production and mortality. PlankTOM12 models the sedimentation processes by distinctly representing two types of organic particles based on size (Figure 2.2). Small POC sink at a constant rate of 3 metres per day, while the larger POC sink at variable speed, from 3 to 150 metres per day, modulated by the ballasting effect of their mineral composition (Buitenhuis et al., 2013a). Additionally, the model incorporates the representation of a dissolved organic carbon (DOC) component, which circulates as a passive tracer with the ocean currents.

In the PlankTOM12 model, the production of POC is a result of the mass transfer from PFTs. This mass transfer is driven by two primary processes: mortality and egestion within the PFTs. Additionally,

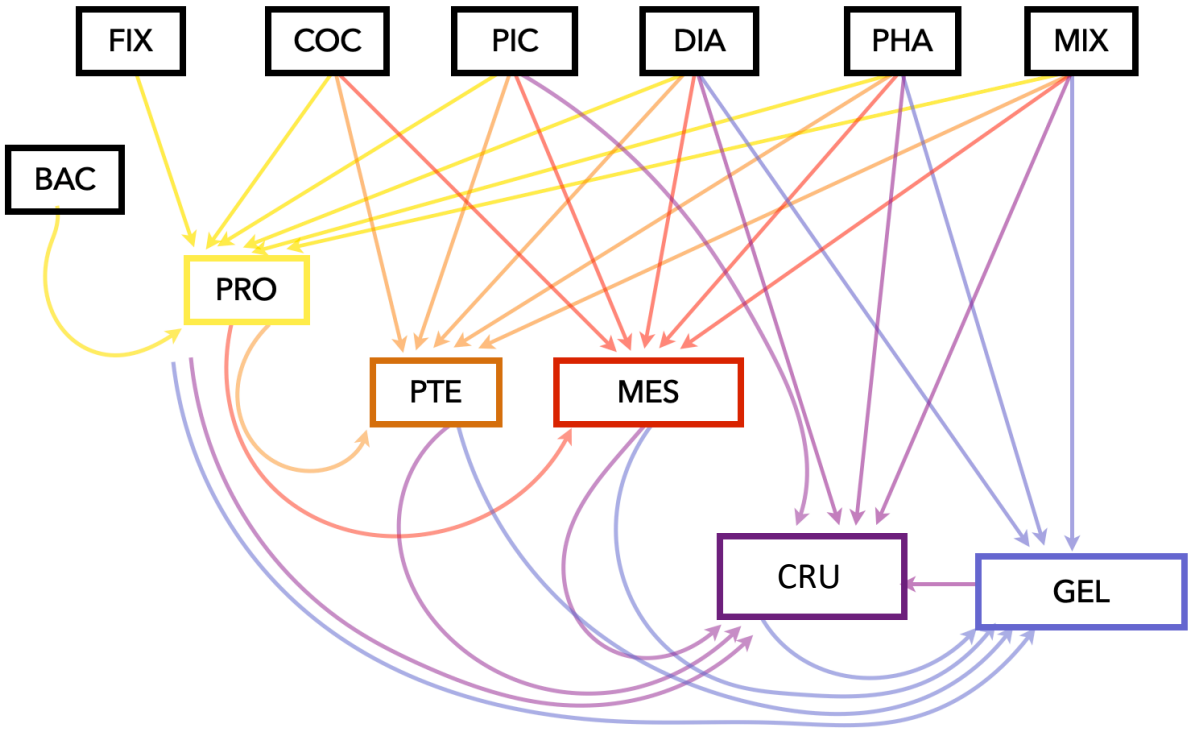

Figure.2.1. Schematic representation of the PlankTOM12 ecosystem, showing: pico-phytoplankton (PIC), N_2-fixers (FIX), coccolithophores (COC), mixed-phytoplankton (MIX), diatoms (DIA), *Phaeocystis* (PHA), bacteria and archaea (BAC), protozooplankton (PRO), pteropods (PTE), mesozooplankton (MES), crustaceous zooplankton (CRU) and gelatinous zooplankton (GEL). Arrows show the relevant fluxes where grazing preference is > 0.1.

aggregation of particles occurs, which can be due to either differences in their sinking rates or the effects of turbulent coagulation. Disaggregation occurs through several pathways: consumption by zooplankton, remineralisation by bacteria, or disintegration due to the impact of shear currents. Importantly, in PlankTOM12, different PFTs contribute differently to the two POC pools. The larger PFTs mainly contribute to the formation of large POC, whereas smaller PFTs mainly contribute to the formation of small POC (Figure 2.2; Le Quéré et al., 2016b). Large PFTs which contribute to the formation of large POC include pteropods (1000-3000 μm), mesozooplankton (200-2000 μm), crustaceous zooplankton (>2000 μm) and gelatinous zooplankton (200-20'000 μm). Small PFTs that don't contribute to the formation of large POC range in size from 0.5 to 360 μm. Small PFTs that don't contribute to the formation of large POC range in size from 0.5 to 360 μm. Small PFTs include picophytoplankton (0.5-2 μm), nitrogen fixers (0.7-2 μm), mixed phytoplankton (2-200 μm), coccolithophores (5-10 μm), diatoms (20-200 μm), *Phaeocystis (120-360 μm)*, protozooplankton (5-200 μm) and bacteria (0.3-1 μm) (Wright et al., 2021).

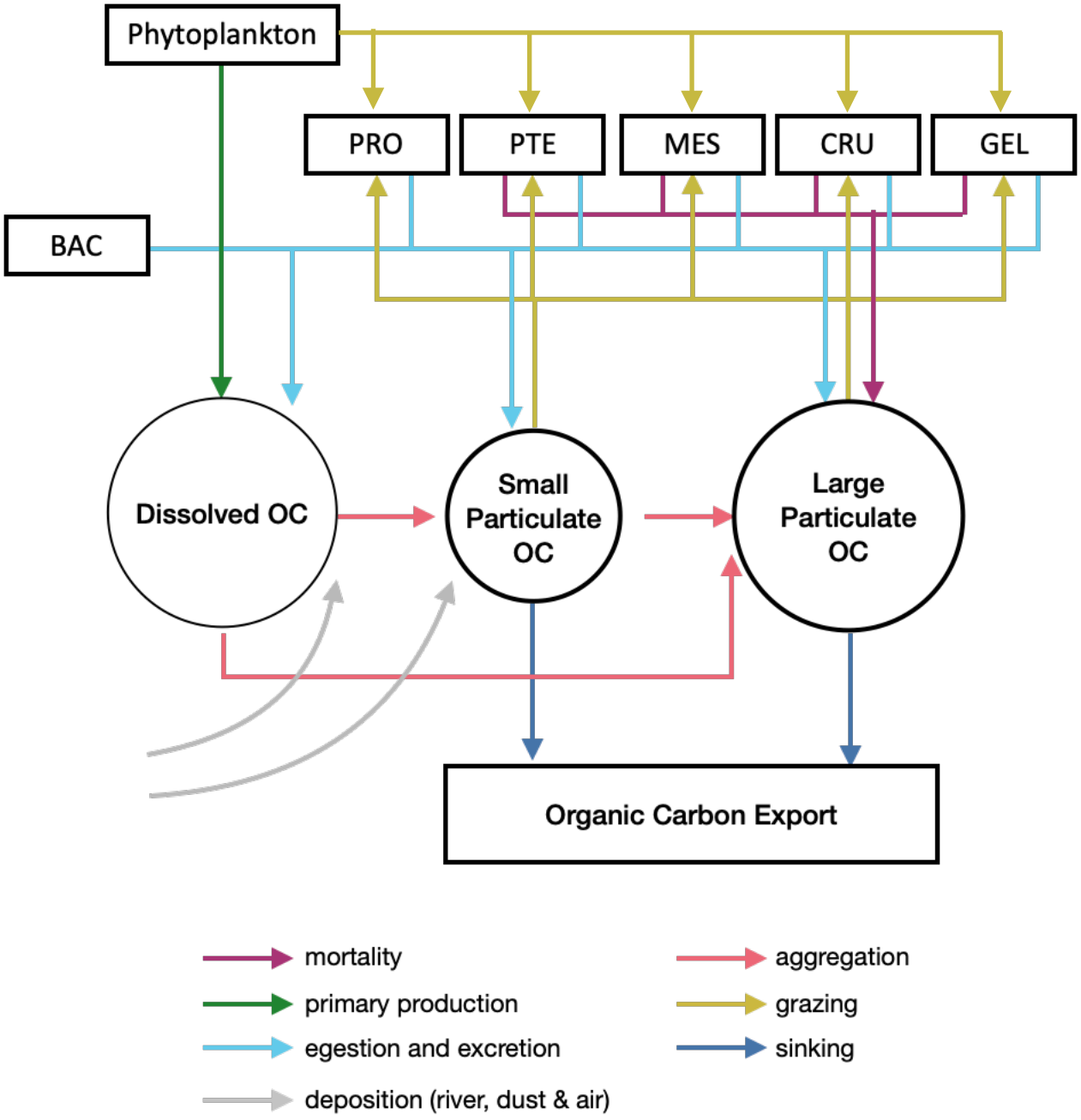

Figure 2.2. Schematic representation of the formation of particulate organic carbon (OC) in the PlankTOM12.2 ecosystem. It displays the interaction and transfer of matter among the two key OC components: small and large POC. The phytoplankton encompassing diatoms (DIA), mixed-phytoplankton (MIX), coccolithophores (COC), picophytoplankton (PIC), *Phaeocystis* (PHA), and nitrogen-fixers (FIX). Zooplankton egestion and excretion and grazing is represented protozooplankton (PRO), pteropods (PTE), mesozooplankton (MES), crustaceous zooplankton (CRU) and gelatinous zooplankton (GEL). Bacteria (BAC) both serves as food for zooplankton and remineralises the OC in all its forms.

Parameters used in the model setup are based on observations where available (e.g. Buitenhuis et al., 2006; 2010; Le Quéré et al., 2016), with loss terms and feeding preferences also guided by the model fit to a global database of PFT carbon biomass (MAREDAT; Buitenhuis et al., 2013) and global surface

chlorophyll from satellite observations (OC-CCIv5; Sathyendranath et al., 2021). I introduced the use of data from lab-based dissolution experiments for calcite (Naviaux et al., 2019) and sediment trap data (Cael, et al., submitted; update of Klaas and Archer 2002; pers. com) to update the existing parameterisation of silica export, and improve organic and inorganic sinking carbon fluxes. A full description of the model is provided in the PlankTOM12 manual, including parameter units and values (doi.org/10.5281/zenodo.8388158 and Supplementary Material A).

PlankTOM12 is coupled to the global ocean general circulation model Nucleus for European Modelling of the Ocean version 3.5 (NEMO v3.5). The NEMO model is projected onto a tripolar orthogonal curvilinear ocean mesh with a horizontal resolution of 2° longitude and approximately 1° latitude. The grid contains 31 vertical levels, which decrease in resolution from 10m between 0 and 100m to 500m at 5km. The model is coupled to the LIMv2 thermodynamic-dynamic sea-ice model. The model is initialised with observations of inorganic carbon and alkalinity, and NO_3, PO_4, SiO_3, O_2, temperature and salinity from the World Ocean Atlas (Leviticus, 2005). Surface salinity restoring was introduced to improve the representation of salinity and related variables, such as MLD, using monthly observations from NODC World Ocean Atlas 1998 data provided by the NOAA PSL, from their website at (Levitius 2013). The NEMO-PlankTOM12 model simulations are forced with daily wind stress, precipitation, cloud cover, and surface air temperature from NCEP (Kalnay et al., 1996). River fluxes of nutrients and organic and inorganic carbon are injected in the ocean at river mouths and are correspondingly removed evenly from the sediment layer to conserve mass balance. All simulations are run with inter-annual variable forcing starting at year 1948. All models are initiated from a state that has been spun up from 1750 to December 1948. The restart file incorporates comprehensive ocean physics and ice-related variables, including temperature and salinity, alongside biogeochemical tracers for all state variables including as PFT biomass, nutrients, and total chlorophyll concentrations. The initial conditions for temperature, salinity, NO_3, PO_4 and O_2 are from the World Ocean Atlas data, using the decade 1955-1964 for temperature and salinity (first decade available). Fe data for initial conditions are extrapolated from (Tagliabue et al., 2012). DIC and alkalinity are from GLODAP (Key et al., 2004). PFTs and related state variables (e.g. Fe and chlorophyll content of PFTs) are initialised with a homogenous mean concentration averaged over the worlds' ocean for the top 200m based on the MAREDAT database (Buitenhuis et al., 2013b), and are set to the threshold survival concentration elsewhere (1.e-10). Fields from previous model runs are used for other variables that could not be initialised from observations (e.g. ocean currents). The spin up ensure s that the models operate from a dynamically consistent state that reflects both physical and biological equilibria of approximately the top 500m, which is achieved over the nearly two-century-long spin-up period.

2.2.2. Updates in Model Parameterisation since last Publication

There have been significant changes since the last PlankTOM publication following my evaluation of the PlankTOM12.1 model and its fit to observations relevant to this thesis. My analysis has

highlighted significant departures between the PlankTOM12.1 modelled seasonal Chlorophyll-a and satellite-inferred data, and in the representation of the vertical distribution of POC, PIC, and particulate silica (see Section 2.3). In section 2.2.2 I highlight three of the main changes made by others to the model since the last published version (Friedlingstein et al., 2022) following my diagnosis of issues with the seasonality. These changes are outlined in detail in the PlankTOM12.2 user manual (https://doi.org/10.5281/zenodo.8388158). In sections 2.2.3-2.2.6 I describe the changes and associated data and model simulations I have made myself as part of this thesis.

First, a simple sediment module was introduced to PlankTOM12 to avoid the accumulation of organic matter in the deepest model layer. The sediment module stores material from sinking fluxes that reach the bottom of the ocean, where it can accumulate and be remineralised over longer time-scales (Giering et al., 2020).

Second, the remineralisation rate of silica was updated to produce a more realistic relationship as a function of temperature. The relationship between the remineralisation of silica and temperature is calculated as:

$$\beta_{Si} = min\left(rem_{DSI} e \frac{ret_{DSI}}{273.15 + T}, rem_{max,DSI}\right) \eta_O \qquad Equation\ 2.1$$

where β_{Si} is the remineralisation rate, T is temperature, η_O is oxygen limitation, rem_{DSI} is the baseline rate of remineralisation, ret_{DSI} is the temperature dependence of remineralisation rate, and rem_{max} is the maximum remineralisation rate. Before the update, silica exhibited a curvilinear relationship with temperature, achieving a maximum rate of 0.1 d^{-1} at 11°C. Parameters rem_{DSI} and ret_{DSI} were updated from 1.32e16 to 179831 and -11200 to -4365, respectively, to fit observed values (Cael et al., in revision; Supplementary Material B). The revised model now shows a more gradual increase in the remineralisation rate as temperature rises, reaching the same peak rate of 0.1 d^{-1} at a temperature of 30°C. This update lowers the remineralisation of silica in PlankTOM12.2 compared to PlankTOM12.1, and increases the export of detrital Si to be in line with observations.

Third, the temperature dependence of growth rate was updated from a 2-parameter to a 3-parameter formulation that can represent exponential growth while reducing root mean square error of growth rate compared to existing observations in almost all PFTs. The growth rate as a function of temperature μT in the previous 2-parameter growth rate was defined as:

$$\mu^T = \mu_0 \times Q^{\frac{T}{10}} \qquad Equation\ 2.2$$

where μ_0 is the growth at 0°C, Q is the temperature dependence of growth rate, and $\frac{T}{10}$ is the derived temperature dependence of growth. This formulation was modified to the 3-parameter growth rate used by Wright et al., (2021):

$$\mu^T = \mu_{max} \times e^{\left(-1 \cdot \frac{(T - T_{opt})^2}{\Delta T^2}\right)} \qquad Equation\ 2.3$$

where μ_{max} is the maximum growth rate, T_{opt} is the temperature at which the growth rate is optimal, and ΔT^2 is the width of the temperature response curve. The three parameters of this new formulation are refitted to the observed growth rate data for each PFTs (data shown in: Buitenhuis et al., 2019; Le Quéré et al., 2016b; Wright et al., 2021), and model parameters were generally re-tuned to ensure good seasonality and mean carbon fluxes (as in Le Quéré et al., 2016b).

2.2.3. Improvements in the Representation of Organic Carbon Remineralisation

Remineralisation of POC in the PlankTOM model is a function of the bacterial biomass and is dependent on temperature and limited by oxygen. The remineralisation rate (λ^*_{OC}) of POC as a function of bacteria BAC is described as follows:

$$\lambda^*_{OM} = BAC \cdot M_{opt} f(T) \eta_O \left(\frac{\sum_k p^{BAC}_{OC} OM}{K^{BAC}_{OC} + \sum_k p^{BAC}_{OC} OC} \right) \qquad Equation\ 2.4$$

where, M_{opt} is the optimal assimilation rate, $f(T)$ is the temperature-dependence of the growth rate of bacteria and η_O its oxygen limitation. Each source or organic matter (OC) is associated with a preference p^{BAC}, with OC representing dissolved, small particulate and large particulate organic carbon. k^{BAC} is the half-saturation for the mineralisation of organic matter.

Biofilm associated bacteria has been shown to play an important role in the remineralisation of POC. Bacterial concentration has historically been underrepresented in the PlankTOM model ecosystem by one order of magnitude (Le Quéré et al., 2016a), possibly because of the simplified representation of DOC which excludes refractory carbon. Despite model bacterial content increasing from 0.031 PgC to

0.057 PgC in the top 200m following improvements in ecosystem representation since the PlankTOM10 publication, this remains much lower than estimated content of 0.25 PgC (Buitenhuis et al., 2013b). In addition, bacterial concentration below 1000 metres is very close to zero in the model because of the absence of refractory DOC, in contrast to a background positive concentration in reality (Buitenhuis et al., 2013). To simulate the presence of biofilms on POC, I defined a minimum concentration for bacterial remineralisation in the PlankTOM12 model. I do this by replacing BAC in Equation 2.4 with $max(BAC, \beta_{OC}BAC)$, where $\beta_{OC}BAC$ represents the minimum bacterial concentration available for POC remineralisation. In this chapter, I conduct three simulations to assess how introducing simulated deep-sea bacterial biofilms affects the remineralisation of POC in the model system, by setting $\beta_{OC}BAC$ equal to 1e^{-7}, 1e^{-8} and 1e^{-9} mg C m^{-3}. The fit to observations from sinking organic carbon is used to determine the best value of $\beta_{OC}BAC$ in the model, which is 1e^{-8}. This is then used as the default parameter.

2.2.4. Improvements in the Representation of Particulate Inorganic Carbon Export

The rate of PIC dissolution ($\beta_{CO_3}CAL$) is parameterised as a function of the saturation state Ω_{sat}, the rate constant M_{CO_3} and the reaction order (n)(Eq. 2.5).

$$\beta_{CO_3}CAL = M_{CO_3} \cdot (1 - \Omega_{sat})^n \qquad Equation\ 2.5$$

I have fitted this log-linear equation to Calcite Dissolution Kinetics-IV (CDisK-IV) field campaign data taken from (Naviaux et al., 2019). From this I defined three dissolution rate equations to test against observational data highlighted by the blue and orange lines in Figure 2.3. The calcite dissolution rate constant was previously a factor of 10 times greater than observations ($M_{CO_3} = 10.9d^{-1}$), according to this new data. The relationship of was $\beta_{CO_3}CAL = 0.253 \cdot (1 - \Omega_{sat})^2$ was chosen for PlankTOM12.2 as it made significant improvements to the vertical attenuation of calcite when compared with sediment trap observations (Klaas and Archer (updated from 2002 pers. com); Le Moigne 2019; Lutz et al., 2007; Mouw et al., 2016b; Torres-Valdés et al., 2013).

This log-linear model has been drawn into question (Naviaux et al., 2019). Naviaux et al., (2019) note that the dissolution rate equations exhibit a transition at a critical state of Ω ~ 0.8 (Figure 2.2; black line). When Ω > 0.8 the reaction order is low ($\beta_{CO_3}CAL = 5.05(1 - \Omega)^{0.11}$) and when Ω < 0.8 the reaction order is high ($\beta_{CO_3}CAL = 0.0016(1 - \Omega)^{4.7}$). This step change reflects a shift in the dissolution kinetics. At high saturation states, the calcite dissolution kinetics is defined by dissolution of the outermost layer of the calcite crystal along structural features, referred to as step-retreat. As

the saturation state lowers, the dissolution rates increase as etch pits open at defects where the crystal is most vulnerable and then homogeneously across the particle surface (Naviaux et al., 2019; Subhas et al., 2017). However, introducing this step-change in dissolution kinetics represents a substantial increase in complexity, which is based on relatively few data and brings not much benefit. Not only is the linear model sufficient in reproducing the carbon export in the model ecosystem but defining separate rates for above/below the critical state (in the form of if statements) can introduce model instabilities.

These three simulations (Figure 2.2) are used to assess how changing the relationship between the rate of dissolution and the saturation state affects the rate of dissolution at depth and the latitudinal distribution of PIC dissolution (section 2.3.1).

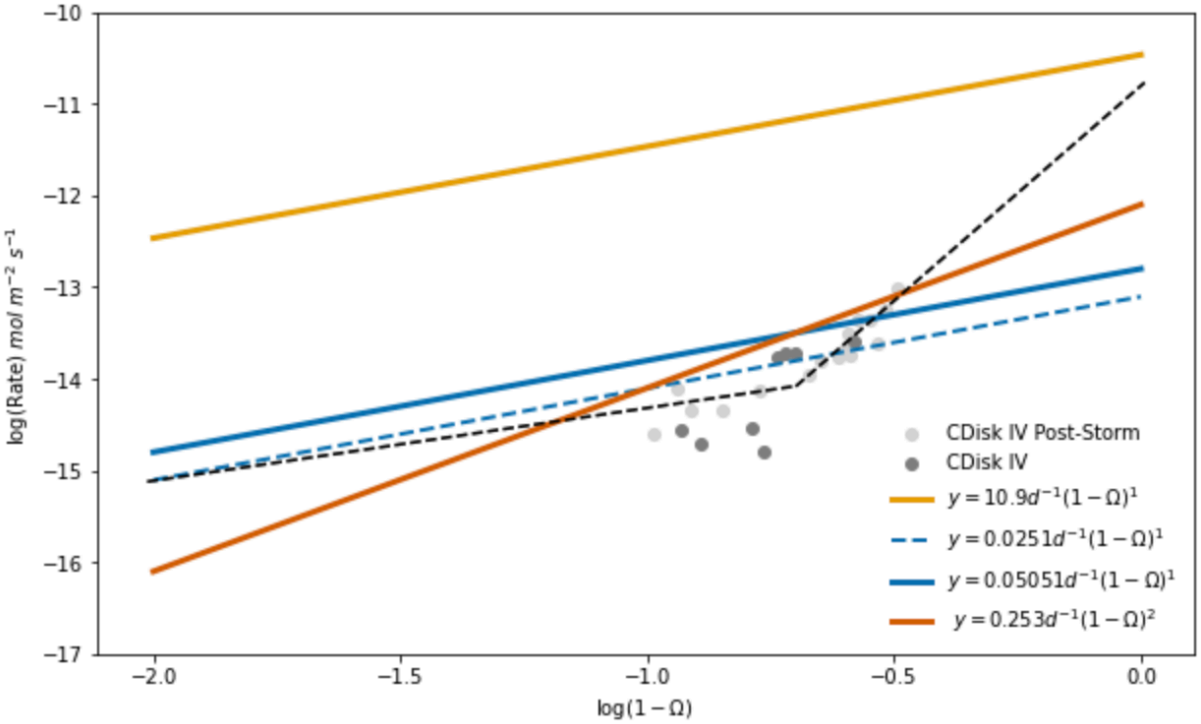

Figure 2.3. Log(dissolution rate; $\beta_{CO_3} CAL$) versus log(1- Ω) for different formulations and parameter values, compared with observations from CDisk-IV and Post-storm (Naviaux et al,. 2019). PlankTOM12.1 and PlankTOM12.2 are shown in yellow and orange, respectively. Sensitivity tests to different parameters for eq. (2.5) are highlighted in dashed blue (S_5) and solid blue lines (S_6). The black dashed line is the recommended relationship for model parameterisation based on the saturation state according to Naviaux, et al., (2019).

2.2.5. Observational Data for model validation

To assess the seasonality of phytoplankton in the model I used the OCCCIv5 daily data of chlorophyll-a and associated bias calculations with a global area coverage at 4-km resolution (Sathyendranath et al., 2021) for the time period 1998-2020. From this I created a daily time series at a 1 deg resolution

for comparability with the model output. To do this, I first created an unbiased product at each pixel using the method outlined in the Product User Guide for v5.0 Dataset (D4.2; 2020). Missing values were then filled by averaging, by equal weight, over the eight neighbouring cells. This was repeated five times to fill by roughly 5° in both longitude and latitude. Different intensities of the spatial fill (between 5° and 20°) method were tested using daily model data, and the filling methods chosen did not have a significant impact on the quality or bias of data (Appendix.7.1). The data were then averaged to a one-degree resolution to allow comparison with model data. A 21-day running mean was applied to remove small peaks in the chlorophyll concentration data, to avoid erroneous estimations of bloom timing. In addition, missing values were first filled by interpolating temporal values (average of 5 days before and after). To identify average patterns of phytoplankton seasonality, I created a climatology for 1st January 1998 - 31st December 2020.

To assess the representation of the modelled silica, PIC and POC fluxes, I used a compiled sediment trap dataset of flux data from Klaas & Archer (updated from 2002 pers. Com), Mouw et al., (2016b) and Le Moigne, (2013). These datasets were combined by Erik Buitenhuis. Using the combined sediment trap database increases the global coverage of data points as opposed to using a single data set. The dataset combines the use of: moored sediment traps, ^{234}Th (Thorium) equilibrium measurements and neutral density sediment traps. The methodologies of sediment traps and ^{234}Th both present documented difficulties in accurately determining POC flux and characterising uncertainty. Sediment traps may exhibit biases due to hydrodynamic interactions with trap design, the inadvertent capture of zooplankton, and the potential for incomplete preservation of material (Mouw et al., 2016b). In contrast, ^{234}Th-based measurements face biases related to local advection, challenges in quantifying particulate adsorption, and variations in the POC : ^{234}Th ratio (Buesseler et al., 2000). Nonetheless, given the limitations in data volume and sampling scope, I opted for the use of combined datasets from both methods rather than relying on a single dataset.

Using the combined sediment trap database increases the global coverage of data points as opposed to using a single data set, and somewhat reduces the bias towards the Northern Hemisphere. The Mouw, et al., (2016) dataset represents a significant proportion of the data collated, with 673 unique locations and 15,792 data points. The Le Moigne, et al., (2019) dataset contains 723 data points which cover 36 out of 52 of the Longhurst provinces. Both the data from Mouw, et al., (2016b) and Le Moigne, (2019) are biased towards the Northern Hemisphere with 85% and 60% of the data points taken from this region. The Klaas, et al., (2013) dataset was chosen to supplement this data for the Southern Hemisphere, as this dataset contains 1907 points with 496 of these taken in the Southern Hemisphere. The final compiled dataset used here is biased towards the Northern Hemisphere with 75% of data points taken from this region. However, this dataset is more comprehensive than data used for similar studies such as Nowicki, et al., (2022) and Henson, et al., (2019). Whilst it is possible to use the data from Tara ocean (Guidi et al., 2016), these estimations of export flux are derived from

Stokes' Law and calculated from images particles as thus do not consider particle composition. As such export of particulate organic and inorganic carbon, and silica, taken from Tara data are not necessarily compatible to sediment trap data and thus are not included here.

2.2.6. Model Simulations

In this Chapter, I have run and analysed nine simulations of the PlankTOM12 model, to assess the impact of the new and updated parameterisations on modelled carbon export and on the seasonality of modelled chlorophyll (Table 2.1). S_1 shows the PlankTOM12.1 with the new sedimentation model and improved silica remineralisation rates. S_{2-4} show the changes as a result of the addition of minimum bacterial remineralisation in particles, with values of 1e^{-7}, 1e^{-8} and 1e^{-9} (see section 2.2.3). Values outside of this range were not tested because values of 1e^{-7} and 1e^{-9} resulted in excess/ reduced organic carbon flux relative to observations. S_{5-7} show the changes in the calcite dissolution rates which were chosen as a range of interpretations of the best fit of calcite dissolution rates and described in 2.2.4. $S_{PlankTOM12.2}$ highlights the changes caused by the addition of a three-parameter growth model and salinity restoration.

Table 2.1. Differences between model simulations of relevant parameters including biofilm associated bacterial concentrations, rate constant of particulate inorganic carbon (PIC), reaction order of dissolution, number of growth parameters and base model changes.

Parameters	Biofilm Associated Bacteria Concentration (mg m^{-2})	Rate Constant of PIC	Reaction Order of PIC dissolution	Number of Growth Rate Parameters	Base Model Changes from PlankTOM12.0
$S_{PlankTOM12.0}$	0	10.9	1	2	-
S_1	0	10.9	1	2	Sediment + silica
S_2	1e^{-9}	10.9	1	2	
S_3	1e^{-8}	10.9	1	2	
S_4	1e^{-7}	10.9	1	2	
S_5	1e^{-8}	0.0231	1	2	
S_6	1e^{-8}	0.05051	1	2	
S_7	1e^{-8}	0.253	2	2	
$S_{PlankTOM12.2}$	1e^{-8}	0.253	2	3	Salinity restoring

2.3. Results

In the context of this thesis, the following section delves into the empirical findings derived from the described simulations to assess the suitability of the PlankTOM12.2 model for exploring seasonality of phytoplankton and the associated carbon export. Reproduction of observed patterns is important to give confidence in results of subsequent chapters of this thesis on trends in phytoplankton seasonality (Chapter 3) and associated impacts on carbon export in past (Chapter 4) and future (Chapter 5) decades. The purpose of presenting these results here is to offer a comprehensive understanding of the model response to changes in parameters, setting the stage for the in-depth discussion on the response to climate variability and climate trends in subsequent chapters. I employed a combination of qualitative exploration and quantitative analysis of POC, PIC and particulate silica fluxes as a function of depth (2.3.1), of latitude (2.3.2). I also examine the resulting phytoplankton seasonality (2.3.4). A broader model evaluation of PlankTOM12.2 is provided in Wright, et al., (in prep) covering analysis of PFT and total chlorophyll distributions, dissolved carbon and alkalinity, nutrients, and pCO_2. Overall, the PlankTOM12.2 model provides a robust foundation for the work presented in Chapters 3-5.

2.3.1. Fluxes to Depth

Overall, the $S_{PlankTOM12.2}$ model shows significant improvement compared to the $S_{PlankTOM12.0}$ simulation following the updates made in this thesis. Most improvements occur in the deep ocean due to improved parameterisation of remineralisation and dissolution rates. The root mean squared error (RMSE) of simulated POC, PIC and particulate silica all decrease by ~50% in $S_{PlankTOM12.2}$ compared to $S_{PlankTOM12.0}$ (Table.2.2). The RMSE showed a small increase in the surface ocean for POC and PIC. This is due to the decrease in surface concentrations of POC and PIC in the $S_{PlankTOM12.2}$ model (Figure 2.4), possibly caused by low NPP. The observational means of POC flux is greater than any of the PlankTOM12 simulations at the surface but decreases quickly between 0 and 500 metres to below levels found in the model (Figure 2.4). The most significant improvement was seen for particulate silica, as $S_{PlankTOM12.0}$ simulated no silica flux under 1000m, whereas $S_{PlankTOM12.2}$ has a similar mean particulate silica flux compared to observations (17.7 vs 15.6 mg m^{-2} d^{-1}). In addition, the silica flux above 1000 metres was improved marginally with the updated PFT growth parameterisation. Overall, reduced POC fluxes in the surface layer in $S_{PlankTOM12.2}$ reduce accuracy above 1000m, whereas below 1000m accuracy is increased in $S_{PlankTOM12.2}$ compared to previous versions.

The introduction of bacterial biofilms greatly improved the vertical distribution of POC flux. PlankTOM12.0 reproduced high fluxes of POC below 500m. Introducing simulated bacterial biofilm concentrations increase bacterial remineralisation, resulting in lower POC flux between 1000 and 5000 metres in $S_{PlankTOM12.2}$ compared to $S_{PlankTOM12.0}$ and $S_{1,4}$. If simulated bacterial biofilm concentrations are set too low (S_4), rather than an asymptotic curve, the POC flux plateaus at around 1000 metre depth and doesn't decrease until 3500 metres. This curve is closer to the shape of the curve seen in observations, however the remineralisation isn't sufficient at the surface and carbon flux remains too high. In contrast, in S_2, the concentration of biofilm bacteria is too high resulting in POC flux decreasing too quickly in comparison to the observational mean and reaching zero at ~2000 metres (S_2; Figure 2.4.a). The new dissolution rates of $S_{PlankTOM12.2}$ have an asymptotic decrease towards zero which is closer to observations.

Table 2.2. Mean and Root Mean Squared Error (RMSE) for particulate organic carbon (POC; mg C m-2 d-1), particulate inorganic carbon (PIC; mg C m-2 d-1) and particulate silica (P-Si; mg Si m-2 d-1) flux. Values are calculated from the upper 1000m (Surface Ocean) and between 1000-5000m (Deep Ocean).

	Surface Ocean (0-1000m)						Deep Ocean (1000-5000m)					
	POC Flux		PIC Flux		P-Si Flux		POC Flux		PIC Flux		P-Si Flux	
	Mean	RMSE	Mean	RMSE	Mean	RMSE	Mean	RMSE	Mean	RMSE	Mean	RMSE
OBS	72.5	-	13.2	-	83.3	-	6.2	-	5.2	-	15.6	-
$S_{PlankTOM12.0}$	62.9	60.8	9.6	8.7	8.1	120.7	15.4	10.0	6.2	5.0	0.0	17.1
S_1	44.7	71.3	7.6	9.4	14.3	118.7	15.4	9.5	2.7	4.0	11.7	9.0
S_2	39.7	69.9	9.9	8.1	14.3	118.6	1.0	5.5	2.4	4.1	12.9	8.3
S_3	48.8	69.5	10.5	8.1	7.4	122.2	7.8	4.7	3.4	4.2	5.1	11.9
S_4	48.6	69.5	8.8	8.8	13.7	118.9	14.3	8.5	3.0	4.1	11.0	9.2
S_5	44.7	71.6	8.2	9.2	14.4	118.6	8.2	4.5	6.6	2.9	12.4	8.6
S_6	44.7	71.6	8.0	9.3	14.4	118.6	8.0	4.4	5.1	2.8	12.3	8.6
S_7	44.7	71.6	8.3	9.2	14.4	118.6	8.4	4.5	9.2	4.4	12.5	8.5
$S_{PlankTOM12.2}$	44.5	71.2	4.8	11.3	20.9	115.9	7.0	5.8	4.9	1.5	17.1	9.2

The refitting of the relationship between saturation state and PIC dissolution greatly improved the representation of the vertical distribution of inorganic carbon flux in the model (Figure 2.4). The $S_{PlankTOM12.2}$ simulation reproduces the global average PIC flux in observations (Figure 2.1). In the $S_{PlankTOM12.0}$ model, the PIC flux decreased rapidly to zero between 2500 and 4000 metres, this is in contrast to observations which show a slight decrease in PIC flux between 1000 and 5000 metres

depth (Figure 2.1). In the new $S_{PlankTOM12.2}$ model the PIC flux falls slowly throughout the model depths, due to the introduced sediment model and silica dissolution improvements (S_1). However, the high dissolution rate of 10.9 d^{-1} results in PIC flux falling quickly, reaching zero by 3500 metres. Decreasing the rate constant to 0.0231 d^{-1} and 0.05051 d^{-1} as seen in S_5 and S_6 leads to an excess of PIC flux at depth, however the slope of change in the vertical distribution is still too steep in comparison to observations. Increasing the reaction order (S_7) strengthened dissolution in areas of low saturation rates and weakened dissolution in regions of high saturation states. This leads to stronger dissolution rates at the surface and lower dissolution rates at depth. In the model this results in a plateau of the inorganic carbon flux between 1000 and 3500 metres, similar to that in observations. Finally, the introduction of the 3-parameter growth model in PlankTOM12.2 reduced the concentration of calcifiers at the surface. This resulted in a closer representation in the vertical distribution of POC flux compared to observations. These results highlight the sensitivity of the relationship between dissolution and saturation states in model systems.

Differences in POC flux between simulations is due to differences in the concentrations of small and large POC, as well as the bacterial concentration. Coccolithophores and pteropods control the production of PIC in the model and thus the concentration of PIC in the surface ocean available to sink. High concentrations of POC in $S_{PlankTOM12.2}$ in the upper 1000 metres compared to the observational mean (Figure 2.5.b) is a result of low bacterial concentration in the mesopelagic depths of the $S_{PlankTOM12.2}$ simulation (Figure 2.5.c). The 3-parameter growth model results in $S_{PlankTOM12.2}$

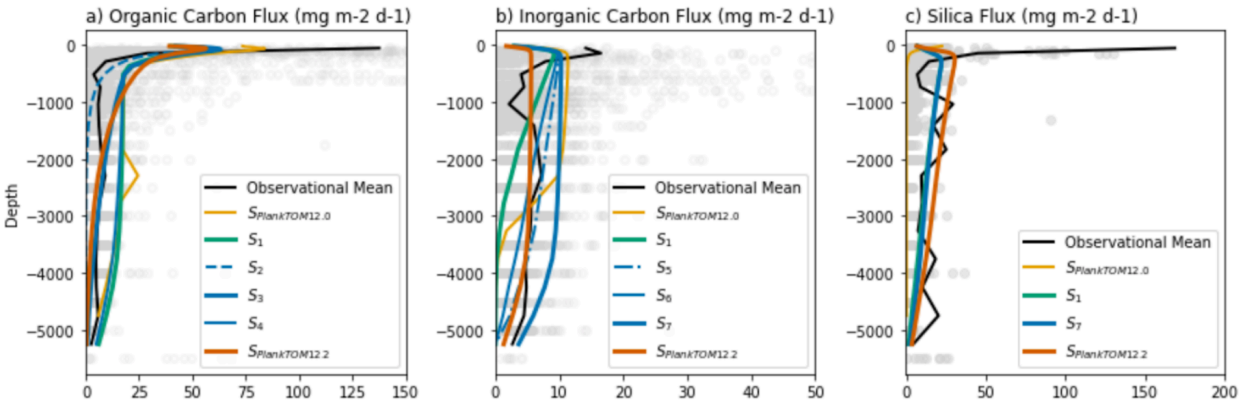

Figure 2.4. Vertical distribution of a) particulate organic carbon flux, b) particulate inorganic carbon flux and c) particulate silica in mg m^{-2} d^{-1}. Individual sediment trap observations are displayed with grey dots. Global average across datapoints is displayed for observational samples (black), $S_{PlankTOM12.0}$ (yellow), S_1 (green), $S_{2,3}$ (blue dashed), $S_{4,6}$ (blue), $S_{3,7}$ (blue thick) and $S_{PlankTOM12.2}$ (orange). Observations are taken from: (Klaas & Archer (updated from 2002 pers. com); Lutz et al., 2007; Torres-Valdés et al., 2013; Mouw et al., 2016b; Le Moigne 2019). Observations are first grouped into model depth boxes for easier comparison, data is then averaged between 0-100, 100-200, 200-500 metres and subsequently at each depth box.

containing significantly lower concentration of bacteria on the surface compared to S_{1-4}. The reduction in mesopelagic bacteria in the $S_{PlankTOM12.2}$ simulation resulted in increased concentration of POC in the top 1000m compared to previous models. This highlights the importance of improving mesopelagic bacteria in POC export in future model versions. However, given that the model bacterial concentration in the upper 200 metres is ~5 times lower than observations (2.2.4), increasing bacterial remineralisation in the deep ocean improves both the representation of bacterial behaviour classes in the $S_{PlankTOM12.2}$ model as well as the representation of carbon export.

Both changes in the dissolution rate of PIC and the overall production of PIC controls the concentration of PIC throughout the model. Decreasing the dissolution rate of PIC increases the concentration of PIC with depth (Figure 2.5.d). In S_1, where the rate constant of PIC dissolution is 10.9 d^{-1}, PIC concentration decreases quickly, almost halving by 1000 metre depth. Introducing a lower dissolution rate in line with observations reduced dissolution rates in the surface ocean, so that PIC concentration falls much more slowly in simulations S_{5-7}. Despite a net increase in PIC-producing PFT

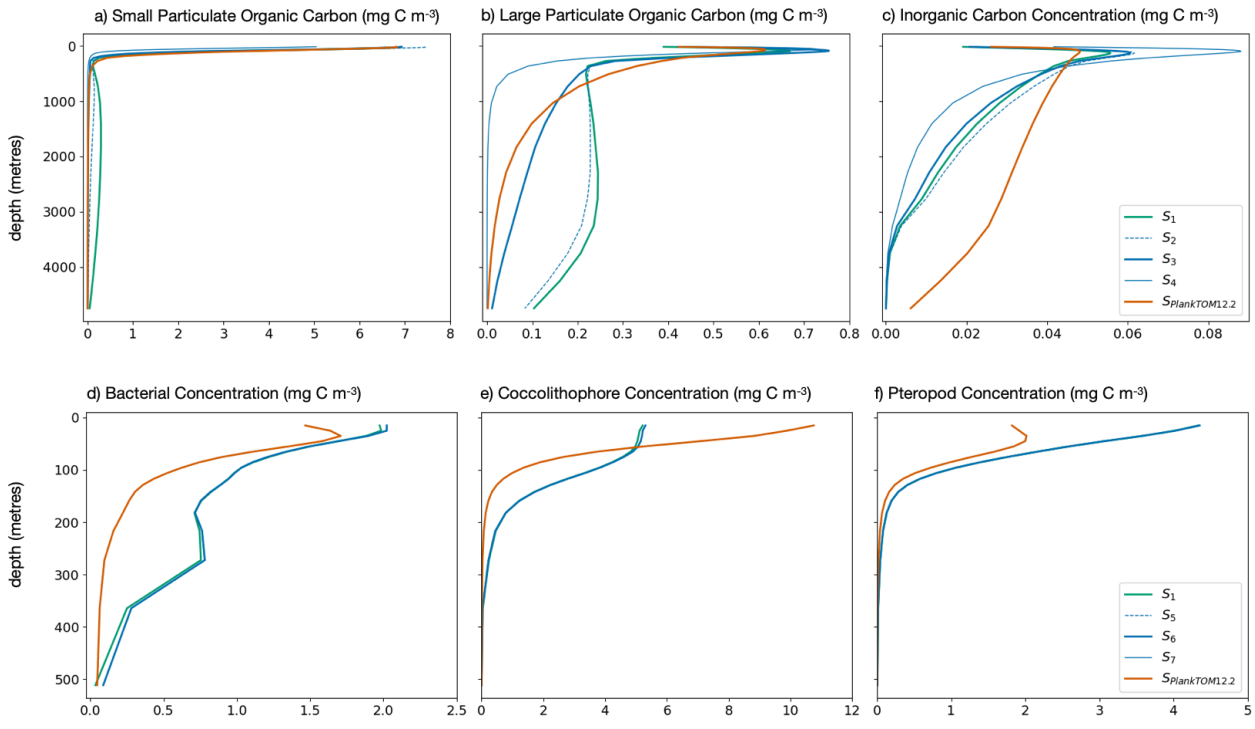

Figure 2.5. Global average concentration as a function of depth of a) small particulate organic carbon, b) large particulate organic carbon, c) bacteria, d) inorganic carbon, e) coccolithophores and f) pteropods in mg C m-3. Lines show the different simulations: S_1 (green), $S_{2,3}$ (blue dashed), $S_{4,6}$ (blue), $S_{3,7}$ (blue thick) and $S_{PlankTOM12.2}$ (orange). Carbon concentrations are shown between 100 and 5000 metres, bacterial concentrations are shown between 0 and 3000 metres and coccolithophore/pteropod concentrations are shown between 0 and 400/500 metres. All data are averaged between 1998 and 2019.

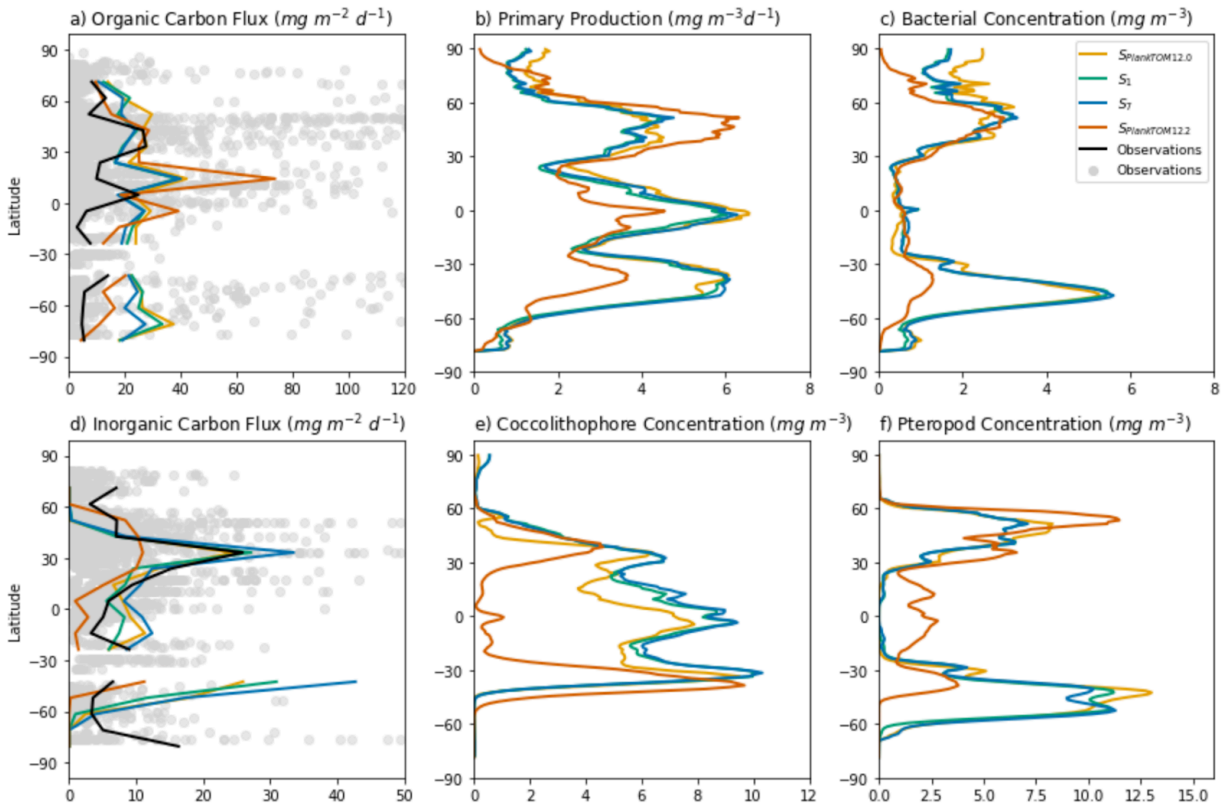

Figure 2.6. Latitudinal average of a) particulate organic carbon flux, b) primary production (top 100m) and c) bacterial concentration (top 100m), d) particulate inorganic carbon flux, e) coccolithophore concentration (top 100m) and f) Pteropod concentration (top 100m). The particulate organic carbon flux and inorganic carbon flux is an average of data between 100 and 1250m, averaged every 10°. Primary production, bacterial, coccolithophore and pteropod concentration data is averaged over the top 100m. Observations of flux are taken from: (Klaas & Archer (updated from 2002 pers. com); Lutz et al., 2007; Torres-Valdés et al., 2013; Mouw et al., 2016b; Le Moigne 2019).

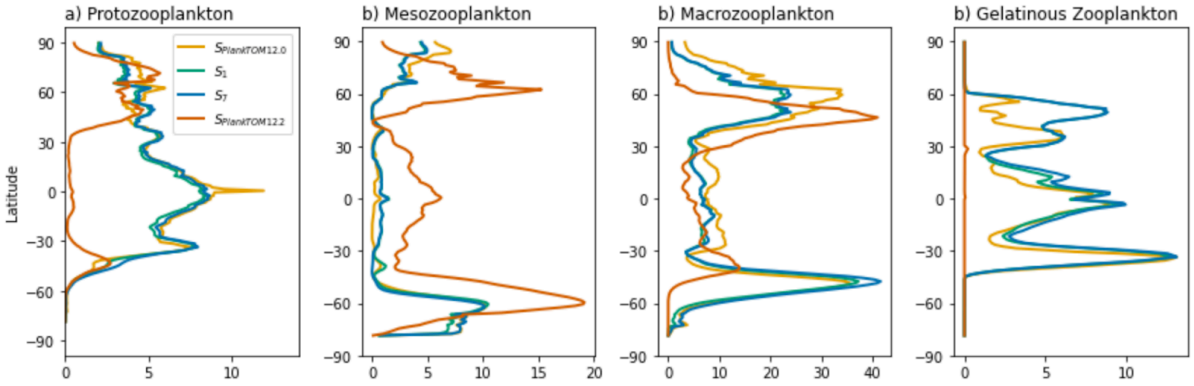

Figure 2.7. Latitudinal average of the top 100m of PlankTOM12 for: a) protozooplankton, b) mesozooplankton, c) macrozooplankton, d) gelatinous zooplankton, in mg C m^{-3}.

concentration (Figure 2.4) from S_{1-7} to $S_{PlankTOM12.2}$ PIC concentration is significantly lower in $S_{PlankTOM12.2}$. This difference likely stems from broader changes in community composition, as $S_{PlankTOM12.2}$ has a greater concentration of mesozooplankton and macrozooplankton that $S_{PlankTOM12.0}$ and S_{1-7} (described fully in Section 2.3.2, Figure 2.6).

2.3.2. Latitudinal Averages in Carbon Fluxes

To gain insights on the drivers of difference in POC and PIC fluxes between models at different latitudes, I compare the latitudinal averages POC and PIC flux against NPP, bacteria, coccolithophore and pteropod concentrations. The $S_{PlankTOM12.2}$ simulation roughly follows the latitudinal distribution in observed POC flux, however, POC flux is higher than observations in the tropics and lower in the subtropical north (Figure 2.5). Specifically there is a large peak around 15°N which is strengthened in $S_{PlankTOM12.2}$ compared to S_7 which does not appear to be driven by higher NPP or lower bacterial concentration in the top 100m of the surface ocean. These differences are likely driven by structural differences in the model ecosystem, such as increasing mesozooplankton concentration, and thus faecal pellet export, around 15°N (Figure 2.6). The latitudinal distribution of POC flux follows roughly the patterns seen in previous model iterations. Previous model simulations ($S_{PlankTOM12.0}$ and S_{1-7}) show elevated POC flux in the Southern Ocean compared to $S_{PlankTOM12.2}$ and observations. POC flux in the Southern Ocean and polar north has decreased in the $S_{PlankTOM12.2}$ closer to observations due to decreasing NPP. The changes to bacterial concentration do not significantly differ from the regional distribution of POC flux in the model and only decrease POC flux at depth.

The changes in the growth parameters and new parameterisation have altered the distribution of PIC concentration significantly (Figure 2.5) in $S_{PlankTOM12.2}$ compared to $S_{PlankTOM12.0}$ and S_{1-7}. PIC concentration has decreased significantly around 30°N and 45°S driven by a reduction in coccolithophore concentration and pteropods, respectively. In addition, due to the reduction of coccolithophore concentration in the tropics, the PIC flux has fallen below observations between 30°N/S. Furthermore, Pteropod concentration decreased significantly below 45°S in $S_{PlankTOM12.2}$ compared to $S_{PlankTOM12.0}$, S_{1-7} and the observations. Decreases in coccolithophores and mesozooplankton are likely driven by increases in mesozooplankton populations in both the tropics and subpolar regions (Figure 2.6). This highlights the importance of community composition in controlling the regional variability of inorganic carbon flux in the model system.

As mentioned previously, the latitudinal distribution of zooplankton was altered significantly by the updated PFT growth model, salinity restoring and other parameterisation updates made to

$S_{PlankTOM12.2}$. Namely, the distribution of zooplankton has shifted from being dominated by mesozooplankton rather than protozooplankton and macrozooplankton. (Figure 2.7). The concentration of both protozooplankton and gelatinous zooplankton decreased significantly; gelatinous zooplankton becoming functionally absent in the $S_{PlankTOM12.2}$ simulation.

2.3.3. Chlorophyll Seasonal Cycle

Despite some of the drawbacks described in the previous section in the $S_{PlankTOM12.2}$ simulation, the seasonality of chlorophyll has been greatly improved. In the polar north, where growing periods are characterised by short intense blooms, and often primary and secondary blooms, simulations $S_{PlankTOM12.0}$ and S_{1-7} failed to characterise the annual variability of the polar north. However, whilst the $S_{PlankTOM12.2}$ simulation replicates the polar north variability, the timing of the maximum is delayed by two months compared to the observations and $S_{PlankTOM12.0}$, S_1 and S_6 simulations. In comparison, in the Southern Ocean, the seasonal cycle of phytoplankton in the $S_{PlankTOM12.0}$ and S_{1-7} simulations peak in September and are lowest in January. Whilst the timing of the maximum is delayed by two months compared to observations, the $S_{PlankTOM12.2}$ model replicates the timing of the minimum and represents a substantial improvement of Southern Ocean bloom dynamics compared to previous model iterations.

Improvements are also evident in the chlorophyll bloom dynamics in the subtropical south. $S_{PlankTOM12.2}$ shows reduced annual variability, which is closer to the long low-amplitude growing periods seen in the observations than that of $S_{PlankTOM12.0}$. In addition, the growing period amplitude in the subtropical south peaks in October, the same as observations. In comparison, in the tropics and subtropical north, the $S_{PlankTOM12.2}$ simulation shows greater variability than its predecessors. In the tropics, the $S_{PlankTOM12.2}$ simulation has higher annual variability of chlorophyll than present in observations, however, the timing of the minimum and maximum amplitude, as well as the overall shape of the bloom has improved compared to $S_{PlankTOM12.0}$ and S_{1-7}. Furthermore, the chlorophyll concentration increased in both regions, which moves the annual average chlorophyll concentration closer to observations and also improves the north/south chlorophyll ratio. In the subtropical north, the annual variability of chlorophyll concentration remains similar in $S_{PlankTOM12.2}$ to that of $S_{PlankTOM12.0}$ however, the timing of the maximum and minimum amplitude is much closer to observations. Overall, the 3-parameter growth model and improved parameterisation of chlorophyll has greatly improved the chlorophyll seasonal dynamics in the new $S_{PlankTOM12.2}$ simulation. This highlights the importance of constructing a standardised procedure for model parameterisation on a wider scale, to ensure the comparability of model data.

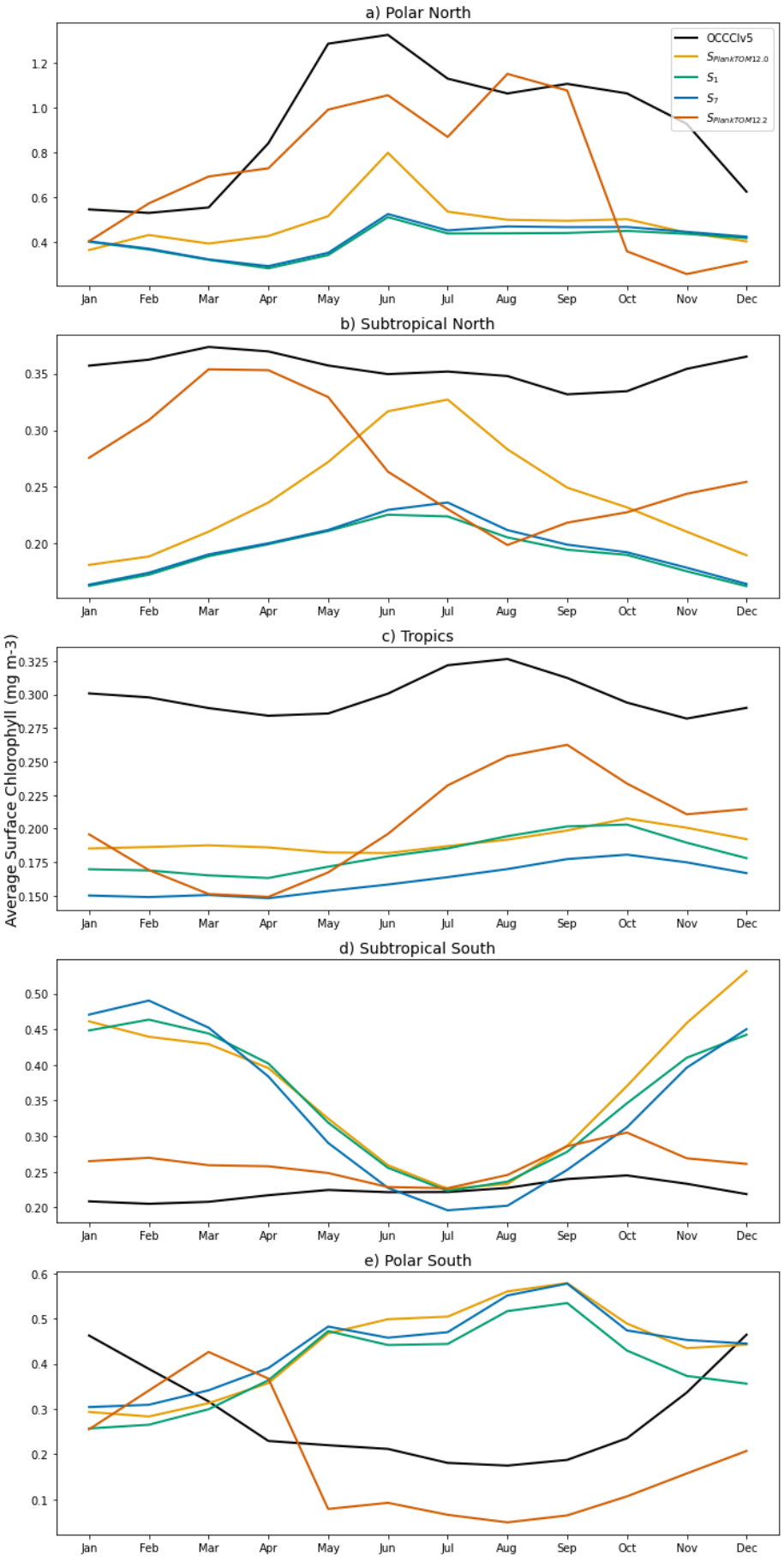

Figure. 2.8. Average monthly chlorophyll concentration in mg m^{-3} for the surface ocean for 5 latitudinal bands: polar north (>45N), subtropical north (45N:15N), tropics (15N:15N), subtropical south (15S:45S) and polar south (<45S). For observations (OCCCIv5; black) and models: $S_{PlankTOM12.0}$ (yellow), S_1 (green), S_6 (blue) and $S_{PlankTOM12.2}$ (red).

As expected, decreasing the PIC dissolution rate and increasing bacterial remineralisation have little impact on the seasonal cycle of chlorophyll (Figure 2.4; S_1 vs S_6). Lower concentrations of chlorophyll in the surface ocean are present in the tropics and subtropical south, as a result of decreases in PIC dissolution and increasing bacterial remineralisation rates. In the tropics, this likely stems from reduced recycling of inorganic carbon at the surface and lower coccolithophore concentrations. Whereas, in the Southern Ocean, increased chlorophyll concentrations in S_6 compared to S_1 is likely a result of decreased grazing on phytoplankton PFTs by pteropods. Furthermore, the seasonal cycle of S_1 and S_6 are similar to that of the $S_{PlankTOM12.0}$ model, showing that the sedimentation and salinity restoration do not significantly alter the seasonal cycle of chlorophyll. Therefore, large differences between the $S_{PlankTOM12.0}$ and $S_{PlankTOM12.2}$ simulations can be attributed to the 3-parameter growth update and improved parameterisation of chlorophyll. A thorough analysis of the seasonal cycle of phytoplankton is available in Chapter 3.

2.4. Discussion

In this chapter, I presented an evaluation of PlankTOM12 parameterisations which involve updates to the bacterial remineralisation of POC, the dissolution rate of PIC compared to the saturation state, a 3-parameter growth model, salinity restoring, as well as an improved and tested method for parameterisation of model runs (Wright, et al., in prep). I compared nine simulations representing the step-changes in the PlankTOM12 model over the course of the updates. The results indicate that these changes have significantly improved the representation of organic and inorganic carbon flux to depth, as well as the seasonality of phytoplankton. By improving our representation of carbon fluxes and bloom dynamics, I conclude that PlankTOM12.2 is well suited to assess changes of phytoplankton seasonality and subsequent impact on carbon export.

Firstly, the dissolution of POC and PIC flux to depth has been improved. These improvements are attributed to the introduction of simulated biofilm bacteria as a factor for POC remineralisation and updating of the PIC dissolution rates' relationship to the saturation state to match more recent observational values from (Naviaux et al., 2019). The average global POC and PIC fluxes were compared to an extensive sediment trap database. The results of our best run ($S_{PlankTOM12.2}$) produce a more realistic estimation of globally averaged POC and PIC fluxes across depths of 2000-5000 metres. However, care must be taken when assessing global POC flux at ~1000 metres as surface remineralisation is still quite low compared to observations due to an underestimation of mesopelagic bacteria concentration. My results highlight the importance of better representing bacterial concentration in the model, but this is beyond the scope of this project. In addition, improving representation of marine mesopelagic bacteria will also help to assess the impact of increased respiration rates on export as a result of rising ocean temperatures.

Secondly, the latitudinal average of POC flux is relatively close to observations. The variability of POC flux latitudinally follows the pattern seen in previous models; however in $S_{PlankTOM12.2}$ biases reduced in the polar north and south and deteriorated at ~15 °N. In contrast, the updated tuning and growth model have resulted in large changes to the latitudinal average patterns of PIC. Prior model runs ($S_{PlankTOM12.0}$ and S_{1-7}) simulated the latitudinal average of PIC flux accurately between 30°S and 45°N, however in the $S_{PlankTOM12.2}$ run, we have reduced latitudinal variability in the northern hemisphere which is not reflective of observations. This is likely due to increased mesozooplankton concentration globally. Furthermore, the resultant lack of a functional gelatinous zooplankton PFT in the $S_{PlankTOM12.2}$ highlights the need for continued exploration in PFT dynamics in the model.

Thirdly, $S_{PlankTOM12.2}$ captures the characteristics of phytoplankton seasonality across five latitudinal bands (polar north, subtropical north, Tropics, subtropical north, polar north). In previous models ($S_{PlankTOM12.0}$ and S_{1-7}) the minimum annual chlorophyll concentration was in January, where observations are at their maximum. The 3-parameter growth rate and improved tuning to chlorophyll concentration in the most recent model have enabled us to represent the seasonal cycle of phytoplankton more accurately.

Overall, these improvements in the PlankTOM12.2 model create a useful tool for studying both carbon export and the phenology of phytoplankton. Despite these improvements, there are still some obvious biases in the PlankTOM12.2 model, many of which are reflected in previous versions of the model. For example, the concentration of total chlorophyll is still generally too low in the model (Table 2.2) but is too high in the subtropical south. Some of these biases within $S_{PlankTOM12.2}$ are larger than those in $S_{PlankTOM12.0}$ and S_{1-7}, such as the increased export flux ~30°N and the low concentration of mesopelagic bacteria. Increasing the concentration of surface and mesopelagic bacteria should be a focus in the future as it is likely to improve the representation of carbon export. Improving bacterial concentration could also narrow estimates surrounding positive feedback loops due to increased bacterial respiration under a warming ocean. In addition, to improve the representation of inorganic carbon flux in the Southern Ocean, ecosystem dynamics of the Southern Ocean should be explored further due to low concentrations of pteropods and coccolithophores. Care should therefore be taken when assessing regional trends as the model contains biases in the Southern Ocean and ~30°N. Specifically, PlankTOM12.2 may underestimate changes in PIC fluxes ~30°N, and north/south of 65°N/S, due to the low concentrations of coccolithophores and pteropods (respectively) in these regions.

2.4. Conclusion

In conclusion, the parameterisations completed in this chapter have enhanced the accuracy of PlankTOM12.2 in modelling POC, PIC and Si fluxes, as well as the seasonal cycles of the global ocean.

The PlankTOM12.2 simulation shows significant improvements in predicting the dissolution of POC at depth in the ocean, due to improved representation of bacteria life types. The introduction of simulated biofilm-associated bacteria and subsequent changes in remineralisation of POC highlights the importance of accurate representation of microbial processes. In future model versions, a focus on increasing both surface and mesopelagic bacterial concentrations may help advance our understanding of how changes in temperature may change rates of POC dissolution. The PlankTOM12.2 model also accurately represents dissolution rate equations of PIC and has a similar PIC flux to depth as observations. This was achieved by reducing the remineralisation rate in line with lab data and changing the rate equation so that lower PIC concentrations result in lower dissolution rates. Finally, the introduction of the 3-parameter growth model and parameterisation of PFTs based on satellite chlorophyll concentrations have resulted in a more accurate representation of phytoplankton seasonal cycles, which I explore further in Chapter 3. These collective improvements in the PlankTOM12.2 model highlight its utility as a tool for predicting future changes in marine carbon flux. In the following chapters, I will use an almost identical model with updating temperature restoration to explore the impact of changing seasonal cycles on the carbon export flux.

Chapter 3. Global Phenology of Phytoplankton in a Biogeochemical Model

Abstract

Phytoplankton generate about half of primary production on a global scale and are the base for the entire marine food chain. Phytoplankton are sensitive indicators of the ocean's biological response to environmental changes because their rapid turnover time means they respond quickly to changes in their environment. Here I compare the mean and trends in phenology of the global ocean phytoplankton using satellite data from OC-CCIv5 and the PlankTOM12.2 model between 1998 and 2020. The global patterns of phytoplankton phenology calculated here for the 1998-2020 period are consistent with estimates from previous studies covering shorter periods, with generally longer growing periods starting later in the year in the subtropics compared to the subpolar regions. The PlankTOM12.2 model reproduces the observed phenology of phytoplankton at a regional resolution. The estimated trends from satellite observations show that growing periods have generally shortened in the tropics and lengthened by up to 90 days per decade in high-latitude regions. The PlankTOM12.2 model also reproduces the global trends of phytoplankton phenology over the two decades, but only when the contribution of surface ocean warming is taken into account using temperature restoring. The examination of biases in phenology show that whilst bias in sea surface temperature (SST), sea surface salinity (SSS) and mixed layer depth (MLD) posit some control over the bias in phytoplankton phenology, they do not explain the majority of the variance in bias of phytoplankton phenology in the model. Those findings highlight the PlankTOM12.2 model as a useful tool in understanding the complex interactions of phytoplankton phenology and related processes such as export.

3.1. Introduction

Phytoplankton contribute almost half of global net primary production (NPP)(Behrenfeld 2014; Behrenfeld et al., 2006; Kulk et al., 2020) and fundamentally support the entire ocean food web and ecosystem (Henson et al., 2021). The seasonality of phytoplankton biomass varies, both in the timing of its seasonal growth and in amplitude, with regional differences due to differences in environmental drivers (Racault et al., 2012). At high-latitudes, growing periods are short and intense, forming huge spring blooms, whereas at low- and mid- latitudes growing periods are long and low in magnitude (Friedland et al., 2018; Racault et al., 2012). Previous research suggested that in high-latitudes, growth is initiated as shallowing of the mixed layer at the end of winter results in alleviation of light limitation in spring (Behrenfeld 2010; Chiswell 2011; Racault et al., 2012; Sverdrup 1953; Taylor and Ferrari 2011). However, more recent understanding suggests that deepening of the mixed layer at the tail end of winter leads to dilution of predators and reduced grazing may trigger growing periods in some high-latitude regions, before the mixed-layer starts to shallow (Behrenfeld 2010; Behrenfeld 2014; Behrenfeld et al., 2013; Sallée et al., 2015). In high-latitude regions, namely the north Atlantic and Southern Ocean, the termination of the growing period is associated with increased grazing and nutrient limitation (Ardyna and Arrigo 2020; Ardyna et al., 2017; Kahru et al., 2016; Moore et al., 2004; Racault et al., 2012; Ryan-Keogh et al., 2023; Thomalla et al., 2023b; Thomalla et al., 2015). In comparison, in the low- and mid- latitudes, growth initiation and termination is controlled by the timing of stratification and associated vertical nutrient supply (Friedland et al., 2018; Gittings et al., 2018; Racault et al., 2012; Racault et al., 2017a).

Phytoplankton growing periods are closely linked with organisms higher up the food chain, and regional changes in the timing of phytoplankton blooms are likely to result in tropic mismatch leading to species extirpation (Asch et al., 2019; Cushing 1959; Dezutter et al., 2019; Edwards and Richardson 2004; Platt et al., 2003; Vikebø et al., 2021). Changes in the timing of the phytoplankton growing period and amplitude have already led to trophic mismatch between primary and tertiary production (Edwards and Richardson 2004; Kassi et al., 2018; Koeller et al., 2009). For example, a delayed ice melt resulted in a mismatch between herbivorous copepods and microalgae in the Beaufort Sea in 2013 (Dezutter et al., 2019). Likewise, delayed bloom initiation have also been found to lead to reduced fish stock recruitment due to low food availability for larvae in the Red Sea (Gittings et al., 2021; Gittings et al., 2018). Not only is there evidence that significant changes in marine trophodynamics have occurred due to mismatch in temporal synchrony, but also that this will continue into the coming decades as the ocean continues to warm (Chivers et al., 2020; Edwards and Richardson 2004). In high-latitudes, mismatches resulting in fish recruitment failure are likely to increase 10-fold in some areas in a high emissions scenario (RCP 8.5; Asch et al., 2019). In low-latitude regions, increased temperatures have been shown to result in delayed and shortened growing periods of low magnitude (Racault et al., 2017b). In tropical reef ecosystems, phytoplankton form a crucial food source for sponges, bi-valves and pelagic larvae (Gittings et al., 2018). Therefore,

changes in phytoplankton phenology combined with observed poleward range shifts (Beaugrand et al., 2015a; Cooley et al. 2022) may have severe consequences for low-latitude ecosystems. Whilst physical influx of low-latitude species into higher latitudes may, in part, offset the changes in phenology seen in cooler waters (Asch et al., 2019; Cooley et al. 2022), shifts in species distribution and phenology are likely to lead to ecosystem restructuring (Chivers et al., 2020; Gregg et al., 2017). Regions dominated by strong seasonal cycles may be replaced by longer, lower-magnitude growing period events more typical of mid-latitudes regions due to expansion of low-latitude conditions.

Models have historically failed to replicate the complexity of phytoplankton dynamics and thus the seasonal cycle of phytoplankton in the global ocean. Most carbon cycle models used for future ocean projections only have 1-2 phytoplankton functional types (Henson et al., 2021). In addition, models often contain limited zooplankton representation where grazing is a function of the phytoplankton concentration (Behrenfeld et al., 2013; Yamaguchi et al., 2022). However, zooplankton representation is important as zooplankton populations exhibit top-down controls on phytoplankton populations. In fact, zooplankton representation and phytoplankton losses via grazing is the largest source of inter-variability between CMIP5 models, contributing to up to over 3 times the uncertainty as primary production (Rohr et al., 2023). Increases in grazing by zooplankton populations due to increased resource availability can suppress phytoplankton populations, and even lead to the collapse of spring growing periods (Thackeray 2012; Thackeray et al., 2016). The model used here, PlankTOM12.2 (described in Chapter 2), controls phytoplankton concentration not only through nutrient supply and temperature growth limitations, but also through trophic dynamics involving grazing by 5 zooplankton functional types, among themselves and on six phytoplankton functional types, and explicit recycling of organic matter by bacteria. Thus, PlankTOM12.2 represents a more extensive ecosystem structure that enables additional insights into how the phytoplankton phenology may respond to both physical, chemical and community structure changes. PlankTOM12.2 is embedded in the NEMOv3.5 global ocean general circulation model (see Chapter 2 for a description).

In this chapter, I use two decades of satellite and model data to: (1) update knowledge on mean and trends in phenology using 23 years of inter-sensor bias corrected, climate quality controlled data; (2) compare the global spatial dynamics of the primary phytoplankton growing period to ensure the validity of the PlankTOM12.2 model for this analysis; (3) gain insights into the drivers of trends of phytoplankton phenology using the PlankTOM12.2 model and observations.

3.2. Methods

3.2.1. Global Ocean Colour

The European Space Agency (ESA) Ocean Colour-Climate Change Initiative version 5 (OC-CCIv5; Sathyendranath et al., 2019) daily (1998-2020) chlorophyll-a data and associated bias calculations with a global area coverage at 4-km resolution were downloaded from https://climate.esa.int/en/

projects/ocean-colour/. The OCCCIv5 dataset integrates data from five satellites, including SeaWiFS, MODIS, VIIRS, OLCI, and MERIS and is a validated and error-characterised chlorophyll-a concentration product. The 23-years of data was subject to preprocessing which involved: removing bias from individual grid cells, filling missing spatial and temporal values, applying a temporal box-smooth and removing data above and below 65°N/S. A full description of this preprocessing is outlined in Chapter 2.2.5. To identify spatial patterns of phytoplankton phenology, we created a 23-year climatology from 1st January 1998 - 31st December 2020. In addition, to identify trends in phenology metrics over the two decades of available data, I created two time series of biennial climatologies with 11 data points each, starting at different years: (i) 1998-2019, (ii) 1999-2020. Two-year climatologies are needed to capture the full seasonal cycles because of the opposite seasonality in the two hemispheres. Using two time-series of biennial climatologies to analyse trends allows us to reduce variability and verify that trends are robust across two unique datasets. The two datasets will be referred to throughout this document as the delimitated datasets.

Whilst previous understanding suggested that a minimum of three decades of observations are required to separate climate change responses from inter-annual variability (Henson et al., 2012), more recent research suggests that climate trends can emerge using only two decades of observational data (Cael et al., 2023).

3.2.2. Ecological Indices

Phenology indices are metrics calculated from surface chlorophyll concentrations to identify the timing of the growing periods of phytoplankton in the ocean. These indices are used because they are relative metrics that are influenced less by the differences in satellite sensors across the time series and are therefore a more accurate representation of ecosystem shifts (Platt and Sathyendranath 2008). The phenological indices used in this paper are taken from Racault, *et al.,* (2012; Table.3.1). First, the date of the maximum amplitude (b_m) is identified. To find the timing of initiation (b_i) and termination (b_t) I search before and after the date of the maximum amplitude to find the point in time where the chlorophyll concentration falls below a threshold. The duration of the growing period is defined as the number of days between the initiation and termination dates. To be consistent with previous studies (e.g., Racault et al., 2012; Siegel et al., 2002) the threshold was defined as the median chlorophyll concentration plus 5%. This choice is unlikely to impact results; Siegel, *et al.,* (2002) found that there was little difference between phenology metrics calculated using threshold definitions between 1-30%. However, unlike previous studies, I use the median of each biennial climatology rather than the long-term median chlorophyll concentration to prevent increases in the chlorophyll concentration resulting in increases in growing period duration (b_d). This method only highlights the characteristics of the primary phytoplankton growing period, i.e., the growing period

associated with the maximum chlorophyll concentration. A review comparing the methodology used to estimate phenological indices is available in Brody et al., (2013).

Table 3.1. Phenology indices modified from Racault, et al., (2012). Indices calculated from remotely sensed satellite radiances in the ocean colour (OCCCIv5).

Index	**Label**	**Units**
Timing of initiation	b_i	Day of the Year
Timing of maximum amplitude	b_m	Day of the Year
Timing of termination	b_t	Day of the Year
Duration	b_d	Days
Average concentration over the growing period	b_c	mg m^{-3}
Maximum amplitude	b_a	mg m^{-3}
Average chlorophyll concentration (biennial climatology)	b_{chl}	mg m^{-3}

The maximum amplitude (b_a) is the maximum concentration of chlorophyll in a biennial climatology, whilst the average concentration over the growing period (b_c) is the average chlorophyll concentration between the initiation date and termination date. The relative maximum amplitude ($REL\Delta b_a$) and concentration over the growing period ($REL\Delta b_c$) were then calculated by taking the difference between the maximum amplitude for each biennial climatology and the biennial climatological average of surface chlorophyll concentration (b_{chl}), divided by b_{chl} and multiplying by 100 (Equation. 3.1). Again, the biennial climatological mean is used rather than the long term mean to create these relative indices to assess the magnitude of seasonal change in a given period. Finally, coastal data within 2 degrees are removed as the observations have large biases in coastal regions.

$$REL\Delta b_{a,c} = \left(\frac{b_{a,c} - b_{chl}}{b_{chl}} \right) \times 100 \qquad Equation\ 3.1$$

To prevent detection of large trends during a change in date across the calendar boundary, i.e., from January to December (1 to 365) or vice versa, the dates of initiation, maximum amplitude and termination are standardised. I identify any dates where growing periods occurred in each pixel across the time-series. I defined the longest series of dates where no growing periods were found as

the “off-season”, and centred the standardisation around this date. A full description of this method is outlined in Appendix. 7.2.

3.2.3. Physical Variables

Monthly SST and SSS variables were downloaded from E.U. Copernicus Marine Service Information (https://doi.org/10.48670/moi-00052). Variables were regridded from a ¼° to 1° resolution and an average of the top 3 depth boxes was taken to represent the surface model depth box of 0-10m. 2D MLD variables were also downloaded, the MLD here represents the depth at which the temperature decreases by 0.2°C compared to the surface. Biennial climatologies were then produced between 1999 and 2020 to create one time-series of biennial climatologies containing each 11 points, for SST and SSS in the same format as the phenology indices. The biennial climatological average of these metrics were then used in the statistical analysis.

3.2.4. Statistical Analysis

To identify differences in the means and variability between climatologies (averaged over 1998-2020) of OCCCIv5 and PlankTOM12.2 I use Mann-Whitney U tests and K-smirnoff tests. These tests were conducted on both the global gridded database and for regional averages. A map of regional boundaries is provided in Appendix 7.3. In addition, I calculate the trends over the full time period using Theil-Sens slopes calculated using each pixel, and global and regional averages. Sens-slope trends are used as a robust alternative to linear regression because our data is susceptible to outlier bias due to inter-annual variability (Salgado-Hernanz et al., 2019). I discuss the spatial trends for each pixel, regardless of significance, to allow us to assess spatial patterns of trends.

To assess the drivers of bias in phenology between the observations and models, I conduct linear regressions between the absolute bias, which I refer to as the model error, of the physical and phenology indices (Equation 3.2). First, I find the error $\varepsilon^{sst,sss,b_{i-a}}$ between the model and observations for SST (Y_{sst}), SSS (Y_{sss}) and phenology indices ($Y_{b_{i-a}}$) for each biennial climatology between 1999 and 2020 and calculate 10° longitudinal and latitudinal averages. Linear regression analysis was performed between the absolute bias in SST/SSS and the absolute bias in phenological indices.

$$\varepsilon^{sst,sss} = a + \beta(\varepsilon^{b_{i-a}}) \qquad Equation\ 3.2.$$

$$where,\ \ \varepsilon^{sst,sss,b_{i-a}} = |\, Y^{mod}_{sst,sss,b_{i-a}} - Y^{obs}_{sst,sss,b_{i-a}}|$$

3.3.Results and Discussion

3.3.1. Global Patterns in Phenology

Observed phenological patterns calculated here and updated to 2020 closely match previous global oceans' analysis of Racault et al., (2012) based on the period 1998-2007 and that of Friedland et al., (2018) based on the period 1998-2015, showing results are robust to methodological differences among the studies. Phytoplankton phenology shows generally longer growing periods starting later in the year in the subtropics compared to the subpolar regions. The PlankTOM12.2 model closely reproduces the latitudinal averages of growing period phenology of phytoplankton, but with significant regional differences.

For latitudes above 40°N and below 40°S, growing period initiation in the observations begins in spring around ~May and ~October, respectively (Figure 3.1a). This is in line with previous research which shows that in the poles, initiation of growing periods coincide with the alleviation of light limitation or grazer dilution, resulting in an average bloom initiation (b_i) in spring/Winter (Behrenfeld 2010; Behrenfeld et al., 2013; Sallée et al., 2015). Significant differences persist in the PlankTOM12.2 model for latitudes poleward of 40° at the regional level. In particular, growing periods occurred an average of 90 days earlier than observations in the north subpolar regions and ~40 days earlier in the southern subpolar regions (Figure 3.1). The earlier growing period initiation in PlankTOM12.2 may be triggered by the dilution of zooplankton grazing in the model. Increasing complexity of zooplankton representation in a model system was found to shift the drivers of growing period initiation; from shallowing of the MLD and an increase in light availability, to a deepening of the MLD and dilution of grazers (Karakuş et al., 2021). As our model system contains six zooplankton this is likely the root of the early initiation found in the PlankTOM12.2 model. I explore the drivers of bloom timing in Chapter 4.

Between the subpolar- and subtropical latitudes, there is a discernible gradation from spring to winter growing periods. This is due to a shift in the drivers influencing growth limitation, from light limitation and grazer density in the poles to nutrient limitation in the tropical- and subtropical-latitudes. In observations, growing periods occur between October and March in the Northern Hemisphere around 30°N, and between May and October in the Southern Hemisphere around 30°S (Figure 3.1). The shift between the timing of the Northern and Southern Hemisphere phenology patterns is relatively smooth, although there is regional patchiness in the transition around the equator. The model is in agreement with observations of initiation, date of maximum amplitude, and termination through these latitudes (Figure 3.1). However, growing periods are ~30 days earlier in the PlankTOM12.2 than observations at 30°N. This discrepancy appears to be due to growing periods of the subpolar north extending further south in the north Pacific than in observations. PlankTOM12.2 growing periods also occur later than observations around 0° due to the absence of a spring bloom in the equatorial Pacific. The phenology here is closely linked to equatorial upwelling,

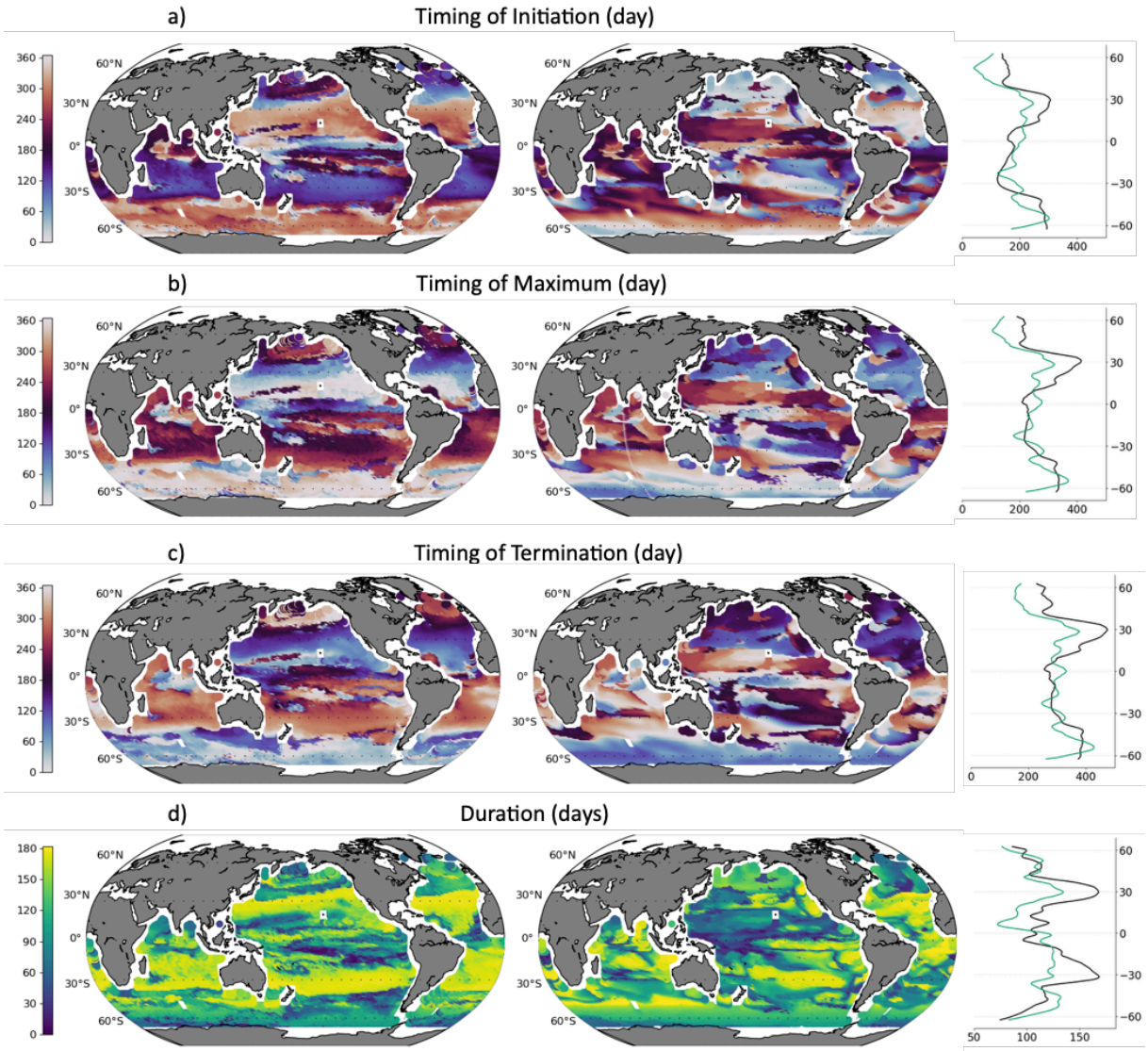

Figure.3.1.(a-d) Global mean patterns of phytoplankton phenology indices. Data were created from climatologies averaged between 1998 - 2020. Total chlorophyll concentration (mg m^{-3}) were taken from OCCCIv5 (left) and PlankTOM12.2(right). The right hand panels show the latitudinal average of phenological indices from OCCCIv5 (black) and PlankTOM12.2(green) smoothed by 5°. Days greater than 365 are representative of growing periods that span the edges of the calendar year. For example, 400 and 500 represent ~February and ~April, respectively.

where large phytoplankton biomass is supported by influx of nutrient rich waters from depth (Racault et al., 2017a). This suggests upwelling in this region may be delayed in PlankTOM12.2 compared to observations, resulting in a delay in phytoplankton bloom in these regions. Furthermore, the observations show more latitudinal distinction between regions. In the south Pacific, growing periods begin around April in observations, however in the model there is large regional variability with initiation date varying between March and October. Discrepancies between the model and observations are mostly present in the Pacific Ocean and likely stem from issues with the model representation of surface salinity and mixing depth (Mayot et al., 2023).

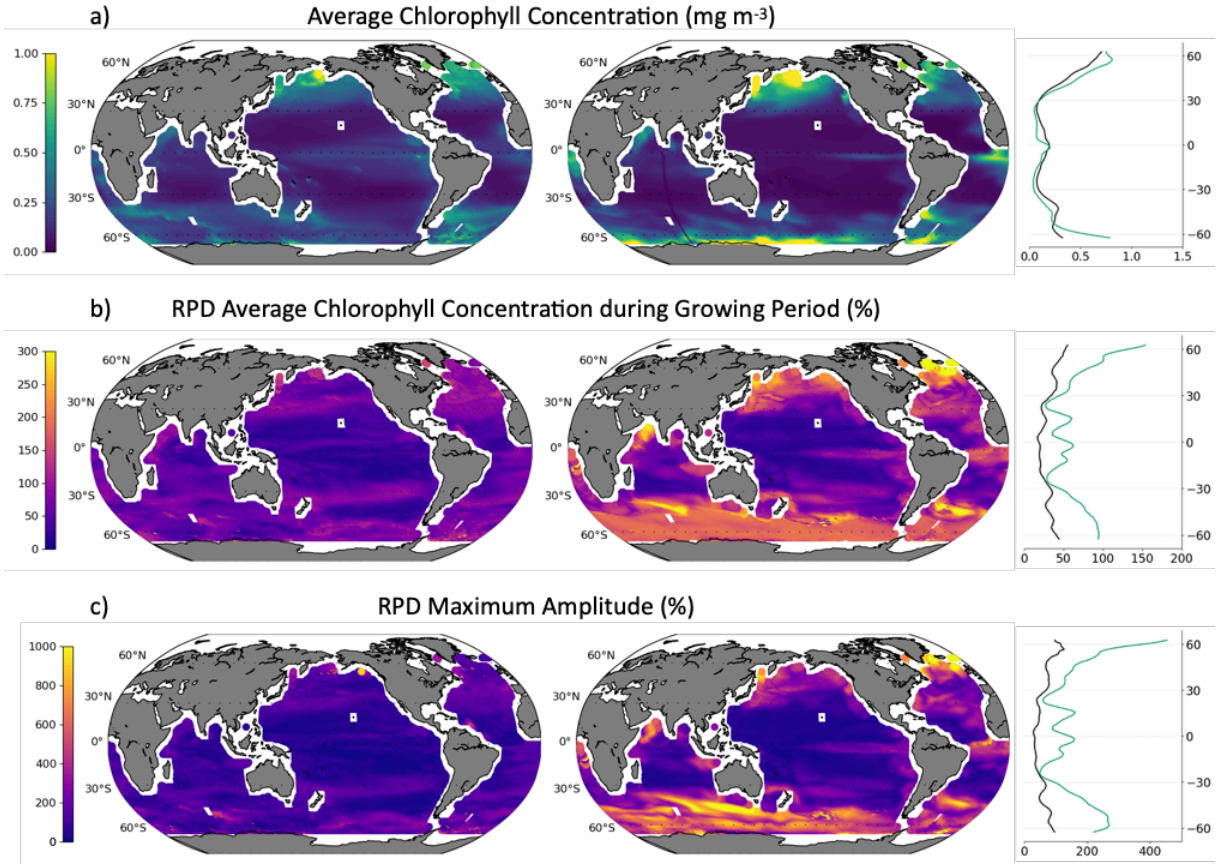

Figure.3.2.(a-c) Indices of magnitude of phytoplankton growth. Data were created from climatologies averaged between 1998 - 2020. Relative maximum amplitude is the relative percentage difference (RPD) between the mean and (b) the average chlorophyll concentration during growing period and (c) the maximum amplitude. Total chlorophyll concentration (mg m-3) were taken from OCCCIv5 (left) and PlankTOM12.2(right). The right hand panels show the latitudinal average of traits from OCCCIv5 (black) and PlankTOM12.2(green) smoothed by 5°. RPDs are calculated as: $RELΔb_{a,c} = ((b_{a,c} - b_{chl})/b_{chl}) \times 100$, where b_{chl} is the average yearly chlorophyll concentration, b_c is the average concentration over the growing period and b_a is the maximum amplitude.

Between the subtropical and tropical latitudes, the difference in duration in the observations is higher than in previous studies (Figure 3.1d). I identify a ~63 day difference in growing period duration between subtropical and tropical latitudes, while Racault, *et al.,* (2012) find a ~50 day difference in growing period. This difference is likely due to differences in the data products and time periods used. Racault, *et al.,* (2012) used ocean colour radiance data from SeaWIFs, a single satellite, over the years 1997-2007. In contrast, we use the OCCCIv5 dataset which merges five satellites (SeaWiFS, MODIS, VIIRS, OLCI and MERIS) and computes per-pixel uncertainty estimates, to create a validated and error-characterised chlorophyll-a concentration product from 1998-2020. Other estimates from Friedland, *et al.,* (2018) find a variation of ~30-40 days between the tropical and subtropical latitudes. However this difference is likely due to the alternative methodology as they utilise a “sequential t-test analysis of regime shifts” which identifies shorter bloom durations than the threshold method used in this chapter.

Overall, PlankTOM12.2 follows the latitudinal averages for duration of the growing period identified in observations (Figure 3.1d). Growing period duration is 2-3 months in the subpolar regions in both PlankTOM12.2 and observations, however growing periods are shorter in the PlankTOM12.2 model in the subtropics. Spatially this is most apparent in the north subtropical Pacific and south subtropical Atlantic and Indian Oceans, where the duration of the growing periods can be significantly shorter than observations (dark green in model vs yellow in observations). Furthermore, in the Southern Ocean, the model growing period is on average ~20 days longer than in observations. This is primarily driven by longer growing periods in the southern Indian Ocean where duration of the growing period is ~170 days compared to ~130 days in observations. This is mostly a result of both a 30 day advancement in initiation (b_i) and a 15 day delay in termination (b_t) in this region compared to observations (Figure 3.1a-c). This could be due to a wide variety of factors, from SST, MLD, differences in the distribution of nutrient limitations or grazing. I explore the primary drivers of bloom timing in PlankTOM12.2 in more detail in Chapter 4.

Globally, PlankTOM12.2 captures the regional patterns of average chlorophyll concentration, with high concentrations in the subpolar regions and low concentrations generally in the subtropics and in the tropics outside upwelling regions (Figure 3.2). The model underestimates the average chlorophyll concentration in the tropics and overestimates the average chlorophyll concentration in the subpolar regions (Figure 3.2.a). In low productivity oligotrophic gyres, such as the subtropical Pacific, PlankTOM12.2 follows roughly the spatial patterns in the maximum amplitude and the concentration over the growing period. In contrast, values of relative chlorophyll concentration over the growing period ($RELΔb_c$) are 60% larger in the subpolar north and 110% larger in subpolar south in PlankTOM12.2 (Figure 3.2b). Additionally, in these regions, relative maximum amplitude ($RELΔb_a$) is overestimated in PlankTOM12.2 by 200% in the subpolar north and 400% in the subpolar south (Figure 3.2c). This suggests that in the subpolar regions and the tropics, PlankTOM12.2 overestimates the regional seasonal variability in chlorophyll concentration, especially in the subpolar Southern Ocean where relative growing period magnitude is up to 4 times greater than in observations. This is unusual as previous models have underestimated the magnitude of interannual variability in chlorophyll concentration (Le Quéré et al., 2016a). The discrepancies in magnitude of the growing period are especially relevant for Chapter 4, as the importance of NPP during the growing period may result in overestimations of the influence of phytoplankton phenology on export.

Table 3.2. Mann-Whitney U and K-smirnoff results for a) the global database and b) regional averages. Averages, 25% and 75% percentiles are calculated for timing of initiation, maximum and termination (day of the year), duration (days), average concentration of chlorophyll during the growing period (mg m-3) and maximum amplitude (mg m-3). Significant Mann-Whitney U and K-Smirnoff tests represent where the PlankTOM12.2 model and OCCCIv5 variables are significantly different.

a) Global Database (n~33412)

	Mann Whitney U			**Distribution (Percentile)**				**K-Smirnoff**
	Mean			OCCCIv5		PlankTOM12		
	OCCCIv5	**Model**	**P-value**	**25%**	**75%**	**25%**	**75%**	**P-value**
Timing of Initiation	216.1	195.2	2.8E-94	130.0	303.0	89.0	295.0	7.9E-300
Timing of Maximum	203.7	174.8	1.9E-155	93.0	315.0	74.0	282.0	0.0E+00
Timing of Termination	172.3	170.9	4.8E-03	63.0	288.0	82.0	270.0	1.8E-88
Duration	122.0	112.3	1.0E-142	91.0	165.0	78.0	147.0	6.5E-182
Average Concentration During Growing Period	0.025	0.187	4.1E-69	0.115	0.339	0.054	0.499	0.0E+00
Maximum Amplitude	0.037	0.034	7.0E-01	0.129	0.427	0.059	0.893	0.0E+00

b) Regional Averages (n=13)

	Mann Whitney U			**Distribution (Percentile)**				**K-Smirnoff**
	Mean			OCCCIv5		PlankTOM12		
	OCCCIv5	**Model**	**P-value**	**25%**	**75%**	**25%**	**75%**	**P-value**
Timing of Initiation	218.8	186.2	0.305	184.4	274.9	171.7	206.5	0.588
Timing of Maximum	202.6	163.6	0.124	171.5	233.0	119.3	220.5	0.588
Timing of Termination	169.9	162.8	0.573	110.9	239.5	139.9	195.3	0.300
Duration	120.5	112.6	0.330	100.3	136.9	97.0	128.6	0.588
Average Concentration During Growing Period	0.266	0.343	0.383	0.186	0.323	0.162	0.869	0.300
Maximum Amplitude	0.332	0.541	0.701	0.129	0.427	0.059	0.893	0.000

At a 1 degree resolution (n~33412), expectedly, the model is significantly different from the observations across all variables (Table 3.2a). Density plots showing the distribution of these differences are shown in Appendix 7.4. Timing of the growing period was more likely to occur earlier in the year in PlankTOM12.2 compared to the OCCCIv5 observations. Variability of model timing of

initiation (b_i) is higher in the model than observational calculations, as shown by the broader range of the 25% and 75% percentile distributions (Table 3.2), whereas variability in timing of maximum (b_t) and termination (b_i) was lower in PlankTOM12.2. Furthermore, PlankTOM12.2 has a slightly lower mean duration compared to the observations, however the variation of duration across regions is similar. This is likely stemming from the absence of long, subtropical growing period conditions seen in the north subtropical Pacific, south subtropical Indian and Atlantic Oceans. The relative concentration over the growing period (b_c) and maximum amplitude (b_a) is greater in the models than it is in observations. The variability of the maximum amplitude (b_a) is significantly greater in the model than the observations even at a regional resolution. These findings indicate that the surface chlorophyll concentration in the PlankTOM12.2 model displays more significant seasonal variability and greater interannual variability than observations. Despite these discrepancies, the statistical analysis presented here shows that most of the model phenology is not significantly different from observations when scrutinised at a regional scale (Table.3.2b). Hence the model is proficient in predicting the phenology of phytoplankton in the global ocean at the regional scale.

3.3.2. Bias in Physical Variables and Phenological Indices

Here I assess biases in the model's representation of SST, SSS, MLD, and phenological indices. SST and SSS are selected because of the reliability of the observations and their relevance as indicators of the representation of ocean physical processes in the model. Biases are calculated by subtracting the observations from model values, and thus positive biases indicate regions where model values are greater and negative values indicate regions where model values are lower than observations.

The modelled SST is 0.2°C greater than observations for most of the ocean except in the subpolar north, where temperature bias is -0.6°C (Figure 3.3a). The modelled SSS is generally close to observations, with a bias of 0.25 PSU around 0° latitude, decreasing to -0.6 PSU in the subpolar north. Lower values of SSS in the subpolar north originate from the north Atlantic, with an opposite bias in the north Pacific. These differences in SST and SSS likely stem from biases in the model forcing from NCEP reanalysis, which display higher bias in surface air temperature and precipitation in the north Pacific than subsequent reanalysis products (Saha et al., 2010). Bias in MLD is much larger than those of SSS and SST, due to higher variability (Figure.3.3c). Between 40°N and 40°S, MLD in PlankTOM12.2 is 14.5 metres shallower than observations. In comparison, with polewards of 40°N and 50°S, MLD in PlankTOM12.2 is 41.8 and 89.6 metres deeper than observations suggest.

Biases in maximum amplitude and concentration over the growing period are clearly related to these biases in MLD. In the subpolar regions of PlankTOM12.2, where MLD is deeper than in observations, maximum amplitude and concentration over the growing period are also significantly larger than observations. These strong latitudinal biases appear to be driven by deeper MLD and elevated

chlorophyll concentrations in the Indian Ocean (25°) and the Pacific Ocean (120°; Figure 3.3). This suggests that increased nutrient supply in these regions may drive the large variability in chlorophyll concentration in the model. In comparison, the relationship between biases in other physical indices and the timing of the growing period is less clear and so is explored using linear regressions in section 3.3.5. However, around the equator it is possible that high SSS in PlankTOM12.2 is resulting in later and shorter growing periods compared to observations.

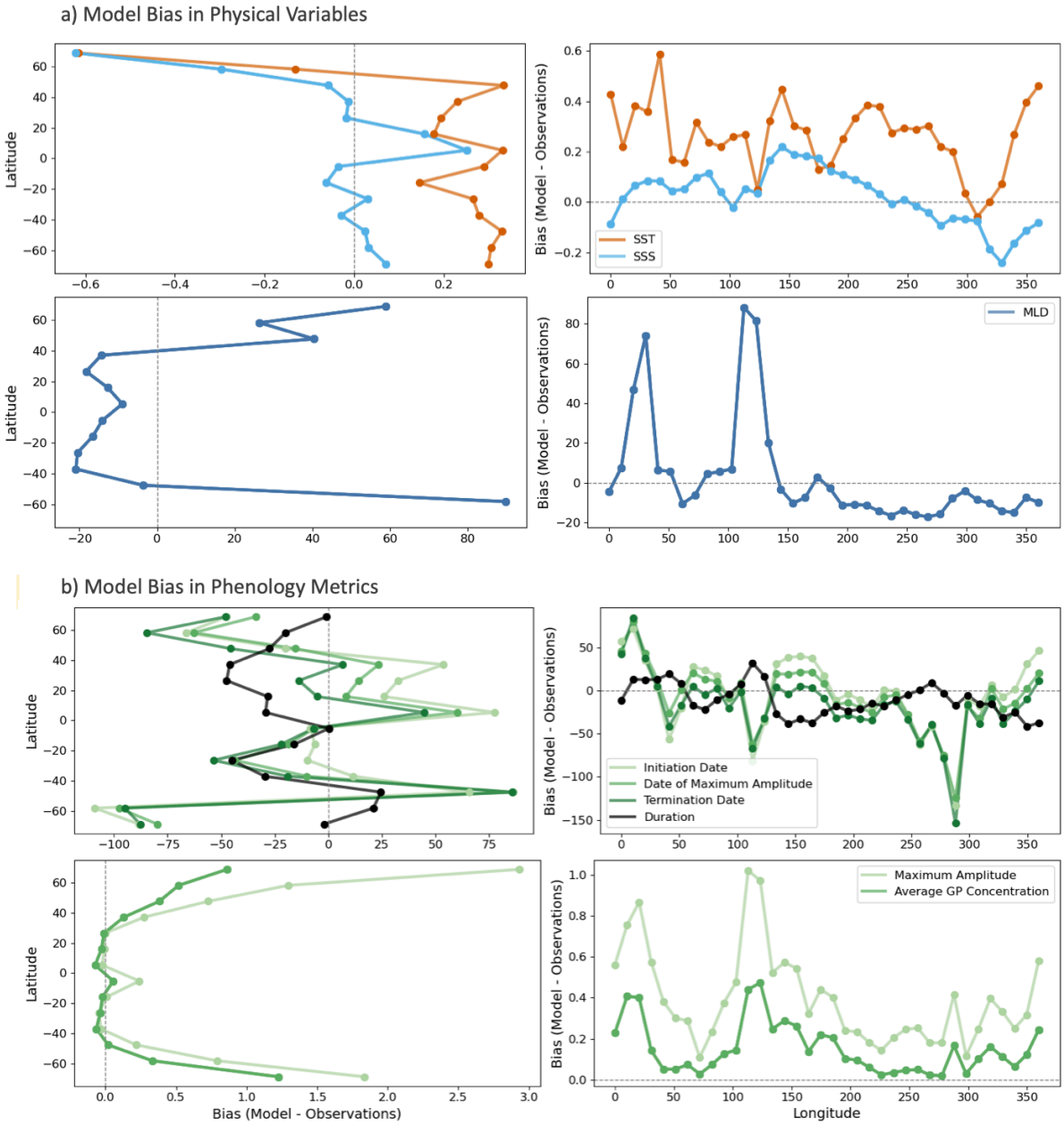

Figure.3.3. Average bias as represented by the mean difference between the NEMO-PlankTOM12.2 model and observations for a) sea surface temperature (SST; °C) and sea surface salinity (SSS; PSU) and mixed layer depth (MLD; metres); and b) initiation (day), timing of maximum (day) and termination date (day), duration (days), maximum amplitude (mg m^{-3}) and average concentration over the growing period (GP; mg m^{-3}). Observations are subtracted from model values. Positive biases are therefore representative of regions where model values are greater than observations.

Bias in phenology indices is much more variable over latitude and longitude. Biases in date of initiation, maximum amplitude and termination range from -100 to +75 days (Figure 3.3b). Timing of initiation and maximum amplitude generally appears earlier in the model in the subpolar north and south, and late in the subtropical north. In addition, the direction of bias in duration varies significantly with longitude. Late bias in growing periods appears to be driven by initiation date, whereas early biases in growing periods are often driven by termination date. Between 0° and 40°N, biases in duration tend to be driven by initiation date, whereas above 40°N and below the equator biases in duration are driven by biases in termination. Duration appears to be more robust to biases than the timing of the growing period, likely because biases in initiation and termination are often unidirectional. For example, in the subpolar south where growing period timing is advanced by >3 months, the model bias for duration is close to 0 days. This highlights duration as the most reliable indicator among those explored here. Duration will thus be used, alongside initiation date, for assessing the impact of phenology on export, which I explore in Chapter 4 of this thesis.

These systematic deviations in SST, SSS and MLD are critical for understanding the biases in phenological indices in the PlankTOM12 model. Specifically, SST influences the metabolic activities of marine phytoplankton, with warmer waters accelerating growth which may lead to shorter bloom periods. This is particularly evident in the tropics where higher SST biases correlate with delayed initiation of growing periods and shorter growing period duration. In addition, salinity may indirectly affect phytoplankton phenology due to its effect on the density and buoyancy of seawater. High salinity increases water density, leading to more stratified, stable water columns that inhibit vertical mixing. This stability can reduce the upward flux of nutrients from deeper waters to the euphotic zone. This may mean that positive biases in salinity in the model representative of freshening may lead to shorter growing periods due to lower nutrient concentrations available for growth.

Similarly, biases in the MLD play a fundamental role in phenological biases in the PlankTOM12 model. Deeper mixed layers, as observed in some subpolar regions of the model, may enhance nutrient availability due to increased mixing but concurrently increase light limitation. This is evident in the increase in the maximum amplitude and the average concentration over the growing period duration, which is much higher in the PlankTOM12 model than in observations. This mechanistic link between physical parameters and biological responses is vital for understanding the model's ability to predict phenology of phytoplankton. To further explain the relationships between errors in physical indices (model versus observed values) and their impact on phenological indices within the model, the next section will conduct linear regressions between physical model errors and phenological errors. This analysis aims to identify which physical factors serve as primary drivers of the observed phenological biases, thereby enhancing our understanding of how these mechanistic effects may drive differences between the model and observed phenologies.

3.3.3. Impact of Physical Model Error on Phenology Errors

Here I assess the error (absolute biases) between the model and observation. Linear regression is conducted between the errors in the physical indices (SST, SSS and MLD) and phenological indices (e.g. |ΔSST| = a + b|ΔInitiation|). As all error metrics are positive, this analysis only highlights whether increases in the difference between PlankTOM12.2 and observations results in increases or decreases in errors of phenology and not the direction of the difference. Positive relationships therefore indicate that increases in the error between model and observations for physical indices resulted in increases in the error in phenological indices.

There appears to be some relationship between errors observed in physical variables ($\varepsilon_{sst,sss,mld}$) and the errors observed in phenology indices ($\varepsilon_{phenology}$), however this is widely variable between regions (Figure 3.4; Figure 3.5; Figure 3.6). In the southern and tropical ocean latitudes increases in $\varepsilon_{sst,sss,mld}$ may lead to increases in $\varepsilon_{phenology}$. These positive relationships between $\varepsilon_{sst,sss,mld}$ and $\varepsilon_{maximum\ amplitude}$ and $\varepsilon_{termination}$ are also present in the subpolar north. However, I find limited significance in these relationships across both latitude and longitude. Between ε_{sst} and $\varepsilon_{initiation}$, significance is only found when increases in ε_{sst} result in decreases in $\varepsilon_{initiation}$, suggesting that ε_{sst} does not drive $\varepsilon_{initiation}$ (Figure 3.4). Increases in ε_{sst} occur alongside increases in $\varepsilon_{timing\ of\ maximum}$ and $\varepsilon_{termination}$ in the Atlantic Ocean (Figure 3.4). However, the variance of $\varepsilon_{timing\ of\ maximum}$ and $\varepsilon_{termination}$ explained by the ε_{sst} is low (r^2 = 0.04 and 0.06), suggesting that ε_{sst} does not contribute significantly to $\varepsilon_{phenology}$. However, ε_{sst} does appear somewhat important when describing $\varepsilon_{maximum\ amplitude}$ as 56% of variance in $\varepsilon_{maximum\ amplitude}$ is explained by ε_{sst} between 0° and 10°S. Despite some large biases in SST and SSS (up to 0.6°C/PSU), ε_{sst} appears to explains only a small portion of the variance associated with $\varepsilon_{phenology}$.

SSS errors (ε_{sss}) explain more of the variability in $\varepsilon_{phenology}$ than ε_{sst} (Figure 3.5). ~57% of the variability in $\varepsilon_{timing\ of\ maximum}$ and $\varepsilon_{termination}$ is explained by ε_{sss} around 10-20°N, and also 40-50°S for $\varepsilon_{termination}$. This relationship is mainly present in the Indian Ocean for $\varepsilon_{timing\ of\ maximum}$ and in the Eastern Pacific for the $\varepsilon_{termination}$. Increases in ε_{sss} may result in increases in $\varepsilon_{duration}$ around 30-40°N and 40-50°S. These effects of ε_{sss} are mainly in the centre and eastern Pacific as shown by the latitudinal plots. Furthermore, 7 out of 10 of the latitudinal bands between 50°N/S showed

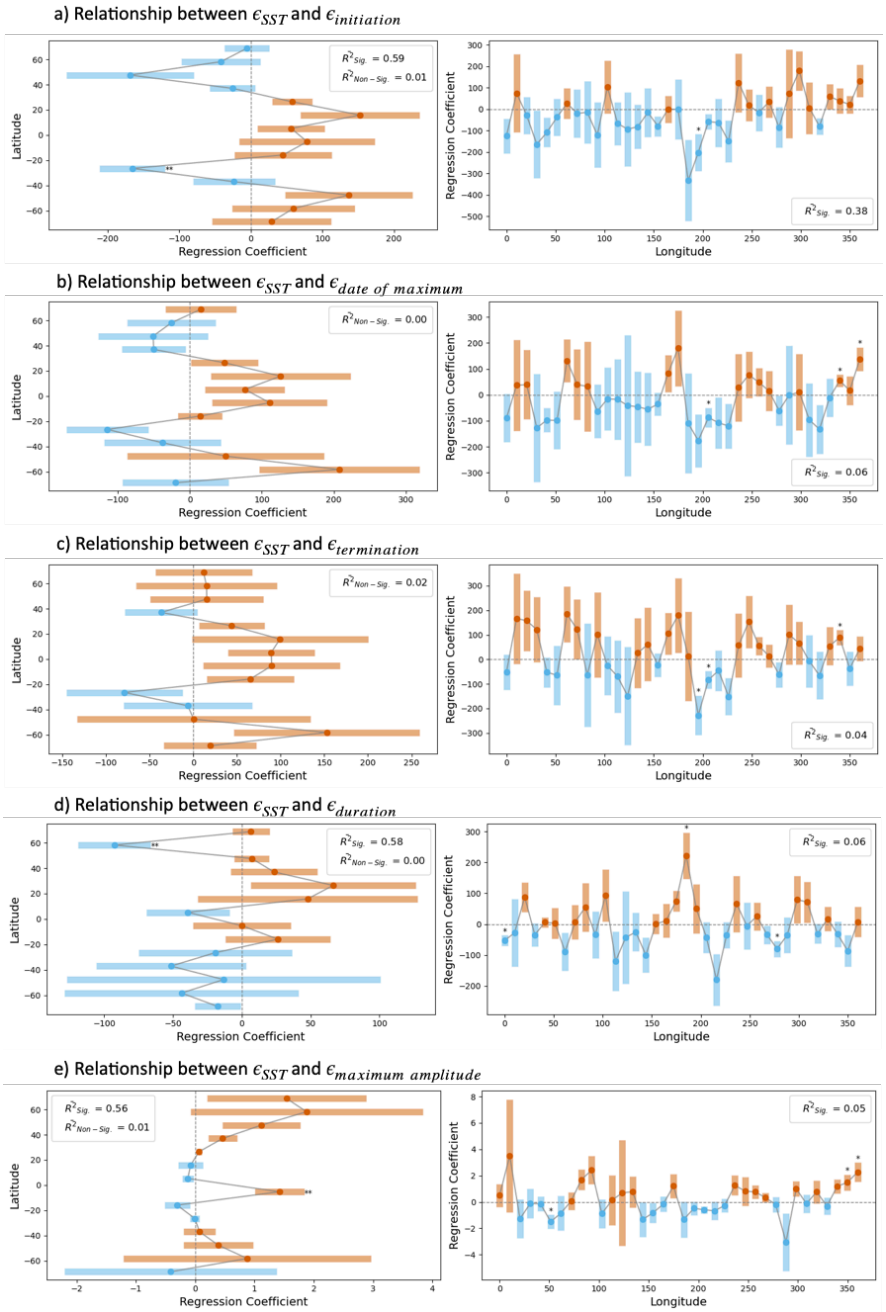

Figure 3.4. Relationship between Error in Model estimation of Sea Surface Temperature (ε_{sst}) on Error observed in phenology varies ($\varepsilon_{phenology}$; 1999-2020). Absolute annual mean errors of SST (|ΔSST|) and Phenology indices (|ΔPhenology|) are calculated by |model - observations|. The absolute errors are then regressed by |ΔSST| = a + b|ΔPhenology|, where n=11 and positive values represent where larger |ΔSST| result in larger |ΔPhenology|. Left/right panels show 10° mean latitudinal/longitudinal averages respectively. Points represent the regression coefficient and the error bars show the standard error. Significance is represented with asterisk, where * p < 0.05, ** p < 0.01, *** p < 0.001. Average R^2 values are presented for significant points (p < 0.05).

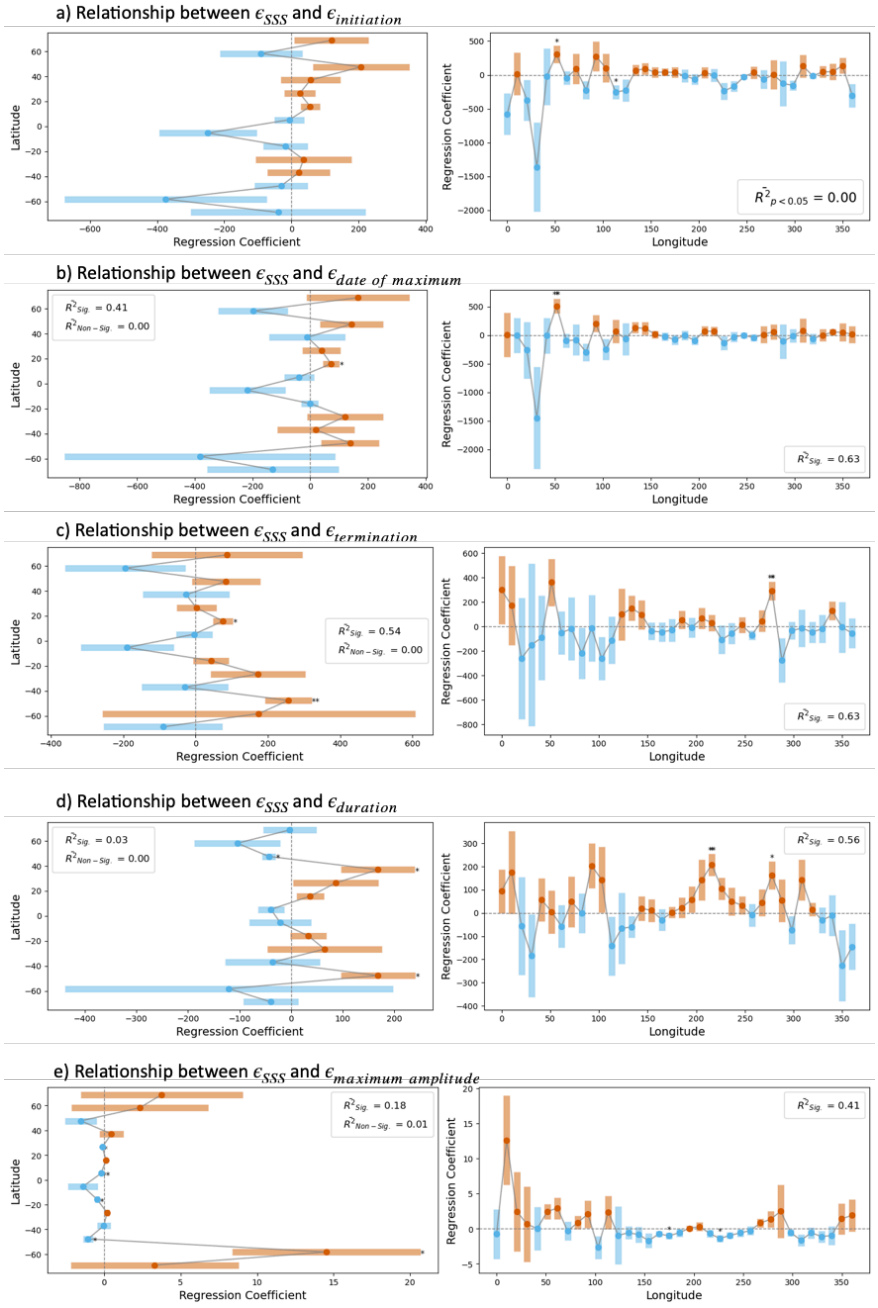

Figure 3.5. Relationship between Error in Model estimation of Sea Surface Salinity (ε_{sss}) on Error observed in phenology varies ($\varepsilon_{phenology}$; 1999-2020). Absolute annual mean errors of SSS (|ΔSSS|) and Phenology indices (|ΔPhenology|) are calculated by |model - observations|. The absolute errors are then regressed by |ΔSSS| = a + b|ΔPhenology|, where n=11 and positive values represent where larger |ΔSSS| result in larger |ΔPhenology|. Left/right panels show 10° mean latitudinal/longitudinal averages respectively. Points represent the regression coefficient and the error bars show the standard error. Significance is represented with asterisk, where * p < 0.05, ** p < 0.01, *** p < 0.001. Average R^2 values are presented for significant points (p < 0.05).

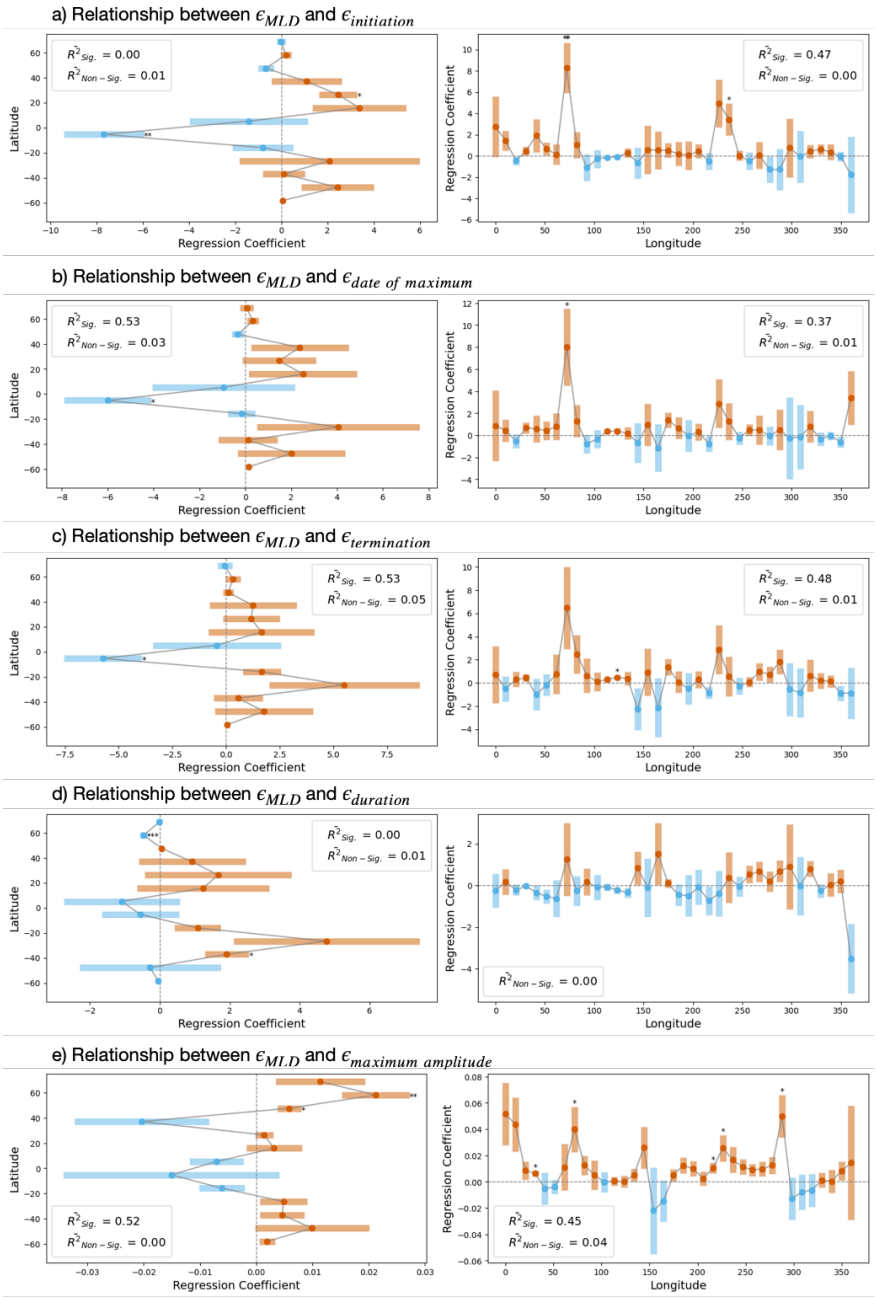

Figure 3.6. Relationship between Error in Model estimation of Mixed Layer Depth (ε_{mld}) on Error observed in phenology varies ($\varepsilon_{phenology}$; 1999-2020). Absolute annual mean errors of MLD (|ΔMLD|) and Phenology indices (|ΔPhenology|) are calculated by |model - observations|. The absolute errors are then regressed by |ΔMLD| = a + b|ΔPhenology|, where n=11 and positive values represent where larger |ΔMLD| result in larger |ΔPhenology|. Left/right panels show 10° mean latitudinal/longitudinal averages respectively. Points represent the regression coefficient and the error bars show the standard error. Significance is represented with asterisk, where * $p < 0.05$, ** $p < 0.01$, *** $p < 0.001$. Average R^2 values are presented for significant points ($p < 0.05$).

decreases in $\varepsilon_{maximum\ amplitude}$ in response to increases in ε_{sss} (4 significant). This indicates that the ε_{sss} in these regions are opposing the effects of another driver on $\varepsilon_{maximum\ amplitude}$, in the tropics ε_{sst} is partially responsible, but ε_{sst} alone does not explain the variation.

Mixed layer depth errors (ε_{mld}) again explain more variability in $\varepsilon_{phenology}$ than either ε_{sst} or ε_{sss} (Figure 3.6). Significant positive relationships occur between ε_{mld} and, $\varepsilon_{initiation}$ and $\varepsilon_{termination}$ in the Indian Ocean and western Pacific oceans. In the subpolar regions, despite large biases present in MLD (section 3.3.2), increases in ε_{mld} decrease $\varepsilon_{duration}$ and increase $\varepsilon_{maximum\ amplitude}$. The relationship between ε_{mld} and $\varepsilon_{maximum\ amplitude}$is the strongest of the variables tested, as expected from biases seen in section 3.3.2. In the significant points of subtropical and subpolar north, ε_{mld} explains 52% of the variance in $\varepsilon_{maximum\ amplitude}$. Furthermore, 5 of 36 latitudinal bands show significant positive relationships between ε_{mld} and $\varepsilon_{maximum\ amplitude}$ that an average explain 45% of the variation in ε_{mld}.

Although some relationships between ε_{sst} and $\varepsilon_{phenology}$ are statistically significant, low values of r^2 indicate that SST accounts for only a small fraction of the variance $\varepsilon_{phenology}$. Significant relationships between ε_{sst} and $\varepsilon_{phenology}$ indices on average accounts for only 26% of variance in $\varepsilon_{phenology}$. In comparison, ε_{sss} and ε_{mld} describe an average of 37% of variance associated with $\varepsilon_{phenology}$ in cases of significant relationships. Furthermore, significant relationships between $\varepsilon_{sst,sss}$ and $\varepsilon_{phenology}$ over longitudinal and latitudinal averages are uncommon. ε_{sss} and $\varepsilon_{maximum\ amplitude}$ have the most significant relationships over latitudes, yet only 5 out of 14 latitudinal bands demonstrating significant trends. However, 4 of 5 of these latitudinal bands showed negative trends, indicating that ε_{sss} coincide with reduction in $\varepsilon_{maximum\ amplitude}$. In addition, ε_{mld} and $\varepsilon_{maximum\ amplitude}$ have the most significant relationships over longitudes, with 5 of 36 longitudinal bands demonstrating significant positive relationships. These findings suggest that variations in nutrient supply, driven predominantly by salinity-induced stratification and depth of mixing, are likely driving a large proportion of the underlying the discrepancies in phenology observed within the model system. Other factors not included here, such as nutrients, grazing, or ecosystem dynamics must explain the remaining of the variance in the phenology of phytoplankton in the model ecosystem.

3.3.4. Global Trends in Total Chlorophyll

Globally the PlankTOM12.2 model contains lower chlorophyll concentrations than observations (Figure 3.7), but a similar magnitude of change between seasons. Strong interannual variation in the model and observations limit our ability to identify significant trends in chlorophyll concentrations; both the model and observations show non-significant trends over the two decades (Figure 3.7).

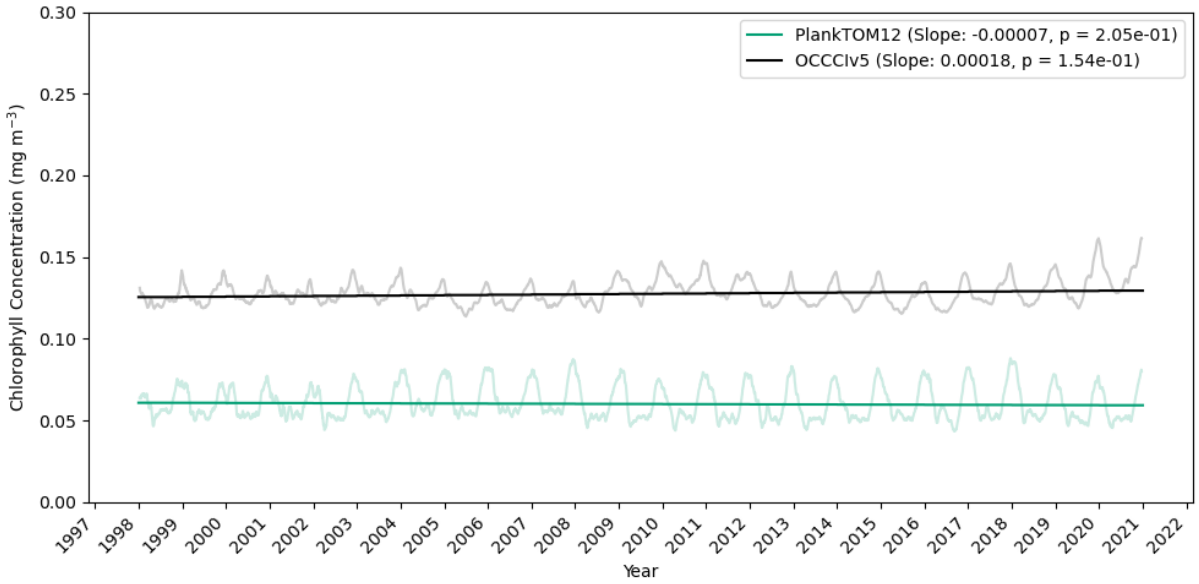

Figure.3.7. Global average total chlorophyll concentration (mg m^{-3}) for PlankTOM12.2(light green) and OCCCIv5 (grey) between 1998 and 2020. Dark green and black lines are Thiel-Sens slope for the yearly averaged chlorophyll concentration. The slope and p-value for these lines is displayed in the label. Global averages were calculated as follows: $10^{\overline{log(data)}}$ this reduces the chlorophyll concentration as it removes bias caused by spatial distortion at high latitudes; i.e. geographic projection netcdf files add additional weight to the high latitude regions in comparison to the sinusoidal projection data.

Despite regional biases in phenology between PlankTOM12.2 and observations, the model replicates the direction of global trends in initiation, termination and duration (Figure 3.8). Both the observations and model show trends towards earlier initiation by 2.9 days per decade between 1998 and 2020, which are visible for both delineated time series but are not statistically significant at the 95% level. Previous estimates of global trends suggest that the growing period became 2 weeks earlier on average per decade between 1998 and 2015 (average of grid cells where $p < 0.05$; Friedland et al., 2018). Termination dates became later between 1999 and 2020 in both PlankTOM12.2 and the observations by 6.3 and 2.6 days per decade respectively. Trends in termination were significant for both the observations (in one of the two time series; 1999-2020) and the model (both time series; Figure. 3.8). Previous research has focused on the initiation and duration of the growing period in regards to trends, rather than the termination date. However, both the

results presented in this Chapter and Racault, et al., (2012) support the idea that longer growing periods are associated with earlier initiation dates and later termination dates. Whereas, Friedland, et al., (2018) show a smaller trend in duration than in initiation date, suggesting that termination date becomes earlier as duration becomes longer globally. This difference is likely due to differences in the method used to calculate the phenology indices, both this chapter and Racault, et al., (2012) use the threshold method whereas Friedland, et al., (2018) use a change point algorithm.

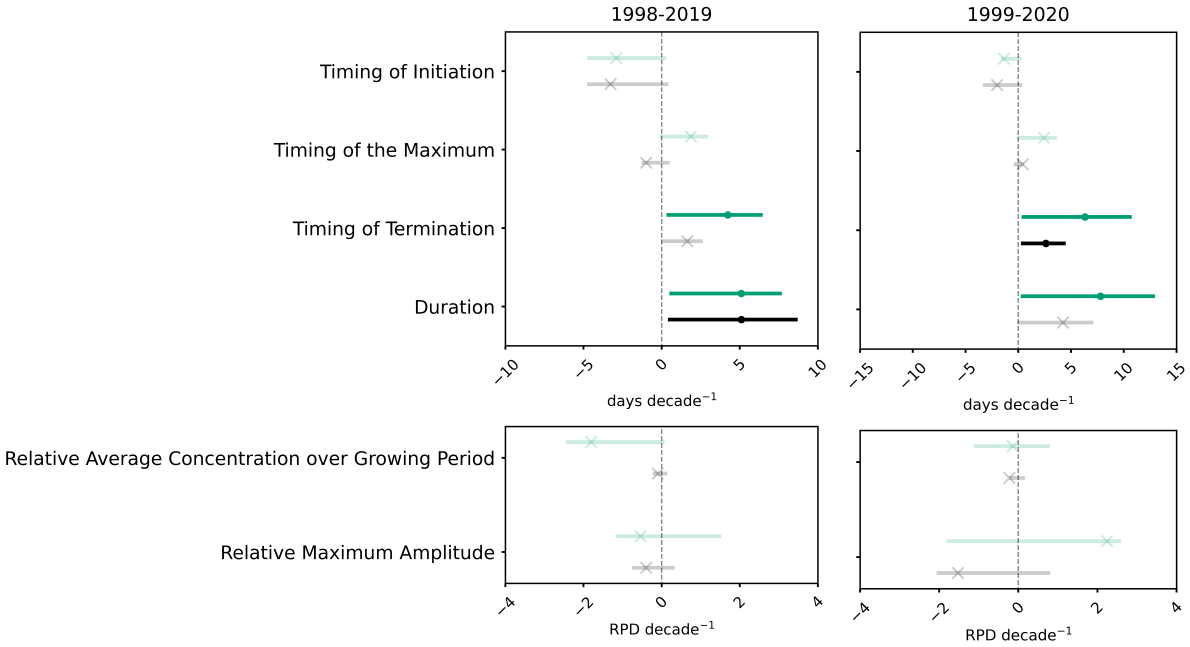

Figure.3.8. Global average trends in phenology indices for 11 biennial climatologies, from 1998-2019 and 1999-2020. Green represents PlankTOM12.2 and black represents OCCCIv5. Darker colours show significant trends.

Opposing trends in initiation and termination drive increases in duration of 5.1-7.8 days per decade, which are significant in both the observations (in one of the two time series) and the model (both time series; Figure 3.5). Localised trends in the timing of either initiation or termination sometimes also cancel out, resulting in trends in duration that are smaller than expected from the sum of trends in initiation and termination. Trends found here in duration are consistent with previous studies (Friedland, et al., 2018), who find that growing periods increased in duration of 7 days (where $p < 0.05$) between 1998 and 2015. Furthermore, I find that initiation became earlier and termination later between 1998 and 2020, whilst Friedland, *et al.,* (2018) suggest that both initiation and termination dates became earlier between 1998 and 2015. The presence of significant trends in termination in both PlankTOM12.2 and observations may suggest that termination date plays a more important role in driving the trends in growing period duration than previously thought.

Trends in the indicators describing the amplitude of the bloom are less conclusive. We find no significant global trends in the relative average concentration over the growing period ($RELΔb_c$) or the maximum amplitude ($RELΔb_a$). Differences in the direction of trends for $RELΔb_c$ between the two delimited datasets (1998-2019; 1999-2020) demonstrate inconclusive results in global trends of average concentration. In comparison, $RELΔb_a$ shows non-significant decreases over time periods of between 0.3-1% and 0.5-3% for observations and PlankTOM12.2 respectively. This would suggest that the relative maximum amplitude is a more consistent metric for change in the global ocean, as thus may be a more predictable metric for predicting changes in export in Chapter 4. The overall signals of trends towards longer growing period duration and lower relative maximum amplitude together suggest an evolution away from short, intense blooms, towards longer, lower intensity blooms.

Both delineated datasets are used here to show that there is general agreement between the two time series (Figure 3.9; Appendix 7.5). However, for brevity, only results from the time series between 1999 and 2020 are shown throughout the remainder of the chapter. This time series between 1999 and 2020 is likely to be a more accurate comparison of trends in contrast to the dataset ranging from 1998 to 2019 because there are significant gaps in the first few years of data. This is particularly apparent in 1998 which has just 10.5e6 points of good data compared to an average of 12.5e6 points of good data in the whole time series.

3.3.5. Regional Trends in Phytoplankton Phenology

To determine the differences in trends between the phenology of the model and observations, I compare the theil-sens slopes of the phenology indices calculated from observations and PlankTOM12.2 (Figure 3.8; 3.9). I also compare the longitudinal averages of trend in date of initiation, maximum amplitude and termination, duration, relative concentration over the growing period ($RELΔb_c$) and relative maximum amplitude ($RELΔb_a$). The PlankTOM12.2 simulation roughly follows the latitudinal trends in phenology timing indices between 40°N/S, however there are some marked differences. Trends in SST, SSS, MLD and phenological indices identified in this chapter are a result of temperature and salinity restoring, which increases trends in temperature and salinity to match observational levels. Versions of the PlankTOM12.2 model without temperature restoring successfully capture the regional variability of phenological indices, however these models exhibited lower trends in temperature compared to observations, and therefore have smaller trends in the termination and duration of the growing period compared to simulations where temperature is restored to observations. The restoring of salinity is important to correct mean model biases but has a smaller effect on regional and global trends than temperature restoring. Model versions forced with constant climate (and hence restoring to constant temperature and salinity) do not produce trends in duration of the growing period, suggesting that climate change is the driver of these phenological

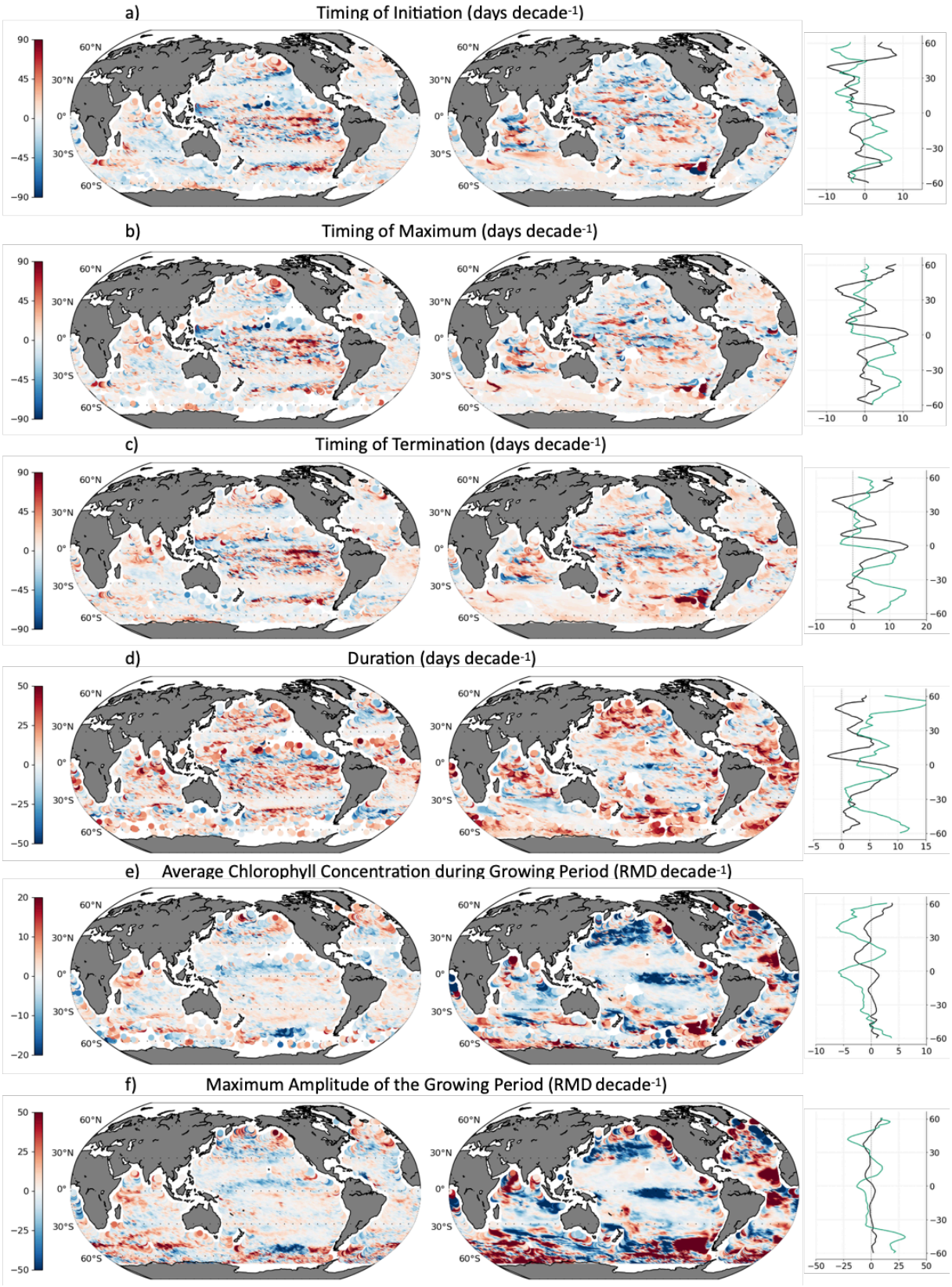

Figure.3.9. (a-f) Trends in phenology indices from OCCCIv5 (left) and PlankTOM12.2(right) using 11 biennial climatologies (1999-2020). Right panel shows latitudinal averages smoothed by 10° where black line shows observations and the green line shows PlankTOM12.2.

changes.

In observations, trends of delayed date of initiation, maximum amplitude and termination of the growing period are evident in the subarctic over the two decades (Figure 3.9). In comparison, the model shows trends towards earlier initiation, late termination and limited change in the timing of maximum amplitude. This is reflected in differences in the trends in duration, where the duration increases by 5 days per decade in observations and by 15 days per decade in PlankTOM12.2. These differences are most apparent in the north Pacific, however similar differences in trends of duration are seen in the Southern Ocean driven where model termination is delayed at 4x the rate of observations. These differences may originate from differences in the physical variables; however, the strong top-down control of phytoplankton in the model due to increased zooplankton representation is likely to also impact these trends.

In addition, whilst the general latitudinal pattern of phenology trends is replicated in PlankTOM12.2, there is a ~10° latitudinal divergence from observations (Figure 3.9). For example, a peak in trends of ~5 days per decade in initiation date are present at 0° in observations but occur at 15°S in PlankTOM12.2. This divergence is driven by trends towards early initiation dates (blue) in the equatorial Indian Ocean and late initiation dates (red) at 15°S in the Pacific and Indian Oceans. Similar trends in regional patterns are found in observations as previous global studies, despite methodological differences (Friedland, et al., 2018). However, I find much more spatial coherence in trends in duration across the ocean. Specifically, we show limited change in phenology indices in low-productivity subtropical regions and high rates of change in high-productivity tropical and subpolar regions.

In both the observations and model, the regions with the largest trends are concentrated in the tropics and the subpolar north/south. Trends are particularly extreme in the southern Pacific subtropical subpolar convergence zone (~40°S) where the initiation and termination date changed by up to -/+90 days per decade in the Western/Eastern Pacific between 1999 and 2020. In the Western regions these earlier trends resulted in longer growing period duration, whereas in the Eastern regions late blooms were associated with shorter duration. In the tropical Pacific, regional differences in the regional variability in phenology trends appear to coincide with differences in trends of SST and SSS (section 3.3.3).

Whilst relative maximum amplitude ($REL\Delta b_a$) and concentration over the growing period ($REL\Delta b_c$) both decrease globally between 1998 and 2019, increases in concentration metrics are identified locally (Figure 3.9). Both PlankTOM12.2 and the observations show increases in concentration metrics in the subpolar north, tropical Pacific and southern subtropical subpolar Pacific

convergence zone. However, relative concentration of the bloom and maximum amplitude increases consistently over the entire Indian Ocean in the PlankTOM12.2 model (Figure 3.9.f). However, there is some variability between the regions with strong trends in both $RELΔb_a$ and $RELΔb_c$. For example, $RELΔb_{a,c}$ increases around 0° in PlankTOM12.2 but around 15°N in observations. This is discrepancy in latitudinal average is driven by strong increase in $RELΔb_{a,c}$ at 0° in the Pacific, and large decreases in $RELΔb_{a,c}$ at 15°N in the Atlantic. In addition, trends have more variability between regions in PlankTOM12.2 compared to observations. This indicates that PlankTOM12.2 may overestimate trends in relative concentration indices, however over longer time periods this effect is likely to be reduced due to limitations eventually imposed by nutrients, light or grazing. This is especially relevant for Chapter 5, where I investigate the changes in phenology indices and export by 2100.

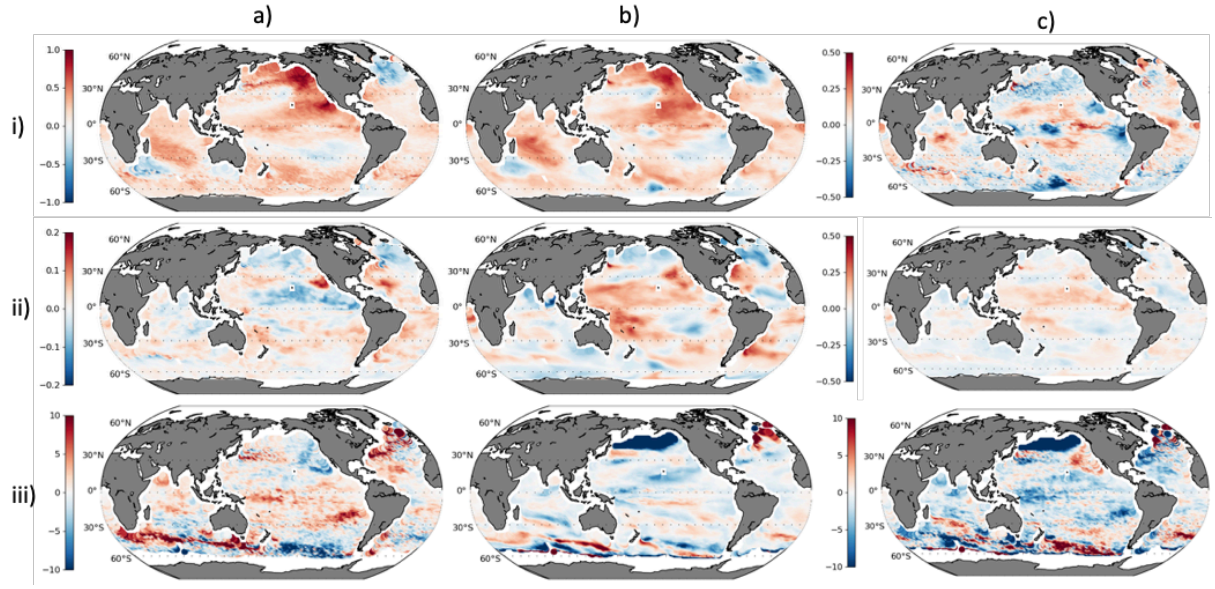

Figure.3.10. Trends in i) sea surface temperature (°C), ii) salinity (PSU) and iii) mixed layer depth (metres) in observations (a) and PlankTOM12.2 (b). Trends are calculated with sens-slope over 11 biennial climatologies, from 1999-2020. Panel c) shows the difference between model and observations, where red indicates where model trends are greater than trends in observations and blue indicates where model trends are lower than observations.

These differences in phenology between the observations and model are likely rooted in differences in forcing metrics. Trends in SST are similar between the model and observations, although there is some divergence in magnitude (Figure 3.10). SST trends are greater in the Atlantic and tropical Pacific in the model, and lower in the central equatorial Pacific and polar regions. In comparison, trends in SSS, although small, appear quite different in the model compared to observations. Specifically, freshening trends observed between 0° and 15°N in the Pacific Ocean are absent in the model, which instead shows an increase in SSS of ~0.1 PSU in this region (Figure 3.10.ii). Furthermore, differences in trends in MLD between the observations and model are widespread (Figure 3.10.c.iii). In the

subpolar Pacific the MLD shallowed by 100 metres per decade in PlankTOM12.2, whereas in the observations the changes are much less extreme. The PlankTOM12.2 model shows a shallowing of MLD over the two decades in the majority of the ocean, whereas the observations suggest that shallowing is much less common. Differences in MLD trends are likely to be more influential in driving the differences in trends between the observations and models than SST or SSS. MLD appears particularly influential in the tropical Pacific where increases in $RELΔb_{a,c}$ appear to coincide with areas of freshening and deepening of the MLD. These confirm findings of section 3.3.3 which found that errors in SSS and MLD are more related to errors in phenology indices than SST errors.

3.4. Conclusion

This chapter evaluates the performance of PlankTOM12.2 in reproducing phytoplankton phenology and spatial patterns and trends in the global ocean. By comparing the average phenology over the time series, trends in phenology indices, as well as analysing bias of the trends I highlight PlankTOM12.2 as a valuable instrument for studying changes in phenology of phytoplankton. Overall, the model demonstrates a good agreement with observations in phenology indices and trends of phytoplankton phenology, particularly when averaged latitudinally. However, there are notable local deviations from observations.

For climatological differences, PlankTOM12.2 has earlier growing periods in the north subtropical Pacific and subpolar latitudes compared to observations. Other studies have suggested that increasing zooplankton complexity alters the mechanism controlling the initiation date, resulting in earlier blooms (Karakuş et al., 2021). As PlankTOM12.2 has 6 zooplankton functional types, it is likely that the additional top-down pressure of zooplankton is impacting phytoplankton phenology. Additionally, the duration of the growing period tends to be lower in the model in most areas of the global ocean, where a lack of latitudinal banding in duration is observed. This bias in duration is much smaller compared to the bias in individual timing indices, suggesting that duration is a more stable metric for predicting phenology impact. The model also exhibits higher variability of total chlorophyll in all regions, except in a small band of the subtropics. In observations, relative maximum amplitude decreases from +75% in the subpolar regions to just +25% of the yearly average in the tropics. In contrast, in PlankTOM12.2 the $RELΔb_a$ decreases from +125% in the subpolar latitudes, to +40% in the subtropics, but then increases again in the tropical regions to +90%. This indicates that not only is seasonal phytoplankton variability higher over the global ocean, but that seasonal variability in the tropics is more representative of variability seen in polar regions. Despite these local differences, at a regional resolution there is no statistical difference between the phenology of PlankTOM12.2 and observations.

Trends found from observational phenology metrics are consistent with previous studies (Friedland et al., 2018; Gittings et al., 2018; Racault et al., 2012; Zeng et al., 2013). PlankTOM12.2 successfully

captures the direction of these global trends in the timing of initiation, termination, duration, and maximum amplitude. There are regional differences when comparing the trends in phenology indices between the model and observations. In the north Atlantic, the model exhibits a trend towards earlier initiation of the growing period, while observations trend towards later initiation. Model trends in duration align well with latitudinal patterns from observations, however large increases in duration occur in the subpolar regions of the model. These large trends are driven by early initiation in the north and late termination in the south. Furthermore, in there is a marked difference in trends in the Northern Hemisphere for $REL\Delta b_{a,c}$. Whilst the observations show a peak in trend of 2.5% per decade around 15°N, the PlankTOM12.2 model predicts large trends in $REL\Delta b_{a,c}$ around 0°. To assess the drivers of these biases in the trends of phenology in the PlankTOM12.2 model, regressions were conducted between $REL\Delta b_{sst,sss}$ and $\varepsilon_{phenology}$.

Overall it is clear that whilst errors in SST, SSS and MLD are partially responsible for phenological errors, metrics not explored in this chapter are responsible for the majority of errors in the model phenology indices. While the model's phenology indices were generally not significantly different from observations at a regional scale, biases and discrepancies were found in the underlying physical variables. The model tended to overestimate SST trends in the Atlantic and tropical Pacific, while underestimating them in the central equatorial Pacific and polar regions. Additionally, the model showed differences in SSS trends compared to observations. In particular, freshening trends observed in the Pacific between 0° and 15°N were absent in the model, which instead showed an increase in SSS in this region. The PlankTOM12.2 produces global trends towards shallowing MLD whereas the observations show a global deepening of MLD during the period examined here. Despite these differences in SST and SSS, we find that ε_{sst} only explains a small amount of variable in $\varepsilon_{phenology}$. Changes in ε_{mld} and ε_{sss} explain 37% to the variance in $\varepsilon_{phenology}$ (where $p < 0.05$), however a substantial portion of the variability of $\varepsilon_{phenology}$ remains unconstrained. Therefore, differences in other variables such as irradiance, nutrients, and grazing are likely to contribute to the errors in the phenology of the PlankTOM12.2 model.

In conclusion, whilst there are local deviations in the spatial patterns and trends of phytoplankton phenology in PlankTOM12.2, at a regional resolution PlankTOM12.2 phenology is similar to observations. It is clear that errors in SST, SSS and MLD do not drive the error in phytoplankton phenology alone, adding to a growing body of literature that suggests that other factors such as nutrients and community structure play a large role in phytoplankton phenology (Henson et al., 2019; Henson et al., 2017; Yamaguchi et al., 2022). Further investigation into the drivers of phytoplankton phenology in the model is conducted as part of Chapter 4 in order to constrain the complex dynamics of phytoplankton communities and their responses to environmental factors in PlankTOM12.2. Whilst

caution should be exercised when interpreting regional differences, the findings suggest that the PlankTOM12.2 model is a useful tool for studying phytoplankton phenology.

Chapter 4. Ecological Drivers of Export in the ecosystem models PlankTOM12.2

Abstract

This chapter presents an analysis of the relationship between changes in phytoplankton phenology focusing on duration and initiation of the growing period, and changes in organic carbon export production (EP) and export efficiency (EF) in the global ocean, using the newly developed PlankTOM12.2 (outlined in Chapters 2 and 3). The analysis uses 11 biennial climatologies spanning 1999-2020, categorises them into 'long' and 'short' growing periods, and identifies the related anomalies in the initiation dates, sea surface temperature (SST), mixed layer depth (MLD), net primary production (NPP), as well as EP and EF at the global and regional level. A multiple regression analysis with bootstrapped standard errors is conducted to isolate the potential impact of various physical and ecological drivers on EP and EF across 13 ocean regions, and to infer the underlying processes. The findings reveal small but significant regional variations in EP and EF that are related to the duration of phytoplankton growing periods. In polar regions, longer growing periods are mostly associated with enhanced carbon EP, whilst in the tropics longer growing periods are mostly associated with reduced EP. In general, the impact of phenological changes on EP and EF is small relative to the impacts of NPP, MLD and SST. However, in some regions of the Southern Ocean, the impact of duration on EP is equal to or greater than that of MLD. For example, in the subpolar southern Pacific, an increase of 1 standard deviation in both MLD and growing period duration were related to a 12.6% decrease in EF; a change equivalent to 2.9 times the standard deviation of EF. This highlights the complexity of the interactions between physical and ecological drivers, as well as the limits of our understanding of the mechanisms underpinning the role of the ecosystem for carbon EP and EF.

4.1. Introduction

The export of organic matter from the ocean's surface to its depths plays a pivotal role in the Earth's carbon cycle. Global export from the euphotic layer is approximately 10 petagrams of carbon (Pg C) annually, critically regulating atmospheric CO_2 levels (Nowicki et al., 2022). Notably, only about 1% to 30% of the fixed organic carbon is transported out of the euphotic zone, depending on the region, with the bulk of net primary production (NPP) being recycled in the ocean's upper layers (Steinberg and Landry 2017; Chapter 1). Phytoplankton, with their rapid life cycles and sensitivity to environmental changes, serve as key indicators of environmental change. Extensive research has focused on their response to climate change, particularly in terms of growing period timing, NPP, and ecosystem community structure (Behrenfeld 2010; Friedland et al., 2018; Martinez et al., 2009; Racault et al., 2017a; Thomalla et al., 2023b). Studies also highlight the significant changes in phytoplankton communities under environmental stressors, with implications for the structure of marine ecosystems (Anderson et al., 2021; Behrenfeld et al., 2015; Chivers et al., 2020; Gregg et al., 2017). Phenological studies, examining the timing of phytoplankton blooms, show variations across ocean regions influenced by factors such as light availability and mixed layer depth (MLD)(Friedland et al., 2018; Henson et al., 2018; Racault et al., 2012). However, the direct impact of phytoplankton growing period timing on carbon export remains a critical gap in our knowledge.

Warming oceans and increased occurrence of extreme climate events are significantly reshaping the phenology of phytoplankton in the global ocean. These alterations have resulted in large-scale shifts towards earlier, longer growing periods (Cooley et al. 2022; Henson et al., 2018). Such variations in the onset and duration of growing periods are likely to impact marine food webs. Mismatches between the timing of phytoplankton growth and the feeding periods of higher trophic levels can disrupt ecological interactions (Cushing 1990; Edwards and Richardson 2004; Ferreira et al., 2023; Koeller et al., 2009; Platt et al., 2003), potentially influencing the efficiency of carbon export by misaligning peak phytoplankton production and consumption. For instance, extended periods of carbon sequestration or changes in the depth distribution of organic matter due to prolonged phytoplankton blooms could increase carbon export to deeper waters (Friedland et al., 2018). However, research by Karakuş, et al., (2021) showed that increasing zooplankton complexity in a model system from one to three PFTs resulted in a 25% increase in net NPP and a 10% decrease in export production (EP). This underlines the critical role of zooplankton in carbon export dynamics, however most frequently used models for predicting export changes have insufficient representation of zooplankton dynamics (Henson et al., 2022). This limits our understanding of the full impact of phenological changes on the marine ecosystem and carbon export.

To date, the direct influence of phytoplankton growing period timing on carbon export remains largely unexplored, despite extensive study surrounding phytoplankton phenology, ecosystem structure, composition of POC flux, impact of $CaCO_3$ ballasting, mismatch hypothesis and carbon

export. Most current models used for predicting carbon export are lacking critical variables such as temperature/oxygen-dependent remineralisation, fragmentation, and zooplankton complexity, all important processes for accurate carbon export modelling and understanding the biological carbon pump's efficiency (Henson et al., 2018). This gap underscores the complexity of marine ecosystems and the necessity for comprehensive modelling approaches that integrate these essential factors. Furthermore, accurately predicting EP in the ocean is challenging, due to the complex interplay of oceanographic and ecological processes. Studies, such as those by Henson, et al., (2018) and Yamaguchi, et al., (2022) have forecasted significant shifts in ocean phenology due to global warming, with profound implications for marine ecosystems. However, the specific impact of phenological changes on carbon export, a crucial factor in understanding Earth's future climate system, remains unknown (Cooley, et al., 2022). The variability in climatic change responses across different ocean regions adds to this challenge, necessitating models that can accommodate region-specific factors influencing carbon export (Bindoff et al., 2019).

The aim of this chapter is to provide a first estimate of how variations in growing period duration and initiation date could shape the patterns and efficiency of organic carbon export using the PlankTOM12.2 model.

4.2. Methods

4.2.1. PlankTOM12.2 Data

Data on sea surface temperature (SST), MLD, NPP, surface chlorophyll concentration, and export at 100m (EP) were obtained from the PlankTOM12.2 model, described in Chapter 2 (doi.org/10.5281/zenodo.8388158). The integrated NPP within the upper 100 metres of the global ocean was calculated. Eleven biennial climatologies were calculated for the interval between 1999 and 2020. The duration and initiation date of the phytoplankton growing period was calculated from total chlorophyll concentration using the threshold method (described in Chapter 3), for each biennial climatology. The threshold was set to the median chlorophyll concentration plus 5% for comparability with previous studies. Export efficiency (EF) was quantified by the ratio of EP to NPP, which was then multiplied by 100 to represent it as a percentage of NPP.

4.2.2. Calculation of Anomalies between Long and Short Growing Periods

The 11 climatologies were ranked for each model grid cell based on the duration of phytoplankton growing periods, and were subsequently divided into two groups: one characterised by 'long growing periods' and the other by 'short growing periods', each comprising five climatologies. The median climatology was excluded from this analysis to enable a distinct categorisation of the two groups. Anomalies in NPP, MLD, SST, EP, and EF were calculated by subtracting the average values of these variables in the 'short growing period' group from those in the 'long growing period' group. For all

parameters except the initiation date of the growing period and the SST, relative anomalies were determined. Relative anomalies aren't applicable to initiation date as initiation date varies globally between from 1 and 365; a change in initiation date from 365 to 340 (relative change = -7%) is more significant than a change in initiation date from 1-2 (relative change = +100%). Furthermore, whilst SSTs are much higher in the tropics than the polar regions, there is evidence to suggest that thermal breadth does not increase with latitude (Chen 2015). Relative anomalies were calculated by dividing these differences by the average values from the 'long growing period' group and then multiplying by 100 to express them as a percentage. This method allowed for insights into the relative importance of changes in each parameter, considering the typical values for each region.

4.2.3. Statistical Analysis to Isolate the Contributions to Export Production and Efficiency

The effects of duration, initiation, SST, MLD, and NPP on the EP and EF in the global ocean were explored through multiple linear regression analyses with bootstrapped standard errors, using the 11 biennial climatologies as calculated from the PlankTOM12.2 model over the 1999-2020 period. This method provides quantitative estimates of the independent contributions of each ecological (duration, initiation, NPP) or physical (SST, MLD) variable on the two export variables (production and efficiency). These regression coefficients are then examined in light of the processes included in the PlankTOM12.2 model to infer the underlying processes. Despite the significance of SSS in explaining the bias of phenology identified in Chapter 3, SSS was not included in this analysis due to its strong intercorrelation with MLD. Including intercorrelated variables like SSS and MLD could inflate variance, reduce precision, and complicate the interpretation of each variable's effect, ultimately obscuring the true relationships within the model. MLD was selected for its role in regulating nutrient availability and light limitation. These factors, in turn, are crucial for the growth and development of phytoplankton, directly influencing phenological events in marine ecosystems. Unlike salinity metrics, MLD offers a clearer and more direct link to these fundamental biological processes by controlling the environmental conditions that directly limit or enhance phytoplankton growth.

Bootstrapped standard errors were employed for the calculation of standard errors and confidence intervals, due to the non-normal distribution of residuals. Standard errors were computed using a repeated bootstrapping method, where each of the 1000 iterations involved resampling a number of data points equal to the original count specific to each region. Z-transformation was applied to all variables to ensure a normal distribution and to address unequal variances. The resulting z-scores were then subjected to multiple regression analyses across thirteen regions of the global ocean. In addition, Variance Inflation Factor (VIF) scores were computed for all variable z-scores within each region to ensure absence of multicollinearity.

The regression coefficients, standard errors, and confidence intervals were subsequently transformed back into the units of 'y' by multiplying them by the regional standard deviation (SD) of EP and EF, to

enable interpretation in the context-specific units (mg m^{-2} d^{-1} SD^{-1} and % SD^{-1}, respectively). The use of changes relative to one SD enables the direct comparison of the amplitude of the regression factors among all variables.

4.3.Results

4.3.1. Anomalies between Long and Short Growing Periods

There are widespread anomalies in initiation date, SST, and MLD between long and short growing periods in the PlankTOM12.2 model. There is large variability in the duration of the growing period over the two decades. Longer growing periods of close to +100% are widespread in the Northern Hemisphere where growing periods are historically shorter (~45 days; Figure 4.1.a.A). In regions with longer growing periods such as the south Indian/Pacific Ocean (60-40°S; 50°-150°) duration averages 126.2 days and varies on average by 19.3% between long and short growing periods. The relationship between growing period duration and initiation date shows clear patterns, with earlier initiation date generally corresponding to longer growing periods, as highlighted in Chapter 3 (Figure 4.1.b). This variance is particularly pronounced in subpolar regions, where initiation dates of long growing periods can be earlier than those of short growing periods up to six months (Figure 4.1.b.B). In comparison, in the subtropical Pacific there is a discernible delay in the onset of growing periods by

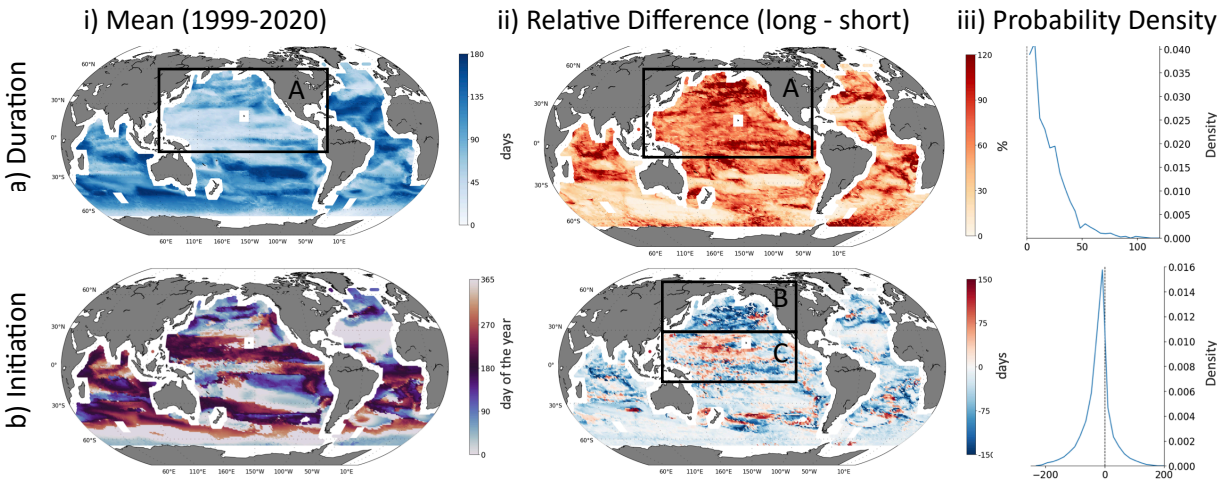

Figure 4.1. Maps of average a) duration of the growing period (days), and b) initiation date (day of the year[1]). Average calculated of the yearly average value of 11 biennial climatologies between 1999 and 2020. Panel (i; left) shows average calculated of the yearly average value of 11 biennial climatologies between 1999 and 2020. Panel (ii; right) shows a) the relative percentage difference and b) the absolute difference between the values in the longest and shortest growing periods over the two decades of data (1999-2020). Panel (iii) are histograms of panel (ii) showing the probability density of a) relative percentage difference and b) absolute difference between long and short growing periods.

an average of 44 days during long growing periods (Figure 4.1.b.C). There are also some instances of long growing periods coinciding with later initiation dates in the subtropical Pacific and Atlantic, but these are overshadowed by the more prevalent negative anomalies, where longer growing periods

tend to occur alongside earlier initiation dates. These results indicate a strong latitudinal dependency in the timing of phytoplankton blooms relative to the length of the growing period, suggesting significant regional responses to environmental changes.

SSTs generally tend to be warmer during the years where growing periods are longer (Figure 4.2a). SSTs are warmer during long growing periods in the north Pacific by up to 1.7°C . In contrast, SST are cooler during long growing periods in the north Atlantic and tropical Pacific by up to -1.3°C. There is also marked contrast in SST anomalies below 50°S, depending on the duration of phytoplankton growing periods. Below 50°S SST is consistently warmer during longer growing periods by up of 0.55°C. Within the tropical Pacific (Figure 4.2.a.A), SST anomalies show a slight cooling (-0.35°C), demonstrating the limited role of SST for growing period duration in these regions.

The relationship between growing period duration and MLD is less spatially coherent than that of SST, but certain trends are evident (Figure 4.2b). The Southern Ocean shows shallower MLD up to 6% during longer growing periods, likely linked to the warmer temperatures apparent in biennial climatologies with longer growing periods. The subtropical north Atlantic Ocean also has shallower MLD during long growing periods by an average of 5.7% possibly related to lower salinity (freshening;

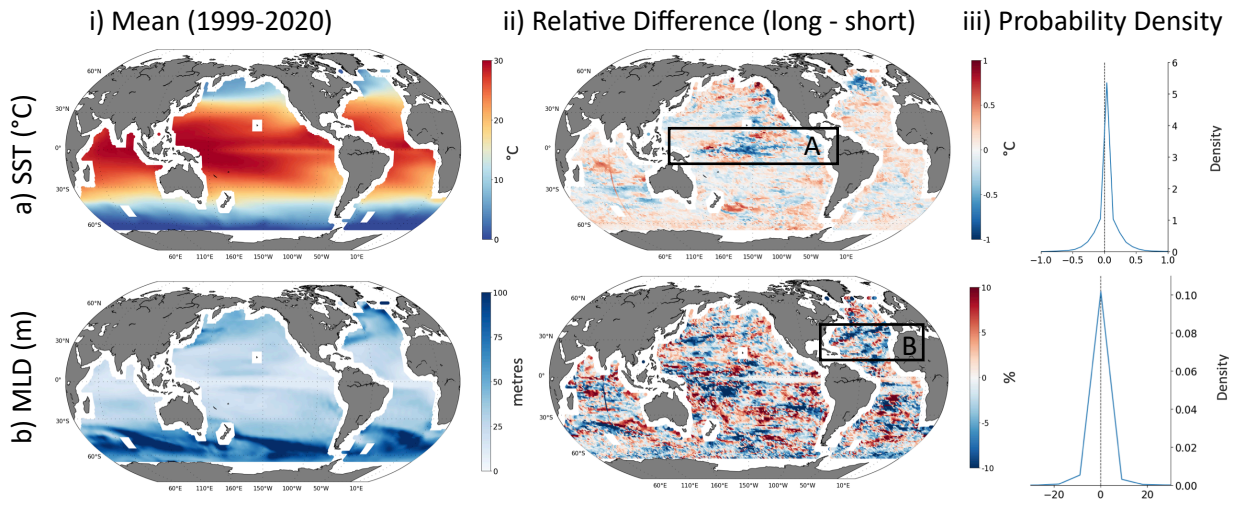

Figure 4.2. Maps of average a) sea surface temperature (SST; °C) and b) mixed layer depth (MLD; metres). Average calculated of the yearly average value of 11 biennial climatologies between 1999 and 2020. Panel (i; left) shows average calculated of the yearly average value of 11 biennial climatologies between 1999 and 2020. Panel (ii; right) shows a) the absolute difference and b) the relative percentage difference between the values in the longest and shortest growing periods over the two decades of data (1999-2020). Panel (iii) are histograms of panel (ii) showing the probability density of a) absolute difference and b) relative percentage difference between long and short growing periods.

Figure 4.2.b.B). In contrast, the subtropical south Pacific has deeper MLD during long growing periods. However, most of the Pacific, tropics, subtropical Atlantic and Indian Oceans exhibit a

patchwork of red and blue, demonstrating the complex and varied influence of MLD on the duration of growing periods in PlankTOM12.2.

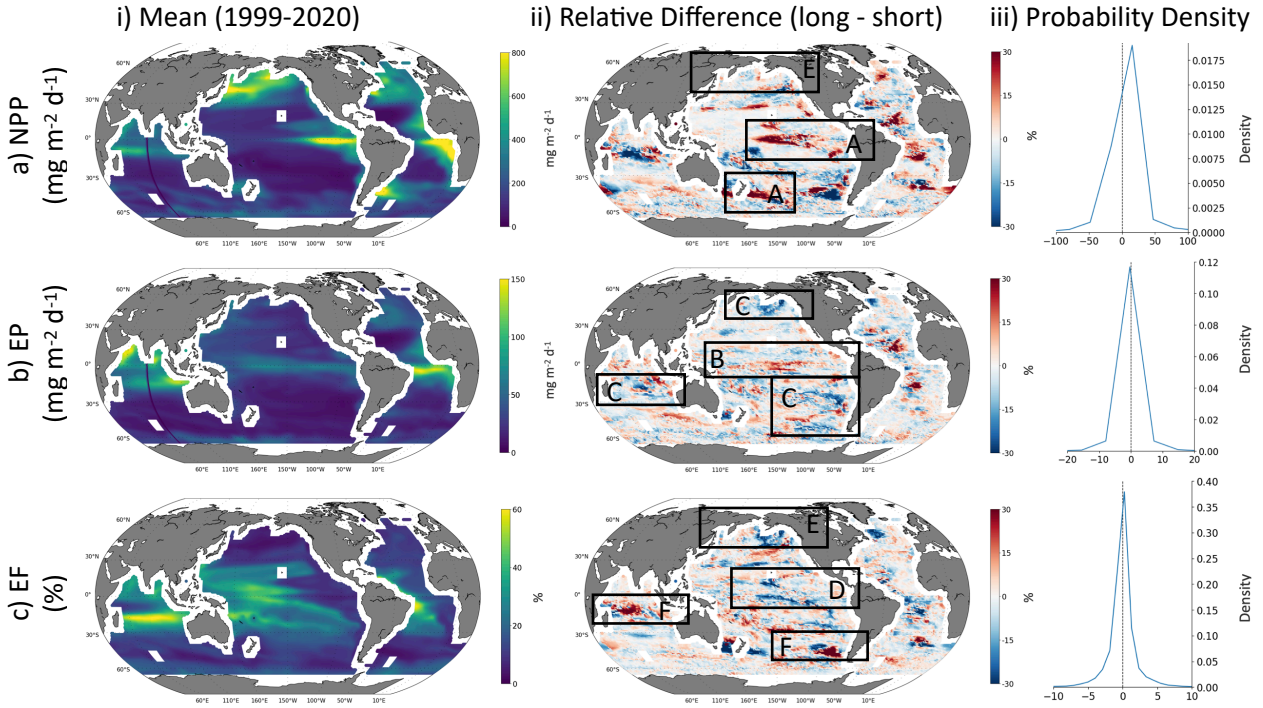

Figure 4.3. Panel i) shows the average a) primary production (mg m^{-2} d^{-1}), b) export production (mg m^{-2} d^{-1}) and c) export efficiency (%) between 1999 and 2020. Average taken of the yearly values of 11 biennial climatologies between 1999 and 2020. Panel ii) shows the relative percentage difference between the values in the longest and shortest growing periods of a) export production and b) export efficiency over the two decades of data (1999-2020). Panel (iii) are histograms of panel (ii) showing the probability density of relative percentage difference between long and short growing periods.

Finally, the relationship between growing period duration and NPP shows strong regional variations. The eastern tropical and south western Pacific has higher NPP during longer growing periods of 15% (Figure 4.3.ii.A), while the tropical Indian and Atlantic Oceans show lower NPP under longer growing periods. The south Pacific in subtropical latitudes displays lower NPP during longer growing periods, particularly off south America's coast where NPP slows by up to 110% compared to shorter growing periods. Conversely, in the Pacific's oligotrophic regions, shaped like '<', there is the smallest relative change in NPP between long and short growing periods. These patterns highlight that the duration of the bloom and the rate of NPP have varied interactions across the ocean regions.

Many of the anomalies in NPP during longer growing periods are evident in anomalies in export during longer growing periods (Figure 4.3a). The central tropical Pacific and the Northern Hemisphere's subtropical regions typically show increased export during longer growing periods by 9% (Figure 4.3.a.ii.B). Conversely, the south Pacific, parts of the north Pacific, and the subtropical

Indian Ocean show decreased export during longer growing periods (Figure 4.3.ii.C). These spatial distributions indicate a nuanced interaction of ecological and environmental factors affecting export rates, with clear differences between the hemispheres and among various oceanic basins. The Atlantic shows a distinct latitudinal pattern in these anomalies; heightened EP during longer growing periods is evident in the northern temperate and subpolar Southern Ocean regions, whilst the subtropical south shows a reduction in export during long growing periods. The Pacific, however, presents a more intricate array of longer and shorter growing period anomalies, suggesting that the response to the duration of growing periods may be more regionally specific than in the Atlantic. The declines in export rates do not always align with regions experiencing reduced NPP rates during longer growing periods. For instance, in the subtropical south Pacific, which has consistent levels of NPP rates regardless of the growing period length, there is a marked decrease in export rates of approximately 20 mg m^{-2} d^{-1} during longer growing periods.

The relationship between EF anomalies and longer growing periods has notable regional variability when compared to anomalies in export. In the tropical Pacific, a region typically characterised by high biological activity, there is a discernible decrease in EF despite apparent increases in NPP by 10.8% (Figure 4.3.c.ii.D). Similarly, the subpolar north pacific also has reduced EF (-11%) during longer growing periods, but this is instead driven by both a decrease in export and NPP (Figure 4.3.c.E). In this region a potential decoupling between NPP and particulate export during prolonged growing periods, possibly due to a variety of factors including nutrient limitations or changes in community structure may be limiting EF during long growing periods. In comparison, the Indian Ocean, subpolar Atlantic Ocean and the south Pacific Ocean exhibit increased EF during longer growing periods (Figure 4.3.c.F). This suggests that in some regions longer growing seasons may expand the temporal window for phytoplankton growth and subsequent export of organic matter.

4.3.2. Drivers of Regional Export Production in the PlankTOM12.2 Model

The multi-regression analysis using the 11 biennial climatologies provides quantitative information to isolate the unique effect of duration, initiation date, NPP, SST and MLD on EP. Results show that the relationships and dominant drivers are highly variable across ocean regions. This reflects the complexity of oceanographic and ecological processes that control the downward flux of organic material. In order to compare the magnitude of effect of the independent variables, regression results are given as the response of export (mg m^{-2} d^{-1}) to a 1SD change in duration, initiation date, NPP, SST and MLD. Although the multiple regression analysis does not provide conclusive information to designate if a correlation reflects a causal effect, strong and systematic correlations, if they correspond to identifiable processes in the model structure, are indicative of likely drivers.

4.3.2.1. Global Picture

Across almost all basins, NPP shows a significant positive relationship with EP, indicating that most increases in NPP are leading to direct effects for EP (Figure 4.4). Warmer sea surface temperatures are associated with decreases in EP in the subpolar regions and tropics, but with increases in the subpolar regions. This is likely due to changes in phytoplankton distribution, as the ocean warms tropical species are predicted to migrate from the tropics into the subtropics whilst large extinction events occur in the poles. In addition, the relationship between the duration and initiation date of the growing period and EP are weaker than other drivers, as suggested by the analysis of the covariance with duration presented above (Section 4.3.1). This implies that phytoplankton phenology is a less significant driver of export dynamics. However, the Southern Ocean is an exception, where the model often suggests the magnitude of the relationship between duration or MLD and EP and EF are comparable. The results of the Southern Ocean underscore the unique interplay of ecological and physical processes in this region, and suggest that adequate ecosystem representation is especially important for models aiming to assess the development of the Southern Ocean carbon sink. Furthermore, the relationship between MLD and EP varies significantly between regions. For example in the tropical Pacific and Atlantic increases in MLD relate to decreases in EP, whereas in the tropical Indian Ocean increases in MLD relates to increases in EP. This is likely due to differences in the regional drivers of phytoplankton growth, i.e. nutrients and light limitation. The variability of these processes is region-specific, and thus, they are detailed on a regional basis in the subsequent sections.

4.3.2.2. Pacific Ocean Trends

In the Pacific Ocean, the relationship between the growing period's duration and EP is typically negative (Figure 4.4). In most regions the effect of duration on export is relatively minor, particularly when weighed against the effects of NPP, SST and MLD. However, in the subtropical and subpolar south Pacific, the influence of duration on export (-1.9 and -11.0 mg m^{-2} d^{-1} SD^{-1}, respectively) is comparable to the effects of MLD (1.2 and -10.9 mg m^{-2} d^{-1} SD^{-1}). The role of MLD as a pivotal factor in predicting EP is well-established, particularly through its influence on nutrient availability, light penetration, and the seasonal dynamics of net community production (Bopp et al., 2015; Silva et al., 2021; Xue et al., 2022). However, these results reveal that, in certain regions such as the subpolar south Pacific, the phenology of the growing period is equally influential. A 30-day (1SD) change in duration corresponds to a 40% decrease in export compared to the average (-10.9 mg m^{-2} d^{-1} SD^{-1} vs 28.2 mg m^{-2} d^{-1}), highlighting the profound effect of growing period duration. In the subpolar southern Pacific, as identified in Chapter 3, the duration increased by an average of approximately 20 days per decade between 1999 and 2020, suggesting a reduction in export by 15 mg m^{-2} d^{-1} attributable to prolonged growing periods. In addition in the Pacific Ocean, the relationship between initiation date and EP often counteracts those seen in duration. Long bloom durations appear to coincide with earlier growing periods (Figure.4.1.c.ii) in the subpolar regions, however earlier growing periods often result in increased export.

Table 4.1. Effect of 1SD change in duration, initiation date, primary production, sea surface temperature and mixed layer depth on export (mg m^{-2} d^{-1} SD^{-1}). Mean and standard deviation are given in days (duration and initiation date), mg m^{-2} d^{-1} (NPP and Export), °C (SST) and metres (MLD). Standard errors are calculated using repeated bootstrapping. Stars represent the significance level where $p < 0.001$ (***), $p < 0.01$ (**), and $p < 0.05$ (*).

Pacific Ocean

		Export (mg m^{-2} d^{-1})	Duration	Start Date	PPT	SST	MLD
Subpolar North	Mean ± SD	27.5 ± 10.2	83.5 ± 47.0	113.1 ± 106.4	513.9 ± 183.6	10.3 ± 2.9	42.0 ± 7.3
	Slope ± SE (Significance)	-	-0.25 ± 0.13 (ns)	-1.6 ± 0.11 (***)	7.3 ± 0.09 (***)	-17.5 ± 0.38 (***)	13.9 ± 0.46 (***)
Subtropical North	Mean ± SD	29.8 ± 8.1	65.2 ± 38.4	145.5 ± 130.0	211.3 ± 139.6	23.8 ± 3.8	28.1 ± 8.03
	Slope ± SE (Significance)	-	-1.9 ± 0.06 (***)	0.47 ± 0.04 (***)	5.8 ± 0.07 (***)	3.1 ± 0.13 (***)	9.4 ± 0.19 (***)
Tropics	Mean ± SD	36.8 ± 12.9	57.9 ± 37.2	163.9 ± 99.8	217.1 ± 185.7	27.8 ± 1.7	20.5 ± 7.4
	Slope ± SE (Significance)	-	0.99 ± 0.10 (***)	0.48 ± 0.09 (***)	6.4 ± 0.06 (***)	-8.5 ± 0.39 (***)	-17.3 ± 0.28 (***)
Subtropical South	Mean ± SD	14.5 ± 6.5	111.5 ± 47.9	105.9 ± 104.9	94.0 ± 74.6	20.4 ± 4.9	36.0 ± 16.8
	Slope ± SE (Significance)	-	-1.9 ± 0.03 (***)	0.93 ± 0.04 (***)	13.4 ± 0.12 (***)	0.90 ± 0.05 (***)	1.2 ± 0.04 (***)
Subpolar South	Mean ± SD	28.2 ± 14.8	87.9 ± 34.5	44.6 ± 121.8	204.4 ± 57.3	3.1 ± 2.9	73.1 ± 18.5
	Slope ± SE (Significance)	-	-11.0 ± 0.24 (***)	-4.5 ± 0.11 (***)	47.2 ± 0.32 (***)	-35.0 ± 0.35 (***)	-10.9 ± 0.17 (***)

Atlantic Ocean

		Export (mg m^{-2} d^{-1})	Duration	Start Date	PPT	SST	MLD
Subpolar North	Mean ± SD	41.2 ± 8.9	63.8 ± 27.8	101.3 ± 65.8	404.4 ± 101.1	10.4 ± 3.1	51.6 ± 16.3
	Slope ± SE (Significance)	-	0.82 ± 0.24 (***)	-1.8 ± 0.26 (***)	12.1 ± 0.23 (***)	-0.23 ± 0.37 (ns)	-7.3 ± 0.21 (***)
Subtropical North	Mean ± SD	31.9 ± 18.8	119.1 ± 52.7	22.0 ± 71.3	264.3 ± 177.8	23.0 ± 3.2	33.2 ± 11.9
	Slope ± SE (Significance)	-	-7.3 ± 0.12 (***)	5.0 ± 0.27 (***)	22.6 ± 0.08 (***)	-37.1 ± 0.34 (***)	23.1 ± 0.32 (***)
Tropics	Mean ± SD	80.5 ± 36.6	115.4 ± 52.1	151.9 ± 91.6	457.6 ± 253.8	27.0 ± 1.32	19.7 ± 8.3
	Slope ± SE (Significance)	-	6.8 ± 0.39 (***)	8.9 ± 0.49 (***)	22.2 ± 0.24 (***)	-30.3 ± 2.9 (***)	-64.0 ± 1.1 (***)
Subtropical South	Mean ± SD	21.9 ± 7.7	95.6 ± 41.1	139.5 ± 119.7	230.6 ± 165.8	18.0 ± 5.4	45.5 ± 22.6
	Slope ± SE (Significance)	-	-0.22 ± 0.09 (*)	0.62 ± 0.06 (***)	3.9 ± 0.11 (***)	2.1 ± 0.08 (***)	0.56 ± 0.06 (***)
Subpolar South	Mean ± SD	26.3 ± 6.8	61.5 ± 33.7	50.5 ± 82.0	175.6 ± 47.4	0.40 ± 1.57	72.2 ± 13.0
	Slope ± SE (Significance)	-	-4.3 ± 0.14 (***)	-2.8 ± 0.15 (***)	-0.08 ± 0.67 (ns)	-25.4 ± 0.42 (***)	-6.8 ± 0.20 (***)

Indian Ocean

		Export (mg m^{-2} d^{-1})	Duration	Start Date	PPT	SST	MLD
Tropics	Mean ± SD	87.1 ± 29.6	114.4 ± 49.3	201.3 ± 82.9	330.5 ± 113.3	28.4 ± 0.78	18.9 ± 5.2
	Slope ± SE (Significance)	-	-0.03 ± 0.36 (ns)	-3.3 ± 0.36 (***)	7.4 ± 0.79 (***)	-105.1 ± 3.5 (***)	60.7 ± 1.6 (***)
Subtropical South	Mean ± SD	20.8 ± 17.6	117.7 ± 41.7	170.6 ± 98.6	118.1 ± 49.7	17.3 ± 5.9	51.0 ± 28.8
	Slope ± SE (Significance)	-	0.47 ± 0.16 (**)	0.03 ± 0.11 (ns)	14.0 ± 0.75 (***)	15.9 ± 0.21 (***)	-5.8 ± 0.08 (***)
Subpolar South	Mean ± SD	26.9 ± 10.1	82.0 ± 34.6	10.1 ± 49.8	174.4 ± 56.9	1.1 ± 1.9	69.5 ± 18.1
	Slope ± SE (Significance)	-	-8.4 ± 0.10 (***)	4.1 ± 0.39 (***)	29.7 ± 0.19 (***)	-32.8 ± 0.23 (***)	-10.5 ± 0.10 (***)

The effect of duration on EP varies independently of the direction of effect of SST and MLD (Figure 4.4; Table 4.1). For example, in the subpolar south Pacific longer growing periods tend to be associated with decreased export, while in the tropical Pacific longer growing periods tend to be associated with increased export. This indicates divergent regional responses of export to phenology of phytoplankton. However, in the subpolar south and tropical Pacific the relationships between SST and MLD on export are consistent, with warmer temperatures and shallower depths associated with reduced export. As detailed in Chapter 3, the growing period became longer in the subpolar Pacific and shorter in the tropical regions between 1998 and 2020. This pattern suggests that longer growing

periods in the subpolar Pacific and shorter growing periods in the tropical Pacific both contribute to a decrease in EP. This means that changes in the length of the growing period may strengthen reductions in EP associated with ocean warming. While shallowing MLD and increasing NPP in these regions could counter some of these changes, the complex interplay among these variables makes predicting changes in EP challenging. Notably, unlike other regions where SST and MLD influences diverge, the subpolar north shows that both warmer SST and a shallower MLD decrease export, underscoring the nuanced and complex environmental and ecosystem interactions that effect EP.

4.3.2.2. Atlantic Ocean Trends

In the Atlantic Ocean, the connection between physical and ecological drivers and EP is distinct from that found in the Pacific. Duration exhibits a positive relationship with EP in the subpolar north and tropical Atlantic, with notable slopes of 0.82 and 6.8 mg m^{-2} d^{-1} SD^{-1}, respectively (Table 4.1). This indicates that in these regions, longer growing periods result in increased EP, however unlike in the subpolar north Pacific the scale of these changes are more pronounced compared to the effect of SST changes. Furthermore, in the subtropical north Atlantic, shorter growing periods and later initiation dates are related to an increase in export, with slopes of -7.3 and 5 mg m^{-2} d^{-1} SD^{-1}, respectively. Chapter 3 highlights trends in this region of increasing SSTs, shortening growing periods and delayed initiation dates over the last two decades. This suggests that a reduction in duration and delayed initiation date may have lessened the effect of temperature rise by more than 30%. In fact, the combined effect of changes in phenology and NPP may completely offset the changes in SST in this region of the model. This highlights the complex variation across ocean regions, both between the physical process and ecosystem dynamics but also between phenological characteristics themselves.

4.3.2.3. Indian Ocean Trends

In the Indian Ocean, the relationships between the variables explored is also unique in comparison to the Pacific and Atlantic Ocean (Table.4.1). In the subpolar southern Indian Ocean the effect of growing period duration on export is substantial, with the effect of a 1SD increase in duration on export (-8.4 mg m^{-2} d^{-1} SD^{-1}) approximating 87% of the response to a 1SD change in MLD (10.5 mg m^{-2} d^{-1} SD^{-1}). In addition, earlier initiation dates in this region result in 4.1 mg m^{-2} d^{-1} SD^{-1} change in EP. Furthermore, the response of export to MLD is highly variable across regions. In the subpolar Indian Ocean, shallow MLD counteracts the effect of increased SST on export, while in the tropics it amplifies it. This is likely because shallow MLD results in both increased light availability and less nutrient availability due to decreased mixing with deep nutrient-rich waters. Therefore, production increases in the high-latitudes where growth is in part limited by light availability and decreases in the tropics where nutrients are the limiting factor for growth.

4.3.3. Drivers of Regional Export Efficiency in the PlankTOM12.2 Model

Export efficiency, defined here as the fraction of NPP exported below 100m, is a critical component of the biological carbon pump. This analysis aims to discern the influence of growing period duration and initiation date on EF, controlling for other influential drivers such as MLD, NPP, and SST.

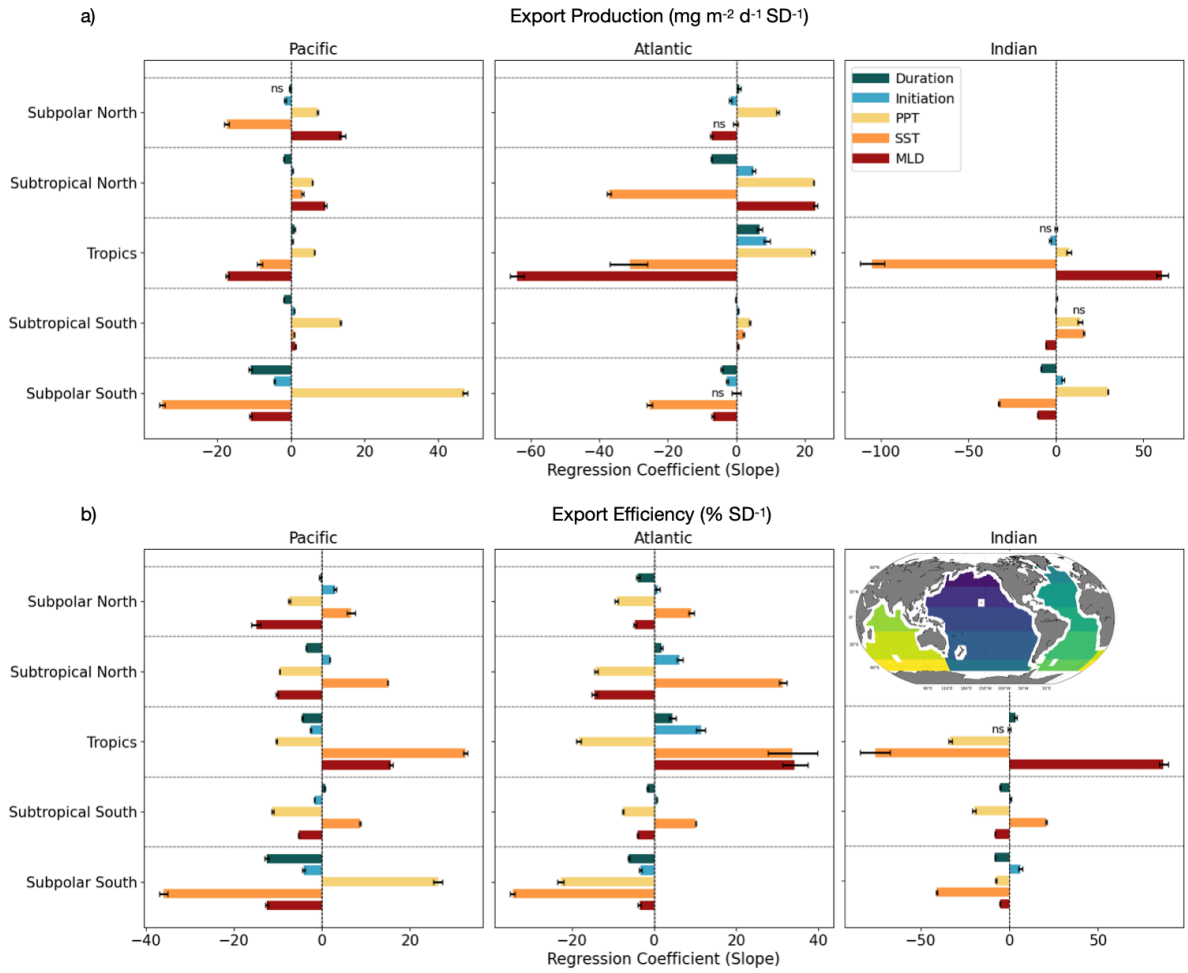

Figure.4.4. Coefficients of multiple regression between five independent variables: duration, initiation, primary production, sea surface temperature and mixed layer depth; and 2 dependent variables: export production and export efficiency. Coefficients are representative of the effect of a change of 1SD of Duration (days), initiation date (days), Sea surface temperature (°C) and mixed layer depth (metres) on a) export (mg m^{-2} d^{-1} SD^{-1}) and b) export efficiency (% SD^{-1}). Error bars show 95% confidence intervals and non-significant results are indicated with ns. Regional masks are shown on the map in panel 3 of b) Export Efficiency (%).

4.3.3.1. Pacific Ocean Trends

In the Pacific Ocean, duration of the growing period has a significant negative effect on EF within the subpolar north and subtropical north, with respective coefficients of -0.45 and -3.59 (% SD^{-1}; Figure 4.2, Table 4.2). Although most of the effects are statistically significant, the influence of duration on EF is comparatively minor next to alterations brought about by other variables affecting EF. However,

Table 4.2. Effect of 1SD change in duration, initiation date, primary production, sea surface temperature and mixed layer depth on export efficiency (% SD^{-1}). Mean and standard deviation are given in days (duration and initiation date), mg m^{-2} d^{-1} (NPP), °C (SST) and metres (MLD). Standard errors are calculated using repeated bootstrapping. Stars represent the significance level where $p < 0.001$ (***), $p < 0.01$ (**), and $p < 0.05$ (*).

		Pacific Ocean					
		Export Efficiency (%)	Duration	Start	PPT	SST	MLD
Subpolar North	Mean ± SD	5.9 ± 2.4	83.6 ± 47.0	113.1 ± 106.4	513.9 ± 183.6	10.3 ± 3.0	42.0 ± 7.3
	Slope ± SE (Significance)	-	-0.45 ± 0.14 (**)	2.9 ± 0.16 (***)	-7.4 ± 0.14 (***)	6.6 ± 0.51 (***)	-15.0 ± 0.62 (***)
Subtropical North	Mean ± SD	18.3 ± 8.6	65.3 ± 38.4	145.5 ± 130.0	211.3 ± 139.6	23.8 ± 3.8	28.10 ± 8.03
	Slope ± SE (Significance)	-	-3.6 ± 0.06 (***)	1.8 ± 0.05 (***)	-9.6 ± 0.06 (***)	14.9 ± 0.07 (***)	-10.26 ± 0.15 (***)
Tropics	Mean ± SD	24.0 ± 12.5	58.0 ± 37.2	164.0 ± 99.8	58.0 ± 37.2	217.1 ± 185.7	27.8 ± 1.7
	Slope ± SE (Significance)	-	-4.4 ± 0.09 (***)	-2.6 ± 0.08 (***)	-10.3 ± 0.09 (***)	32.6 ± 0.26 (***)	15.6 ± 0.26 (***)
Subtropical South	Mean ± SD	18.9 ± 7.7	111.5 ± 48.0	106.0 ± 104.9	94.0 ± 74.7	20.4 ± 5.0	36.0 ± 16.8
	Slope ± SE (Significance)	-	0.64 ± 0.04 (***)	-1.7 ± 0.04 (***)	-11.2 ± 0.09 (***)	8.6 ± 0.05 (***)	-5.3 ± 0.06 (***)
Subpolar South	Mean ± SD	13.2 ± 4.3	87.9 ± 34.5	44.6 ± 121.8	204.4 ± 57.3	3.1 ± 2.9	73.1 ± 18.5
	Slope ± SE (Significance)	-	-12.6 ± 0.22 (***)	-4.2 ± 0.14 (***)	26.3 ± 0.50 (***)	-36.0 ± 0.48 (***)	-12.6 ± 0.18 (***)

		Atlantic Ocean					
		Export Efficiency (%)	Duration	Start	PPT	SST	MLD
Subpolar North	Mean ± SD	10.5 ± 2.0	63.8 ± 27.8	101.3 ± 65.8	404.4 ± 101.1	10.4 ± 3.1	51.6 ± 16.3
	Slope ± SE (Significance)	-	-4.0 ± 0.21 (***)	0.92 ± 0.23 (***)	-9.2 ± 0.22 (***)	9.0 ± 0.33 (***)	-4.7 ± 0.17 (***)
Subtropical North	Mean ± SD	14.6 ± 6.1	119.1 ± 52.7	22.0 ± 71.3	264.3 ± 177.8	23.0 ± 3.2	33.2 ± 11.9
	Slope ± SE (Significance)	-	1.9 ± 0.13 (***)	6.2 ± 0.39 (***)	-14.2 ± 0.20 (***)	31.6 ± 0.48 (***)	-14.6 ± 0.33 (***)
Tropics	Mean ± SD	21.1 ± 10.7	115.4 ± 52.1	151.9 ± 91.6	457.6 ± 253.8	26.9 ± 1.3	19.7 ± 8.3
	Slope ± SE (Significance)	-	4.5 ± 0.40 (***)	11.5 ± 0.55 (***)	-18.6 ± 0.32 (***)	33.8 ± 3.0 (***)	34.3 ± 1.6 (***)
Subtropical South	Mean ± SD	14.1 ± 8.7	95.6 ± 41.1	139.5 ± 119.7	230.6 ± 165.8	18.0 ± 5.4	45.5 ± 22.6
	Slope ± SE (Significance)	-	-1.6 ± 0.07 (***)	0.70 ± 0.06 (***)	-7.6 ± 0.07 (***)	10.2 ± 0.07 (***)	-4.0 ± 0.05 (***)
Subpolar South	Mean ± SD	15.9 ± 4.6	61.5 ± 33.7	50.5 ± 82.0	175.7 ± 47.4	0.40 ± 1.6	72.2 ± 13.00
	Slope ± SE (Significance)	-	-6.2 ± 0.14 (***)	-3.4 ± 0.19 (***)	-22.8 ± 0.36 (***)	-34.5 ± 0.30 (***)	-3.6 ± 0.20 (***)

		Indian Ocean					
		Export Efficiency (%)	Duration	Start	PPT	SST	MLD
Tropics	Mean ± SD	28.6 ± 11.0	114.4 ± 49.3	201.3 ± 82.9	330.5 ± 113.3	28.4 ± 0.78	18.9 ± 5.2
	Slope ± SE (Significance)	-	3.4 ± 0.37 (***)	-0.26 ± 0.40 (ns)	-33.3 ± 0.53 (***)	-76.7 ± 4.1 (***)	87.0 ± 1.4 (***)
Subtropical South	Mean ± SD	19.1 ± 13.5	117.8 ± 41.7	170.6 ± 98.6	118.1 ± 49.7	17.3 ± 5.9	51.0 ± 28.8
	Slope ± SE (Significance)	-	-5.3 ± 0.16 (***)	0.64 ± 0.14 (***)	-19.9 ± 0.48 (***)	20.8 ± 0.15 (***)	-8.1 ± 0.08 (***)
Subpolar South	Mean ± SD	15.7 ± 4.0	82.0 ± 34.6	10.1 ± 49.8	174.4 ± 56.9	1.1 ± 1.9	69.5 ± 18.1
	Slope ± SE (Significance)	-	-8.2 ± 0.13 (***)	6.1 ± 0.57 (***)	-7.5 ± 0.27 (***)	-40.9 ± 0.24 (***)	-5.4 ± 0.14 (***)

similarly to EP, in the subpolar southern Pacific, the influence of growing period duration on EF (-12.6 % SD^{-1}) is comparable to the strong negative correlation exhibited by MLD in the same region (-12.6 % SD^{-1}; Table 4.2). In some regions of the subtropical south Pacific, duration increased by 50 days per decade (Chapter 3), indicating that changes in duration may have reduced EF by 18% in some regions. Furthermore, the effects of start date on EF are independent of the effect of the duration of the bloom. In the Northern Hemisphere of the Pacific, earlier initiation dates result in higher EF, whereas the opposite is found in the tropics and the Southern Hemisphere. This highlights that even between phenological indices there is significant variation in the effect on EF. Additionally, it is noteworthy that the subpolar southern Pacific is the sole region examined where an increase in the rate of NPP is

related to increased EF. This finding shows that in most oceanic regions a rise in NPP does not equate to a proportional increase in EF, highlighting the complex interactions within marine carbon cycles.

4.3.3.2. Atlantic Ocean Trends

In the Atlantic Ocean, the PlankTOM12.2 model demonstrates a significant negative relationship between growing period duration and export efficiency, particularly within the subpolar regions. The subpolar north and south manifest the most notable changes, with declines of -4.0 and -6.2 ± (% SD^{-1}) respectively (Figure 4.2). Again, in the subpolar south, the influence of a standard deviation increase in growing period duration on export efficiency is significant in relation to export. A 1SD increase in duration results in a change in export that is 70% greater than that of a 1SD increase in MLD. In addition, changes in initiation date in this region, result in similar magnitude of changes in export efficiency (% SD^{-1}) as MLD. This suggests that the initiation date may be more influential on export efficiency than EP. In addition, relationships between NPP, SST, MLD and export efficiency are often the opposite of their relationships with EP. For example, whilst increases in SST across the Northern Hemisphere of the Atlantic are related to decreases in EP, increases in SST in these regions are related to increased export efficiency. This highlights that increases in EP often do not coincide with increases in export efficiency, suggesting that controlling for ecosystem dynamics and phenology are crucial when modelling export efficiency.

4.3.3.3. Indian Ocean Trends

The Indian Ocean also shows significant interregional variation in relationships between the phenology, physical drivers and export efficiency. In the tropical Indian Ocean, there is a significant relationship between duration and export efficiency, which contrasts with the lack of significant trend observed between duration and EP (Table 4.2). The subtropical and subpolar southern regions exhibit a substantial negative effect of duration on export efficiency, with decreases of -5.3 and -8.2 % SD^{-1}, respectively (Table 4.2). Again, in these regions the effect of duration of the growing period appears substantial, approximating 65% and 150% of the effect of MLD in the subtropical and subpolar south, respectively. This is also reflected in the effect of initiation date, where earlier growing periods result in decreases in the export efficiency at a similar magnitude of changes in MLD. In fact, the effect of duration of the bloom on export efficiency is only rivalled by temperature in the subpolar Southern Indian Ocean (Table 4.2). Despite the simplified representation of ecosystem dynamics and sinking particles in the PlankTOM12.2 system, there is still significant variation and effect on export efficiency from ecosystem dynamics. This underscores the critical importance of sufficient ecosystem dynamics within models when examining export efficiency.

These findings emphasise the crucial role of ecosystem phenology in understanding EF. The duration of growing periods has a marked effect on EF, despite the simplified representation of ecosystem dynamics and particle sinking contained in the PlankTOM12.2 model. The PlankTOM12.2 model is also significantly more complex, and contains much more of the key variables outlined as important

for EP and EF (Henson, et al., 2022). This highlights the necessity of incorporating higher complexity ecosystem communities into models to accurately capture the processes of marine export. These results also highlight the need to develop evaluation metrics that can constrain the functionality of models beyond the validation of mean fields.

4.4. Discussion

This chapter highlights key trends in the dynamics of carbon export, building upon existing research and exploring new grounds estimating the effect of phenological variations. Firstly, there is a clear link between increased NPP and increased EP in the PlankTOM12.2 model, a relationship well-established in previous studies. For example, Laufkötter, et al., (2015) demonstrated a direct connection between NPP and export processes. Furthermore, increased NPP is mostly associated with decreased EF in the PlankTOM12.2 model. This is again consistent with previous findings that NPP and EF have an inverse relationship (Cavan et al., 2015; Henson et al., 2019; Laws and Maiti 2019). Henson, et al., (2019) argue that the global inverse relationship of NPP and EF may be driven by the decoupling of processes acting to remineralise carbon in the upper ocean. High EF may occur if the growth of phytoplankton outpace the growth of zooplankton or bacteria at the start of the growing period or if the concentration of zooplankton and bacteria is low (Henson, et al., 2019). Previous models have demonstrated an inverse relationship between NPP and EF, but showed limited variability in the relationships between NPP, EP and EF compared to PlankTOM12.2 (Henson et al., 2015). This suggests that further research could delve into the optimal number of PFTs required in order to capture the complexity of influence that ecosystem structure has over EP and EF. This also highlights the need for observation metrics to be developed in order to validate the variability of the relationship between NPP and EF in the global ocean.

Furthermore, this chapter adds to the current body of literature suggesting that increases in ocean temperatures result in decreases in EF (Cael et al., 2017; Henson et al., 2019). Complementing this, our findings are also in agreement with those of Laufkötter, et al., (2016) who highlight EP decrease by between -1-12% under RCP8.5. Furthermore, PlankTOM12.2 supports the hypothesis that a shallower MLD enhances EP in polar regions, and decreases EP in oligotrophic gyres. This pattern, closely related to shifts in light availability and nutrient dynamics, aligns with the observations that shallower MLD results in increased production in the high-latitudes and decreased production in the tropics (Sasai et al., 2016). The distinct effects of temperature and MLD on EP underscore the importance of incorporating regional environmental variables into our broader understanding of these oceanic processes.

Finally, the influence of phenology on EP and EF, examined for the first time in this study, reveals region-specific responses that challenge previous literature. Notably, the duration of the growing period emerges as a key factor in the subpolar Southern Ocean, with an influence on export

equivalent to that of MLD. The following sections explore the potential mechanisms behind these findings and suggest avenues for future research to unravel the role of phenology in controlling export dynamics in that region.

4.4.1. Potential Mechanisms for reduced export during long growing periods

Changes in phytoplankton bloom phenology, particularly the duration of the growing period, significantly affect carbon export, even though the effect is small compared to that of other variables. In the Southern Ocean where the effect is largest, a 1SD change in bloom duration can exert a comparable effect on export as a 1SD change in MLD. In contrast, previous studies have not analysed but suggested in passing that these extended bloom durations due to climate change might enhance the efficiency of the biological carbon pump (Ardyna and Arrigo 2020; Friedland et al., 2018; Thomalla et al., 2023a; Thomalla et al., 2015). Whilst this remains true in some tropical regions and the north Atlantic, my findings suggest that in both the subpolar north and Southern Ocean, increased duration of phytoplankton growing periods are associated with reduced EP and EF. The effects of phenology discussed in this Chapter are in addition to the effects of changes in NPP, and are therefore related to interactions within the ecosystem.

The expected shift towards smaller phytoplankton size classes under climate change, as outlined by Li et al., (2009), is a critical aspect of altering marine ecosystems. In fact, reduced body size is suspected to be a universal ecological response to global warming, alongside poleward latitudinal shifts and shifts in phenology of organisms (Daufresne et al., 2009). Shifting distribution of size classes is a possible mechanism for change in the PlankTOM12.2 model, as the model incorporates varying optimal temperatures for each PFT (Wright et al., 2021). In the PlankTOM12.2 ecosystem, this is demonstrated with a clear regional distribution of PFTs, with smaller PFTs more abundant in the tropics and subtropics. This is mostly due to small PFTs affinity for growth in low nutrient conditions and partially to their, generally, maximum growth rates at higher temperatures (Wright et al., 2021). In comparison, larger PFTs such as Diatoms and Phaeocystis are primarily found at high latitudes in the model. This is comparable to observations made by Aiken, et al., (2007) who note that picoplankton thrive in permanently stratified environments with limited nutrients, while microplankton are better adapted to dynamic, nutrient-rich settings. While these mechanisms are not directly examined in this study, if extended bloom periods are dominated by smaller phytoplankton, longer growing periods could indicate ecosystem community shifts towards smaller phytoplankton. Consequently, the observed decrease in export production during these longer growing periods may be attributable to these shifts.

Furthermore, smaller phytoplankton are less likely to contribute significantly to carbon export in high latitude regions. Smaller and less dense phytoplankton taxa, such as picoplanktonic cyanobacteria, are commonly considered to have a marginal effect on carbon flux in colder, high-latitude waters

(Richardson 2019). In contrast to large phytoplankton, such as *Phaeocystis* and diatoms, which play a crucial role in EP at these latitudes (Nissen and Vogt 2021; Tréguer et al., 2017). The significant contribution of larger species is largely attributed to their considerable mass and/or ballasting properties, which gets further compacted through grazing processes. For example, diatoms, due to their denser structure, sink faster, thus facilitating a more efficient transfer of sequestered carbon from the upper ocean layers to the deep ocean (Richardson 2019). The smaller phytoplankton, while playing a significant role in carbon flux in tropical regions and oligotrophic gyres, do not sink as rapidly, reducing their effectiveness in carbon export.

The reduced EP and EF present during longer growing periods in the PlankTOM12.2 model may be reflective of these mechanisms of change. Literature demonstrates that a shift to smaller phytoplankton in high-latitude regions would likely result in longer growing period durations, reduced EP, and reduced EF. The PlankTOM12.2 model incorporates a variety of PFTs and their optimal temperature ranges and therefore could represent these mechanisms of change that could alter the dynamics of carbon export during longer growing periods. PFT modulations between generally consistent with this hypothesis, although they are also modified by a range of other environmental and ecosystems factors that make it difficult to attribute directly part of the changes in export-related variables to shifts in PFTs.

4.4.2. Potential Mechanisms for increased export due to early initiation

In some regions, results suggest that long growing periods and later initiation were associated with increased carbon EP, despite much of the ocean appearing to have earlier initiation during longer blooms. Specifically, in both the subtropical north and south of the Atlantic and Pacific oceans, as well as the tropical Indian Ocean, earlier blooms result in increases in carbon EP. The mismatch hypothesis suggests that early blooms could either mitigate or amplify carbon export, contingent on the ecological context. In ecosystems where export is predominantly driven by the sinking of larger particulate organic matter, such as carcasses, early blooms and the ensuing mismatch with higher trophic levels might increase export through aggregation processes (Takeuchi et al., 2019). For instance, in the Southern Ocean, where export at the beginning of the bloom is dominated by diatoms, a temporal mismatch may intensify organic carbon export (Krumhardt et al., 2022). In contrast, in regions and time periods dominated by small phytoplankton, a temporal mismatch may decrease carbon export as grazing will have a higher reliance on repackaging smaller phytoplankton into faecal pellets (Richardson 2019).

Likewise, in regions where early initiation dates are related to increased EF, EP may be dominated by larger PFTs, such as diatoms, and organic particles with a high content on shells with high weight and ballasting (Thomalla et al., 2023a). In contrast, where early initiation dates are related to low EF, EP may be dominated by smaller PFTs repackaged by zooplankton into organic particles with low

ballasting. These mechanisms are consistent with the structure and output of the PlankTOM12.2 model. Generally, I find that earlier bloom durations result in increased EP and EF at high-latitudes and decreased EP and EF at low-latitudes. It is therefore crucial to unpack the dynamics of how early bloom initiation dates may lead to increases in EP at the regional level, as growing periods are becoming earlier and longer due to ocean warming, particularly in the high-latitudes (Chapter 3; Henson et al., 2018; Cooley, et al. 2022). Thus, future research should focus on the PFTs and their contributions to the phenology of the global ocean, assessing how timing mismatches and community shifts influence export during early initiation of the growing period.

4.5. Conclusion

This chapter advances our understanding of the mechanisms that control the biological carbon pump by exploring the role of phytoplankton phenology using the PlankTOM12.2 model. The findings reveal that variations in the duration and initiation dates of phytoplankton growing periods, whilst not the dominant drivers, can have significant influence on carbon export dynamics and EF at the regional level. Whilst the effect of duration on EP and EF is often much lower than that of physical drivers and NPP, in the Southern Ocean the effect is often equivalent to that of MLD. Notably, longer growing periods are related to lower export in the polar regions, which literature suggests may be driven by community shifts towards smaller phytoplankton. Furthermore, this analysis shows that earlier growing periods can either enhance or reduce EP depending on the region. These findings suggest that the mismatch hypothesis could be a valuable framework for understanding the effect of phenological changes on EP. Moreover, regional variations in effect of phenology and physical drivers on EF further emphasise the interplay between ecosystem dynamics, physical drivers and phenology in influencing EF.

Given these insights, one area for future research might be to focus on understanding the relationships between PFT dynamics, bloom phenology and carbon export. Whilst this Chapter shows that phenology plays a role in driving changes in EP and EF, especially in the Southern Ocean, the exact mechanisms behind these changes haven't been explored within the model system. Additionally, it is clear from these results that the incorporation of more detailed ecosystem dynamics into biogeochemical models is important for accurate predictions of carbon export changes in a warming ocean.

Chapter 5. Shifts in phenology, primary production, and export production under climate change to 2100 using the PlankTOM12.2 ecosystem model

Abstract

This chapter explores the effects of future climate change as represented by Shared Socioeconomic Pathway (SSP) low emissions (SSP1-2.6) and high emissions (SSP3-7.0) scenarios on marine phytoplankton phenology, primary production (NPP), and their consequent impacts on carbon export, using the PlankTOM12.2 model. The focus of this chapter centres on the interactions among phytoplankton, zooplankton, and abiotic factors in shaping the dynamics of marine ecosystems, highlighting both regional variability and potential global implications. Projections of sea surface temperature (SST) and mixed layer depth (MLD) are consistent with previous projections, with global warming of 3.7°C and shallowing of 5.3 metres on average under SSP3-7.0. Shifts in duration and timing of initiation in the growing period have similar structure, and more extensive, to those found between 1998-2020. Namely, initiation of the growing periods becomes earlier and the duration longer across most of the ocean by 2100 under SSP1-2.6 and SSP3-7.0. Projected NPP decreases overall, in line with a general decrease in phytoplankton biomass, but has more regional variability than projections using simpler ecosystem models. In addition, in the Northern Hemisphere NPP increases strongly in the spring (by up to 89.8 mg m^{-2} d^{-1}) and decreases in the autumn (by up to 23.2 mg m^{-2} d^{-1}) under SSP3-7.0. The overall decrease in NPP does not propagate to carbon export, which increases overall, except in the Southern Ocean. This is explained by export efficiency (EF), which has an inverse relationship with NPP, with an increase overall. Shifts amongst species, namely decreases in concentration of bacteria and zooplankton appear to drive this inverse relationship. Results also show non-linearity in ecosystem responses as a function of warming level. These results add to the growing literature which have identified that inverse relationships between NPP and export efficiency (EF) are driven by shifting ecosystem structures under climate change scenarios. However, the need for widespread validation and improvement of model ecosystem representation to more accurately depict mechanisms of carbon export is evident.

5.1. Introduction

Marine ecosystems, pivotal in regulating atmospheric carbon dioxide levels, are undergoing significant changes due to shifts in phenology and ecosystem dynamics under climate change (Chapters 3 & 4). The biological carbon pump (BCP), fundamental to this regulation, involves the fixation of inorganic carbon by phytoplankton and its subsequent export and sequestration to deeper waters (Henson et al., 2019; Parekh et al., 2006). Zooplankton play a crucial role in the BCP, influencing the efficiency of carbon export through their feeding habits, faecal pellet production, and active transport of carbon below the thermocline (Schnack-Schiel and Isla 2005; Steinberg and Landry 2017; Turner 2015). Fragmentation of particulate matter by zooplankton and subsequent remineralisation by bacteria, transforms particulate organic carbon into dissolved organic carbon, subsequently redistributing carbon and nutrients in the upper ocean and reducing export efficiency (EF; the ratio of particulate organic carbon that sinks below 100 metres relative to NPP in the upper 100 metres). This chapter delves into how alterations in phytoplankton phenology and ecosystem dynamics under varying climate change scenarios impact the carbon export, and hence the functioning of the BCP, to 2100.

In recent decades, phenological shifts in the global ocean have been observed, with phytoplankton blooms starting earlier and lasting longer, especially in high-latitude regions (Friedland et al., 2018; Chapter 3). These changes in bloom timing and duration have significant consequences for the function of food webs and thus the export of particulate organic carbon (Chapter 4). Early and prolonged blooms likely impact energy flow pathways, favouring the productivity of different species and influencing the sequestration of carbon in ocean ecosystems (Friedland et al., 2018). In addition, climate change is projected to further alter these phenological patterns. Projections indicate a continuation of the trend towards earlier and longer phytoplankton growing periods, with substantial regional variations (Yamaguchi et al., 2022). Anticipated shifts in growing period dynamics may be driven by alterations in the existing balance between phytoplankton growth and zooplankton predation, leading to trophic level decoupling (Yamaguchi et al., 2022). In addition, decreased nutrient availability in the tropics and increased biomass in high-latitude regions due to sea ice retreat and prolonged growing seasons will also contribute to ecosystem changes (Henson et al., 2017).

One of the predicted drivers of phenological shifts is the predicted change in community structure. Alterations in phytoplankton community composition towards a dominance of smaller phytoplankton is anticipated under climate change. Communities dominated by smaller phytoplankton typically support less productive food webs and sequester less organic carbon in the deep ocean (Boyd et al., 2019). Therefore, a shift towards smaller phytoplankton is likely to decrease EF. In addition, EF is highly dependent on the degree of coupling or decoupling between primary productivity and upper ocean grazing and remineralisation processes (Henson et al., 2019). Low primary productivity coupled with high EF regimes tend to occur when macrozooplankton and bacterial abundance are low,

suggesting a decoupling between primary productivity and upper ocean remineralisation processes (Henson et al., 2019). The ongoing shifts in phytoplankton community structures, with their significant repercussions for the biological carbon pump, highlight the need for an in-depth understanding of these dynamics. Most models' predictive capabilities have been limited, as numerous existing models lack sufficient ecosystem complexity and do not include crucial carbon export mechanisms (Henson, 2021; Chapter 2). Furthermore, global future projections of phenology have been completed less than a handful of times by Henson, et al., (2013), Yamaguchi et al., (2022) and Henson, et al., (2018) with simple to medium complexity ecosystem models. However, as detailed in Chapter 2, the PlankTOM12.2 model addresses many existing gaps, providing a useful tool to explore changes in phenology and associated export production (EP) with a more complete representation of ecosystem dynamics.

This chapter aims to project and analyse future shifts in phytoplankton phenology and their consequent impacts on carbon export under a high and a low emissions scenario to 2100, based on the Shared Socioeconomic Pathways (SSPs) scenarios SSP1-2.6 and SSP3-7.0 (O'Neill et al., 2016). The SSP1-2.6 pathway caps the increase in radiative forcing at 2.6 W/m^2 and global temperatures at 1.8°C above pre-industrial levels by the year 2100 on average across models (IPCC WGI SPM). This pathway involves rigorous mitigation strategies for CO_2 emissions, with a target of achieving net zero emissions by 2075 (Gidden et al., 2019). In contrast, the SSP3-7.0 pathway is characterised by medium to high future emissions with a radiative forcing at 7.0 W/m^2 leading to global temperatures of 3.6°C above pre-industrial levels by 2100 on average (IPCC WGI SPM). This scenario projects CO_2 emissions to approximately double from their 2015 levels by 2100 and also projects a significant rise in methane (CH_4) emissions (Sellar et al., 2019). The selection of SSP1-2.6 and SSP3-7.0 offers a broad spectrum of climate outcomes, ranging from ambitious mitigation to high-end emission scenarios, thus providing insights into diverse plausible climatic and environmental impacts. This chapter aims to provide a qualitative understanding of how physical changes in the climate system can lead to changes in marine ecosystems and phenology, and in turn alter the efficiency of carbon export dynamics, by forcing the PlankTOM12.2 model with climate model output following these scenarios to 2100. The focus will be on examining the interplay between phytoplankton, zooplankton, and abiotic factors in shaping carbon flux, with an emphasis on understanding the regional variability and the potential global implications of changes in phenology and ecosystem structure. Compared to previous studies (Bopp et al., 2013; Henson et al., 2022; Kwiatkowski et al., 2020; Moore et al., 2018), the current analysis has a more extensive representation of ecosystem dynamics, and it takes a close look at the influence of phenology independently from that of NPP.

5.2. Methods

In this chapter, I utilise the PlankTOM12.2 model, previously detailed in Chapter 2..

5.2.1. Model Forcing

Model simulations from the UK Earth System Model (UKESM1) submissions to the Coupled Model Inter-comparison Project 6 (CMIP6) were used for both historic and future simulations of PlankTOM12.2, covering the period 1950-2100 (Mulcahy et al., 2020). UKESM1 incorporates the HadGEM3-GC3 global atmosphere-ocean climate model (Sellar et al., 2019), the NEMO ocean general circulation model at 1 degree resolution (Storkey et al., 2018), and the CICE ice model (Ridley et al., 2018). The atmospheric segment of UKESM1 has a horizontal resolution of about 135 km (1.25° × 1.875°) and includes 85 vertical layers. The atmospheric chemistry component includes interactive ozone and is based on the U.K Chemistry and Aerosols (UKCA) model, detailed in Archibald et al., (2020).

The UKESM1 surface atmospheric conditions were used to force the NEMO-PlankTOM12.2 model described in Chapter 2. UKESM1's historical forcing effectively replicates wind speed patterns and variations as described in the ERA5 reanalysis of historical data (Hersbach et al., 2020), as detailed in Jarníková et al., (in prep.). Atmospheric forcing is taken from two distinct simulations within UKESM1, following scenarios SSP1-2.6 and SSP3-7.0. The model simulations with NEMO-PlankTOM12.2 were first developed by Jarníkova, T., as described in Jarníková, et al., (in prep.), using the updated PlankTOM12.2 model setup improved as part of this thesis. The model simulations were repeated here from 1998 to extract model output with daily resolution until 2100, for the two scenarios SSP1-2.6 and SSP3-7.0.

5.2.2. Seasonal Differences and Anomaly Calculations

The model evaluation focuses on SST (°C), MLD (metres), surface chlorophyll concentration (mg m^{-3}), integrated primary production (NPP; upper 100 metres; mg m^{-2} d^{-1}), export at 100 metre depth (mg m^{-2} d^{-1}), EF (%), and the distribution of biomass among the 12 Plankton Functional Types (PFTs) represented in PlankTOM12.2 (see Chapter 2). Export efficiency is calculated by dividing export at 100 metres by the integrated NPP above 100m and multiplying by 100. Three decadal climatologies were calculated for: 1) the historical baseline (2000-2010), 2) the low-emissions scenario (SSP1-2.6; 2090-2100) and 3) the high-emissions scenario (SSP3-7.0; 2090-2100). For each decadal climatology, the date of initiation and duration of the growing period was calculated from the surface chlorophyll concentration as outlined in Chapter 3. To confirm that the historical baseline (2000-2010) is comparable to the IPCC historical baseline (1996-2013) a comparison of the SST, MLD, NPP, export at 100m and the seasonal chlorophyll concentration is available in Appendix 7.6.

The analysis focuses first on the changes in the seasonal cycle of SST, MLD, surface chlorophyll concentration, NPP, EP and EF because of their relations to ecosystem processes. The decadal climatological average of the low-emissions and high-emissions scenarios are compared to the historical period in the Northern (0°:65°N) and Southern hemisphere (0°:65°S) separately. Regional differences in these variables are analysed for 5 latitudinal bands (subpolar regions (50-65°N/S), subtropical regions (30-50°N/S) and tropics (30°N-30°S). Finally, results are compared to the integrated concentrations of all Plankton Functional Types (PFTs) from the upper 100m of the ocean over the 5 latitudinal bands.

5.2.3. CMIP6 Model Comparison

The changes in NPP and EP are compared between PlankTOM12.2 and the CMIP6 model outputs. The difference for each parameter is computed as the percentage change relative to a baseline period spanning from 1975 to 2015. This method quantifies the deviation from the baseline, providing a normalised measure of change over time, as in Henson et al., (2022; see Chapter 1). Data were processed to ensure consistency across different models and scenarios. Monthly data points from 1945 to 2100 were first aligned and then subjected to a 5-year rolling mean to smooth out short-term variability and better reveal the underlying trends. This smoothing was applied across historical data, SSP126, and SSP370 scenarios for each of the six CMIP6 models included in our study: IPSL, NCC, CCCma, CSIRO, CMCC, and MPI. All data used in this analysis are sourced from freely available CMIP6 outputs, accessible via the Earth System Grid Federation (ESGF) at https://esgf-data.dkrz.de/projects/cmip6-dkrz/. This methodology allows for a comparative analysis across models and scenarios, highlighting differences in biological responses to climate drivers, as projected by the climate models within the CMIP6 framework. The focus on percentage changes allows for an intuitive understanding of changes in magnitude relative to a historical baseline, which controls for differences in the initial conditions between models.

5.3.Results

5.3.1. Seasonal Changes in Response to Climate Change

Distinct hemispheric responses to climate change are evident, varying in both seasonality and magnitude across various physical and ecosystem variables (Figure 5.1). SST becomes warmer on average under SSP1-2.6 and SSP3-7.0 compared to the historical baseline. Under SSP1-2.6, SST warms by 1.6°C relative to the historical baseline by 2100. Under SSP3-7.0, there is a notable enhancement in SST warming; the Northern Hemisphere exhibits a pronounced summertime maximum temperature surge of 4.2°C above the historical baseline, compared to 1.9°C in the wintertime, suggesting an increase in the Northern Hemisphere variability in annual temperature cycles due to climate change. In comparison, the Southern Hemisphere warming in SST is lower and more consistent throughout the year. Wintertime and summertime averages vary by just 0.19°C and 0.47°C

under SSP1-2.6 and SSP3-7.0, respectively by 2100. The maximum increase in temperature is also lower in the Southern Hemisphere compared to the Northern Hemisphere, with warming reaching 2.4°C and 1.9°C under SSP1-2.6 and SSP3-7.0, respectively. The observed patterns suggest heightened sensitivity of Northern Hemisphere SSTs to climate change, with summertime SSTs potentially experiencing greater warming relative to wintertime SSTs.

Increased seasonal variability of MLD is also evident under both SSP1-2.6 and SSP3-7.0. In the Northern Hemisphere, MLD becomes deeper in the summer by 0.93m and 1.1m on average under SSP1-2.6 and SSP3-7.0 respectively, by 2100. In comparison, in the wintertime MLD deepens by 1.0m and 4.3m under SSP1-2.6 and SSP3-7.0, respectively. The deepening of the MLD in the summertime is likely attributable to enhanced turbulence at the surface, overcoming the increased stabilisation beneath the mixed layer, and thus increasing the MLD (section 5.4). In comparison, in the Southern Hemisphere MLD shallows in both the summer- and wintertime, though shallowing in the summertime is less severe. MLD shallows by 0.85m and 11.4m in summer- and wintertime respectively under SSP3-7.0 by 2100.

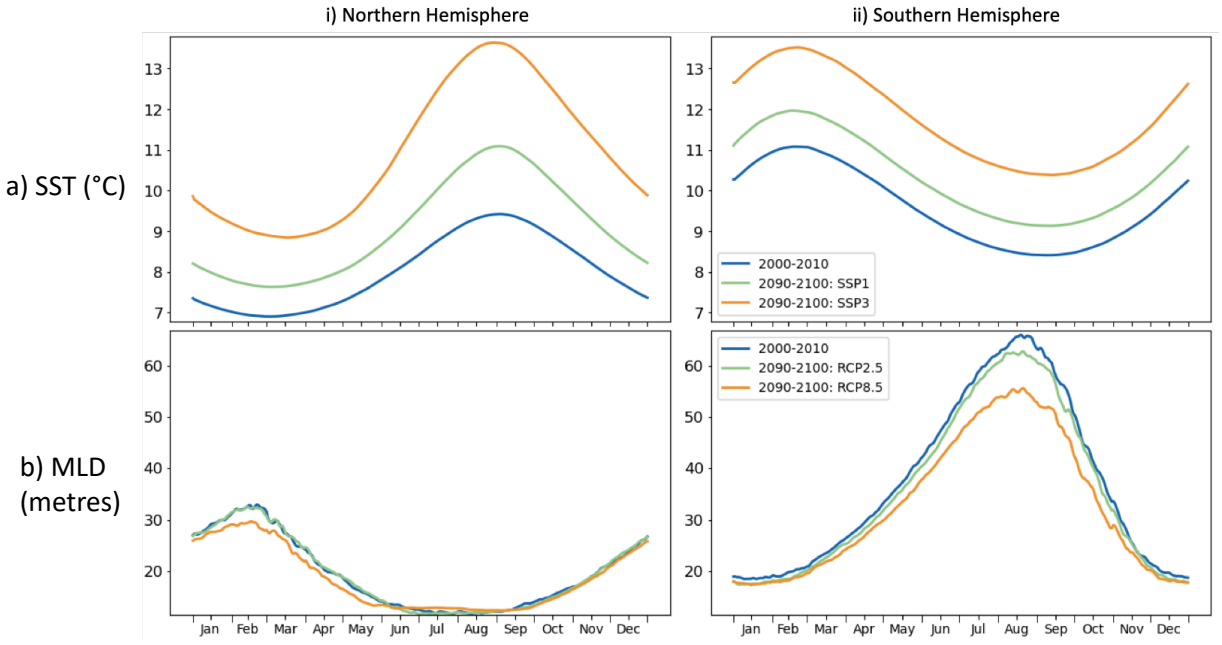

Figure 5.1. Global average of a) sea surface temperature (°C) and b) mixed layer depth (metres). Average calculated of the yearly average value of 11 years of data from PlankTOM12.2 with historical forcing (blue), SSP1-2.6(low-emission scenario; green) and SSP3-7.0 (high-emission scenario; orange). Historical decadal climatology is calculated for 2000-2010, whilst the low- and high-emission scenarios are calculated between 2090 and 2100. Panel (i) shows the Northern Hemisphere, whilst panel (ii) shows the Southern Hemisphere.

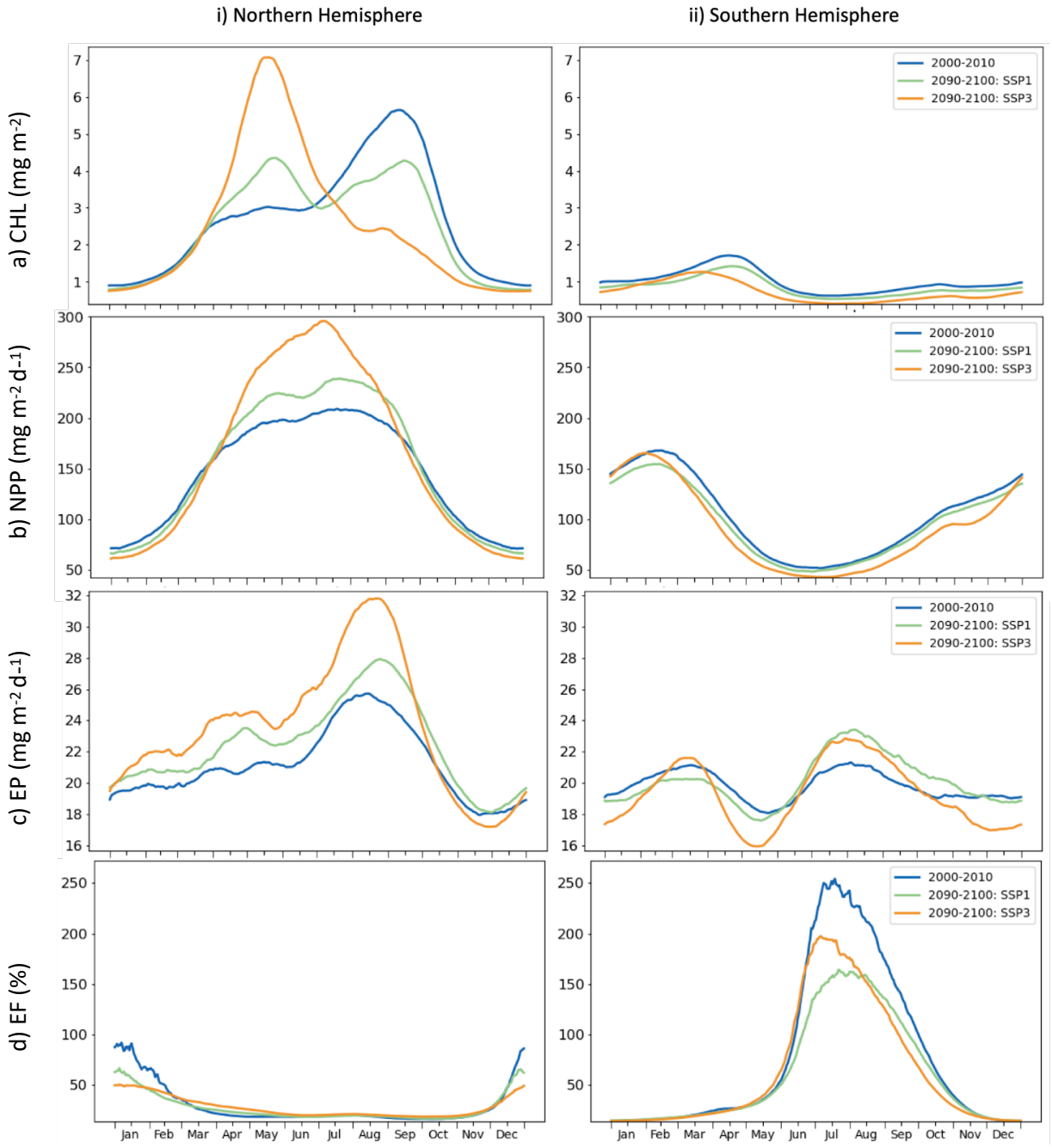

Figure 5.2. Global average of a) surface chlorophyll concentration (CHL; mg m^{-3}), b) primary production integrated at the top 100 metres (NPP; mg m^{-2} d^{-1}), c) export production at 100 metres (EP; mg m^{-2} d^{-1}) and d) export efficiency (EF; %). Average calculated of the yearly average value of 11 years of data from PlankTOM12.2 with historical forcing (blue), SSP1-2.6(low-emission scenario; green) and SSP3-7.0(high-emission scenario; orange). Historical decadal climatology is calculated for 2000-2010, whilst the low- and high-emission scenarios are calculated between 2090 and 2100. Panel (i) shows the Northern Hemisphere, whilst panel (ii) shows the Southern Hemisphere.

There is a notable shift in surface chlorophyll concentrations (representing the phenology of phytoplankton) under the SSP3-7.0 scenario (Figure 5.2.a). In the Northern Hemisphere, there is a pronounced advancement of peak surface chlorophyll concentration from September to May.

Conversely, under SSP1-2.6, a reduction in the intensity of growing periods is observed, accompanied by the emergence of biannual peaks in May and October. The October peak under historical conditions is more pronounced (0.45 mg m^{-3}) compared to either peak under SSP1-2.6 (0.35 mg m^{-3}). This pattern indicates shifts towards earlier and more intense growing periods are significantly more extreme under SSP3-7.0 than SSP1-2.6 (Figure 5.2a). In contrast, a relatively modest shift in the timing of peak total chlorophyll is present in the Southern Hemisphere. Here, decreases in total chlorophyll concentration are modest and there is no shift in the timing of the growing period in the SSP1-2.6 scenario compared to the historical baseline. The SSP3-7.0 scenario, however, presents a further reduction in chlorophyll concentration and an advance in timing by approximately 30 days. This identifies that changes in the phenology of phytoplankton growing periods is likely to be more extreme in SSP3-7.0 than SSP1-2.6, especially in the northern hemisphere where the autumn growing period becomes almost entirely absent in SSP3-7.0.

NPP also decreases in the wintertime and increases in the summertime under SSP1-2.6 and SSP3-7.0 similarly to surface chlorophyll concentration (Figure 5.2b). In the Northern Hemisphere, NPP increases by up to 15 and 43% under SSP1-2.6 and SSP3-7.0, respectively, compared to the historic baseline. In comparison, in the Southern Hemisphere, it diminishes by as much as 10 and 22% under SSP1-2.6 and SSP3-7.0. However, this general trend is not consistent across the year. In the Northern Hemisphere NPP is marginally lower during the winter months by 9 and 16% under SSP1-2.6 and SSP3-7.0 compared to the historical baseline. In the Southern Hemisphere, periods from December to February show an increase in NPP by up to 9% under SSP3-7.0 compared to SSP1-2.6, despite the predominant trend of decreasing NPP under more intense climate scenarios. This shows that although climate-related alterations typically intensify under more severe emissions projections, NPP changes are likely to differ seasonally.

Increases in EP do not align directly with peaks in NPP (Figure 5.2c). In the Northern Hemisphere, there is an increase in EP around August, following increases in NPP in July under SSP1-2.6 and SSP3-7.0. However, there are numerous instances throughout the year when EP rises, despite decreases in NPP under SSP1-2.6 and SSP3-7.0 compared to the historical baseline. In the Northern Hemisphere, EP is 8% and 16% greater on average between January and March under SSP1-2.6 and SSP3-7.0, compared to the historical baseline, despite reductions in NPP. Furthermore, the Southern Hemisphere exhibits highly variable patterns compared to NPP, a complexity more typically anticipated in Northern Hemisphere dynamics. Whilst a peak in export does typically follow a NPP peak in February, there is also a peak in EP in August despite a decline in NPP. Increases in EP are present in March and July in SSP3-7.0 compared to the historical baseline, despite decreases in these months in NPP. This highlights that the relationship between NPP and EP is complex, highly regional, and highly dependent on the ecosystem dynamics (detailed in section 5.3.2).

EF shows a distinct inverse relationship with NPP, a trend that is particularly prominent in the Northern Hemisphere under both the SSP1-2.6 and SSP3-7.0 scenarios. In the Northern Hemisphere, there is a summertime NPP increase of 31.2 and 89.9 mg m^{-2} d^{-1} respectively under SSP1-2.6 and SSP3-7.0, and wintertime decreases of 7.6 and 16.6 mg m^{-2} d^{-1}. This pattern is mirrored in EF, with a wintertime increase of 2.7% and 5.6%, and a significant summertime decrease of 288.4% and 308.1% under SSP1-2.6 and SSP3-7.0, respectively. In the Southern Hemisphere, the trends are more subdued. Under SSP1-2.6, NPP shows a summertime decrease of 1.50 mg m^{-2} d^{-1} and a wintertime decrease of 17.0 mg m^{-2} d^{-1}, while EF exhibits a wintertime increase of 0.68% and a summertime decrease of 89.2%. SSP3-7.0 follows a similar pattern, with a summertime NPP increase of 2.9 mg m^{-2} d^{-1} and a wintertime decrease of 23.2 mg m^{-2} d^{-1}, alongside a wintertime EF increase of 14.8% and a summertime decrease of 59.5%. This demonstrates that NPP and EF has a negative relationship in the PlankTOM12.2 model.

5.3.2. Global Patterns in Response to Climate Scenarios

Building upon the insights from the analysis of hemispherical responses to changing climate scenarios, the following section offers a more detailed examination of the anomalies between historical data and projections under SSP1-2.6 and SSP3-7.0. This section aims to understand the magnitude and spatial patterns of deviations in SST, MLD, phytoplankton phenology, NPP, EP and EF.

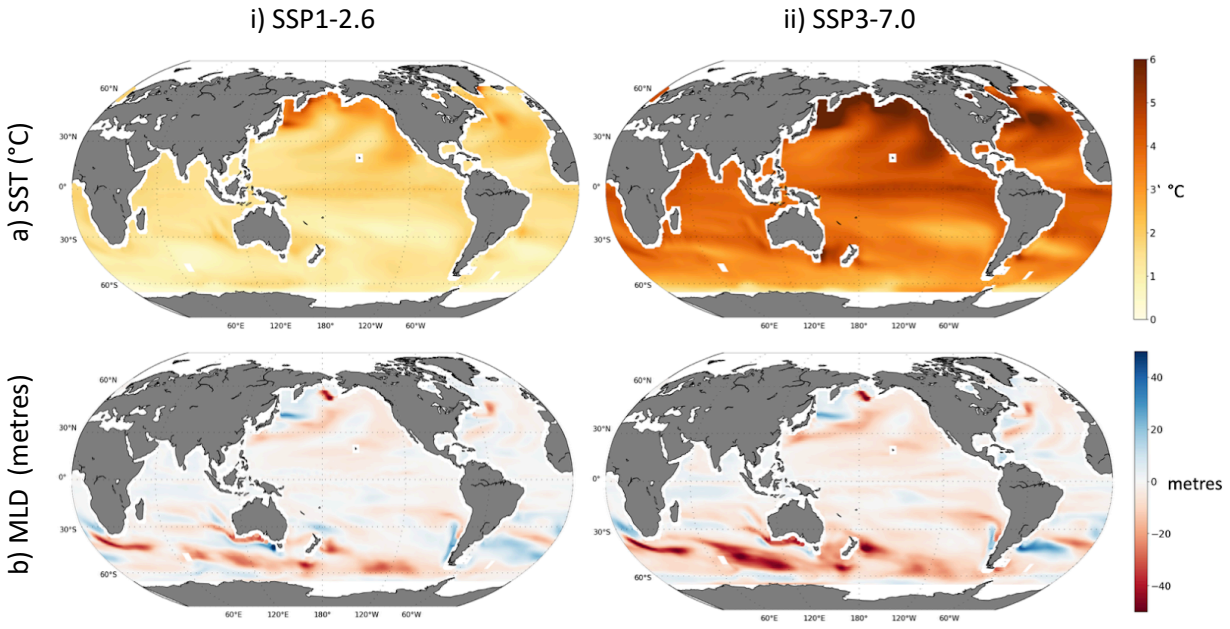

Figure 5.3. Anomalies between the historical average (2000-2010) and i) low-emissions scenario (SSP1-2.6; 2090-2100) and (ii) high-emissions scenario (SSP3-7.0; 2090-2100), for a) sea surface temperature (°C) and b) mixed layer depth (metres). The anomalies given in percentage are relative to the historical average (e.g. ((SSP3-Historical)/Historical)*100).

5.3.2.1. Changes in Physical Indices, Chlorophyll and Net Primary Production

Globally SSTs increased by 1.4°C and 3.7°C (Figure 5.5) under SSP1-2.6 and SSP3-7.0 respectively compared to the historical baseline, however there are strong regional differences in SST response to scenarios. In the subpolar north Pacific, SSTs increase by as much as 3.9 °C and 8.1°C under SSP1-2.6 and SSP3-7.0 respectively. This represents an increase of 60% in SSP1-2.6 and of 112.3% in SSP3-7.0; indicating an escalation of SST rise under high emissions scenarios. In comparison, SSTs in the Southern Ocean increased by 0.97°C under SSP1-2.6 and by 2.5°C under SSP3-7.0 compared to the historic baseline. Indicating that SSTs are consistently warming under SSP3-7.0 compared to SSP1-2.6. However, the difference between regions of moderate vs extreme warming becomes more apparent in SSP3-7.0 compared to SSP1-7.0. For example, the equatorial Pacific is characterised by notably higher warming rates compared to the moderate warming observed in the eastern subtropical south Pacific. The equatorial Pacific SST increased by 1.8°C, while the eastern subtropical south Pacific SSTs increased by 1.13°C, leading to a regional warming differential of 0.67°C under SSP1-2.6. In contrast, under SSP3-7.0, the warming differential escalates significantly, with the equatorial Pacific SST increasing by 4.48°C and the eastern subtropical south Pacific SST increasing by 3.09°C rise, resulting in a differential of 1.39°C. This indicates that regional warming is not uniform and intensifies under higher emissions scenarios.

The variations in MLD display notable discrepancies, both across the SSP1-2.6 and SSP3-7.0 climate scenarios and on a regional scale (Figure 5.3b). In regions such as the Southern Ocean, Pacific, and Indian Ocean, there is a pronounced trend towards shallower MLDs, with reductions reaching as high as 60 metres. Conversely, in the Southern Ocean, particularly in the subtropical south Atlantic, MLD exhibits substantial increases, up to 50 metres. This is in contrast to a smaller increase of about 30 metres observed in the subpolar north Pacific. These changes in MLD are not consistently parallel with temperature trends. For instance, in the subpolar Pacific, the escalation in MLD is directly correlated with one of the most significant temperature rises, indicating a complex interplay between oceanic temperature changes and MLD dynamics.

There is a general global decline in total chlorophyll concentrations by 2090-2100 under both SSP1-2.6 and SSP3-7.0 scenarios, relative to historical baselines (Figure 5.4a; Figure 5.5). Generally, declines in total chlorophyll are related to declines in iron and nitrate, however there is large regionally variability which suggests that drivers other than nutrients may play a role in controlling total chlorophyll concentration. The north subtropical Pacific presents a notable deviation with large increases in chlorophyll concentrations in both SSP1-2.6 and SSP3-7.0. Increases here likely contribute to the earlier onset and greater intensity of the growing period observed in the Northern Hemisphere under SSP1-2.6 and SSP3-7.0 (as shown in Figure 5.2a). While some regional increases in surface chlorophyll in parts of the south Pacific and the tropical Atlantic are apparent under SSP1-2.6, these increases are not observed under the SSP3-7.0 scenario. This suggests that there are significant

differences in the distribution of positive and negative changes in total chlorophyll between SSP1-2.6 and SSP3-7.0.

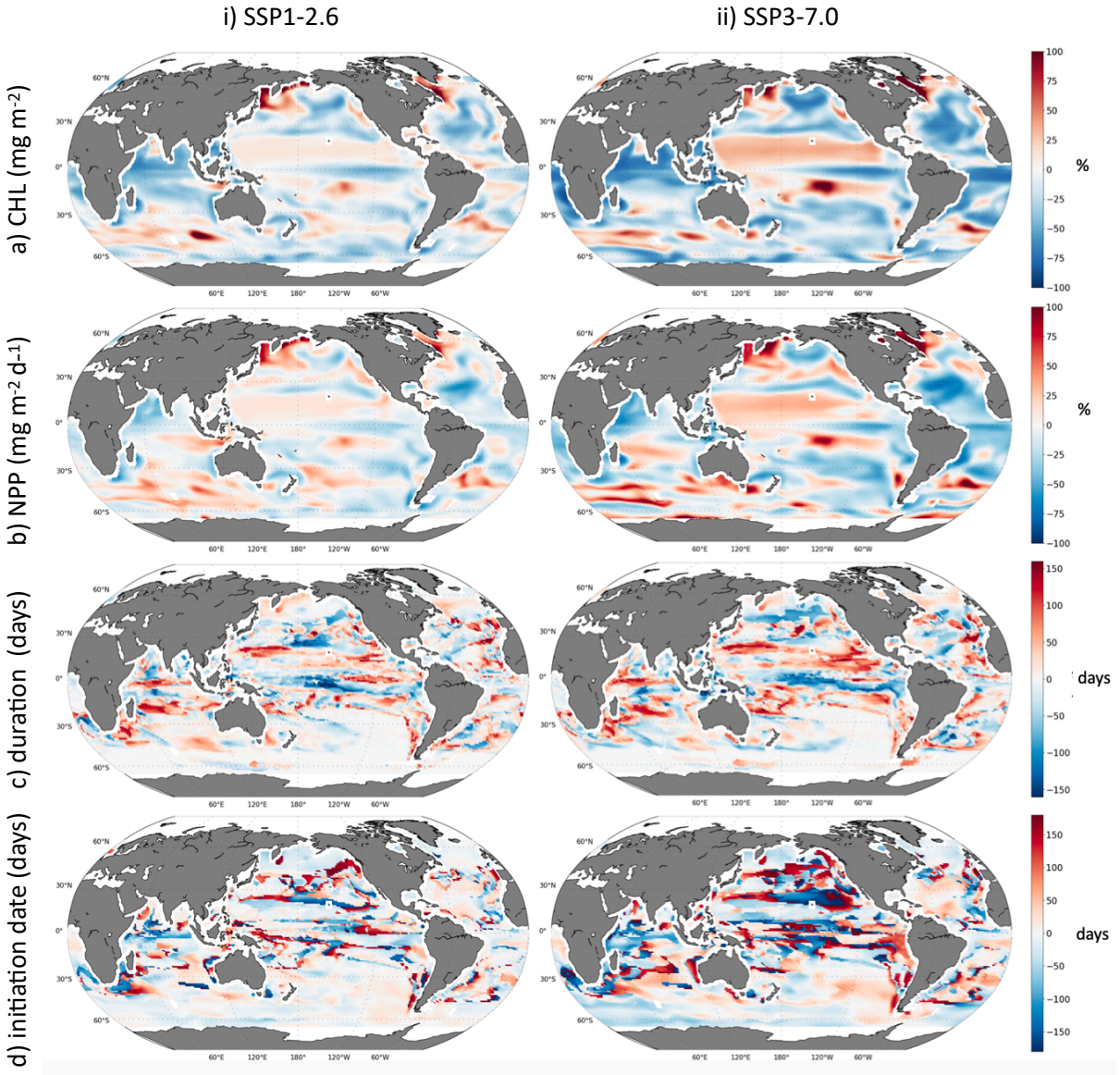

Figure 5.4. Anomalies between the historical average and i) low-emissions scenario (SSP1) and (ii) high-emissions scenario (SSP3), for a) total chlorophyll concentration (%), b) net primary production (%), c) duration (days) and d) initiation date (days). The anomalies given in percentage are relative to the historical average (e.g. ((SSP3-Historical)/Historical)*100).

Most increases in surface chlorophyll concentration under SSP1-2.6 and SSP3-7.0 occur in similar regions to increased rates of NPP (Figure. 5.4b; Figure 5.5). Nevertheless, there are exceptions: for example in the central south Pacific, enhanced NPP does not coincide with an equivalent increase in total chlorophyll. This phenomenon is likely due to increased grazing activity (Figure 5.6), which limits the accumulation of chlorophyll. Conversely, in the tropical Indian Ocean, an increase in total chlorophyll is present alongside a decrease in NPP under both SSP1-2.6 and SSP3-7.0 scenarios,

suggesting a possible reduction in grazing pressure. This suggests that chlorophyll concentration is not only dependent on the level of NPP, but also zooplankton concentration and grazing which differentially favour certain PFTs and result in enhancing/diminishing total chlorophyll concentration.

5.3.2.2. Changes in Phenological Indices

Shifts in phytoplankton phenology are significantly more widespread under SSP3-7.0 than SSP1-2.6 by the end of the century (Figure 5.4c/d; Figure 5.5; Figure 5.7). In the north subtropical Pacific, there is a marked increase in NPP and total chlorophyll, along with lengthening of the growing period by ~20 days and ~75 days under SSP1-2.6 and SSP3-7.0, respectively. In this region, the onset of the growth season under SSP3-7.0 may occur as much as 180 days earlier or later. While similar shifts in the start of the growth period are observed in some areas under SSP1-2.6, the magnitude of these changes is less extensive. Additionally, in some areas within both the subtropical northern and tropical Pacific

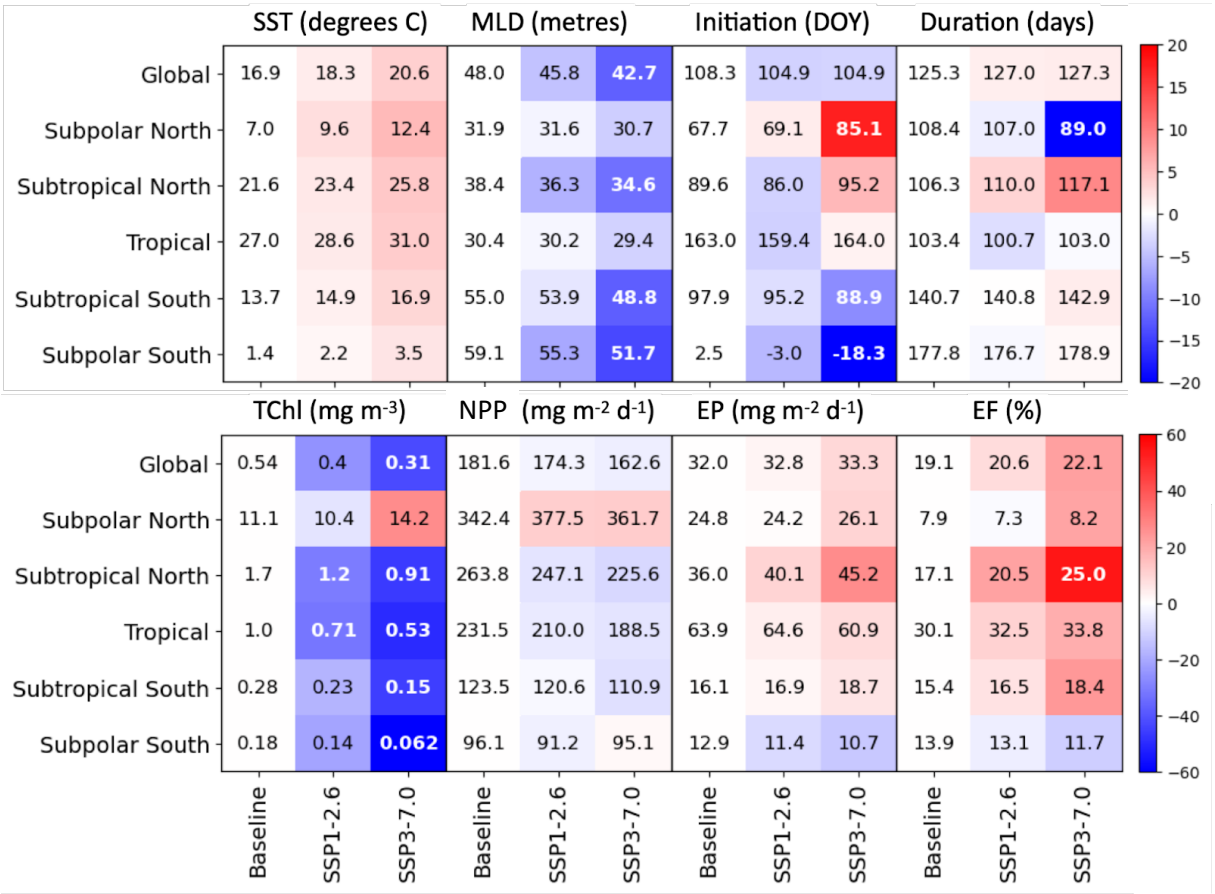

Figure 5.5. Average sea surface temperature (SST), mixed layer depth (MLD), Initiation (day of the year), Duration (days), surface chlorophyll concentration (TChl), primary production integrated over the upper 100 metres (NPP), export production at 100 metres (EXP), export efficiency from the historical baseline (2000-2010), low-emissions scenario (SSP1-2.6; 2090-2100) and a high-emissions scenario (SSP3-7.0; 2090-2100). Colours for SST and Initiation show absolute differences between SSP1-2.6/SSP3-7.0 and the historical baseline. Colours for the remaining variables show the percentage difference between SSP1-2.6/ SSP3-7.0 and the historical baseline.

regions, the growing period shortens more under the SSP1-2.6 scenario than under SSP3-7.0, compared to historical data. In the Atlantic Ocean, changes in growing periods do not show as much latitudinal variation. The western north Atlantic experiences shorter growing periods and delayed initiation dates, in contrast to the eastern regions where there is a lengthening of growing periods with earlier initiation date under SSP1-2.6 and SSP3-7.0 scenarios. The south Atlantic shows an opposing pattern.

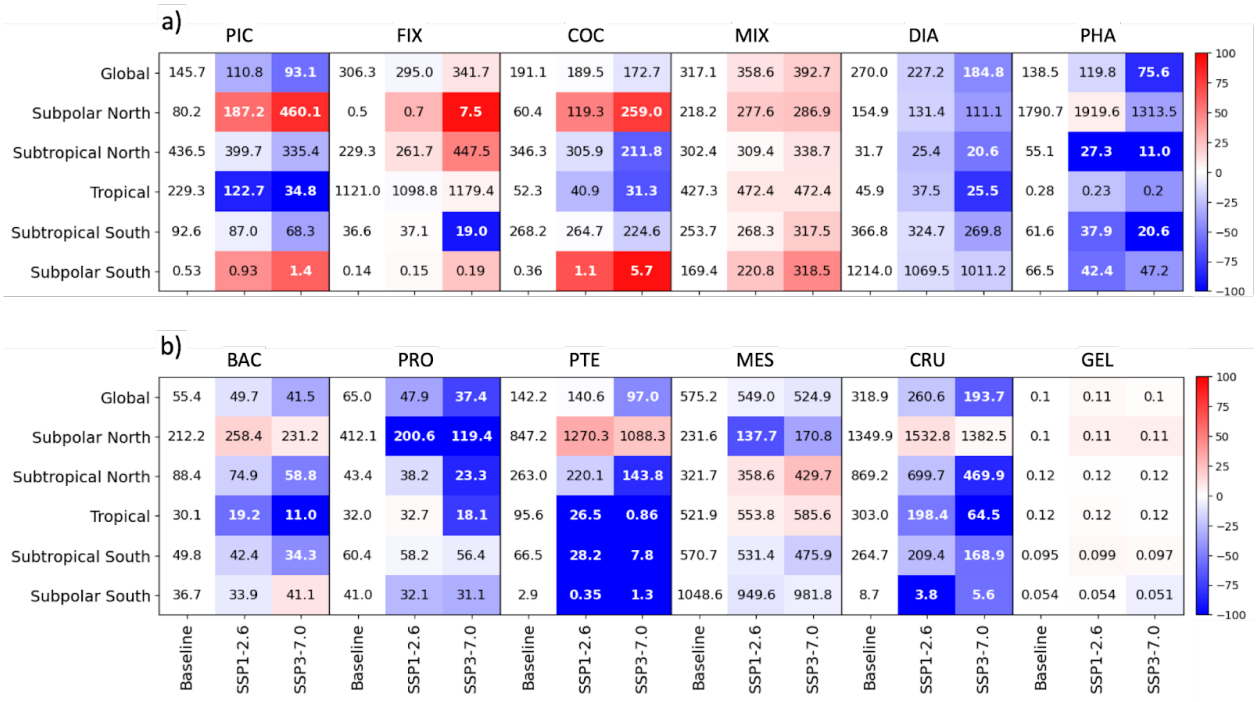

Figure 5.6. Average integrated concentration (mg m^{-2}) in the upper 100 metres of the PlankTOM12.2 model of twelve plankton functional types: picophytoplankton (PIC), nitrogen fixers (FIX), coccolithophores (COC), mixed phytoplankton (MIX), diatoms (DIA), *Phaeocystis* (PHA), bacteria (BAC), protozooplankton (PRO), pteropods (PTE), mixed phytoplankton (MES), crustaceous zooplankton (CRU) and gelatinous zooplankton (GEL). Averages are taken from: the historical baseline (2000-2010), a low-emissions scenario (SSP1-2.6; 2090-2100) and a high-emissions scenario (SSP3-7.0; 2090-2100). Colours represent the percentage difference between SSP1-2.6/ SSP3-7.0 and the historical baseline.

In most regions, except for the eastern Pacific, the initiation date is ~50 days earlier under SSP3-7.0 and ~20 days earlier under SSP1-2.6 compared to the historical baseline (Figure 5.5). These results suggest that the change of the initiation of the growing period is likely to shift at more than double the magnitude under a high-emission scenario compared to a low-emissions scenario. These anomalies in initiation date are patchy due to the high-resolution temporal data and the magnitude of changes (close to ½ a year), however reducing the resolution of seasonal changes make these ecological shifts clearer (Figure 5.7). In fact, PlankTOM12.2 projected that 19.7% of the ocean will experience a shift in initiation date of more than one season (> 90 days; Figure 5.7). The changes include the reduction of spring growing periods in the north subpolar regions that are replaced by

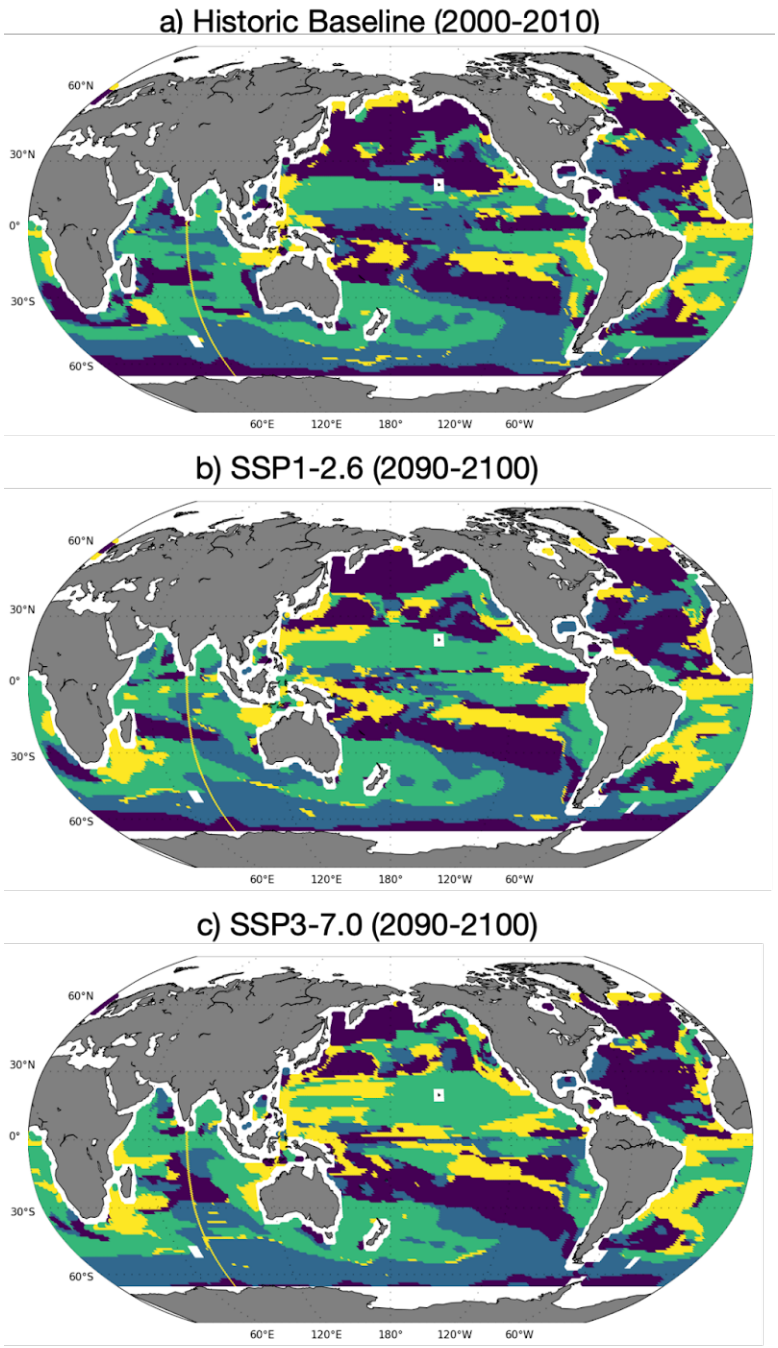

Figure 5.7. The season of the initiation date of the growing period for a) the historic baseline (2000-2010), b) SSP1-2.6 (2090-2100) and c) SSP3-7.0 (2090-2100). Seasons are defined as: spring - March 21 to June 20 (days 80 to 171); Summer - June 21 to September 22 (days 172 to 264); Autumn - September 23 to December 20 (days 265 to 354); and Winter - December 21 to March 20 (days 355 to 79, considering a non-leap year).

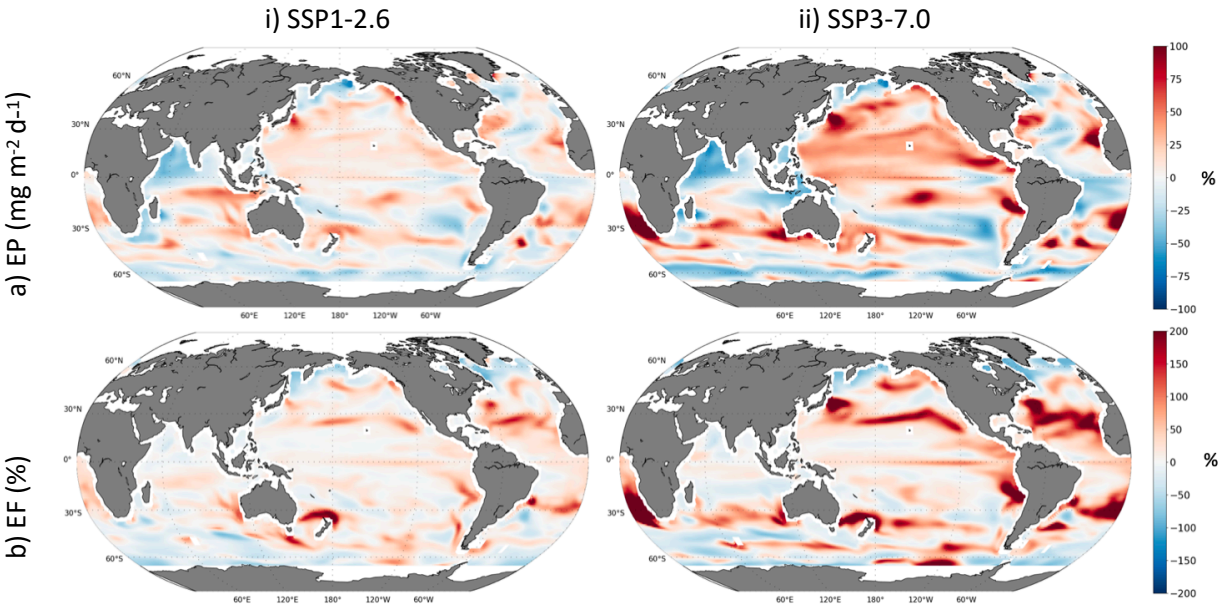

Figure 5.8. Relative anomalies between the historical average and i) low-emissions scenario (SSP1) and (ii) high-emissions scenario (SSP3), for a) export production (%) and b) export efficiency. Relative anomalies are given in percentage are relative to the historical average (e.g. ((SSP3-Historical)/Historical)*100).

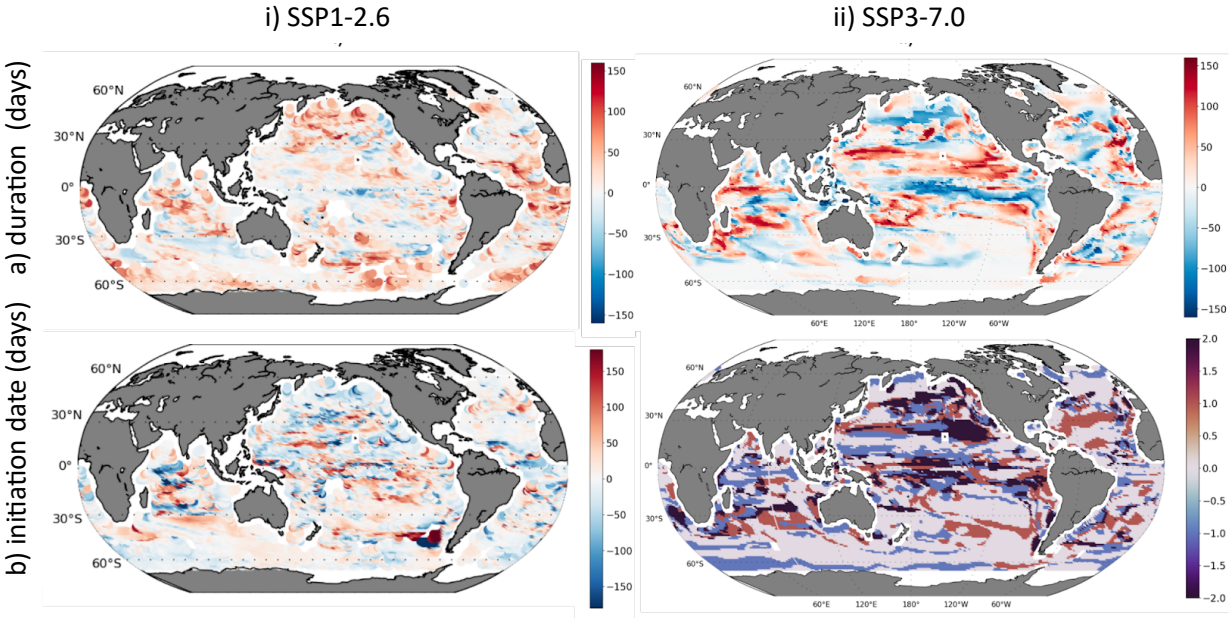

Figure 5.9. Difference in trends between the a) duration of the growing period and b) the timing of initiation for the historical period (1998-2020) and the future scenario (SSP3-7.0; 2000-2010 vs 2090-2100). Panel i) shows the Theil-sens slope trends over two decades (1999-2020; PlankTOM12.2). Panel ii) shows anomalies between the historical average and high-emissions scenario (SSP3), for a) duration (days) and b) initiation date (season).

poleward shifting winter growing periods. In the Southern Ocean, there is a reduction in summer growing period initiations that are replaced by growing periods that initiate in the spring. In the tropics, growing periods that initiate in the summer become more prevalent in SSP3-7.0 compared to SSP1-7.0 and subsequently the historical baseline. This highlights the magnitude of the shifts possible at a global change under climate change, with 4.9% of the global ocean undergoing a change in initiation date of two seasons, representing a complete seasonal shift in the growing period.

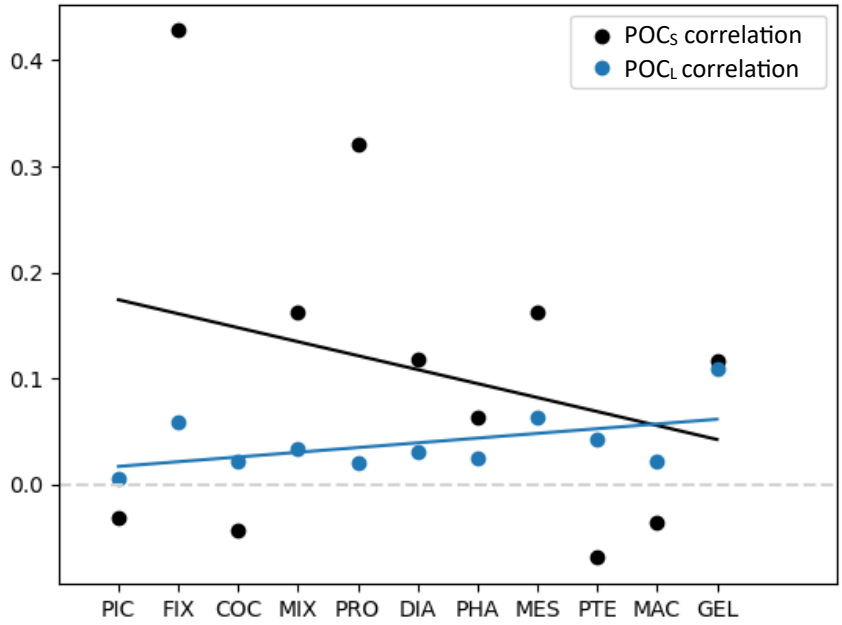

Figure 5.10. Correlation coefficients of small and large particulate organic carbon with PFTs in PlankTOM12.2. POC_S and POC_L were correlated with PFT concentrations in the upper 100 metres of the model. PFTs include picophytoplankton (PIC), N2-fixing phytoplankton (FIX), coccolithophores (COC), mixed phytoplankton (MIX), protozooplankton (PRO), diatoms (DIA), *Phaeocystis* (PHA), mesozooplankton (MES), pteropods (PTE), macrozooplankton (MAC), and gelatinous zooplankton (GEL). These are in size order. Solid lines indicate linear regression fits for POC_S and POC_L correlations.

5.3.2.3. Changes in Export Production and Export Efficiency

EP and EF increase in SSP1-2.6 and SSP3-7.0 relative to the historic baseline over much of the global ocean (Figure 5.5; Figure 5.8; Figure 5.11). The strongest increases in export efficiency, in the north Pacific and subtropical Atlantic ocean are the same regions where some of the largest declines in NPP are present (Figure 5.4; Figure 5.8). This inverse relationship between NPP and export efficiency is not only present in space but also in time. The subpolar regions are an exception to this rule, where there are positive relationships between NPP and export efficiency (Figure 5.5). In the subpolar north, increases in export efficiency are co-located with increases in NPP. The subpolar north is the only region of PlankTOM12.2 where the total concentration of phytoplankton PFTs increases in the upper 100m under SSP1-2.6 and SSP3-7.0 (Table 3.3), especially for the small PFTs. The differing response in

the subpolar north may be because the greatest temperature increases are observed in this region, given that many ecosystem processes are temperature-dependent (Figure 5.3). In this region, shifts towards smaller PFTs and increases in Pteropod concentration suggest that faecal pellet production could result in increases in export production and efficiency, despite a decline in fast sinking large POC produced by large PFTs. Larger PFTs in general do contribute more to large POC and small PFTs more to small POC, despite PlankTOM12.2 containing only two particle sizes (Figure 5.10). This is due to the inclusion of explicitly modelled bacteria remineralisation, mineral ballasting, fragmentation and aggregation processes as well as zooplankton grazing and faecal pellet production. However, the relationship between PFTs and POC concentration is highly non-linear (Sommer et al. 2024), which explains the low correlations. Nevertheless, changes in ecosystem structure will effect the concentration of small and large POC, and therefore the export production.

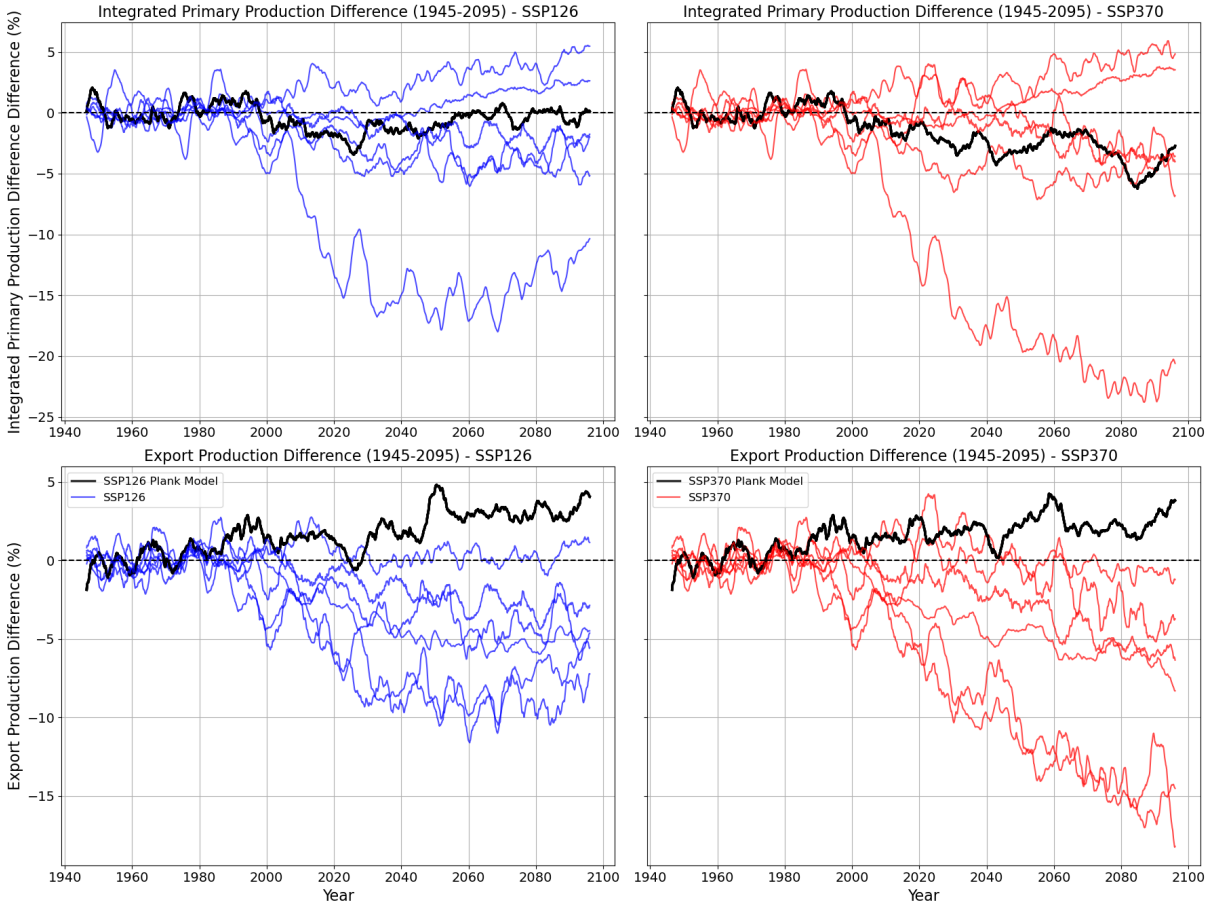

Figure 5.11. Differences in Net Primary Production (NPP) and Export Production over the period 1945-2095, expressed as percentage changes from the baseline period (1940-1990). Panel a) depicts the NPP differences, and panel b) shows the differences in export production. Both panels include data smoothed with a 5-year rolling mean to highlight trends over time. The models included are from the CMIP6 dataset: IPSL-CM6A-LR, NCC-NorESM2-MM, CCCma-CanESM5-1, CSIRO-ACCESS-ESM1-5, CMCC-ESM2, and MPI-ESM1-2-LR. Historical data (1945-2014) are shown in grey, SSP1-2.6 projections (2015-2100) in blue, and SSP3-7.0 projections in red. All model runs are from r1i1p1f1.

Although the global inverse relationship between NPP and EP appears unusual in PlankTOM12.2 as most CMIP6 models predict that decreases in NPP lead to subsequent decreases in export production at the global level (Figure 5.11), there are CMIP6 models which have similar regional inverse relationships between NPP and EP as in PlankTOM12.2 (e.g. Appendix. 7.7). Bopp et al., (2022) demonstrated that the presence of nitrogen fixers can alter the global trend of NPP, we show here that the ecosystem likely has a strong influence on both NPP, EP and subsequently EF. Furthermore, the spread of future predictions of NPP and EP changes in CMIP6 simulations suggests that changes in EP and how they relate to NPP is still subject to large uncertainty (Figure 5.11). Therefore, PlankTOM12.2 is further evidence that current available models are unable to agree on the direction of change for export production and efficiency, and that the response of ecosystems to a changing climate can alter model results.

There are many occurrences where changes in PFTs are not linear between the historic baseline, SSP1-2.6 and SSP3-7.0. In the subpolar south concentration of pteropods decreased by 88% under SSP1-2.6 compared to the historic baseline, but by only 57% under SSP3-7.0 (Figure 5.6). In the Southern Ocean, bacterial concentrations decreased by 2.8 mg m^{-2} under SSP1-2.6 but increased by 4.1 mg m^{-2} under SSP3-7.0 compared to the historic baseline. This is also apparent in phytoplankton; in the subtropical north *Phaeocystis* increases by 11 mg m^{-2} under SSP1-2.6 and decreases by 16.8 mg m^{-2} under SSP3-7.0. This highlights that not only is the entire ecosystem structure crucial in controlling the EP and EF of the global ocean, but that changes under SSP1-2.6 and SSP3-7.0 may result in different impacts on ecosystem community structure.

5.4. Discussion

5.4.1. Physical Changes of SST and MLD

Climate change projections from simulations forced by the UKESM1 atmospheric conditions show warmer SSTs and generally shallower MLD that are amplified at high latitudes, especially in the north (Fox-Kemper et al., 2023). The PlankTOM12.2 model forced by UKESM1 output shows larger warming in the Northern Hemisphere compared to the Southern Hemisphere (4.4°C vs 3.2°C), consistently with both the UKESM1 simulations themselves and with the larger ensemble of CMIP6 models. Globally, SST increased by 1.4 and 3.7°C under SSP1-2.6 and SSP3-7.0, respectively. Projections conducted here lie marginally outside the upper range of the CMIP5 *very likely* SST global average of 1.2°C and 3.5°C, under SSP1-2.6 and SSP3-7.0, respectively (Fox-Kemper, et al., 2023). Furthermore, changes in MLD the PlankTOM12.2 model shows similar patterns of regional variability as the CMIP5 ensemble, with shallowing in the Southern Ocean, tropics and north Atlantic. PlankTOM12.2 shifts in summertime MLD are significantly lower magnitude than shifts in wintertime MLD; CMIP5 ensembles show a range of ±20 metres in the summertime and ±300 metres in the wintertime under SSP3-7.0. This demonstrates that the PlankTOM12.2 model forced by UKESM1 has

a similar magnitude of change under SSP1-2.6 and SSP3-7.0 in SST and MLD to CMIP5 ensembles (Fox-Kemper, et al., 2023) and is suitable for the analysis of ecosystem changes this century, and related carbon export.

MLD became shallower globally in both SSP1-2.6 (0.77m) and SSP3-7.0 (2.7m) by the end of the century relative to the historical baseline, with the strongest effect in the summer in both hemispheres, with some regions of increasing MLD that are more patchy. These findings reinforce the current understanding of the response of MLD under future climate change. Somavilla et al., (2017) demonstrated that increased SSTs are not exclusively linked to surface warming and high-latitude freshening. Instead, they underscore the significance of altered oceanic circulation and atmospheric dynamics in driving regional variations in MLD and hence in SST (Somavilla et al., 2017).

Additionally, in the Northern Hemisphere in PlankTOM12.2, the average summertime MLD deepens, despite widespread shallowing of the MLD (Figure 5.1). This supports the results by Sallée et al., (2021) who show that summertime MLD deepens in some regions, despite the strengthening of summer pycnocline stratification (Sallee et al., 2021). They attribute the deepening of the mixed layer in some areas to the amplification of surface turbulence, effectively counteracting the enhanced stability beneath the mixed layer. The findings show that despite the low-resolution of the PlankTOM12.2 model used here, the relationship between SST and MLD reflects the general patterns reported in the IPCC, but also shows complex regional interplay that reflect specific interactions among physical drivers. While a general shallowing of average MLD is expected and reproduced globally here under SSP1-2.6 and SSP3-7.0, the regional fluctuations strengthen the evidence for the existence of regions where surface turbulence might override the effects of stratification, leading to a deepening of the MLD. The influence of regional fluctuations are further amplified with the ecosystem response.

5.4.2. Ecosystem Response

Projected changes in ecosystem response to climate change in the PlankTOM12.2 model tends to show more regional variations than assessed previously using simpler ecosystem models (e.g. Bopp et al., 2013; Kwiatkowski et al., 2020). Previous publications showed that climate change would lead to decreasing NPP in the tropics from increased nutrient limitation driven by stratification, and increasing NPP at high latitudes from decreased light also driven by stratification. Whereas the large-scale physical patterns reproduce those of other models here, the ecosystem response for NPP shows much more regional variations, which we link to the important shifts in ecosystem composition produced by the PlankTOM12.2 model. In our model simulations, the regions of NPP decreases are largely compensated by regions of NPP increases, with a global change of -10.46% (Figure 5.11). Likewise, decreases and increases in export cancel one-another for a global change in export that is +4.36%. Most global biogeochemistry models project decreases in NPP and export globally (Henson

et al., 2022). Here we show that the difference in behaviour between NPP and export is sensitive to the response of the ecosystem structure to climate change.

5.4.3. Phenological Response

The projected changes in duration under climate scenarios SSP1-2.6 and SSP3-7.0 tend to show a longer duration of the seasonal growing period; this is mostly consistent with both the observations and the model results for the period 1999-2020 (Chapter 3). Shortening of the growing period is more prevalent in the SSP3-7.0 by 2100, than between 1999 and 2020 (Figure 5.9a). However, most regions where growing periods become shorter are present to a lesser extent in the 1998-2020 trends (Figure 5.9a). The trends in the Southern Ocean are lower magnitude than predicted from trends between 1999 and 2020. This is likely the result of longer growing periods in the PlankTOM12.2 model simulations that are forced with UKESM1, compared to the simulations forced NCEP reanalysis between 1998-2020 used in Chapters 3 and 4. Another disparity is present in the subpolar north, where growing periods became longer between 1998-2020 and shorter between 2000-2100 under SSP3-7.0. This is likely related to the poleward extension of autumn initiation dates in the SSP3-7.0 projection (Figure 5.7). Throughout the tropics, there are similar patterns of change in both the historical and projected models, where growing periods become longer in the subtropics and shorter in the tropical regions.

Moreover, the PlankTOM12.2 model shows the greatest magnitude of changes in both bloom duration and initiation in the tropical regions and the Northern Hemisphere. Similarly to trends detected between 1999-2020 initiation becomes earlier over the majority of the ocean. Delayed initiation dates are present in both the historical period (1999-2020) and under SSP3-7.0 in the Indian Ocean, south Pacific and north Atlantic. It is clear that many of these changes appear due to extensions of current biogeographical regions (Figure 5.7): the prevalence of spring and summer growing periods increases globally by 3.3% and 5.1% under SSP3-7.0. Conversely, the prevalence of autumn and winter growing periods decreasing by 5.9% and 2.6% and similarly, to the changes over two decades, in most of the ocean growing periods become earlier. These projections of change are also similar in magnitude to previous studies.

Projections in phenology under climate scenarios have been done previously (Henson et al., 2013; Henson et al., 2018; Yamaguchi et al., 2022). Models used in these studies do not offer a good representation of ecosystem diversity as they contain at most medium-complexity ecosystems of two phytoplankton and two zooplankton (Friedland et al., 2018; Henson et al., 2013; Yamaguchi et al., 2022). In addition, the variability in trends of peak timing of the growing period between the six models in Henson, et al., (2013) is as large as between the multi-model means (Henson, et al., 2018) and PlankTOM12.2. As a result, there is no consensus on the direction of change, neither globally or at the regional level. For example, the projected change in peak timing of the growing period in the

Arctic ranged from a delay of 50 days to an advancement of 50 days between the 6 models (Henson et al., 2013). In comparison, multi-model means from Henson, et al., (2018) produce earlier blooms in the subpolar and tropics of a similar magnitude to PlankTOM12.2 at average of ~25 days per decade. In the subtropics, Henson, et al., (2018) identifies delays in initiation of the growing period with a similar magnitude to the polar regions. In contrast, in PlankTOM12.2 the direction of trends is mixed and there is a much higher magnitude of change of initiation date in these regions. Furthermore, studies differ significantly in where they identify the highest magnitude of change. Henson, et al., (2018) highlights the polar regions and northern subtropics will experience the highest magnitude of change. Yamaguchi, *et al.,* (2022) identify that the Southern Hemisphere has more diverse and lower magnitude trends in initiation date compared to the Northern Hemisphere (2080-2100 minus 1990-2010; RCP 8.5). Whilst here PlankTOM12.2 projects large variations and high magnitude changes in both the growing period duration and initiation date in the Northern Hemisphere and limited change in the Southern Hemisphere. The large differences between models suggests that multi-model means of high-complexity ecosystems will be required to further constrain the predicted changes in ecosystem phenology. However, PlankTOM12.2 provides a more realistic ecosystem structure compared to other commonly used models. The importance of ecosystem structure on export highlighted in this Chapter and previous work, highlights that 1) ecosystem models need to contain higher complexity of ecosystems and 2) more precise metrics to track ecosystem changes need to be developed.

The shifts projected in phenology and ecosystem structure in PlankTOM12.2 under SSP1-2.6 and SSP3-7.0, and their relationship with export, is supported by observations. This chapter identifies decreases in EF with increasing NPP in the subpolar south and increasing EF with decreasing NPP in the tropics and subtropics (Figure 5.5). Evidence from MAREDAT and satellite observations highlight that the inverse relationship between NPP and EF were not just present in the Southern Ocean (Le Moigne et al., 2016), but across the global ocean (Henson et al., 2019). Furthermore, declines in bacteria and crustaceous zooplankton are projected by the model throughout the mid-latitudes and tropics, where EF increases under SSP1-2.6 and SSP3-7.0 (Figure 5.5). Henson et al., (2019) also identify that regimes with low primary productivity (NPP) and high EF typically coincide with lower abundances of macrozooplankton and bacteria. However, decreases in the Southern Ocean export appear driven by a change in the phytoplankton community structure, with reduced concentrations of *Phaeocystis* and diatoms, and increased concentrations of mixotrophs and coccolithophores (Figure 5.6). These changes occur alongside decreases in all zooplankton other than bacteria, highlighting that shifting phytoplankton and bacteria community structures can contribute to reductions in EF even alongside grazer decline.

5.5. Conclusion

In conclusion, this Chapter provides an exploration of possible shifts in marine ecosystems including phytoplankton phenology as represented in the PlankTOM12.2, and their implications for carbon

export dynamics under the SSP scenarios SSP1-2.6 and SSP3-7.0. This chapter highlights the intricate regional responses to climate change and the critical interplay of various factors shaping marine ecosystems. The results underscore significant hemispherical disparities in SST and MLD responses, coupled with alterations in phytoplankton growth periods and community structures under projected climate scenarios. The complexity of regional variations in physical processes become amplified at the ecosystem level due to regional responses of ecosystem dynamics.

This chapter supports the theory of a negative relationship between NPP and EF. This phenomenon appears driven by the shifting ecosystem structure and is evident in phenological changes, making phenology a key indicator for shifting ecosystem structure. This relationship appears to be a critical component in understanding the broader implications of climate change on marine ecosystems. In addition, this chapter contributes to the growing body of evidence that ecosystem structure and phenology significantly influences the efficiency of the biological carbon pump (Chapter 4). The abundance of macrozooplankton and bacteria, along with changes in the phytoplankton community, emerge as key factors in this complex dynamic. This Chapter also identifies more regional variability in the phenological response of marine ecosystems to climate change than Yamaguchi, et al., (2022). This may be driven by the higher complexity of the ecosystem represented in PlankTOM12.2 compared to models used in other studies such as Yamaguchi, et al., (2022) and Henson, et al., (2018). Increase of small phytoplankton and declines in large-bodied phytoplankton are often related to reductions in EP and EF. In other regions of the ocean, increased concentrations of zooplankton and bacteria are identified as key drivers of increases in EP and EF.

For future research, it is essential to further explore the mechanisms underpinning these patterns and their implications for the global carbon cycle. This includes a more detailed examination of the roles of zooplankton and microbial processes in carbon export and efficiency. This Chapter highlights the need for the widespread improvement of model ecosystem representation to enhance predictive capabilities. Using multi-model means of high-complexity ecosystem models may enable us to further constrain the effects of ecosystem dynamics on EP and EF. In parallel, observational indices need to be developed that monitor shifts in ecosystems more closely, rather than relying on satellite observations. Nevertheless, this Chapter represents a crucial step in highlighting more mechanisms behind EP and EF, emphasising the intricacy of underlying drivers and the pronounced differences in regional response under a changing climate.

Chapter 6: Conclusion

6.1. Précis of Key Results

This thesis primarily focuses on advancing understanding of phenological and ecological drivers of carbon export production (EP) and efficiency (EF). The thesis first encompasses an evaluation of the PlankTOM12.2 model's predictive capacity of oceanic carbon dynamics (Chapter 2) and phytoplankton phenology (Chapter 3). It provides an explanation for the observed trends in phenology based on the processes incorporated in the PlankTOM12.2 model (Chapter 3). This is then followed by an investigation into the interplay between phytoplankton phenology and carbon export during the historical period (Chapter 4), and to 2100 under future climate scenarios, also incorporating more broadly and exploration of future changes in ecosystem dynamics (Chapter 5). The significant findings of this research are presented next, consistent with the research goals established in Section 1.8.

6.1.1. Evaluate the accuracy of the PlankTOM12.2 model in simulating Particulate Organic, Inorganic Carbon, and Silica Fluxes.

Chapter 2 delves into the refinement of the PlankTOM12 model parameterisations, with a focus on the remineralisation of organic carbon and dissolution of inorganic carbon, and on the seasonal dynamics of phytoplankton, which are at the core of this thesis. I compared nine distinct model simulations, each representing an incremental enhancement of the model parameterisation, assessing the impact of new and updated parameterisations on modelled carbon export and the seasonal cycle of chlorophyll. The introduction of bacterial biofilms to the model was a pivotal development, specifically aimed at improving the vertical distribution of organic carbon flux. In previous model iterations, excessive fluxes of organic carbon were observed below 500 metres, because bacterial concentrations in the water were too low to degrade organic carbon below that depth. PlankTOM12 uniquely represents bacteria explicitly, meaning any weakness in the bacteria representation will have repercussions on remineralisation of organic carbon. The representation of bacterial biofilms, a process not considered until now, significantly enhanced the model's accuracy in simulating organic carbon flux, decreasing organic carbon flux by ~50% below 500 metres. Another major improvement was the refitting of the relationship between saturation state and calcite dissolution. Previous model versions overestimated the rate of calcite dissolution by a factor of 10 because of the lack of observations at the time of model conception. The refitting to recent data improved the representation of the vertical distribution of inorganic carbon flux by increasing PIC to depth. Both POC and PIC flux in PlankTOM12.2 now align more closely with recent empirical data (Mouw et al., 2016a) (Mouw et al., (2016), Klaas and Archer (updated from 2002; pers. com), Torres-Valdés et al., (2013); Le Moigne (2019) and Lutz et al., (2007)).

The new PlankTOM12.2 model also demonstrated significant improvements in the seasonality of chlorophyll due to the update from a 2-parameter to a 3-parameter growth model, recognising that

the PFT approach enables the distinction of specific temperature optimal ranges. In the Southern Ocean, previous seasonal cycles of chlorophyll were more similar to Northern Hemisphere observations. The new seasonal cycle of phytoplankton in the Southern Ocean now peaks in September and is lowest in January. While the timing of the Southern Ocean maximum chlorophyll concentration is delayed by two months compared to observations, the model accurately replicates the timing of the minimum, indicating a marked improvement in simulating Southern Ocean bloom dynamics. In addition, the PlankTOM12.2 has a more accurate representation of short, intense bloom periods in the polar north, a feature that was previously not well captured. Furthermore, in the subtropical south, the improved PlankTOM12.2 model shows reduced annual variability in chlorophyll bloom dynamics, aligning more closely with observed long, low-amplitude growing periods, indicating an advancement in the model's capability to simulate phytoplankton seasonality between different ocean regions. These enhancements render PlankTOM12.2 a useful tool for in-depth study and analysis of shifts in ecosystem structure and phytoplankton seasonality, and their subsequent impact on carbon export.

6.1.2. Assess the replication of Phytoplankton Phenology and its trends over the past two decades by PlankTOM12.

In Chapter 3, a global estimate of trends in phenology using the latest satellite data was first updated with satellite observations (OC-CCIv5). Results reproduced general patterns published previously but with more systematic trends. Friedland et al., (2018) suggested there had been little systematic change in the duration of the growing period between 1998 and 2015. The analysis presented in this thesis highlights, for the first time, systematic regional trends in duration of the growing period derived from satellite imagery. The duration of phytoplankton growing periods increased globally by approximately 5.1-7.8 days per decade, as both observational data and PlankTOM12.2 model indicate. This aligns with findings by Friedland et al., (2018), who reported a similar trend with an increase in duration of about 7 days per decade between 1998 and 2015. However, trends presented here are much more regionally systematic; duration of the growing period shortened in mid-latitude regions, while in higher latitudes the duration of the growing periods became longer. Globally, the initiation of the phytoplankton growing period advanced by about 2.9 days per decade, although this trend was not statistically significant at the 95% level. This is a slower advancement compared to the 2-week per decade advance reported by Friedland et al., (2018) for the period between 1998 and 2015. Termination dates for phytoplankton growing periods shifted later by 6.3 and 2.6 days per decade in the PlankTOM12.2 model and observations, respectively. This shift indicates a significant change in the phenology of phytoplankton, suggesting the growing period's termination may play a more influential role in phenological changes than previously recognised (Racault et al., 2012; Friedland, et al., 2018).

The performance of the PlankTOM12.2 model in replicating phytoplankton phenology and spatial patterns in the global ocean from 1998 to 2020 was then evaluated. I reproduced the Friedland et al., (2018) analysis using a slightly different method, but also importantly applied it to both observations and a model. I calculated phenology indices from surface chlorophyll concentrations using the threshold method. Phenological indices assessed include: the timing of initiation, maximum amplitude and termination, as well as the duration, maximum amplitude and concentration over the growing period. Additionally, monthly SST, SSS and MLD variables were integrated into the analysis.

At a coarse regional scale, statistical analysis shows that most phenological indices in the PlankTOM12.2 model are not significantly different from observations, and thus that PlankTOM12.2 is able to reproduce observed trends at the regional level. However this good match breaks down at the level of the model grid. Specifically, the timing of the growing period in the PlankTOM12.2 model was more likely to occur earlier in the year compared to the OCCCIv5 observations. Additionally, PlankTOM12.2 had a slightly lower mean duration of the growing period compared to the observations, although the variation in duration across regions was similar. This variation likely stems from the absence of long-subtropical growing period conditions seen in various oceanic regions. The variability of the relative maximum amplitude was significantly greater in the model than in the observations, even at a regional resolution.

A detailed analysis revealed physical biases in the PlankTOM12.2 model, affecting SST, SSS, and MLD. Model SST and SSS are higher in the tropics and lower in the subpolar north compared to observations. In contrast, MLD is shallower in the tropics and deeper in subpolar regions compared to observations. PlankTOM12.2's phytoplankton growing period is generally shorter than observed, except in the subpolar south. These biases in duration tend to be smaller than biases in initiation date and termination, because biases in initiation date and termination were often unidirectional. In high latitudes, the model shows higher chlorophyll concentration, possibly due to excessive nutrient supply, whereas tropical regions have lower concentrations due to nutrient restrictions. However, these errors appear to explain only some of the variance in errors of phenological indices in the PlankTOM12.2 model. Other factors, such as nutrients, grazing and ecosystem structure likely play substantial roles in influencing the phenology of phytoplankton in the model ecosystem.

6.1.3. Investigate the Effects of Changes in Phytoplankton Phenology on Carbon Export between 1999 and 2020.

Chapter 4 highlights the complex interplay between ecological and physical drivers in shaping the carbon EP and EF in the PlankTOM12.2 model. In this chapter, I assessed the effect of SST, MLD, NPP, duration of the growing period, and initiation of the growing period on EP and EF. This chapter provides an improved understanding of regional drivers in export dynamics across the global ocean, highlighting the significant, though not dominant, influence of phytoplankton phenology. These

findings suggest that the mis-match hypothesis may be a valuable framework for understanding the effect of phenological changes on carbon export.

First I assessed the difference in SST, MLD, initiation date, NPP, EP and EF in years when the growing period was longer, compared to years when the growing period was shorter. Long growing periods were often twice the length of short growing periods in the Northern Hemisphere. Initiation date was earlier across most of the ocean during longer growing periods, with the most extreme changes in the subpolar north Pacific. In contrast, long growing periods were associated with low temperatures in the mid-latitudes and high-temperatures in the high-latitudes. This variation across regions is consistent with our current understanding of phytoplankton phenology which expects: a global shift towards longer and earlier growing periods; shorter growing periods in the tropics related to higher temperatures, shallowing MLD and reduced nutrient influx; longer growing periods in the poles are related to higher temperatures, shallowing MLD and increased insolation. This regional variability during long and short growing periods highlight the diverse response of marine ecosystems to changing environmental conditions.

Second, I conducted a multiple regression model analysis to gain critical insights into the regional drivers of EP and EF in marine ecosystems. Relationships between physical drivers and EP/EF were almost always higher in magnitude than the relationship between phenology indices and EP/EF. However, in the Southern Ocean, a 30 day increase in bloom duration was related to a 50% decrease in the EF. This effect was independent of the effect found from NPP, which was controlled for in the multiple regression model. This challenges our previous understanding of drivers of EP, which suggests that the ecosystem plays a minor role compared to physical drivers, at least in some regions. Furthermore, an inverse relationship was observed between NPP and EF, with regions of high NPP related to regions of reduced EF. This relationship was particularly pronounced in the Southern Ocean, where the inverse relationship is likely a result of ecosystem shifts. I identified decreases in large phytoplankton types and an increase in bacteria and zooplankton in the model used here. Such changes have previously been identified in observations as controlling EF (Henson, et al., 2019). This adds to the current body of literature that suggests that ecosystem structure plays a significant role in modulating carbon EF.

The model's findings reveal a nuanced picture of marine ecosystem responses to ecological and physical drivers, highlighting the complexity of interactions influencing export rates and efficiency. This underscores the importance of incorporating complex ecosystem dynamics in predictive models for a more accurate understanding of the marine carbon cycle in the context of climate change.

6.1.4. Explore the response of Phytoplankton Phenology, Ecosystem Dynamics and Export under Future Climate Scenarios by 2100.

In Chapter 5, I assess the impacts of climate change on marine phytoplankton phenology and carbon export under two Shared Socioeconomic Pathway (SSP) scenarios, and explores how these are related to changes in ecosystem dynamics in the PlankTOM12.2 model. The chapter examines the responses of SST, MLD, initiation date, NPP, EP, EF, and PFT biomass to the SSP1-2.6 and SSP3-7.0 climate scenarios, using the PlankTOM12.2 model.

Chapter 5 reveals significant trends in phytoplankton phenology and carbon export under SSP1-2.6 and SSP3-7.0 to 2100. It shows shifts in the duration and timing of initiation in the growing period, with an earlier initiation and longer duration across most of the ocean by 2100. These shifts are particularly pronounced under the high-emission SSP3-7.0 scenario, suggesting substantial shifts in marine ecosystem dynamics. Additionally, NPP is projected to vary significantly, with increases in the summertime and decreases in the wintertime in the Northern Hemisphere under SSP3-7.0. The projected changes in NPP exhibit more regional variability than previous projections using simpler models, suggesting that PFT diversity is an important factor in predicting shifts in NPP. These trends highlight the necessity of future research to further constrain the complex interactions among phytoplankton, zooplankton, and abiotic factors, particularly under varying climate change scenarios.

Another prominent finding is the inverse relationship between changes in NPP and changes in EF across various marine regions under the SSP1-2.6 and SSP3-7.0 scenarios. I highlight that changes in the ecosystem structure, particularly increases in small PFTs, reductions in zooplankton and bacterial concentrations, shifts towards smaller phytoplankton types, are driving these dynamics. Previous studies have found that the inverse relationship between NPP and EF is controlled by macrozooplankton and bacteria concentration in observations (Henson, et al., 2019). A model study identified that trophic decoupling drives changes in phytoplankton phenology under RCP8.5 (Yamaguchi, et al., 2022). However, this is the first time that these two mechanisms have been connected in a model system. For instance, in the tropics and subtropics, the decrease in bacterial and certain zooplankton concentrations under both climate scenarios were associated with an increase in EF. However, unlike Henson, et al., (2019) I also identify that increase of small PFTs likely plays an important role in changing export dynamics under ocean warming. In subpolar regions of the Southern Ocean, shifts towards smaller PFTs were related to decreases in export efficiency, despite decreases in bacteria and zooplankton concentration.

These findings are significant as they add depth to our understanding of how marine ecosystem structures, particularly shifts in phytoplankton and zooplankton communities, can influence carbon export dynamics. The chapter underscores the complex interplay of ecological changes and their profound impact on the biological carbon pump, highlighting the need for more sophisticated

ecosystem models to improve projections of future changes in marine carbon export under varying climate scenarios. In addition, the development of observational indicators is central to validate model PFT concentrations (e.g. MAREDAT; Buitenhuis, et al., 2013).

6.2. Limitations of the PlankTOM12.2 Model

Although the PlankTOM12.2 model has been validated for its ability to replicate observed particulate organic and inorganic carbon flux, as shown in Chapter 2, the results presented here hinges on the representation of ecosystem dynamics under varying climate conditions which cannot, at this stage, be fully validated because of limited observations on the carbon biomass of PFTs. Furthermore, the PlankTOM12.2 model does not currently represent other processes known to influence carbon export, such as zooplankton and fish diel-vertical migration, Transparent Exopolymer Particle (TEP) production or variable stoichiometry in detritus. These processes are also missing from most other global carbon models and are usually either only present in specialist models or are completely absent.

The inclusion of zooplankton vertical migration should be considered a crucial next step in ecosystem model development due to its significant impact on EP and EF. Diel vertical migration (DVM) refers to the daily oscillation of marine species between deeper waters and surface layers. Typically, these organisms dwell in deeper waters during the day and ascend to the upper regions of the water column at night (Pinti et al., 2019). Zooplankton DVM contributes to the biological carbon pump by transporting organic matter to deeper waters, a process termed 'active flux'. This vertical movement can enhance carbon sequestration in the deep ocean, as zooplankton excrete or egest organic material at depth, or when they die and sink. Moreover, Archibald et al., (2019) have shown that this active flux could be a substantial component of total carbon export, particularly in regions where passive fluxes are low. They identified that carbon export in model simulations including DVM was 14% greater than models that didn't include DVM (Archibald, et al., 2019). In addition, models estimate that fish diel vertical migration (DVM) may contribute significantly (16%) to carbon export out of the euphotic zone, equating to an annual flux of ~1.5 PgC yr^{-1} (Saba et al., 2021).

The absence of fish and zooplankton DVM in models like PlankTOM12.2 may therefore lead to an underestimation of EP, especially in oligotrophic or mesopelagic zones where zooplankton migration may play a larger role in carbon transport (Archibald, et al., 2019). This may also result in the model underestimating increases in EF in the subtropical north under SSP3-7.0 by 2100. In Chapter 5, increases in EF were related to increases in small PFTs and increases in pteropods and crustaceous zooplankton; these increases in EF are likely driven by increase in faecal pellet flux which diel-vertical migration would amplify. Incorporating zooplankton vertical migration into models like PlankTOM12.2 is essential for a more accurate representation of carbon cycling processes in the ocean, thereby enhancing our understanding and prediction of oceanic responses to environmental changes.

Incorporating Transparent Exopolymer Particles (TEP) into ocean ecosystem models is critical for accurate carbon cycling predictions. TEP, primarily composed of acidic polysaccharides, are produced by phytoplankton and bacteria. The roles of TEP in carbon cycling are multifaceted and may include: 1) enhancing particle aggregation owing to their stickiness; 2) contributing to the organic carbon inventory within meso- and bathypelagic layers; and 3) acting as a vital food source for deep-sea bacteria (Nagata et al., 2021; Yamada et al., 2018). However, the low density of TEP can also result in their accumulation at the surface, potentially reducing carbon sequestration (Mari et al., 2017). Lab experiments with diatoms also suggest that increasing TEP production due to warmer temperatures may be related to a lower number of total aggregates (Seebah et al., 2013). Therefore, the precise impact of excluding TEP from models is not defined. This highlights the need for a deeper understanding of TEP dynamics, including production, degradation, and interactions with other marine particles, to accurately predict carbon EF under evolving environmental conditions (Henson et al., 2022).

Furthermore, incorporation of variable stoichiometry in detritus within ocean ecosystem models is also important for further constraining organic carbon flux. Variability in the carbon-to-nitrogen ratio of detritus, driven by ecological processes and environmental shifts, directly impacts the ocean's capacity for carbon sequestration. Increasing CO_2 concentrations resulted in a higher carbon-to-nitrogen (C:N) ratio in the dissolved inorganic carbon drawdown (Riebesell et al., 2007). This change in nutrient stoichiometry led to an enhanced aggregation and sinking of organic matter, affecting the efficiency of carbon export (Riebesell et al., 2007). In Tanioka and Matsumoto's (2017) study, a new power law model was developed to predict the particulate organic matter (POM) phosphorus-to-carbon (P:C) ratio as a function of ambient phosphate concentration. This model allows for flexible stoichiometry and estimates that this plasticity in P:C ratio could buffer a reduction in global carbon export by up to 5% compared to fixed (Redfield) P:C ratios. This underscores the critical importance of incorporating flexible stoichiometry in global carbon cycle models.

Finally, the current representation of particulate carbon size classes in PlankTOM12.2 may be limited for its representation of the global distribution of POC flux. In a recent study using PlankTOM12 model output, Denvil-Sommer et al., (2023) tested the capability of machine learning methods, to reproduce the modelled POC in the ocean based on model physical, biogeochemical, and ecosystem variables. They showed that the inclusion of PFT drivers enhanced the accuracy of reproduction of small particulate organic carbon (POC_S) flux by 58% and large particulate organic carbon flux (POC_L) by 22%. Furthermore, in a model that reproduces both faecal pellets and carcasses, carcasses were found to contribute to ⅓ of zooplankton related carbon flux at 100 metre depth (Clerc et al., 2023). In addition, some models have many more sizes of POC than PlankTOM12.2. The NUM framework introduced by Serra-Pompei (2022), which exclusively incorporates mixotrophs and copepods across various size categories, alongside a classification of eight faecal pellet and eight deadfall size classes, has been shown to replicate the profiles of POC flux except in the deep ocean. This is noteworthy,

especially considering that their model does not represent many PFTs. This highlights the pivotal role of detrital size classes in the accurate simulation of POC flux in marine ecosystems, highlighting that even a model with a relatively narrow representation of PFTs can effectively capture the essential dynamics of POC flux, primarily through a detailed consideration of size classes. These studies highlight the significance of integrating ecosystem drivers into the modelling of POC flux and calls for observations to validate models. This emphasises the need to deepen our understanding of how ecosystem structures influence POC flux and proposes that new observational data could establish connections between surface environmental factors, ecosystem structure, and the distribution of POC within the ocean's interior, enhancing model accuracy and insight into the development of the ocean carbon sink.

However, even after introducing these processes there are many possible inaccuracies in the PlankTOM12 model. Until PFT carbon biomass data are available in a variable climate, the accuracy of the PlankTOM12.2 model in reproducing complex ecosystem dynamics remains unknown. Gathering high-resolution data in time and space on PFTs for biogeochemical models is a challenging endeavour. The MAREDAT project (Buitenhuis, 2013) highlighted this challenge, indicating that while abundance data is relatively well-constrained, the carbon content and elemental composition of PFTs, particularly in vast oceanic areas with low biomass, are less known. Buitenhuis, et al., (2013) also highlighted the disparity in data coverage between high-productivity coastal regions and the more extensive, but less studied, open ocean areas, and the patchiness of the PFT observations, especially for the larger PFTs. The Tara Oceans project (Sunagawa et al., 2020) exemplifies efforts to fill these gaps through comprehensive sampling of plankton across a range of depths and geographic locations. By collecting plankton at 210 globally distributed sites, Tara Oceans has provided an extensive dataset that enhances our understanding of plankton diversity and their roles in ocean ecosystems. However, ecosystem data remain predominantly reported as snapshots of abundance (absolute or relative), which is still difficult to use in model validation. Validating model PFT concentrations using higher-resolution observational data in a variable climate is essential to validate ecosystem dynamics in PlankTOM12.2 and allow us to further constrain POC flux.

6.3. The Bigger Picture

This thesis presents the first assessment of the impact of the timing of phytoplankton growing periods on EP and EF in a model system. Anthropogenic climate change poses a significant risk to ocean ecosystems. The poleward shift of species and extirpation at the poles is anticipated to lead to extensive ocean ecosystem reshuffling (Boyd et al., 2019). Such alterations may have important consequences for organic carbon export, which is at the heart of the biological carbon pump. The IPCC AR6 report warns that shifts in the timing and magnitude of phytoplankton production could disrupt matched phenologies in the food web, potentially leading to decreased survival of dependent species (Cooley, et al., 2022). We find that changes in phenological indices may be a result of ecosystem shifts, though a higher resolution analysis is required to quantify the impacts of ecosystem

shifts on phenology. Therefore, in some regions, phenological changes are likely to result in small but significant alterations to EF (Fu et al., 2016; Henson et al., 2019; Yamaguchi et al., 2022).

Furthermore, the magnitude of carbon export change remains uncertain. In Chapter 5 we identified that change in estimated organic carbon export varies from -15.6 to -0.75% in CMIP6 models under SSP3-7.0, however we project here that the global carbon export will increase by 4.4%. However, most existing models feature a simplistic representation of ecosystems (Rohr et al. 2023), despite research showing that increasing zooplankton complexity from 1 to 3 zooplankton functional types reduces export production by 10% (Karakuş et al., 2021). The lack of adequate ecosystem complexity in most models limits our ability to identify phenological and ecosystem changes, and to constrain the errors associated with these predictions. Although we do not firmly demonstrate that the PlankTOM12.2 model projections are more realistic than simpler models, we do show that adding ecosystem complexity can change projected results substantially, and that the CMIP6 model ensemble does not cover the full range of plausible results.

Another major limitation is the lack of export processes currently represented in ecosystem models. Despite PlankTOM12.2 incorporating over half of the processes outlined in Henson et al., (2022), most models do not include basic processes such as fragmentation (1 out of 19 models), sea viscosity (1 out of 19), mineral ballasting (5 out of 19), and the effect of phytoplankton size on sinking (5 out of 19). Addressing these gaps is critical, especially for accurate predictions of export flux changes due to climate change. Models which either include or exclude these processes are likely to have a significant effect on estimated mean carbon export production, and how export changes under changing conditions. Fragmentation is also critically underrepresented in models and has been shown to reduce carbon flux by half during high export events (Mayor et al., 2020). In contrast, reductions in sea viscosity due to ocean warming may accelerate the speed of carbon export production by ~5%/°C of warming (Taucher et al., 2014). Mineral ballasting has been shown to increase the sinking speed of aggregates by 100% and lithogenic material by 150% (Lombard et al., 2013). Furthermore, size structure has be shown to explain up to 28% of the variance of carbon export production (Dunne et al., 2005). Whilst it is difficult to estimate the combined effect of these missing processes in models it is likely that not representing these processes hinder the accuracy of their predictions of carbon export production due to climate changes. Understanding whether these processes act as significant positive feedback loops or tipping points under climate change is essential for timely and effective climate action. In this thesis (Chapter 4) I show that changes in phenology can both amplify and mitigate the impacts of climate change on export production and efficiency. Current climate models, limited by their poor representation of ecosystem and export processes fail to account for these feedback loops, potentially leading to under-predictions of climate impacts.

In conclusion, this thesis contributes to a growing body of evidence that suggests ecosystem shifts are important drivers of both phenological and export productivity changes (Henson, et al., 2019; Fu et al., 2016; Yamaguchi, et al., 2022). Projections from multiple models are crucial to constrain the errors associated with the impacts of phytoplankton phenology and ecosystem shifts on carbon export. Therefore, future research should aim to improve the representation of model ecosystems to allow for better estimates of ecosystem shifts. Quantifying the number of PFTs required to model accurate ecosystem shifts should be paramount. The collection of higher-resolution observations, such as those from Tara ocean, will help to validate model PFTs on a finer scale. Data collection should focus on both spatial and temporal variability, enabling the validation of the variability of PFTs across the global ocean. Employing a dual approach of introducing emerging properties and validating PFT concentrations with variable climate observations will enhance our understanding of future ecosystem dynamics, phenology, and carbon export, thereby constraining predictions of future climate change impacts.

Appendices

Appendix 7.1. Impact of Data filling on Chlorophyll Concentration

Table 7.1. Global Relative Mean Difference (absolute) and the Relative Mean Bias of filling the PlankTOM12 dataset by ~5, 10, 15 and 20 degrees in each direction (as described in Chapter 3). Data was masked to observations and then filled for 2000, 2004, 2011 and 2014 to ensure the fill did not create biases in the Chlorophyll cConcentration. Due to the methodology of using 2-year climatologies to calculate phenology, a ~5° method of data filling was used, because we were able to calculate phenology metrics over the entire global ocean despite gaps in data.-1-1

Relative Mean Difference				
	5	10	15	20
2000	1.23%	2.45%	3.61%	4.73%
2004	1.28%	2.58%	4.16%	5.04%
2011	1.28%	2.57%	4.13%	5.27%
2014	1.15%	2.32%	3.44%	4.53%
Relative Mean Bias				
	5	10	15	20
2000	-0.002%	-0.006%	-0.012%	-0.019%
2004	-0.001%	-0.003%	-0.007%	-0.014%
2011	-0.003%	-0.007%	-0.013%	-0.029%
2014	0.002%	0.003%	0.004%	0.002%

Appendix 7.2. Description of the Algorithm used for Standardising the Timing of Phenology Indices to use in Regression Analysis

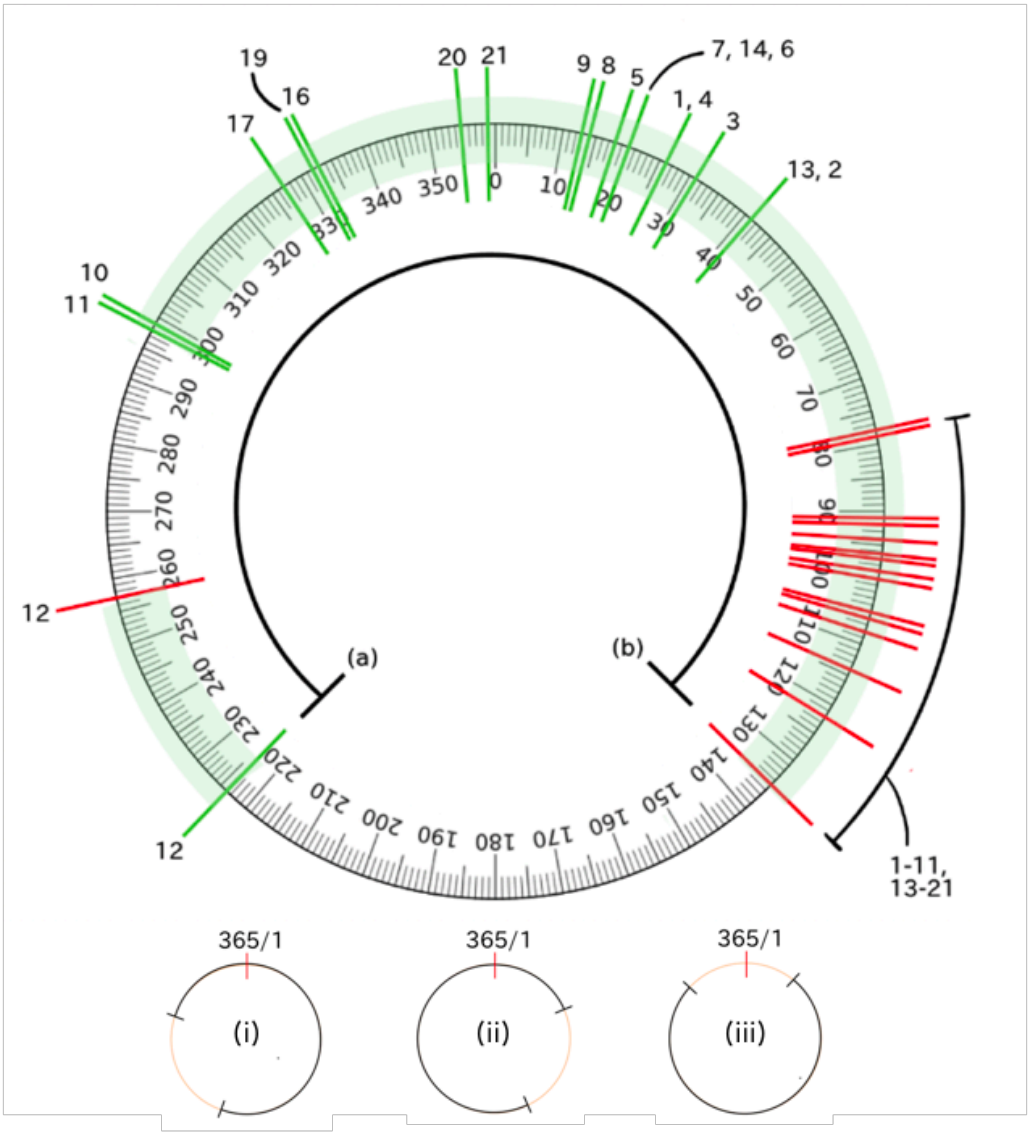

Figure 7.1. Diagram showing a single grid cell growing period variation over 21 temporal points. Green lines represent start dates and red lines represent end dates. The number of the line represents the climatology number, where 1 = 1998-1999, 2 = 1999-2000 etc. The thick green line represents the days where a growing period occurred at least once. (a) represents the start of the bloom variation and (b) represents the end of the bloom variation. The lower diagrams represent examples of where (i) dates from (a) to 365 are identified as "early"; (ii) values from 0 to (b) are considered late; and (iii) where the growing period variation lies within the calendar year.

The indices for the timing of initiation, maximum and termination have values ranging from 1 to -365 where 1 is the 1st of January and 365 is the 31st December. Due to the use of day of the year (DOY) to define these indices, the value for termination can be less than the value for the start date. For example: growing periods that end in December (334-356) could fluctuate into January (1-31). When calculating regression analysis care must be taken because the presence of these outliers can lead to erroneously large trends.

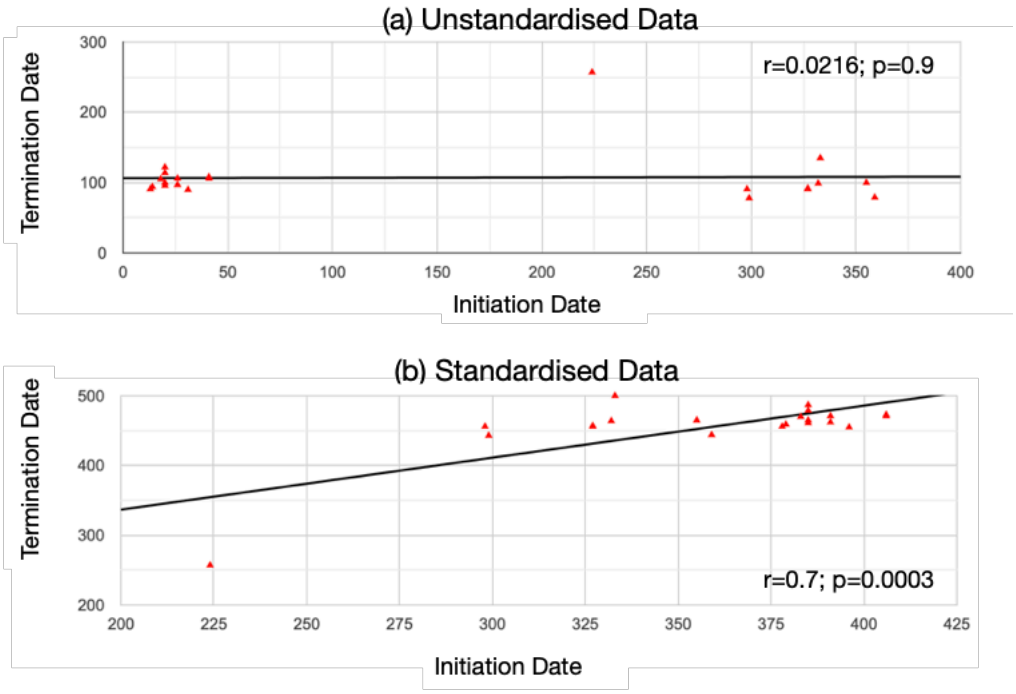

Figure 7.2. Scatter graphs with lines of best fit for initiation dates and termination dates at one grid cell. Correlation coefficient (r) is shown at the top of the graph alongside the p-value.

My algorithm for standardising the timing of the blooms focuses on identifying the bloom variation highlighted in green in Figure 1 ((a) - (b)). I create a binary variable (n=365) where 1 represents a DOY where a bloom is present in at least one biennial climatology and 0's highlights days of the year where blooms have not occurred during the time series. In Figure.7.1, I show an example bloom for our dataset. The linear calendar axis would suggest that the initiation dates in climatologies before 365 (Figure 7.2) are later than those after 365. However, it' is clear that the initiation dates prior to 365 should be defined as early, because the termination date of growing periods that start before 365 and after 0 occur within the same DOY range. Climatology number 12 is less obvious, however I resolve this by defining boundaries of the bloom variation as the largest number of consecutive 0's in this time series (b and a).

There are three possible variations of how blooms can present using this method (i,ii,iii). If a bloom occurs at days 365 and 1, values between (a) and 365 could represent early blooms, or values

between 1 and (b) could be late blooms. I define initiation and termination days between 1 and (b) as late, if the difference between 365 and (a) is greater than the distance between 0 and (b), and remove 365 from the DOY. If the difference between 365 and (a) is less than the distance between 0 and (b) then the values between 0 and (a) are considered early and 365 is added to the value of initiation and termination. If no bloom occurs at either 1 and/or 365, then no changes are made to the initiation or termination dates as the bloom timing variation fits within the calendar year. Finally, the timing of the maximum is corrected so that it is always later than initiation and earlier than termination at each point in the time series. Any pixels which had growing periods identified for every day of the year, due to high variability of the growing period across biennial time series, were removed from the dataset.

In Figure 7.2, I show plots of the date of initiation and termination for the uncorrected and corrected data. The relationship between initiation and termination date in the standardised dataset is mostly positive. Correcting the data results in a significant positive correlation between the timing of the initiation and termination. Although this trend is mostly driven by the lower left point, climatology number 12, trends driven by outliers are unavoidable unless removed. Regardless of how you define the end points of time in the dataset, this growing period will be considered an outlier because it occurs outside of the usual bloom variation. Correcting the datasets allows us to be confident that trends are a result of changes in the growing period, and not a result of using a linear time axis.

Appendix 7.3. Map of Regions used in Regional Analysis

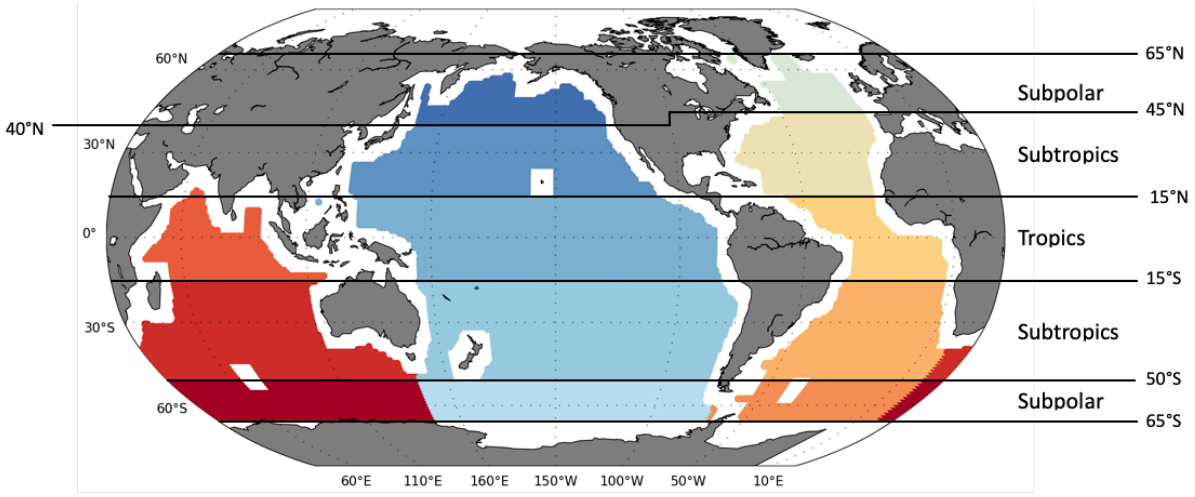

Figure 7.3. Map of 13 regions used for regional analysis in Chapter 3, 4 and 5. Latitudinal bands are split into five latitudinal bands at 65°N, 40/45°N, 15°N, 15°S, 50°S and 65°S. In the Southern Ocean, the Indian Ocean is defined as between 20° and 146°, the Pacific Ocean is between 147° and 289° and the Atlantic Ocean is between 290° and 20°.

Appendix 7.4. Density Plots of Phenological Indices

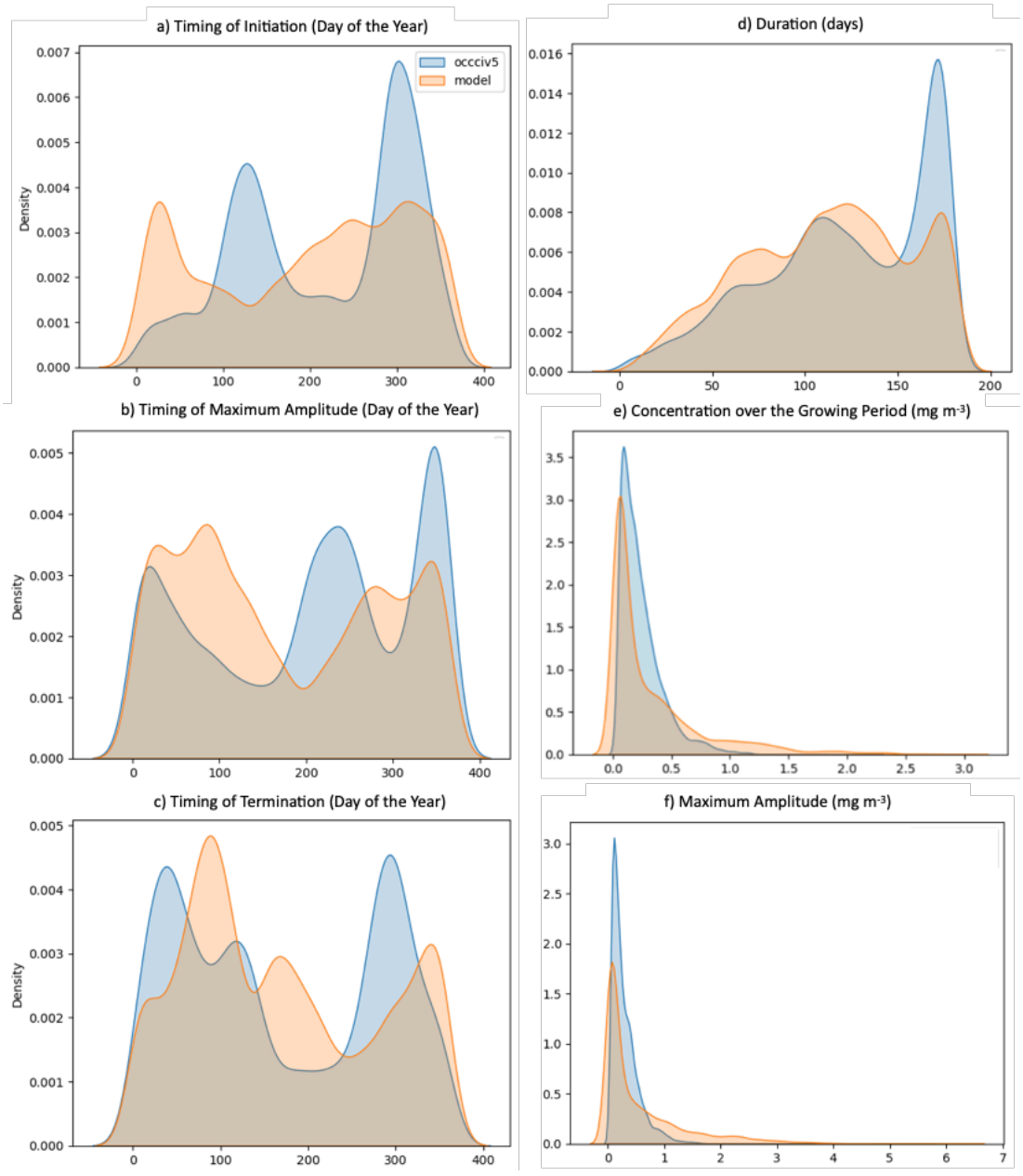

Figure 7.4. (a-e) Density plots of a) timing of initiation, b) timing of maximum amplitude, c) timing of termination, d) duration, e) chlorophyll concentration over the growing period and f) maximum amplitude of the growing period, in the OC-CCIv5 observations (blue) and the PlankTOM12.2 model (orange). Values taken from 1998-2020 climatology.

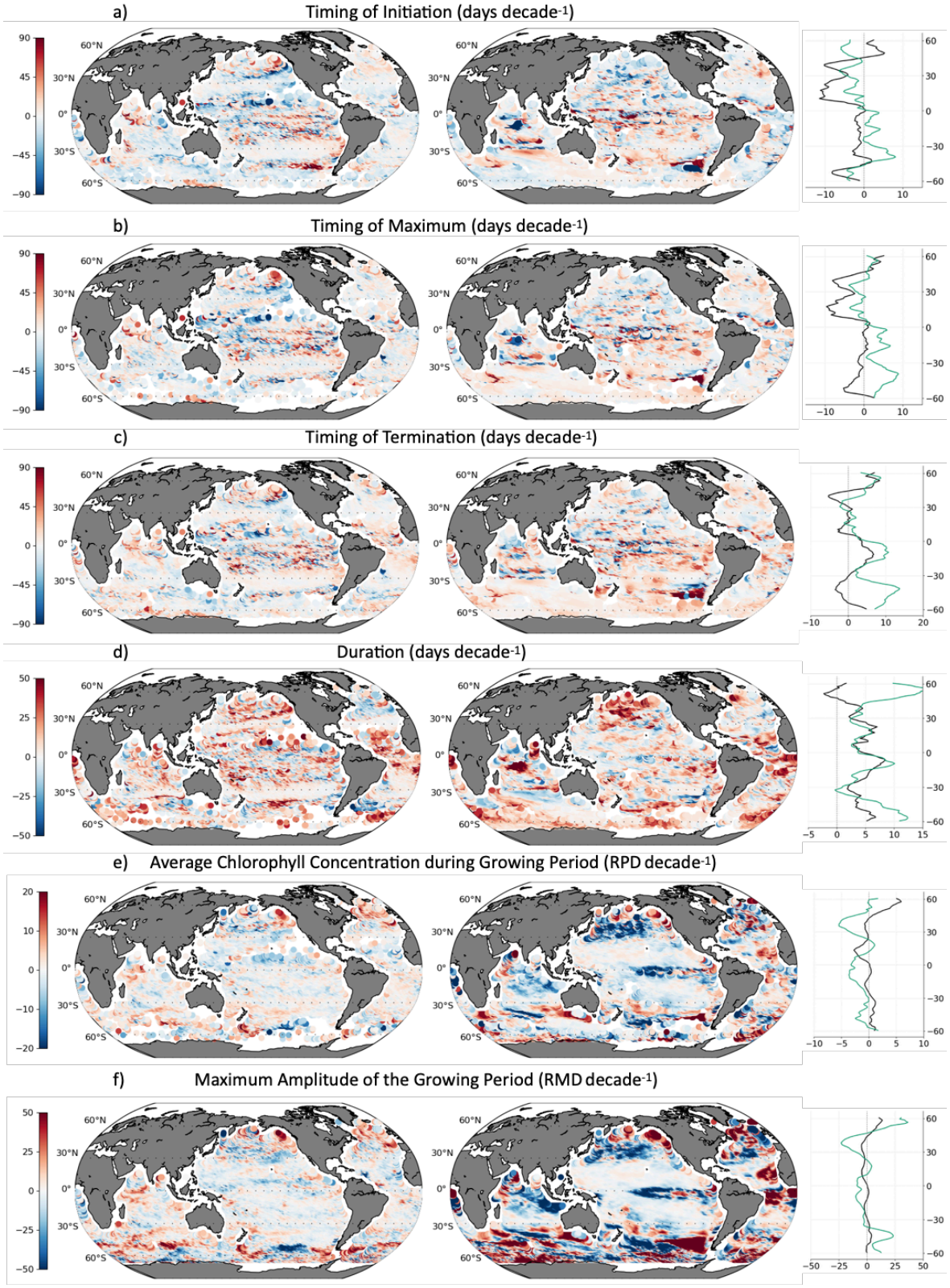

Figure 7.5. (a-f) Trends in phenology indices from OCCCIv5 (left) and PlankTOM12 (right). Trends calculated over 11 2-year climatologies (1998-2019). Right panel shows latitudinal averages smoothed by 10°, where the black line represents the observations and the green line represents PlankTOM12.2.

Appendix 7.5. Trends in Phenological Indices between 1998 and 2019

Appendix 7.6. Comparison of Regions 2000-2010 (used in thesis) and 1993-2013 (used in IPCC reports)

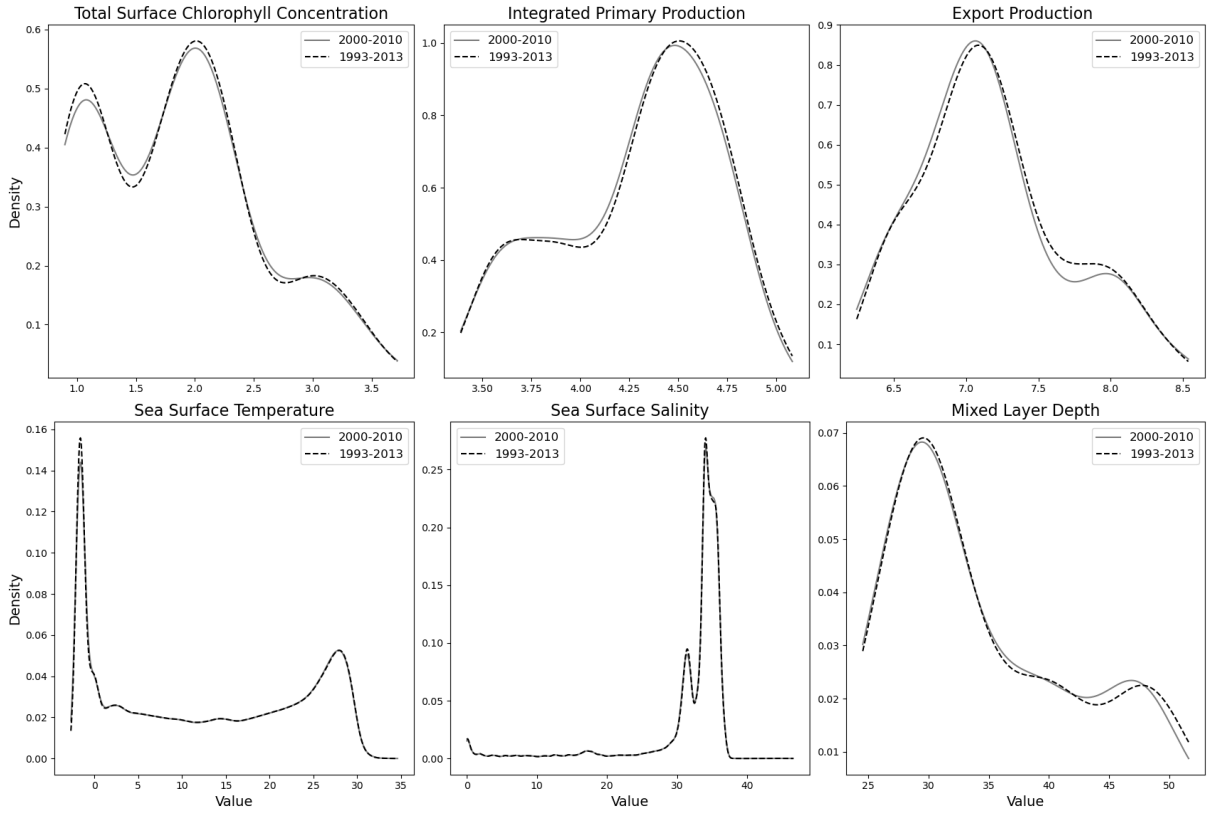

Figure 7.6. Kernel Density Estimation (KDE) Plots of Oceanographic Parameters for the Periods 2000-2010 and 1993-2013. Oceanographic parameters include: Total Surface Chlorophyll Concentration (mg m^{-3}); Integrated Primary Production in the upper 100 metres (mg m^{-2} d^{-1}); Export Production at 100 metres (mg m^{-2} d^{-1}); Sea Surface Temperature (°C); Sea Surface Salinity (PSU); and Mixed Layer Depth (metres). To account for strong negative skewness, Total Surface Chlorophyll, Integrated Primary Production, Export Production, and Mixed Layer Depth values are globally averaged. The grey solid lines denote the KDE plots for the period 2000-2010, while the black dashed lines represent the KDE plots for the period 1993-2013.

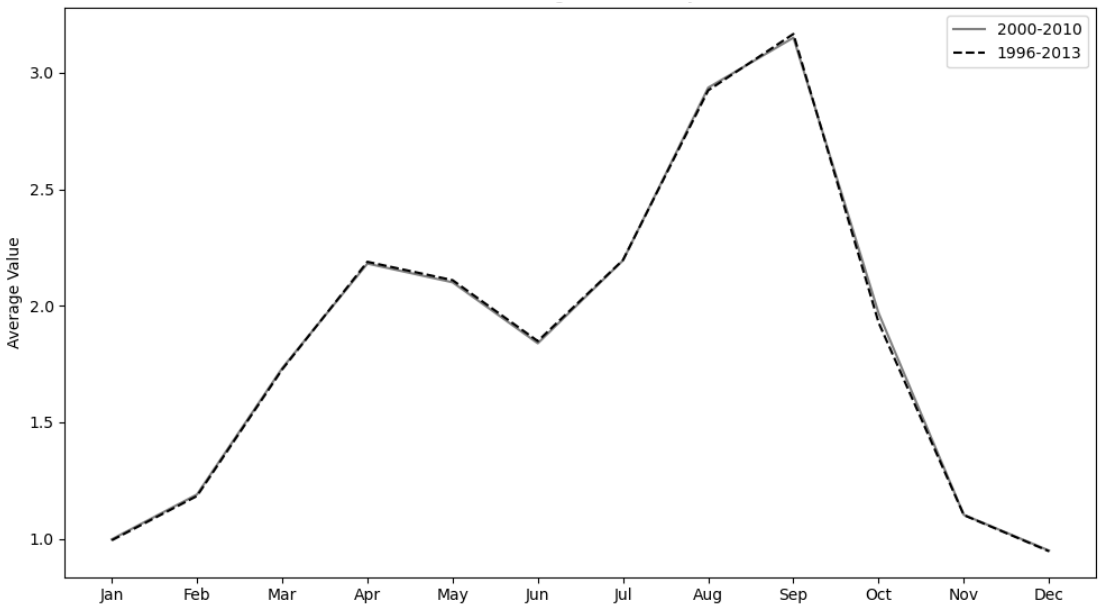

Figure 7.7. Global Average Chlorophyll Concentration (mg m-3) for the Periods 2000-2010 and 1996-2013. This figure presents the global average seasonal cycle of phytoplankton, illustrating the monthly averaged values over two periods: 2000-2010 and 1996-2013. The solid grey line represents the period 2000-2010, while the black dashed line represents the period 1996-2013.

Appendix 7.7. Relationship Between Changes in Net Primary Production (NPP) and Export Production (EP) for 2000-2010 vs. 2090-2100 under SSP3-7.0

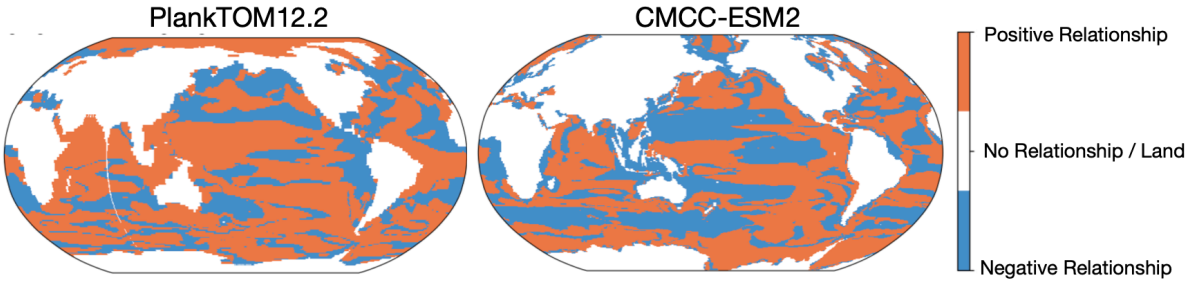

Figure 7.8. Relationship between change of net primary production (NPP) and export production (EP) at 100 metres between 2000-2010 and 2090-2100 under SSP3-7.0 for PlankTOM12.2 and CMCC-ESM2. Value is positive (orange) if NPP increases/decreases and EP increases/decreases between 2000-2010 and 2090-2100, respectively. The value is negative If NPP increases/decreases and EP decreases/increases between 2000-2010 and 2090-2100, respectively, it is a negative relationship.

Bibliography

Aiken, J., Hardman-Mountford, N.J., Barlow, R., Fishwick, J., Hirata, T., & Smyth, T. (2007). Functional links between bioenergetics and bio-optical traits of phytoplankton taxonomic groups: an overarching hypothesis with applications for ocean colour remote sensing. *Journal of Plankton Research, 30*, 165-181

Allen, J.I., & Polimene, L. (2011). Linking physiology to ecology: towards a new generation of plankton models. *Journal of Plankton Research, 33*, 989-997

Anderson, S.I., Barton, A.D., Clayton, S., Dutkiewicz, S., & Rynearson, T.A. (2021). Marine phytoplankton functional types exhibit diverse responses to thermal change. *Nat Commun, 12*, 6413

Andersson, B., Berglund, O., Filipsson, H.L., Kourtchenko, O., Godhe, A., Johannesson, K., Topel, M., Pinder, M.I.M., Hoepfner, L., & Rengefors, K. (2023). Strain-specific metabarcoding reveals rapid evolution of copper tolerance in populations of the coastal diatom Skeletonema marinoi. *Mol Ecol*

Andrews, O.D., Bindoff, N.L., Halloran, P.R., Ilyina, T., & Le Quéré, C. (2013). Detecting an external influence on recent changes in oceanic oxygen using an optimal fingerprinting method. *Biogeosciences, 10*, 1799-1813

Anglada-Ortiz, G., Zamelczyk, K., Meilland, J., Ziveri, P., Chierici, M., Fransson, A., & Rasmussen, T.L. (2021). Planktic Foraminiferal and Pteropod Contributions to Carbon Dynamics in the Arctic Ocean (North Svalbard Margin). *Frontiers in Marine Science, 8*

Archibald, A.T., O'Connor, F.M., Abraham, N.L., Archer-Nicholls, S., Chipperfield, M.P., Dalvi, M., Folberth, G.A., Dennison, F., Dhomse, S.S., Griffiths, P.T., Hardacre, C., Hewitt, A.J., Hill, R.S., Johnson, C.E., Keeble, J., Köhler, M.O., Morgenstern, O., Mulcahy, J.P., Ordóñez, C., Pope, R.J., Rumbold, S.T., Russo, M.R., Savage, N.H., Sellar, A., Stringer, M., Turnock, S.T., Wild, O., & Zeng, G. (2020). Description and evaluation of the UKCA stratosphere–troposphere chemistry scheme (StratTrop vn 1.0) implemented in UKESM1. *Geoscientific Model Development, 13*, 1223-1266

Archibald, K.M., Siegel, D.A., & Doney, S.C. (2019). Modeling the Impact of Zooplankton Diel Vertical Migration on the Carbon Export Flux of the Biological Pump. *Global Biogeochemical Cycles, 33*, 181-199

Ardyna, M., & Arrigo, K.R. (2020). Phytoplankton dynamics in a changing Arctic Ocean. *Nature Climate Change, 10*, 892-903

Ardyna, M., Claustre, H., Sallée, J.B., D'Ovidio, F., Gentili, B., van Dijken, G., D'Ortenzio, F., & Arrigo, K.R. (2017). Delineating environmental control of phytoplankton biomass and phenology in the Southern Ocean. *Geophysical Research Letters, 44*, 5016-5024

Arellano, B., & Rivas, D. (2019). Coastal upwelling will intensify along the Baja California coast under climate change by mid-21st century: Insights from a GCM-nested physical-NPZD coupled numerical ocean model. *Journal of Marine Systems, 199*

Armstrong McKay, D.I., Cornell, S.E., Richardson, K., & Rockström, J. (2021). Resolving ecological feedbacks on the ocean carbon sink in Earth system models. *Earth System Dynamics, 12*, 797-818

Asch, R.G., Stock, C.A., & Sarmiento, J.L. (2019). Climate change impacts on mismatches between phytoplankton blooms and fish spawning phenology. *Glob Chang Biol, 25*, 2544-2559

Barton, E.D., Torres, R., Figueiras, F.G., Gilcoto, M., & Largier, J. (2016). Surface water subduction during a downwelling event in a semienclosed bay. *Journal of Geophysical Research: Oceans, 121*, 7088-7107

Beaugrand, G., Conversi, A., Chiba, S., Edwards, M., Fonda-Umani, S., Greene, C., Mantua, N., Otto, S.A., Reid, P.C., Stachura, M.M., Stemmann, L., & Sugisaki, H. (2015a). Synchronous marine pelagic regime shifts in the Northern Hemisphere. *Philosophical Transactions of the Royal Society B: Biological Sciences, 370*

Beaugrand, G., Edwards, M., Raybaud, V., Goberville, E., & Kirby, R.R. (2015b). Future vulnerability of marine biodiversity compared with contemporary and past changes. *Nature Climate Change, 5*, 695-701

Bednaršek, N., Harvey, C.J., Kaplan, I.C., Feely, R.A., & Možina, J. (2016). Pteropods on the edge: Cumulative effects of ocean acidification, warming, and deoxygenation. *Progress in Oceanography, 145*, 1-24

Bednarsek, N., Tarling, G.A., Bakker, D.C., Fielding, S., & Feely, R.A. (2014). Dissolution dominating calcification process in polar pteropods close to the point of aragonite undersaturation. *PLoS One, 9*, e109183

Bednaršek, N., Tarling, G.A., Bakker, D.C.E., Fielding, S., Jones, E.M., Venables, H.J., Ward, P., Kuzirian, A., Lézé, B., Feely, R.A., & Murphy, E.J. (2012). Extensive dissolution of live pteropods in the Southern Ocean. *Nature Geoscience, 5*, 881-885

Behrenfeld, M.J. (2010). Abandoning Sverdrup's Critical Depth Hypothesis on phytoplankton blooms. *Ecology, 91*, 977-989

Behrenfeld, M.J. (2014). Climate-mediated dance of the plankton. *Nature Climate Change, 4*, 880-887

Behrenfeld, M.J., Doney, S.C., Lima, I., Boss, E.S., & Siegel, D.A. (2013). Annual cycles of ecological disturbance and recovery underlying the subarctic Atlantic spring plankton bloom. *Global Biogeochemical Cycles, 27*, 526-540

Behrenfeld, M.J., O'Malley, R.T., Boss, E.S., Westberry, T.K., Graff, J.R., Halsey, K.H., Milligan, A.J., Siegel, D.A., & Brown, M.B. (2015). Revaluating ocean warming impacts on global phytoplankton. *Nature Climate Change, 6*, 323-330

Behrenfeld, M.J., O'Malley, R.T., Siegel, D.A., McClain, C.R., Sarmiento, J.L., Feldman, G.C., Milligan, A.J., Falkowski, P.G., Letelier, R.M., & Boss, E.S. (2006). Climate-driven trends in contemporary ocean productivity. *Nature, 444*, 752-755

Benner, R., & Amon, R.M. (2015). The size-reactivity continuum of major bioelements in the ocean. *Ann Rev Mar Sci, 7*, 185-205

Bindoff, N.L., Cheung, W.W.L., & Kairo, J.G. (2019). Changing Ocean, Marine Ecosystems, and Dependent Communities. *The Ocean and Cryosphere in a Changing Climate* (pp. 447-588)

Bopp, L., Lévy, M., Resplandy, L., & Sallée, J.B. (2015). Pathways of anthropogenic carbon subduction in the global ocean. *Geophysical Research Letters, 42*, 6416-6423

Bopp, L., Resplandy, L., Orr, J.C., Doney, S.C., Dunne, J.P., Gehlen, M., Halloran, P., Heinze, C., Ilyina, T., Séférian, R., Tjiputra, J., & Vichi, M. (2013). Multiple stressors of ocean ecosystems in the 21st century: projections with CMIP5 models. *Biogeosciences, 10*, 6225-6245

Boscolo-Galazzo, F., Crichton, K.A., Barker, S., & Pearson, P.N. (2018). Temperature dependency of metabolic rates in the upper ocean: A positive feedback to global climate change? *Global and Planetary Change, 170*, 201-212

Boyd, P.W., Claustre, H., Levy, M., Siegel, D.A., & Weber, T. (2019). Multi-faceted particle pumps drive carbon sequestration in the ocean. *Nature, 568*, 327-335

Bramucci, A.R., Labeeuw, L., Orata, F.D., Ryan, E.M., Malmstrom, R.R., & Case, R.J. (2018). The Bacterial Symbiont Phaeobacter inhibens Shapes the Life History of Its Algal Host Emiliania huxleyi. *Frontiers in Marine Science, 5*

Bristow, L.A., Mohr, W., Ahmerkamp, S., & Kuypers, M.M.M. (2017). Nutrients that limit growth in the ocean. *Curr Biol, 27*, R474-R478

Brody, S.R., Lozier, M.S., & Dunne, J.P. (2013). A comparison of methods to determine phytoplankton bloom initiation. *Journal of Geophysical Research: Oceans, 118*, 2345-2357

Brownlee, C., Langer, G., & Wheeler, G.L. (2021). Coccolithophore calcification: Changing paradigms in changing oceans. *Acta Biomater, 120*, 4-11

Buesseler, K.O., Antia, A.N., Chen, M., Fowler, S.W., Gardner, W.D., Gustafsson, O., Harada, K., Michaels, A.F., van der Loeff, M.R., Sarin, M., Steinberg, D.K., & Trull, T.W. (2007). An assessment of the use of sediment traps for estimating upper ocean particle fluxes. *Journal of Marine Research, 65*, 345–416

Buesseler, K.O., Steinberg, D.K., Michaels, A.F., Johnson, R.J., Andrews, J.E., Valdes, J., & Price, J.F. (2000). A comparison of the quatity and composition of material caught in a neutrally bouyant versus surface-tethered sediment trap. *Deep Sea Research Part I: Oceanographic Research Papers, 47*, 227-294

Buitenhuis, E., Guest, J., K., Wright, R.M., Townsend, P., & Le Quere, C. (2023). Description of the PlankTOM Equations (PlankTOM12.2). *Zenodo*

Buitenhuis, E.T., Hashioka, T., & Quéré, C.L. (2013a). Combined constraints on global ocean primary production using observations and models. *Global Biogeochemical Cycles, 27*, 847-858

Buitenhuis, E.T., Le Quéré, C., Bednaršek, N., & Schiebel, R. (2019). Large Contribution of Pteropods to Shallow CaCO3 Export. *Global Biogeochemical Cycles, 33*, 458-468

Buitenhuis, E.T., Vogt, M., Moriarty, R., Bednaršek, N., Doney, S.C., Leblanc, K., Le Quéré, C., Luo, Y.W., O'Brien, C., O'Brien, T., Peloquin, J., Schiebel, R., & Swan, C. (2013b). MAREDAT: towards a world atlas of MARine Ecosystem DATa. *Earth System Science Data, 5*, 227-239

Cael, B.B., Bisson, K., Boss, E., Dutkiewicz, S., & Henson, S. (2023). Global climate-change trends detected in indicators of ocean ecology. *Nature, 619*, 551-554

Cael, B.B., Bisson, K., & Follows, M.J. (2017). How have recent temperature changes affected the efficiency of ocean biological carbon export? *Limnology and Oceanography Letters, 2*, 113-118

Cael, B.B., Moore, M., C., Guest, J., K., Jarníková, T., Mouw, C.B., Bowler, C., Mawji, E., Henson, S., & Le Quéré, C. (in revision). A global ocean opal ballasting-silica relationship. *manuscript submitted*

Cai, W., Santoso, A., Wang, G., Yeh, S.-W., An, S.-I., Cobb, K.M., Collins, M., Guilyardi, E., Jin, F.-F., Kug, J.-S., Lengaigne, M., McPhaden, M.J., Takahashi, K., Timmermann, A., Vecchi, G., Watanabe, M., & Wu, L. (2015). ENSO and greenhouse warming. *Nature Climate Change, 5*, 849-859

Canadell, J.G., Monteiro, P.M.S., Costa, M.H., Da Cunha, L.C., Cox, P.M., Elisev, A.V., Henson, S., Ishii, M., Jaccard, S.L., Koven, C., & al., e. (2021). Global Carbon and other Biogeochemical Cycles and Feedbacks. *IPCC AR6 WGI, Final Government Distribution, chapter 5, 2021.*

Carroll, D., Menemenlis, D., Adkins, J.F., Bowman, K.W., Brix, H., Dutkiewicz, S., Fenty, I., Gierach, M.M., Hill, C., Jahn, O., Landschützer, P., Lauderdale, J.M., Liu, J., Manizza, M., Naviaux, J.D., Rödenbeck, C., Schimel, D.S., Van der Stocken, T., & Zhang, H. (2020). The ECCO-Darwin Data-Assimilative Global Ocean Biogeochemistry Model: Estimates of Seasonal to Multidecadal Surface Ocean pCO2 and Air-Sea CO2 Flux. *Journal of Advances in Modeling Earth Systems, 12*

Cavan, E.L., Le Moigne, F.A.C., Poulton, A.J., Tarling, G.A., Ward, P., Daniels, C.J., Fragoso, G.M., & Sanders, R.J. (2015). Attenuation of particulate organic carbon flux in the Scotia Sea, Southern Ocean, is controlled by zooplankton fecal pellets. *Geophysical Research Letters, 42*, 821-830

Chen, B. (2015). Patterns of thermal limits of phytoplankton. *Journal of Plankton Research, 37*, 285-292

Cheng, L., Abraham, J., Hausfather, Z., & Trenberth, K.E. (2019). How fast are the oceans warming? *Science, 363*

Cheng, L., Abraham, J., Zhu, J., Trenberth, K.E., Fasullo, J., Boyer, T., Locarnini, R., Zhang, B., Yu, F., Wan, L., Chen, X., Song, X., Liu, Y., & Mann, M.E. (2020). Record-Setting Ocean Warmth Continued in 2019. *Advances in Atmospheric Sciences, 37*, 137-142

Cherkasheva, A., Bracher, A., Melsheimer, C., Köberle, C., Gerdes, R., Nöthig, E.M., Bauerfeind, E., & Boetius, A. (2014). Influence of the physical environment on polar phytoplankton blooms: A case study in the Fram Strait. *Journal of Marine Systems, 132*, 196-207

Chevin, L.M., Lande, R., & Mace, G.M. (2010). Adaptation, plasticity, and extinction in a changing environment: towards a predictive theory. *PLoS Biol, 8*, e1000357

Chiswell, S.M. (2011). Annual cycles and spring blooms in phytoplankton: don't abandon Sverdrup completely. *Marine Ecology Progress Series, 443*, 39-50

Chivers, W.J., Edwards, M., Hays, G.C., & Dong, Y. (2020). Phenological shuffling of major marine phytoplankton groups over the last six decades. *Diversity and Distributions, 26*, 536-548

Clerc, C., Bopp, L., Benedetti, F., Vogt, M., & Aumont, O. (2023). Including filter-feeding gelatinous macrozooplankton in a global marine biogeochemical model: model–data comparison and impact on the ocean carbon cycle. *Biogeosciences, 20*, 869-895

Collins, S., Rost, B., & Rynearson, T.A. (2014). Evolutionary potential of marine phytoplankton under ocean acidification. *Evol Appl, 7*, 140-155

Cooley, S., Schoeman, D.S., Bopp, L., Boyd, P.W., Donner, S., Ghebrehiwet, D.Y., Ito, S.-I., Kiessling, W., Martinetto, P., Ojea, E., Racault, M.F., Rost, B., & Skern-Mauritzen, M. (2022). Ocean and Coastal Ecosystems and their Services. In: Climate Change 2022: Impacts, Adaptation, and Vulnerability. Contribution of Working Group II to the Sixth Assessment Report of the Intergovernmental Panel on Climate Change. *[H.-O. Pörtner, D.C. Roberts, M. Tignor, E.S. Poloczanska, K. Mintenbeck, A. Alegría, M. Craig, S. Langsdorf, S. Löschke, V. Möller, A. Okem, B. Rama (eds.)].* (pp. 379-550). UK and New York, NY, USA: Cambridge University Press

Cushing, D.H. (1959). The seasonal variation in oceanic production as a problem in population dynamics. *ICES Journal of Marine Science, 24*, 455-464

Cushing, D.H. (1990). Plankton Production and Year-class Strength in Fish Populations: an Update of the Match/Mismatch Hypothesis. *Advances in Marine Biology Volume 26* (pp. 249-293)

Dall'Olmo, G., Dingle, J., Polimene, L., Brewin, R.J., & Claustre, H. (2016). Substantial energy input to the mesopelagic ecosystem from the seasonal mixed-layer pump. *Nat Geosci, 9*, 820-823

Daufresne, M., Lengfellner, K., & Sommer, U. (2009). <Daufresne et al. - 2009 - Global warming benefits the small in aquatic ecosy.pdf>. *Proc Natl Acad Sci U S A, 106*, 12788–12793

de Melo Virissimo, F., Martin, A.P., & Henson, S.A. (2022). Influence of Seasonal Variability in Flux Attenuation on Global Organic Carbon Fluxes and Nutrient Distributions. *Global Biogeochem Cycles, 36*, e2021GB007101

Denvil-Sommer, A., Buitenhuis, E.T., Kiko, R., Lombard, F., Guidi, L., & Le Quéré, C. (2023). Testing the reconstruction of modelled particulate organic carbon from surface ecosystem components using PlankTOM12 and machine learning. *Geoscientific Model Development, 16*, 2995-3012

DeVries, T., Primeau, F., & Deutsch, C. (2012). The sequestration efficiency of the biological pump. *Geophysical Research Letters, 39*

Dezutter, T., Lalande, C., Dufresne, C., Darnis, G., & Fortier, L. (2019). Mismatch between microalgae and herbivorous copepods due to the record sea ice minimum extent of 2012 and the late sea ice break-up of 2013 in the Beaufort Sea. *Progress in Oceanography, 173*, 66-77

Doney, S.C., Fabry, V.J., Feely, R.A., & Kleypas, J.A. (2009). Ocean acidification: the other CO2 problem. *Ann Rev Mar Sci, 1*, 169-192

Dorantes-Gilardi, M., & Rivas, D. (2019). Effects of the 2013–2016 Northeast Pacific warm anomaly on physical and biogeochemical variables off northwestern Baja California, derived from a numerical NPZD ocean model. *Deep Sea Research Part II: Topical Studies in Oceanography, 169-170*

Ducklow, H.W., Steinberg, D.K., & Buesseler, K.O. (2001). Upper Ocean Carbon Export and the Biological Pump. *Oceanography, 14*, 50-58

Dunne, J.P., Armstrong, R.A., Gnanadesikan, A., & Sarmiento, J.L. (2005). Empirical and mechanistic models for the particle export ratio. *Global Biogeochemical Cycles, 19*

Dutkiewicz, S., Morris, J.J., Follows, M.J., Scott, J., Levitan, O., Dyhrman, S.T., & Berman-Frank, I. (2015). Impact of ocean acidification on the structure of future phytoplankton communities. *Nature Climate Change, 5*, 1002-1006

Edwards, M., & Richardson, A.J. (2004). Impact of climate change on marine pelagic phenolo. *Nature, 430*, 881-884

Feng, Y., Roleda, M.Y., Armstrong, E., Law, C.S., Boyd, P.W., & Hurd, C.L. (2018). Environmental controls on the elemental composition of a Southern Hemisphere strain of the coccolithophore <i>Emiliania huxleyi</i&gt. *Biogeosciences, 15*, 581-595

Fernandez-Gonzalez, C., Perez-Lorenzo, M., Pratt, N., Moore, C.M., Bibby, T.S., & Maranon, E. (2020). Effects of Temperature and Nutrient Supply on Resource Allocation, Photosynthetic Strategy, and Metabolic Rates of Synechococcus sp. *J Phycol, 56*, 818-829

Ferreira, A.S.A., Neuheimer, A.B., Durant, J.M., & Robert, D. (2023). Impacts of the match-mismatch hypothesis across three trophic levels—a case study in the North Sea. *ICES Journal of Marine Science, 80*, 308-316

Field, C.B., Behrenfeld, M.J., Randerson, J.T., & Falkowski, P.G. (1998). Primary Production of the Biosphere: Integrating Terrestrial and Oceanic Components. *Science, 281*, 237-240

Fisher, N.L., Campbell, D.A., Hughes, D.J., Kuzhiumparambil, U., Halsey, K.H., Ralph, P.J., & Suggett, D.J. (2020). Divergence of photosynthetic strategies amongst marine diatoms. *PLoS One, 15*, e0244252

Fisher, N.L., & Halsey, K.H. (2016). Mechanisms that increase the growth efficiency of diatoms in low light. *Photosynth Res, 129*, 183-197

Flemming, H.C., & Wuertz, S. (2019). Bacteria and archaea on Earth and their abundance in biofilms. *Nat Rev Microbiol, 17*, 247-260

Flores, E., Romanovicz, D.K., Nieves-Morion, M., Foster, R.A., & Villareal, T.A. (2022). Adaptation to an Intracellular Lifestyle by a Nitrogen-Fixing, Heterocyst-Forming Cyanobacterial Endosymbiont of a Diatom. *Front Microbiol, 13*, 799362

Fox-Kemper, B., Hewitt, H.T., Xiao, C., Aðalgeirsdóttir, G., Drijfhout, S.S., Edwards, T.L., Golledge, N.R., Hemer, M., Kopp, R.E., Krinner, G., Mix, A.C., Notz, D., Nowicki, S., Nurhati, I.S., Ruiz, L., Sallée, J.B., Slangen, A.B.A., & Yu, Y. (2023). Ocean, Cryosphere and Sea Level Change. In V. Masson-Delmotte, P. Zhai, A. Pirani, S.L. Connors, C. Péan, S. Berger, N. Caud, Y. Chen, L. Goldfarb, M.I. Gomis, M. Huang, K. Leitzell, E. Lonnoy, J.B.R. Matthews, T.K. Maycock, T. Waterfield, O. Yelekçi, R. Yu, & B. Zhou (Eds.), *In Climate Change 2021: The Physical Science Basis. Contribution of Working Group I to the Sixth Assessment Report of the*

Intergovernmental Panel on Climate Change (pp. 1211-1362). Cambridge, United Kingdom and New York, NY, USA.: Cambridge University Press

Frankignoulle, M., Canon, C., & Gattuso, J.P. (2003). Marine calcification as a source of carbon dioxide: Positive feedback of increasing atmospheric CO2. *Limnology and Oceanography, 39*, 458-462

Friedland, K.D., Mouw, C.B., Asch, R.G., Ferreira, A.S.A., Henson, S., Hyde, K.J.W., Morse, R.E., Thomas, A.C., & Brady, D.C. (2018). Phenology and time series trends of the dominant seasonal phytoplankton bloom across global scales. *Global Ecology and Biogeography, 27*, 551-569

Friedlingstein, P., O'Sullivan, M., Jones, M.W., Andrew, R.M., Gregor, L., Hauck, J., Le Quéré, C., Luijkx, I.T., Olsen, A., Peters, G.P., Peters, W., Pongratz, J., Schwingshackl, C., Sitch, S., Canadell, J.G., Ciais, P., Jackson, R.B., Alin, S.R., Alkama, R., Arneth, A., Arora, V.K., Bates, N.R., Becker, M., Bellouin, N., Bittig, H.C., Bopp, L., Chevallier, F., Chini, L.P., Cronin, M., Evans, W., Falk, S., Feely, R.A., Gasser, T., Gehlen, M., Gkritzalis, T., Gloege, L., Grassi, G., Gruber, N., Gürses, Ö., Harris, I., Hefner, M., Houghton, R.A., Hurtt, G.C., Iida, Y., Ilyina, T., Jain, A.K., Jersild, A., Kadono, K., Kato, E., Kennedy, D., Klein Goldewijk, K., Knauer, J., Korsbakken, J.I., Landschützer, P., Lefèvre, N., Lindsay, K., Liu, J., Liu, Z., Marland, G., Mayot, N., McGrath, M.J., Metzl, N., Monacci, N.M., Munro, D.R., Nakaoka, S.-I., Niwa, Y., O'Brien, K., Ono, T., Palmer, P.I., Pan, N., Pierrot, D., Pocock, K., Poulter, B., Resplandy, L., Robertson, E., Rödenbeck, C., Rodriguez, C., Rosan, T.M., Schwinger, J., Séférian, R., Shutler, J.D., Skjelvan, I., Steinhoff, T., Sun, Q., Sutton, A.J., Sweeney, C., Takao, S., Tanhua, T., Tans, P.P., Tian, X., Tian, H., Tilbrook, B., Tsujino, H., Tubiello, F., van der Werf, G.R., Walker, A.P., Wanninkhof, R., Whitehead, C., Willstrand Wranne, A., Wright, R., Yuan, W., Yue, C., Yue, X., Zaehle, S., Zeng, J., & Zheng, B. (2022). Global Carbon Budget 2022. *Earth System Science Data, 14*, 4811-4900

Fu, W., Primeau, F., Keith Moore, J., Lindsay, K., & Randerson, J.T. (2018). Reversal of Increasing Tropical Ocean Hypoxia Trends With Sustained Climate Warming. *Global Biogeochemical Cycles, 32*, 551-564

Fu, W., Randerson, J.T., & Moore, J.K. (2016). Climate change impacts on net primary production (NPP) and export production (EP) regulated by increasing

stratification and phytoplankton community structure in the CMIP5 models. *Biogeosciences, 13*, 5151-5170

Gardes, A., Iversen, M.H., Grossart, H.P., Passow, U., & Ullrich, M.S. (2011). Diatom-associated bacteria are required for aggregation of Thalassiosira weissflogii. *ISME J, 5*, 436-445

Gardner, J., Manno, C., Bakker, D.C.E., Peck, V.L., & Tarling, G.A. (2018). Southern Ocean pteropods at risk from ocean warming and acidification. *Mar Biol, 165*, 8

Gidden, M.J., Riahi, K., Smith, S.J., Fujimori, S., Luderer, G., Kriegler, E., van Vuuren, D.P., van den Berg, M., Feng, L., Klein, D., Calvin, K., Doelman, J.C., Frank, S., Fricko, O., Harmsen, M., Hasegawa, T., Havlik, P., Hilaire, J., Hoesly, R., Horing, J., Popp, A., Stehfest, E., & Takahashi, K. (2019). Global emissions pathways under different socioeconomic scenarios for use in CMIP6: a dataset of harmonized emissions trajectories through the end of the century. *Geoscientific Model Development, 12*, 1443-1475

Giering, S.L.C., Cavan, E.L., Basedow, S.L., Briggs, N., Burd, A.B., Darroch, L.J., Guidi, L., Irisson, J.-O., Iversen, M.H., Kiko, R., Lindsay, D., Marcolin, C.R., McDonnell, A.M.P., Möller, K.O., Passow, U., Thomalla, S., Trull, T.W., & Waite, A.M. (2020). Sinking Organic Particles in the Ocean—Flux Estimates From in situ Optical Devices. *Frontiers in Marine Science, 6*

Gittings, J.A., Raitsos, D.E., Brewin, R.J.W., & Hoteit, I. (2021). Links between Phenology of Large Phytoplankton and Fisheries in the Northern and Central Red Sea. *Remote Sensing, 13*

Gittings, J.A., Raitsos, D.E., Krokos, G., & Hoteit, I. (2018). Impacts of warming on phytoplankton abundance and phenology in a typical tropical marine ecosystem. *Sci Rep, 8*, 2240

Gleich, S.J., Plough, L.V., & Glibert, P.M. (2020). Photosynthetic efficiency and nutrient physiology of the diatom Thalassiosira pseudonana at three growth temperatures. *Marine Biology, 167*

Gregg, W.W., Conkright, M.E., Ginoux, P., O'Reilly, J.E., & Casey, N.W. (2003). Ocean primary production and climate: Global decadal changes. *Geophysical Research Letters, 30*

Gregg, W.W., & Rousseaux, C.S. (2019). Global ocean primary production trends in the modern ocean color satellite record (1998–2015). *Environmental Research Letters, 14*

Gregg, W.W., Rousseaux, C.S., & Franz, B.A. (2017). Global trends in ocean phytoplankton: a new assessment using revised ocean colour data. *Remote Sens Lett, 8*, 1102-1111

Gregory, B., Christophe, L., & Martin, E. (2009). Rapid biogeographical plankton shifts in the North Atlantic Ocean. *Global Change Biology, 15*, 1790-1803

Griffith, E.M., Thomas, E., Lewis, A.R., Penman, D.E., Westerhold, T., & Winguth, A.M.E. (2021). Bentho-Pelagic Decoupling: The Marine Biological Carbon Pump During Eocene Hyperthermals. *Paleoceanography and Paleoclimatology, 36*

Guidi, L., Chaffron, S., Bittner, L., Eveillard, D., Larhlimi, A., Roux, S., Darzi, Y., Audic, S., Berline, L., Brum, J., Coelho, L.P., Espinoza, J.C.I., Malviya, S., Sunagawa, S., Dimier, C., Kandels-Lewis, S., Picheral, M., Poulain, J., Searson, S., Tara Oceans, c., Stemmann, L., Not, F., Hingamp, P., Speich, S., Follows, M., Karp-Boss, L., Boss, E., Ogata, H., Pesant, S., Weissenbach, J., Wincker, P., Acinas, S.G., Bork, P., de Vargas, C., Iudicone, D., Sullivan, M.B., Raes, J., Karsenti, E., Bowler, C., & Gorsky, G. (2016). Plankton networks driving carbon export in the oligotrophic ocean. *Nature, 532*, 465-470

Guidi, L., Stemmann, L., Jackson, G.A., Ibanez, F., Claustre, H., Legendre, L., Picheral, M., & Gorskya, G. (2009). Effects of phytoplankton community on production, size, and export of large aggregates: A world-ocean analysis. *Limnology and Oceanography, 54*, 1951-1963

Guo, K., Chen, J., Yuan, J., Wang, X., Xu, S., Hou, S., & Wang, Y. (2022). Effects of Temperature on Transparent Exopolymer Particle Production and Organic Carbon Allocation of Four Marine Phytoplankton Species. *Biology (Basel), 11*

Hauck, J., & Volker, C. (2015). Rising atmospheric CO(2) leads to large impact of biology on Southern Ocean CO(2) uptake via changes of the Revelle factor. *Geophys Res Lett, 42*, 1459-1464

Heinle, A., & Slawig, T. (2013). Impact of parameter choice on the dynamics of NPZD type ecosystem models. *Ecological Modelling, 267*, 93-101

Heinze, C. (2004). Simulating oceanic CaCO3 export production in the greenhouse. *Geophysical Research Letters, 31*

Heinze, C., Meyer, S., Goris, N., Anderson, L., Steinfeldt, R., Chang, N., Le Quéré, C., & Bakker, D.C.E. (2015). The ocean carbon sink – impacts, vulnerabilities and challenges. *Earth System Dynamics, 6*, 327-358

Helm, K.P., Bindoff, N.L., & Church, J.A. (2011). Observed decreases in oxygen content of the global ocean. *Geophysical Research Letters, 38*, n/a-n/a

Henson, S., Cole, H., Beaulieu, C., & Yool, A. (2013). The impact of global warming on seasonality of ocean primary production. *Biogeosciences, 10*, 4357-4369

Henson, S., Le Moigne, F., & Giering, S. (2019). Drivers of Carbon Export Efficiency in the Global Ocean. *Global Biogeochem Cycles, 33*, 891-903

Henson, S.A., Beaulieu, C., Ilyina, T., John, J.G., Long, M., Seferian, R., Tjiputra, J., & Sarmiento, J.L. (2017). Rapid emergence of climate change in environmental drivers of marine ecosystems. *Nat Commun, 8*, 14682

Henson, S.A., Cael, B.B., Allen, S.R., & Dutkiewicz, S. (2021). Future phytoplankton diversity in a changing climate. *Nat Commun, 12*, 5372

Henson, S.A., Cole, H.S., Hopkins, J., Martin, A.P., & Yool, A. (2018). Detection of climate change-driven trends in phytoplankton phenology. *Glob Chang Biol, 24*, e101-e111

Henson, S.A., Laufkötter, C., Leung, S., Giering, S.L.C., Palevsky, H.I., & Cavan, E.L. (2022). Uncertain response of ocean biological carbon export in a changing world. *Nature Geoscience, 15*, 248-254

Henson, S.A., Sanders, R., & Madsen, E. (2012). Global patterns in efficiency of particulate organic carbon export and transfer to the deep ocean. *Global Biogeochemical Cycles, 26*

Henson, S.A., Yool, A., & Sanders, R. (2015). Variability in efficiency of particulate organic carbon export: A model study. *Global Biogeochemical Cycles, 29*, 33-45

Hersbach, H., Bell, B., Berrisford, P., Hirahara, S., Horányi, A., Muñoz-Sabater, J., Nicolas, J., Peubey, C., Radu, R., Schepers, D., Simmons, A., Soci, C., Abdalla, S., Abellan, X., Balsamo, G., Bechtold, P., Biavati, G., Bidlot, J., Bonavita, M., De Chiara, G., Dahlgren, P., Dee, D., Diamantakis, M., Dragani, R., Flemming, J., Forbes, R., Fuentes, M., Geer, A., Haimberger, L., Healy, S., Hogan, R.J., Hólm, E., Janisková, M., Keeley, S., Laloyaux, P., Lopez, P., Lupu, C., Radnoti, G., de Rosnay, P., Rozum, I., Vamborg, F., Villaume, S., & Thépaut, J.N. (2020). The ERA5 global reanalysis. *Quarterly Journal of the Royal Meteorological Society, 146*, 1999-2049

Hoegh-Guldberg, O., Jacob , D., Bindi , M., Brown , S., Camilloni , I., Diedhiou , A., Djalante , R., Ebi , K., Engelbrecht , F., Guiot , J., Hijioka , Y., Mehrotra , S., Payne , A., Seneviratne , S.I., Thomas , A., Warren , R., Zhou , G., Halim , S.A., Achlatis , M., Alexander , L.V., Allen , M., Berry , P., Boyer , C., Byers , E., Brilli , L., Buckeridge , M., Cheung , W., Craig , M., Ellis , N., Evans , J., Fischer , H., Fraedrich , K., Fuss , S., Ganase , A., Gattuso , J.P., Greve , P., Bolaños , T.G., Hanasaki , N., Hasegawa , T., Hayes , K., Hirsch , A., Jones , C., Jung , T., Kanninen , M., Krinner , G., Lawrence , D., Lenton , T., Ley , D., Liverman , D., Mahowald , N., McInnes , K., Meissner , K.J., Millar , R., Mintenbeck , K., Mitchell , D., Mix , A.C., Notz , D., Nurse , L., Okem , A., Olsson , L., Oppenheimer , M., Paz , S., Petersen , J., Petzold , J., Preuschmann , S., Rahman , M.F., Rogelj , J., Scheuffele , H., Schleussner , C.-F., Scott , D., Séférian , R., Sillmann , J., Singh , C., Slade , R., Stephenson , K., Stephenson , T., Sylla , M.B., Tebboth , M., Tschakert , P., Vautard , R., Wartenburger , R., Wehner , M., Weyer , N.M., Whyte , F., Yohe , G., Zhang , X., & Zougmoré , R.B. (2018). Impacts of 1.5°C Global Warming on Natural and Human systems

Hofmann, G.E., Barry, J.P., Edmunds, P.J., Gates, R.D., Hutchins, D.A., Klinger, T., & Sewell, M.A. (2010). The Effect of Ocean Acidification on Calcifying Organisms in Marine Ecosystems: An Organism-to-Ecosystem Perspective. *Annual Review of Ecology, Evolution, and Systematics, 41*, 127-147

Hood, R.R., Laws, E.A., Armstrong, R.A., Bates, N.R., Brown, C.W., Carlson, C.A., Chai, F., Doney, S.C., Falkowski, P.G., Feely, R.A., Friedrichs, M.A.M., Landry, M.R., Keith Moore, J., Nelson, D.M., Richardson, T.L., Salihoglu, B., Schartau, M., Toole, D.A., & Wiggert, J.D. (2006). Pelagic functional group modeling: Progress, challenges and prospects. *Deep Sea Research Part II: Topical Studies in Oceanography, 53*, 459-512

Hughes, D.J., Alderdice, R., Cooney, C., Kühl, M., Pernice, M., Voolstra, C.R., & Suggett, D.J. (2020). Coral reef survival under accelerating ocean deoxygenation. *Nature Climate Change, 10*, 296-307

Irwin, A.J., Finkel, Z.V., Muller-Karger, F.E., & Troccoli Ghinaglia, L. (2015). Phytoplankton adapt to changing ocean environments. *Proc Natl Acad Sci U S A, 112*, 5762-5766

Ito, T., Minobe, S., Long, M.C., & Deutsch, C. (2017). Upper ocean O2 trends: 1958–2015. *Geophysical Research Letters, 44*, 4214-4223

Jacquet, S.H.M., Dehairs, F., Lefèvre, D., Cavagna, A.J., Planchon, F., Christaki, U., Monin, L., André, L., Closset, I., & Cardinal, D. (2015). Early spring mesopelagic carbon remineralization and transfer efficiency in the naturally iron-fertilized Kerguelen area. *Biogeosciences, 12*, 1713-1731

Jarníková, T., Le Quere, C., Rumbold, S.T., & Jones , C. (in prep.). Greenhouse gas emissions dominate over stratospheric ozone depletion in setting the southern ocean carbon sink from 1950-2100. In

Ji, R., Edwards, M., Mackas, D.L., Runge, J.A., & Thomas, A.C. (2010). Marine plankton phenology and life history in a changing climate: current research and future directions. *J Plankton Res, 32*, 1355-1368

John, E.H., Wilson, J.D., Pearson, P.N., & Ridgwell, A. (2014). Temperature-dependent remineralization and carbon cycling in the warm Eocene oceans. *Palaeogeography, Palaeoclimatology, Palaeoecology, 413*, 158-166

Kahru, M., Lee, Z., Mitchell, B.G., & Nevison, C.D. (2016). Effects of sea ice cover on satellite-detected primary production in the Arctic Ocean. *Biol Lett, 12*

Kalnay, E., Kanamitsu, M., Kistler, R., Collins, W., Deaven, D., Gandin, L., Iredell, M., Saha, S., White, G., Woollen, J., Zhu, Y., Chilliah, M., Ebisuzaki, W., Higgins, W., Janowiak, J., Mo, K.C., Ropelewski, C., Wang, J., Leetmaa, A., Reynolds, R.W., Jenne, R., & Joseph, D. (1996). The NCEP/NCAR 40-Year Reanalysis Project. *AMS*, 437-472

Karakuş, O., Völker, C., Iversen, M., Hagen, W., Wolf-Gladrow, D., Fach, B., & Hauck, J. (2021). Modeling the Impact of Macrozooplankton on Carbon Export Production in the Southern Ocean. *Journal of Geophysical Research: Oceans, 126*

Kassi, J.-B., Racault, M.-F., Mobio, B., Platt, T., Sathyendranath, S., Raitsos, D., & Affian, K. (2018). Remotely Sensing the Biophysical Drivers of Sardinella aurita Variability in Ivorian Waters. *Remote Sensing, 10*

Keppler, L., & Landschutzer, P. (2019). Regional Wind Variability Modulates the Southern Ocean Carbon Sink. *Sci Rep, 9*, 7384

Key, R.M., Kozyr, A., Sabine, C.L., Lee, K., Wanninkhof, R., Bullister, J.L., Feely, R.A., Millero, F.J., Mordy, C., & Peng, T.H. (2004). A global ocean carbon climatology: Results from Global Data Analysis Project (GLODAP). *Global Biogeochemical Cycles, 18*

Kim, T.-W., Lee, K., Duce, R., & Liss, P. (2014). Impact of atmospheric nitrogen deposition on phytoplankton productivity in the South China Sea. *Geophysical Research Letters, 41*, 3156-3162

Klaas, C., & Archer, D.E. (2002). Association of sinking organic matter with various types of mineral ballast in the deep sea: Implications for the rain ratio. *Global Biogeochemical Cycles, 16*

Koeller, P., Fuentes-Yaco, C., Platt, T., Sathyendranath, S., Richards, A., Ouellet, P., Orr, D., Skúladóttir, U., Wieland, K., Savard, L., & Aschan, M. (2009). Basin-Scale Coherence in Phenology of Shrimps and Phytoplankton in the North Atlantic Ocean. *Science, 324*, 791-793

Kroeker, K.J., Kordas, R.L., Crim, R.N., & Singh, G.G. (2010). Meta-analysis reveals negative yet variable effects of ocean acidification on marine organisms. *Ecol Lett, 13*, 1419-1434

Kroeker, K.J., Powell, C., & Donham, E.M. (2020). Windows of vulnerability: Seasonal mismatches in exposure and resource identity determine ocean acidification's effect on a primary consumer at high latitude. *Glob Chang Biol*

Krumhardt, K.M., Long, M.C., Sylvester, Z.T., & Petrik, C.M. (2022). Climate drivers of Southern Ocean phytoplankton community composition and potential impacts on higher trophic levels. *Frontiers in Marine Science, 9*

Krumhardt, K.M., Lovenduski, N.S., Long, M.C., Levy, M., Lindsay, K., Moore, J.K., & Nissen, C. (2019). Coccolithophore Growth and Calcification in an Acidified Ocean: Insights From Community Earth System Model Simulations. *Journal of Advances in Modeling Earth Systems, 11*, 1418-1437

Kulk, G., Platt, T., Dingle, J., Jackson, T., Jönsson, B., Bouman, H., Babin, M., Brewin, R., Doblin, M., Estrada, M., Figueiras, F., Furuya, K., González-Benítez, N., Gudfinnsson, H., Gudmundsson, K., Huang, B., Isada, T., Kovač, Ž., Lutz, V., Marañón, E., Raman, M., Richardson, K., Rozema, P., Poll, W., Segura, V., Tilstone, G., Uitz, J., Dongen-Vogels, V., Yoshikawa, T., & Sathyendranath, S. (2020). Primary Production, an Index of Climate Change in the Ocean: Satellite-Based Estimates over Two Decades. *Remote Sensing, 12*

Kwiatkowski, L., Torres, O., Bopp, L., Aumont, O., Chamberlain, M., Christian, J.R., Dunne, J.P., Gehlen, M., Ilyina, T., John, J.G., Lenton, A., Li, H., Lovenduski, N.S., Orr, J.C., Palmieri, J., Santana-Falcón, Y., Schwinger, J., Séférian, R., Stock, C.A.,

Tagliabue, A., Takano, Y., Tjiputra, J., Toyama, K., Tsujino, H., Watanabe, M., Yamamoto, A., Yool, A., & Ziehn, T. (2020). Twenty-first century ocean warming, acidification, deoxygenation, and upper-ocean nutrient and primary production decline from CMIP6 model projections. *Biogeosciences, 17*, 3439-3470

Kwon, E.Y., Primeau, F., & Sarmiento, J.L. (2009). The impact of remineralization depth on the air–sea carbon balance. *Nature Geoscience, 2*, 630-635

Lacour, L., Llort, J., Briggs, N., Strutton, P.G., & Boyd, P.W. (2023). Seasonality of downward carbon export in the Pacific Southern Ocean revealed by multi-year robotic observations. *Nat Commun, 14*, 1278

Laufkötter, C., Vogt, M., Gruber, N., Aita-Noguchi, M., Aumont, O., Bopp, L., Buitenhuis, E., Doney, S.C., Dunne, J., Hashioka, T., Hauck, J., Hirata, T., John, J., Le Quéré, C., Lima, I.D., Nakano, H., Seferian, R., Totterdell, I., Vichi, M., & Völker, C. (2015). Drivers and uncertainties of future global marine primary production in marine ecosystem models. *Biogeosciences, 12*, 6955-6984

Laufkötter, C., Vogt, M., Gruber, N., Aumont, O., Bopp, L., Doney, S.C., Dunne, J.P., Hauck, J., John, J.G., Lima, I.D., Seferian, R., & Völker, C. (2016). Projected decreases in future marine export production: the role of the carbon flux through the upper ocean ecosystem. *Biogeosciences, 13*, 4023-4047

Laws, E.A., & Maiti, K. (2019). The relationship between primary production and export production in the ocean: Effects of time lags and temporal variability. *Deep Sea Research Part I: Oceanographic Research Papers, 148*, 100-107

Le Moigne, F. (2013). Global database of surface ocean particulate organic carbon export fluxes diagnosed from the 234Th technique [dataset]. In. PANGAEA

Le Moigne, F.A.C. (2019). Pathways of Organic Carbon Downward Transport by the Oceanic Biological Carbon Pump. *Frontiers in Marine Science, 6*

Le Moigne, F.A.C., Henson, S.A., Cavan, E., Georges, C., Pabortsava, K., Achterberg, E.P., Ceballos-Romero, E., Zubkov, M., & Sanders, R.J. (2016). What causes the inverse relationship between primary production and export efficiency in the Southern Ocean? *Geophysical Research Letters, 43*, 4457-4466

Le Quéré, C., Buitenhuis, E.T., Moriarty, R., Alvain, S., Aumont, O., Bopp, L., Chollet, S., Enright, C., Franklin, D.J., Geider, R.J., Harrison, S.P., Hirst, A.G., Larsen, S., Legendre, L., Platt, T., Prentice, I.C., Rivkin, R.B., Sailley, S., Sathyendranath, S., Stephens, N., Vogt, M., & Vallina, S.M. (2016). Role of zooplankton dynamics for

Southern Ocean phytoplankton biomass and global biogeochemical cycles. *Biogeosciences, 13*, 4111-4133

Le Quere, C., Harrison, S.P., Prentice, I.C., Buitenhuis, E., Aumont, O., Bopp, L., Claustre, H., Da Cunha, L.C., Geider, R.J., Giraud, X., Klaas, C., Kohfeld, K., Legendre, L., Manizza, M., Platt, T., Rivkin, R.B., Sathyendranath, S., Uitz, J., Watson, A.J., & Wolf-Gladrow, D. (2005). Ecosystem dynamics based on plankton functional types for global ocean biogeochemistry models. *Global Change Biology, 11*, 2016-2040

Le Quéré, C., Harrison, S.P., Prentice, I.C., Buitenhuis, E., Aumont, O., Bopp, L., Claustre, H., Da Cunha, L.C., Geider, R.J., Giraud, X., Klaas, C., Kohfeld, K., Legendre, L., Manizza, M., Platt, T., Rivkin, R.B., Sathyendranath, S., Uitz, J., Watson, A.J., & Wolf-Gladrow, D. (2005). Ecosystem dynamics based on plankton functional types for global ocean biogeochemistry models. *Global Change Biology, 11*, 2016-2040

Le Quéré, C., Takahashi, T., Buitenhuis, E.T., Rödenbeck, C., & Sutherland, S.C. (2010). Impact of climate change and variability on the global oceanic sink of CO2. *Global Biogeochemical Cycles, 24*

Lenoir, J., Bertrand, R., Comte, L., Bourgeaud, L., Hattab, T., Murienne, J., & Grenouillet, G. (2020). Species better track climate warming in the oceans than on land. *Nat Ecol Evol, 4*, 1044-1059

Leung, J.Y.S., Zhang, S., & Connell, S.D. (2022). Is Ocean Acidification Really a Threat to Marine Calcifiers? A Systematic Review and Meta-Analysis of 980+ Studies Spanning Two Decades. *Small, 18*, e2107407

Levitius, S. (2013). NODC Standard Product: World ocean atlas 2005 (4 disc set) (NCEI Accession 0097967). In U.D.N.N.N.O.D. Center (Ed.). NOAA National Centers for Environmental Information.

Li, C., Huang, J., Ding, L., Liu, X., Yu, H., & Huang, J. (2020). Increasing Escape of Oxygen From Oceans Under Climate Change. *Geophysical Research Letters, 47*

Limburg, K.E., Breitburg, D., Swaney, D.P., & Jacinto, G. (2020). Ocean Deoxygenation: A Primer. *One Earth, 2*, 24-29

Lischka, S., Büdenbender, J., Boxhammer, T., & Riebesell, U. (2011). Impact of ocean acidification and elevated temperatures on early juveniles of the polar shelled

pteropod Limacina helicina: mortality, shell degradation, and shell growth. *Biogeosciences, 8*, 919-932

Lohbeck, K.T., Riebesell, U., & Reusch, T.B.H. (2012). Adaptive evolution of a key phytoplankton species to ocean acidification. *Nature Geoscience, 5*, 346-351

Lombard, F., Guidi, L., & Kiorboe, T. (2013). Effect of type and concentration of ballasting particles on sinking rate of marine snow produced by the appendicularian Oikopleura dioica. *PLoS One, 8*, e75676

Lu, J., Shu, Y., Zhang, H., Zhang, S., Zhu, C., Ding, W., & Zhang, W. (2023). The Landscape of Global Ocean Microbiome: From Bacterioplankton to Biofilms. *Int J Mol Sci, 24*

Lürling, M. (2020). Grazing resistance in phytoplankton. *Hydrobiologia, 848*, 237-249

Lutz, M.J., Caldeira, K., Dunbar, R.B., & Behrenfeld, M.J. (2007). Seasonal rhythms of net primary production and particulate organic carbon flux to depth describe the efficiency of biological pump in the global ocean. *Journal of Geophysical Research: Oceans, 112*

Maerz, J., Six, K.D., Stemmler, I., Ahmerkamp, S., & Ilyina, T. (2020). Microstructure and composition of marine aggregates as co-determinants for vertical particulate organic carbon transfer in the global ocean. *Biogeosciences, 17*, 1765-1803

Manizza, M., Buitenhuis, E.T., & Le Quéré, C. (2010). Sensitivity of global ocean biogeochemical dynamics to ecosystem structure in a future climate. *Geophysical Research Letters, 37*

Manno, C., Bednaršek, N., Tarling, G.A., Peck, V.L., Comeau, S., Adhikari, D., Bakker, D.C.E., Bauerfeind, E., Bergan, A.J., Berning, M.I., Buitenhuis, E., Burridge, A.K., Chierici, M., Flöter, S., Fransson, A., Gardner, J., Howes, E.L., Keul, N., Kimoto, K., Kohnert, P., Lawson, G.L., Lischka, S., Maas, A., Mekkes, L., Oakes, R.L., Pebody, C., Peijnenburg, K.T.C.A., Seifert, M., Skinner, J., Thibodeau, P.S., Wall-Palmer, D., & Ziveri, P. (2017). Shelled pteropods in peril: Assessing vulnerability in a high CO2 ocean. *Earth-Science Reviews, 169*, 132-145

Manno, C., Giglio, F., Stowasser, G., Fielding, S., Enderlein, P., & Tarling, G.A. (2018). Threatened species drive the strength of the carbonate pump in the northern Scotia Sea. *Nat Commun, 9*, 4592

Maranon, E. (2007). Inter-specific scaling of phytoplankton production and cell size in the field. *Journal of Plankton Research, 30*, 157-163

Mari, X., Passow, U., Migon, C., Burd, A.B., & Legendre, L. (2017). Transparent exopolymer particles: Effects on carbon cycling in the ocean. *Progress in Oceanography, 151*, 13-37

Marsay, C.M., Sanders, R.J., Henson, S.A., Pabortsava, K., Achterberg, E.P., & Lampitt, R.S. (2015). Attenuation of sinking particulate organic carbon flux through the mesopelagic ocean. *Proc Natl Acad Sci U S A, 112*, 1089-1094

Martinez, E., Antoine, D., D'Ortenzio, & Gentili, B. (2009). Climate-driven Basin-Scale Decadal Oscillations of Oceanic Phytoplankton. *Science, 326*, 1253-1256

Mayor, D.J., Gentleman, W.C., & Anderson, T.R. (2020). Ocean carbon sequestration: Particle fragmentation by copepods as a significant unrecognised factor?: Explicitly representing the role of copepods in biogeochemical models may fundamentally improve understanding of future ocean carbon storage. *Bioessays, 42*, e2000149

Mayot, N., Le Quere, C., Rodenbeck, C., Bernardello, R., Bopp, L., Djeutchouang, L.M., Gehlen, M., Gregor, L., Gruber, N., Hauck, J., Iida, Y., Ilyina, T., Keeling, R.F., Landschutzer, P., Manning, A.C., Patara, L., Resplandy, L., Schwinger, J., Seferian, R., Watson, A.J., Wright, R.M., & Zeng, J. (2023). Climate-driven variability of the Southern Ocean CO(2) sink. *Philos Trans A Math Phys Eng Sci, 381*, 20220055

Melzner, F., Buchholz, B., Wolf, F., Panknin, U., & Wall, M. (2020). Ocean winter warming induced starvation of predator and prey. *Proc Biol Sci, 287*, 20200970

Meyer, J., & Riebesell, U. (2015). Reviews and Syntheses: Responses of coccolithophores to ocean acidification: a meta-analysis. *Biogeosciences, 12*, 1671-1682

Misumi, K., Lindsay, K., Moore, J.K., Doney, S.C., Bryan, F.O., Tsumune, D., & Yoshida, Y. (2014). The iron budget in ocean surface waters in the 20th and 21st centuries: projections by the Community Earth System Model version 1. *Biogeosciences, 11*, 33-55

Moore, J.K., Doney, S.C., & Lindsay, K. (2004). Upper ocean ecosystem dynamics and iron cycling in a global three-dimensional model. *Global Biogeochemical Cycles, 18*

Moore, J.K., Fu, W., Primeau, F., Britten, G.L., Lindsay, K., Long, M., Doney, S.C., Mahowald , N., Hoffmann, F., & Randerson, J.T. (2018). Sustained climate warming drives declining marine biological productivity. *Science, 359*, 1139-1143

Morley, S.A., Bates, A.E., Clark, M.S., Fitzcharles, E., Smith, R., Stainthorp, R.E., & Peck, L.S. (2024). Testing the Resilience, Physiological Plasticity and Mechanisms Underlying Upper Temperature Limits of Antarctic Marine Ectotherms. *Biology (Basel), 13*

Mouw, C.B., Barnett, A., McKinley, G.A., Gloege, L., & Pilcher, D. (2016). Global ocean particulate organic carbon flux merged with satellite parameters. *Earth System Science Data, 8*, 531-541

Mulcahy, J.P., Jones, C.G., Rumbold, S.T., Kuhlbrodt, T., Dittus, A.J., Blockley, E.W., Yool, A., Walton, J., Hardacre, C., Andrews, T., Bodas-Salcedo, A., Stringer, M., de Mora, L., Harris, P., Hill, R., Kelley, D., Robertson, E., & Tang, Y. (2020). UKESM1.1: Development and evaluation of an updated configuration of the UK Earth System Model. *Geoscientific Model Development*

Nagata, T., Yamada, Y., & Fukuda, H. (2021). Transparent Exopolymer Particles in Deep Oceans: Synthesis and Future Challenges. *Gels, 7*

Naviaux, J.D., Subhas, A.V., Dong, S., Rollins, N.E., Liu, X., Byrne, R.H., Berelson, W.M., & Adkins, J.F. (2019). Calcite dissolution rates in seawater: Lab vs. in-situ measurements and inhibition by organic matter. *Marine Chemistry, 215*

Neukermans, G., Bach, L.T., Butterley, A., Sun, Q., Claustre, H., & Fournier, G.R. (2023). Quantitative and mechanistic understanding of the open ocean carbonate pump - perspectives for remote sensing and autonomous in situ observation. *Earth-Science Reviews, 239*

Nishioka, J., Obata, H., Hirawake, T., Kondo, Y., Yamashita, Y., Misumi, K., & Yasuda, I. (2021). A review: iron and nutrient supply in the subarctic Pacific and its impact on phytoplankton production. *Journal of Oceanography, 77*, 561-587

Nissen, C., & Vogt, M. (2021). Factors controlling the competition between Phaeocystis and diatoms in the Southern Ocean and implications for carbon export fluxes. *Biogeosciences, 18*, 251-283

Nowicki, M., DeVries, T., & Siegel, D.A. (2022). Quantifying the Carbon Export and Sequestration Pathways of the Ocean's Biological Carbon Pump. *Global Biogeochemical Cycles, 36*

O'Neill, B.C., Tebaldi, C., van Vuuren, D.P., Eyring, V., Friedlingstein, P., Hurtt, G., Knutti, R., Kriegler, E., Lamarque, J.-F., Lowe, J., Meehl, G.A., Moss, R., Riahi, K., &

Sanderson, B.M. (2016). The Scenario Model Intercomparison Project (ScenarioMIP) for CMIP6. *Geoscientific Model Development, 9*, 3461-3482

Olivarez Lyle, A., & Lyle, M.W. (2006). Missing organic carbon in Eocene marine sediments: Is metabolism the biological feedback that maintains end-member climates? *Paleoceanography, 21*

Orr, J.C., Fabry, V.J., Aumont, O., Bopp, L., Doney, S.C., Feely, R.A., Gnanadesikan, A., Gruber, N., Ishida, A., Joos, F., Key, R.M., Lindsay, K., Maier-Reimer, E., Matear, R., Monfray, P., Mouchet, A., Najjar, R.G., Plattner, G.K., Rodgers, K.B., Sabine, C.L., Sarmiento, J.L., Schlitzer, R., Slater, R.D., Totterdell, I.J., Weirig, M.F., Yamanaka, Y., & Yool, A. (2005). Anthropogenic ocean acidification over the twenty-first century and its impact on calcifying organisms. *Nature, 437*, 681-686

Oschlies, A., Brandt, P., Stramma, L., & Schmidtko, S. (2018). Drivers and mechanisms of ocean deoxygenation. *Nature Geoscience, 11*, 467-473

Oschlies, A., Schulz, K.G., Riebesell, U., & Schmittner, A. (2008). Simulated 21st century's increase in oceanic suboxia by CO2-enhanced biotic carbon export. *Global Biogeochemical Cycles, 22*

Parekh, P., Follows, M.J., Dutkiewicz, S., & Ito, T. (2006). Physical and biological regulation of the soft tissue carbon pump. *Paleoceanography, 21*

Petrou, K. (2023). Phytoplankton-Bacteria Interactions 1.0. *Microorganisms, 11*

Pinti, J., Kiorboe, T., Thygesen, U.H., & Visser, A.W. (2019). Trophic interactions drive the emergence of diel vertical migration patterns: a game-theoretic model of copepod communities. *Proc Biol Sci, 286*, 20191645

Platt, T., Fuentes-Yaco, C., & Frank, K.T. (2003). Marine ecology: Spring algal bloom and larval fish survival. *Science, 423*, 398-399

Platt, T., & Sathyendranath, S. (2008). Ecological indicators for the pelagic zone of the ocean from remote sensing. *Remote Sensing of Environment, 112*, 3426-3436

Poloczanska, E.S., Brown, C.J., Sydeman, W.J., Kiessling, W., Schoeman, D.S., Moore, P.J., Brander, K., Bruno, J.F., Buckley, L.B., Burrows, M.T., Duarte, C.M., Halpern, B.S., Holding, J., Kappel, C.V., O'Connor, M.I., Pandolfi, J.M., Parmesan, C., Schwing, F., Thompson, S.A., & Richardson, A.J. (2013). Global imprint of climate change on marine life. *Nature Climate Change, 3*, 919-925

Polovina, J.J., Howell, E.A., & Abecassis, M. (2008). Ocean's least productive waters are expanding. *Geophysical Research Letters, 35*

Priester, C.R., Melbourne-Thomas, J., Klocker, A., & Corney, S. (2017). Abrupt transitions in dynamics of a NPZD model across Southern Ocean fronts. *Ecological Modelling, 359*, 372-382

Racault, M.-F., Le Quéré, C., Buitenhuis, E., Sathyendranath, S., & Platt, T. (2012). Phytoplankton phenology in the global ocean. *Ecological Indicators, 14*, 152-163

Racault, M.-F., Sathyendranath, S., Brewin, R.J.W., Raitsos, D.E., Jackson, T., & Platt, T. (2017a). Impact of El Niño Variability on Oceanic Phytoplankton. *Frontiers in Marine Science, 4*

Racault, M.F., Sathyendranath, S., Menon, N., & Platt, T. (2017b). Phenological Responses to ENSO in the Global Oceans. *Surv Geophys, 38*, 277-293

Rathore, S., Bindoff, N.L., Phillips, H.E., & Feng, M. (2020). Recent hemispheric asymmetry in global ocean warming induced by climate change and internal variability. *Nat Commun, 11*, 2008

Rembauville, M., Meilland, J., Ziveri, P., Schiebel, R., Blain, S., & Salter, I. (2016). Planktic foraminifer and coccolith contribution to carbonate export fluxes over the central Kerguelen Plateau. *Deep Sea Research Part I: Oceanographic Research Papers, 111*, 91-101

Ren, H., Chen, Y.-C., Wang, X.T., Wong, G.T.F., Cohen, A.L., DeCarlo, T.M., Weigand, M.A., Mii, H.-S., & Sigman, D.M. (2017). 21st-century rise in anthropogenic nitrogen deposition on a remote coral reef. *Science, 356*, 749-752

Riahi, K., van Vuuren, D.P., Kriegler, E., Edmonds, J., O'Neill, B.C., Fujimori, S., Bauer, N., Calvin, K., Dellink, R., Fricko, O., Lutz, W., Popp, A., Cuaresma, J.C., Kc, S., Leimbach, M., Jiang, L., Kram, T., Rao, S., Emmerling, J., Ebi, K., Hasegawa, T., Havlik, P., Humpenöder, F., Da Silva, L.A., Smith, S., Stehfest, E., Bosetti, V., Eom, J., Gernaat, D., Masui, T., Rogelj, J., Strefler, J., Drouet, L., Krey, V., Luderer, G., Harmsen, M., Takahashi, K., Baumstark, L., Doelman, J.C., Kainuma, M., Klimont, Z., Marangoni, G., Lotze-Campen, H., Obersteiner, M., Tabeau, A., & Tavoni, M. (2017). The Shared Socioeconomic Pathways and their energy, land use, and greenhouse gas emissions implications: An overview. *Global Environmental Change, 42*, 153-168

Richardson, T.R. (2019). Mechanisms and Pathways of Small-Phytoplankton Export from the Surface Ocean. *Annual Review of Marine Science, 11*, 57-74

Ricour, F., Guidi, L., Gehlen, M., DeVries, T., & Legendre, L. (2023). Century-scale carbon sequestration flux throughout the ocean by the biological pump. *Nature Geoscience, 16*, 1105-1113

Ridley, J.K., Blockley, E.W., Keen, A.B., Rae, J.G.L., West, A.E., & Schroeder, D. (2018). The sea ice model component of HadGEM3-GC3.1. *Geoscientific Model Development, 11*, 713-723

Riebesell, U., Schulz, K.G., Bellerby, R.G., Botros, M., Fritsche, P., Meyerhofer, M., Neill, C., Nondal, G., Oschlies, A., Wohlers, J., & Zollner, E. (2007). Enhanced biological carbon consumption in a high CO2 ocean. *Nature, 450*, 545-548

Riemann, L., Steward, G.F., & Azam, F. (2000). Dynamics of Bacterial Community Composition and Activity during a Mesocosm Diatom Bloom. *Applied and Environmental Microbiology, 66*, 578-587

Ries, J.B., Cohen, A.L., & McCorkle, D.C. (2009). Marine calcifiers exhibit mixed responses to CO2-induced ocean acidification. *Geology, 37*, 1131-1134

Rii, Y.M., Brown, S.L., Nencioli, F., Kuwahara, V., Dickey, T., Karl, D.M., & Bidigare, R.R. (2008). The transient oasis: Nutrient-phytoplankton dynamics and particle export in Hawaiian lee cyclones. *Deep Sea Research Part II: Topical Studies in Oceanography, 55*, 1275-1290

Rohr, T., Richardson, A.J., Lenton, A., Chamberlain, M.A., & Shadwick, E.H. (2023). Zooplankton grazing is the largest source of uncertainty for marine carbon cycling in CMIP6 models. *Communications Earth & Environment, 4*

Ruela, R., Sousa, M.C., deCastro, M., & Dias, J.M. (2020). Global and regional evolution of sea surface temperature under climate change. *Global and Planetary Change, 190*

Ryan-Keogh, T.J., Thomalla, S.J., Monteiro, P.M.S., & Tagliabue, A. (2023). Multidecadal trend of increasing iron stress in Southern Ocean phytoplankton. *Science, 379*, 834-840

Saba, G.K., Burd, A.B., Dunne, J.P., Hernández-León, S., Martin, A.H., Rose, K.A., Salisbury, J., Steinberg, D.K., Trueman, C.N., Wilson, R.W., & Wilson, S.E. (2021). Toward a better understanding of fish-based contribution to ocean carbon flux. *Limnology and Oceanography, 66*, 1639-1664

Saha, S., Moorthi, S., Pan, H.-L., Wu, X., Wang, J., Nadiga, S., Tripp, P., Kistler, R., Woollen, J., Behringer, D., Liu, H., Stokes, D., Grumbine, R., Gayno, G., Wang, J.,

Hou, Y.-T., Chuang, H.-y., Juang, H.-M.H., Sela, J., Iredell, M., Treadon, R., Kleist, D., Van Delst, P., Keyser, D., Derber, J., Ek, M., Meng, J., Wei, H., Yang, R., Lord, S., van den Dool, H., Kumar, A., Wang, W., Long, C., Chelliah, M., Xue, Y., Huang, B., Schemm, J.-K., Ebisuzaki, W., Lin, R., Xie, P., Chen, M., Zhou, S., Higgins, W., Zou, C.-Z., Liu, Q., Chen, Y., Han, Y., Cucurull, L., Reynolds, R.W., Rutledge, G., & Goldberg, M. (2010). The NCEP Climate Forecast System Reanalysis. *Bulletin of the American Meteorological Society, 91*, 1015-1058

Salgado-Hernanz, P.M., Racault, M.F., Font-Muñoz, J.S., & Basterretxea, G. (2019). Trends in phytoplankton phenology in the Mediterranean Sea based on ocean-colour remote sensing. *Remote Sensing of Environment, 221*, 50-64

Sallée, J.-B., Llort, J., Tagliabue, A., & Lévy, M. (2015). Characterization of distinct bloom phenology regimes in the Southern Ocean. *ICES Journal of Marine Science, 72*, 1985-1998

Sallee, J.B., Pellichero, V., Akhoudas, C., Pauthenet, E., Vignes, L., Schmidtko, S., Garabato, A.N., Sutherland, P., & Kuusela, M. (2021). Summertime increases in upper-ocean stratification and mixed-layer depth. *Nature, 591*, 592-598

Salter, I., Schiebel, R., Ziveri, P., Movellan, A., Lampitt, R., & Wolff, G.A. (2014). Carbonate counter pump stimulated by natural iron fertilization in the Polar Frontal Zone. *Nature Geoscience, 7*, 885-889

Sasai, Y., Yoshikawa, C., Smith, S.L., Hashioka, T., Matsumoto, K., Wakita, M., Sasaoka, K., & Honda, M.C. (2016). Coupled 1-D physical–biological model study of phytoplankton production at two contrasting time-series stations in the western North Pacific. *Journal of Oceanography, 72*, 509-526

Sathyendranath, S., Brewin, R.J.W., Brockmann, C., Brotas, V., Calton, B., Chuprin, A., Cipollini, P., Couto, A.B., Dingle, J., Doerffer, R., Donlon, C., Dowell, M., Farman, A., Grant, M., Groom, S., Horseman, A., Jackson, T., Krasemann, H., Lavender, S., Martinez-Vicente, V., Mazeran, C., Melin, F., Moore, T.S., Muller, D., Regner, P., Roy, S., Steele, C.J., Steinmetz, F., Swinton, J., Taberner, M., Thompson, A., Valente, A., Zuhlke, M., Brando, V.E., Feng, H., Feldman, G., Franz, B.A., Frouin, R., Gould, R.W., Hooker, S.B., Kahru, M., Kratzer, S., Mitchell, B.G., Muller-Karger, F.E., Sosik, H.M., Voss, K.J., Werdell, J., & Platt, T. (2019). An Ocean-Colour Time Series for Use in Climate Studies: The Experience of the Ocean-Colour Climate Change Initiative (OC-CCI). *Sensors (Basel), 19*

Sathyendranath, S., Jackson, T., Brockmann, C., Brotas, V., Calton, B., Chuprin, A., Clements, O., Cipollini, P., Danne, O., Dingle, J., Donlon, C., Grant, M., Groom, S., Krasemann, H., Lavender, S., Mazeran, C., Mélin, F., Müller, D., Steinmetz, F., Valente, A., Zühlke, M., Feldman, G., Franz, B., Frouin, R., Werdell, J., & Platt, T. (2021). ESA Ocean Colour Climate Change Initiative (Ocean_Colour_cci). In

Schaum, C.E., & Collins, S. (2014). Plasticity predicts evolution in a marine alga. *Proc Biol Sci, 281*

Schmidtko, S., Stramma, L., & Visbeck, M. (2017). Decline in global oceanic oxygen content during the past five decades. *Nature, 542*, 335-339

Schnack-Schiel, S.B., & Isla, E. (2005). The role of zooplankton in the pelagic-benthic coupling of the Southern Ocean. *Sci Mar, 69*, 39-55

Seebah, S., Fairfield, C., Ullrich, M.S., & Passow, U. (2013). Aggregation and Sedimentation of Thalassiosira weissflogii (diatom) in a Warmer and More Acidified Future Ocean. *PLoS One, 9*

Sellar, A.A., Jones, C.G., Mulcahy, J.P., Tang, Y., Yool, A., Wiltshire, A., O'Connor, F.M., Stringer, M., Hill, R., Palmieri, J., Woodward, S., de Mora, L., Kuhlbrodt, T., Rumbold, S.T., Kelley, D.I., Ellis, R., Johnson, C.E., Walton, J., Abraham, N.L., Andrews, M.B., Andrews, T., Archibald, A.T., Berthou, S., Burke, E., Blockley, E., Carslaw, K., Dalvi, M., Edwards, J., Folberth, G.A., Gedney, N., Griffiths, P.T., Harper, A.B., Hendry, M.A., Hewitt, A.J., Johnson, B., Jones, A., Jones, C.D., Keeble, J., Liddicoat, S., Morgenstern, O., Parker, R.J., Predoi, V., Robertson, E., Siahaan, A., Smith, R.S., Swaminathan, R., Woodhouse, M.T., Zeng, G., & Zerroukat, M. (2019). UKESM1: Description and Evaluation of the U.K. Earth System Model. *Journal of Advances in Modeling Earth Systems, 11*, 4513-4558

Serra-Pompei, C., Ward, B.A., Pinti, J., Visser, A.W., Kiørboe, T., & Andersen, K.H. (2022). Linking Plankton Size Spectra and Community Composition to Carbon Export and Its Efficiency. *Global Biogeochemical Cycles, 36*

Shi, J.-R., Xie, S.-P., & Talley, L.D. (2018). Evolving Relative Importance of the Southern Ocean and North Atlantic in Anthropogenic Ocean Heat Uptake. *Journal of Climate, 31*, 7459-7479

Siegel, D.A., Buesseler, K.O., Behrenfeld, M.J., Benitez-Nelson, C.R., Boss, E., Brzezinski, M.A., Burd, A., Carlson, C.A., D'Asaro, E.A., Doney, S.C., Perry, M.J., Stanley, R.H.R., & Steinberg, D.K. (2016). Prediction of the Export and Fate of Global

Ocean Net Primary Production: The EXPORTS Science Plan. *Frontiers in Marine Science, 3*

Siegel, D.A., Maritorena, S., Nelson, N.B., Hansell, D.A., & Lorenzi-Kayser, M. (2002). Global distribution and dynamics of colored dissolved and detrital organic materials. *Journal of Geophysical Research: Oceans, 107*

Silva, E., Counillon, F., Brajard, J., Korosov, A., Pettersson, L.H., Samuelsen, A., & Keenlyside, N. (2021). Twenty-One Years of Phytoplankton Bloom Phenology in the Barents, Norwegian, and North Seas. *Frontiers in Marine Science, 8*

Simon, M., Scheuner, C., Meier-Kolthoff, J.P., Brinkhoff, T., Wagner-Dobler, I., Ulbrich, M., Klenk, H.P., Schomburg, D., Petersen, J., & Goker, M. (2017). Phylogenomics of Rhodobacteraceae reveals evolutionary adaptation to marine and non-marine habitats. *ISME J, 11*, 1483-1499

Somavilla, R., Gonzalez-Pola, C., & Fernandez-Diaz, J. (2017). The warmer the ocean surface, the shallower the mixed layer. How much of this is true? *J Geophys Res Oceans, 122*, 7698-7716

Song, H., Edwards, C.A., Moore, A.M., & Fiechter, J. (2016). Data assimilation in a coupled physical-biogeochemical model of the California current system using an incremental lognormal 4-dimensional variational approach: Part 3—Assimilation in a realistic context using satellite and in situ observations. *Ocean Modelling, 106*, 159-172

Stanley, R.H.R., Kirkpatrick, J.B., Cassar, N., Barnett, B.A., & Bender, M.L. (2010). Net community production and gross primary production rates in the western equatorial Pacific. *Global Biogeochemical Cycles, 24*

Steinberg, D.K., & Landry, M.R. (2017). Zooplankton and the Ocean Carbon Cycle. *Ann Rev Mar Sci, 9*, 413-444

Storkey, D., Blaker, A.T., Mathiot, P., Megann, A., Aksenov, Y., Blockley, E.W., Calvert, D., Graham, T., Hewitt, H.T., Hyder, P., Kuhlbrodt, T., Rae, J.G.L., & Sinha, B. (2018). UK Global Ocean GO6 and GO7: a traceable hierarchy of model resolutions. *Geoscientific Model Development, 11*, 3187-3213

Stuart-Smith, R.D., Edgar, G.J., Barrett, N.S., Kininmonth, S.J., & Bates, A.E. (2015). Thermal biases and vulnerability to warming in the world's marine fauna. *Nature, 528*, 88-92

Subhas, A.V., Adkins, J.F., Rollins, N.E., Naviaux, J., Erez, J., & Berelson, W.M. (2017). Catalysis and chemical mechanisms of calcite dissolution in seawater. *Proc Natl Acad Sci U S A, 114*, 8175-8180

Suchy, K.D., Young, K., Galbraith, M., Perry, R.I., & Costa, M. (2022). Match/ Mismatch Between Phytoplankton and Crustacean Zooplankton Phenology in the Strait of Georgia, Canada. *Frontiers in Marine Science, 9*

Sunagawa, S., Acinas, S.G., Bork, P., Bowler, C., Tara Oceans, C., Eveillard, D., Gorsky, G., Guidi, L., Iudicone, D., Karsenti, E., Lombard, F., Ogata, H., Pesant, S., Sullivan, M.B., Wincker, P., & de Vargas, C. (2020). Tara Oceans: towards global ocean ecosystems biology. *Nat Rev Microbiol, 18*, 428-445

Sverdrup, H.U. (1953). On conditions for the Vernal Blooming of Phytoplankton. *Norsk Polarinstitutt, Oslo.*

Tagliabue, A., Bowie, A.R., Boyd, P.W., Buck, K.N., Johnson, K.S., & Saito, M.A. (2017). The integral role of iron in ocean biogeochemistry. *Nature, 543*, 51-59

Tagliabue, A., Buck, K.N., Sofen, L.E., Twining, B.S., Aumont, O., Boyd, P.W., Caprara, S., Homoky, W.B., Johnson, R., Konig, D., Ohnemus, D.C., Sohst, B., & Sedwick, P. (2023). Authigenic mineral phases as a driver of the upper-ocean iron cycle. *Nature, 620*, 104-109

Tagliabue, A., Mtshali, T., Aumont, O., Bowie, A.R., Klunder, M.B., Roychoudhury, A.N., & Swart, S. (2012). A global compilation of dissolved iron measurements: focus on distributions and processes in the Southern Ocean. *Biogeosciences, 9*, 2333-2349

Takeuchi, M., Doubell, M.J., Jackson, G.A., Yukawa, M., Sagara, Y., & Yamazaki, H. (2019). Turbulence mediates marine aggregate formation and destruction in the upper ocean. *Sci Rep, 9*, 16280

Tanioka, T., & Matsumoto, K. (2017). Buffering of Ocean Export Production by Flexible Elemental Stoichiometry of Particulate Organic Matter. *Global Biogeochemical Cycles, 31*, 1528-1542

Taucher, J., Bach, L.T., Riebesell, U., & Oschlies, A. (2014). The viscosity effect on marine particle flux: A climate relevant feedback mechanism. *Global Biogeochemical Cycles, 28*, 415-422

Taylor, J.R., & Ferrari, R. (2011). Shutdown of turbulent convection as a new criterion for the onset of spring phytoplankton blooms. *Limnology and Oceanography, 56*, 2293-2307

Thackeray, S.J. (2012). Mismatch revisited: what is trophic mismatching from the perspective of the plankton? *Journal of Plankton Research, 34*, 1001-1010

Thackeray, S.J., Henrys, P.A., Hemming, D., Bell, J.R., Botham, M.S., Burthe, S., Helaouet, P., Johns, D.G., Jones, I.D., Leech, D.I., Mackay, E.B., Massimino, D., Atkinson, S., Bacon, P.J., Brereton, T.M., Carvalho, L., Clutton-Brock, T.H., Duck, C., Edwards, M., Elliott, J.M., Hall, S.J., Harrington, R., Pearce-Higgins, J.W., Hoye, T.T., Kruuk, L.E., Pemberton, J.M., Sparks, T.H., Thompson, P.M., White, I., Winfield, I.J., & Wanless, S. (2016). Phenological sensitivity to climate across taxa and trophic levels. *Nature, 535*, 241-245

Thomalla, S.J., Du Plessis, M., Fauchereau, N., Giddy, I., Gregor, L., Henson, S., Joubert, W.R., Little, H., Monteiro, P.M.S., Mtshali, T., Nicholson, S., Ryan-Keogh, T.J., & Swart, S. (2023a). Southern Ocean phytoplankton dynamics and carbon export: insights from a seasonal cycle approach. *Philos Trans A Math Phys Eng Sci, 381*, 20220068

Thomalla, S.J., Nicholson, S.-A., Ryan-Keogh, T.J., & Smith, M.E. (2023b). Widespread changes in Southern Ocean phytoplankton blooms linked to climate drivers. *Nature Climate Change, 13*, 975-984

Thomalla, S.J., Racault, M.-F., Swart, S., & Monteiro, P.M.S. (2015). High-resolution view of the spring bloom initiation and net community production in the Subantarctic Southern Ocean using glider data. *ICES Journal of Marine Science, 72*, 1999-2020

Thomas, M.K., Kremer, C.T., Klausmeier, C.A., & Litchman, E. (2012). A global pattern of thermal adaptation in marine phytoplankton. *Science, 338*, 1085-1088

Torres, M.A., Ritchie, R.J., Lilley, R., Grillet, C., & Larkum, A.W.D. (2013). Measurement of photosynthesis and photosynthetic efficiency in two diatoms. *New Zealand Journal of Botany, 52*, 6-27

Torres-Valdés, S., Tsubouchi, T., Bacon, S., Naveira-Garabato, A.C., Sanders, R., McLaughlin, F.A., Petrie, B., Kattner, G., Azetsu-Scott, K., & Whitledge, T.E. (2013). Export of nutrients from the Arctic Ocean. *Journal of Geophysical Research: Oceans, 118*, 1625-1644

Tréguer, P., Bowler, C., Moriceau, B., Dutkiewicz, S., Gehlen, M., Aumont, O., Bittner, L., Dugdale, R., Finkel, Z., Iudicone, D., Jahn, O., Guidi, L., Lasbleiz, M., Leblanc, K., Levy, M., & Pondaven, P. (2017). Influence of diatom diversity on the ocean biological carbon pump. *Nature Geoscience, 11*, 27-37

Turner, J.T. (2015). Zooplankton fecal pellets, marine snow, phytodetritus and the ocean's biological pump. *Progress in Oceanography, 130*, 205-248

van Vuuren, D.P., Edmonds, J., Kainuma, M., Riahi, K., Thomson, A., Hibbard, K., Hurtt, G.C., Kram, T., Krey, V., Lamarque, J.-F., Masui, T., Meinshausen, M., Nakicenovic, N., Smith, S.J., & Rose, S.K. (2011). The representative concentration pathways: an overview. *Climatic Change, 109*, 5-31

Vikebø, F.B., Broch, O.J., Endo, C.A.K., Frøysa, H.G., Carroll, J., Juselius, J., & Langangen, Ø. (2021). Northeast Arctic Cod and Prey Match-Mismatch in a High-Latitude Spring-Bloom System. *Frontiers in Marine Science, 8*

Ward, B.A., Collins, S., Dutkiewicz, S., Gibbs, S., Bown, P., Ridgwell, A., Sauterey, B., Wilson, J.D., & Oschlies, A. (2019). Considering the Role of Adaptive Evolution in Models of the Ocean and Climate System. *J Adv Model Earth Syst, 11*, 3343-3361

Wijffels, S., Roemmich, D., Monselesan, D., Church, J., & Gilson, J. (2016). Ocean temperatures chronicle the ongoing warming of Earth. *Nature Climate Change, 6*, 116-118

Winder, M., & Sommer, U. (2012). Phytoplankton response to a changing climate. *Hydrobiologia, 698*, 5-16

Wright, R.M., Le Quéré, C., Buitenhuis, E., Pitois, S., & Gibbons, M.J. (2021). Role of jellyfish in the plankton ecosystem revealed using a global ocean biogeochemical model. *Biogeosciences, 18*, 1291-1320

Xue, T., Frenger, I., Oschlies, A., Stock, C.A., Koeve, W., John, J.G., & Prowe, A.E.F. (2022). Mixed Layer Depth Promotes Trophic Amplification on a Seasonal Scale. *Geophysical Research Letters, 49*

Yamada, Y., Tomaru, Y., Fukuda, H., & Nagata, T. (2018). Aggregate Formation During the Viral Lysis of a Marine Diatom. *Frontiers in Marine Science, 5*

Yamaguchi, R., Rodgers, K.B., Timmermann, A., Stein, K., Schlunegger, S., Bianchi, D., Dunne, J.P., & Slater, R.D. (2022). Trophic level decoupling drives future changes in phytoplankton bloom phenology. *Nature Climate Change, 12*, 469-476

Yamaguchi, R., & Suga, T. (2019). Trend and Variability in Global Upper-Ocean Stratification Since the 1960s. *Journal of Geophysical Research: Oceans, 124*, 8933-8948

Zeng, H., Jia, G., & Forbes, B.C. (2013). Shifts in Arctic phenology in response to climate and anthropogenic factors as detected from multiple satellite time series. *Environmental Research Letters, 8*

Zhao, H., Matsuoka, A., Manizza, M., & Winter, A. (2022). Recent Changes of Phytoplankton Bloom Phenology in the Northern High-Latitude Oceans (2003–2020). *Journal of Geophysical Research: Oceans, 127*

Zhou, L., Wu, S., Gu, W., Wang, L., Wang, J., Gao, S., & Wang, G. (2021). Photosynthesis acclimation under severely fluctuating light conditions allows faster growth of diatoms compared with dinoflagellates. *BMC Plant Biol, 21*, 164

Supplementary Material A

Description of the PlankTOM12.2 equations

Erik Buitenhuis, Joe K. Guest, Rebecca M. Wright,
Philip Townsend and Corinne Le Quéré

September 2023

Contents

1 Introduction

This Supplement presents a full description of the PlankTOM model, a global marine biogeochemical model based on the representation of twelve Plankton Functional Types (PFTs), including six phytoplankton (pPFTs), five zooplankton (zPFTs) and bacteria. PlankTOM also represents the full cycles of C, O_2, P and Si and simplified cycles for Fe and N. This version comprises of 41-51 biogeochemical tracers (Table 1).

1.1 Notation

In the following sections, we will show the equations governing tracer and food-web dynamics. These equations are mostly semi-empirical, and have been developed and tested using a multitude of laboratory and field data. As long as not otherwise indicated, both tracers and their respective concentrations will be designated by capital letters, with

- P_i: concentration of pPFT$_i$ with $i \in \{1, 6\}$,
- Z_j: concentration of zPFT$_j$, with $j \in \{1, 5\}$,
- F_k: concentration of food k; where F_k includes phytoplankton and other food sources
- PRO: proto-zooplankton concentration,
- NO3: concentration of nitrate, etc.

All concentrations are calculated in $\frac{mol}{L}$ except for PO_4, which is in $\frac{molC}{L}$, chlorophyll, which is in $\frac{gCHL}{L}$, and alkalinity, which is in $\frac{equivalent}{L}$.

Tables and an index are provided which link the mathematical symbols with the variable names used in the Fortran code. Where subscript j includes pico-heterotrophs in addition to the zoo-plankton types this is stated explicitly.

The plankton functional types and the tracers are shown in Figure 1. Figures of this type showing the processes governing the evolution of the PFTs and tracers are included in the following sections.

1.2 Tracer Transport

The temporal evolution of all passive tracers T is governed by the balance between its local sources and sinks ('Sources-Minus-Sinks' (SMS), biogeochemical part) and by the physical transport processes (advection and diffusion), hence

$$\frac{dT}{dt} = \nabla \cdot (\vec{u}T) + \nabla \cdot (\vec{K}\nabla T) + SMS, \tag{1}$$

where $\vec{K}$ is the 3-dimensional tracer diffusion coefficient and $\vec{u}$ is the fluid velocity, calculated in the physical model.

To ensure numerical stability, the sinks processes in SMS are set to zero then the concentration of passive tracers fall below a set threshold (1.e-10).

Table 1: List of biogeochemical Tracers in PlankTOM

Abbreviation	**Description**	**Units**
ALK	alkalinity	eq L^{-1}
ARA	aragonite	mol L^{-1}
B14B	bomb 14C	mol L^{-1}
BAC	pico-heterotrophs	mol L^{-1}
BFE	Fe in large POM	mol L^{-1}
BSI	biogenic particulate silica	mol L^{-1}
C11	CFC11	mol L^{-1}
C14B	no-bomb 14C	mol L^{-1}
CAL	sinking $CaCO_3$	mol L^{-1}
CCH	chlorophyll in calcifiers	g L^{-1}
CFE	Fe in calcifiers	mol L^{-1}
CH4	methane	mol L^{-1}
COC	calcifying phytoplankton	mol L^{-1}
DCH	chlorophyll in silicifiers	g L^{-1}
DFE	Fe in silicifiers	mol L^{-1}
DIA	silicifying phytoplankton	mol L^{-1}
DIC	dissolved inorganic carbon	mol L^{-1}
DOC	dissolved organic carbon	mol L^{-1}
DMS	dimethylsulphide	mol L^{-1}
DMD	dimethylsulphoniopropionate	mol L^{-1}
DSI	sinking particulate silica	mol L^{-1}
FCH	chlorophyll in N_2 fixers	g L^{-1}
FER	dissolved iron	mol L^{-1}
FFE	Fe in N_2 fixers	mol L^{-1}
FIX	N_2 fixing phytoplankton	mol L^{-1}
FOR	foraminifers	mol L^{-1}
GEL	jellyfish / gelatinous zooplankton	mol L^{-1}
GOC	large particulate organic carbon	mol L^{-1}
GON	large particulate organic nitrogen	mol L^{-1}
HCH	chlorophyll in DMSP producers	mol L^{-1}
HFE	Fe in DMSP producers	mol L^{-1}
MAC	(crustacean) macrozooplankton	mol L^{-1}
MES	mesozooplankton	mol L^{-1}
MIX	mixed phytoplankton	mol L^{-1}
N2O	prognostic nitrous oxide	mol L^{-1}
N2S	diagnostic nitrous oxide	mol L^{-1}
NCH	chlorophyll in mixed phytoplankton	g L^{-1}
NFE	Fe in mixed phytoplankton	mol L^{-1}
NH4	ammonium + ammonia	mol L^{-1}
NO3	nitrate	mol L^{-1}
OXY	dissolved oxygen	mol L^{-1}
PCH	chlorophyll in pico-phytoplankton	g L^{-1}
PFE	Fe in pico-phytoplankton	mol L^{-1}
PIC	pico-phytoplankton	mol L^{-1}
PHA	DMSp producing phytoplankton	mol L^{-1}
PIIC	pre-industrial DIC	mol L^{-1}
PO4	phosphate	mol C L^{-1}
POC	small particulate organic carbon	mol L^{-1}
PRO	proto-zooplankton	mol L^{-1}
PTE	pteropods	mol L^{-1}
SFE	Fe in small POM	mol L^{-1}
SIL	dissolved SiO_3	mol L^{-1}

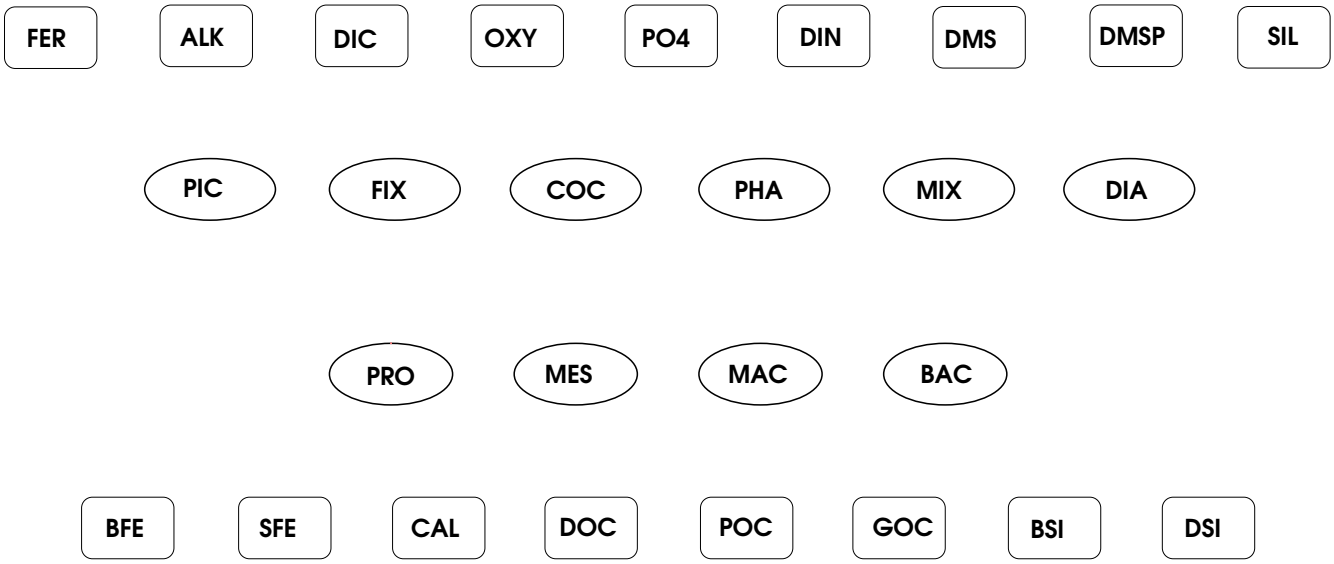

Figure 1: The constituents of PlankTOM; PFTs are shown as ellipses and tracers as rounded rectangles.There are also tracers for the chlorophyll and iron content of the individual pPFTs but these have been omitted from the figures for clarity.

2 Autotrophs

2.1 Primary Production, Photosynthesis and Phytoplankton Biomass - PIC, FIX, COC, PHA, MIX, DIA

The processes governing evolution of phytoplankton biomass for each P_i is shown in Figure 2. Evolution in terms of carbon is described in this section; chlorophyll (Section 2.3) and iron in phytoplankton (Section 2.2) are modelled similarly. Growth of phytoplankton modifies dissolved organic carbon (Section 4.1), silica (Section 6.2), calcium carbonate (Section 5.1), phosphate, dissolved inorganic nitrogen (Section 6.3), alkalinity (Section 5.3) and oxygen (Section 6.4) in the ocean.

The temporal evolution of phytoplankton biomass is given in the equation below:

$$\frac{\partial P_i}{\partial t} = \underbrace{\mu^{P_i} P_i}_{production} - \underbrace{\mu^{P_i} \delta^{P_i} P_i}_{loss} - \underbrace{\sum_j g_{P_i}^{Z_j} Z_j P_i}_{grazing} \tag{2}$$

$g_{P_i}^{Z_j} * Z_j * P_i$ describes the amount of biomass lost in grazing by the zPFT $Z_j, j \in \{1, 5\}$ as described in Section 3. In the present configuration of the model all available phytoplankton are grazed so there is no mortality term.

μ_P is the phytoplankton growth rate and is a function of temperature, light and nutrient availability:

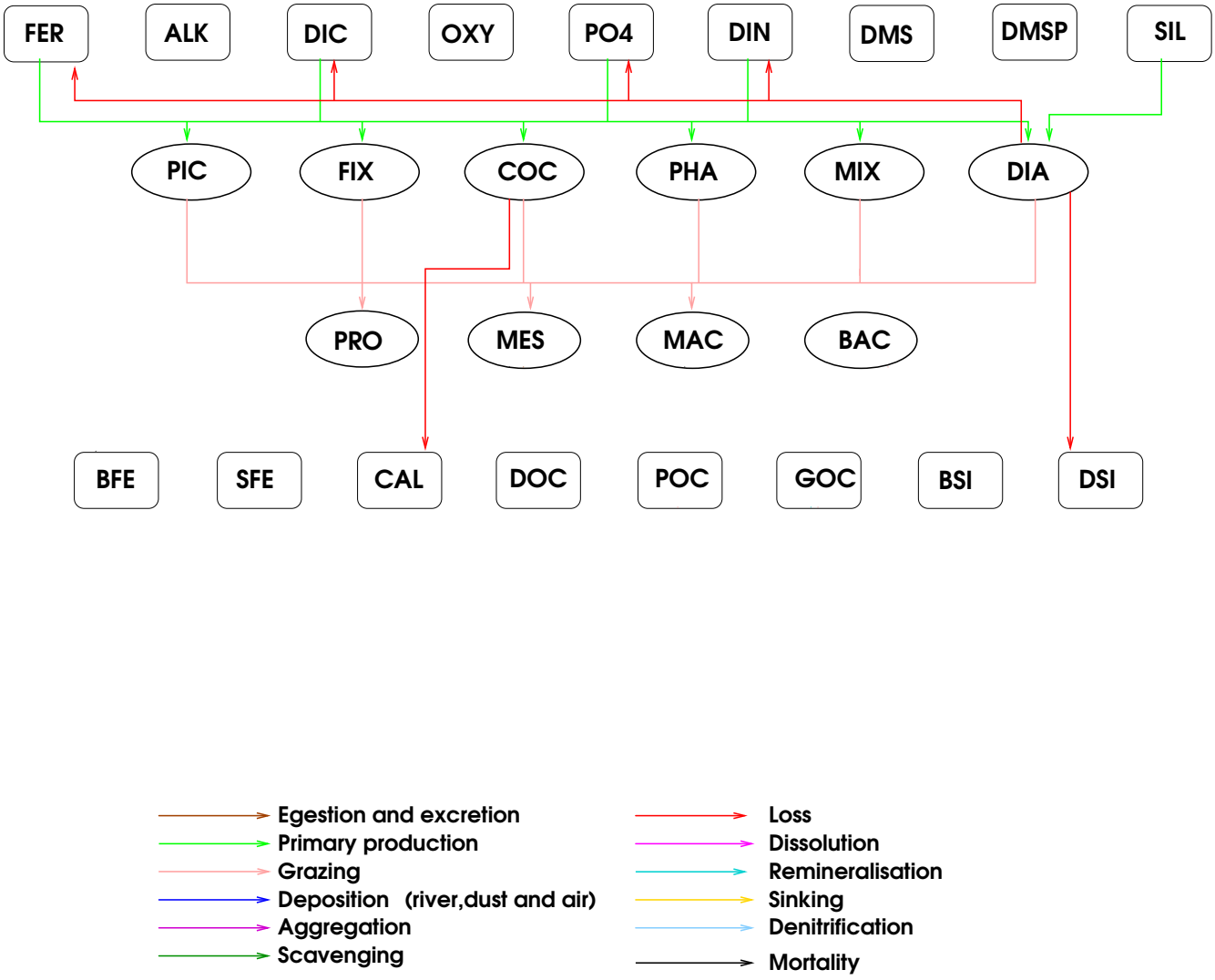

Figure 2: The processes governing the development of the phytoplankton.

$$\begin{aligned}\mu^{P_i} &= \mu_{opt}^{P_i} * (1 + \delta^{P_i}) * f(T) * f(PAR) * f(nut) \\ &= \mu_{opt}^{P_i} * (1 + \delta^{P_i}) * f(T) * L_{light}^{P_i} * L_{nut}^{P_i} \end{aligned} \tag{3}$$

where $\mu_{opt}^{P_i}$ is the optimum growth rate, and δ^{P_i} is the fraction of particulate photosynthesis that is respired.

The temperature dependence of the growth rate is

$$f(T) = e^{-1 * \frac{(T - Topt)^2}{\Delta T^2}} \tag{4}$$

where T_{opt} is the optimum temperature, at which $\mu = \mu_{opt}$, ΔT is the width of the temperature response, such that $\mu = \frac{\mu_{opt}}{e}$ at $T = T_{opt} \pm \Delta T$, and T is the seawater temperature in $^{\circ}$Celsius.

For coccolithophorids the growth rate below 10° is reduced to $(0.2 + 0.8 * \frac{T}{10.}) * f(T)$.

The radiation available for photosynthesis is dependent on the wavelength and the depth:

$$\begin{aligned} PAR(z + \Delta z) &= .215 * Q_{sr} * e^{-\left(\sum_i x_g + CHL^{P_i} * y_g^{P_i}\right)\Delta z} \\ &+ .215 * Q_{sr} * e^{-\left(\sum_i x_r + CHL^{P_i} * y_r^{P_i}\right)\Delta z}. \end{aligned} \tag{5}$$

where the fraction of available solar radiation Q_{sr} which is in the photosynthetically active wavelength range has been divided between the blue/green and red wavelengths, x_g, x_r are the extinction coefficients of pure water for blue/green and red wavelengths and $y_g^{P_i}$, $y_r^{P_i}$ are the extinction coefficients of chlorophyll.

$$perfrm = \alpha^{P_i} * \frac{CHL^{P_i}}{P_i} 4.6 * PAR(z) \tag{6}$$

and

$$pctnut = \mu_0^{P_i} * (1 + \delta^{P_i}) * f(T) * L_{nut}^{P_i} \tag{7}$$

then

$$L_{light} = 1 - e^{-\frac{perfrm}{pctnut}} \tag{8}$$

The nutrient limitation ($L_{nut}^{P_i}$) determines the limitation of the growth rate due to the availability of nutrients. It is assumed that nutrient limitation follows Michaelis-Menten kinetics and that growth is determined by the least available nutrient. Hence, for phytoplankton other than silicifiers and nitrogen fixers:

Hence, for phytoplankton other than silicifiers and nitrogen fixers:

$$L_{nut}^{P_i} = \min\left(\frac{PO_4}{PO_4 + K_{PO_4}^{P_i}}, \frac{\frac{Fe_{P_i}}{P_i} - Fe_{P_i}^{min}}{Fe_{P_i}^{opt} - Fe_{P_i}^{min}}, dinlim\right) \tag{9}$$

$$dinlim = \frac{NH_4}{NH_4 + K_{NH4}^{P_i}} + \frac{NO_3(1 - \frac{NH_4}{NH_4 + K_{NH4}^{P_i}})}{NO_3 + K_{NO3}^{P_i}} \tag{10}$$

for silicifiers:

$$L_{nut}^{DIA} = \min\left(\frac{PO_4}{PO_4 + K_{PO_4}^{DIA}}, \frac{\frac{Fe_{DIA}}{DIA} - Fe_{DIA}^{min}}{Fe_{DIA}^{opt} - Fe_{DIA}^{min}}, dinlim, \frac{Si}{Si + K_{Si}^{DIA}}\right). \tag{11}$$

and for nitrogen fixers:

$$L_{nut}^{FIX} = \min\left(\frac{PO_4}{PO_4 + K_{PO_4}^{FIX}}, \frac{\frac{Fe_{FIX}}{FIX} - Fe_{FIX}^{min}}{Fe_{FIX}^{opt} - Fe_{FIX}^{min}}, dinlim + R_{FIX}\,(1 - dinlim)\right) \tag{12}$$

R_{fix} is the fraction of the maximum growth rate that can be achieved when growing on N_2.

2.2 Iron in phytoplankton / Fe in pPFTs - DFe, NFe, CFe, PFe, HFe, FFe

The iron content of phytoplankton (DFE for silicifiers, NFE for mixed-phytoplankton, CFE for calcifiers, PFE for picophytoplankton, HFE for DMS producers and FFE for N_2-fixers) is given by:

The iron content of phytoplankton (DFE for silicifiers, NFE for mixed-phytoplankton, CFE for calcifiers, PFE for picophytoplankton, HFE for DMS producers and FFE for N_2-fixers) is given by:

$$\begin{aligned}\frac{\partial Fe^{P_i}}{\partial t} &= \underbrace{\mu_{opt}^{P_i}(1+\delta^{P_i})f(T)L_{Q_{Fe}}^{P_i}L_{nutFe}^{P_i}P_i}_{production} - \underbrace{\mu_{opt}^{P_i}\delta_{P_i}f(T)L_{Q_{Fe}}^{P_i}L_{nutFe}^{P_i}P_i}_{loss} \\ &- \underbrace{\sum_j g_{P_i}^{Z_j} Z_j * Fe^{P_i}}_{grazing}\end{aligned} \tag{13}$$

$\rho_{Fe}^{P_i}$ describes the iron-light colimitation to phytoplankton growth [Buitenhuis and Geider, 2010] and is given by:

$$L_{Q_{Fe}}^{P_i} = \left(\frac{(\frac{\rho max}{\rho min} Fe_{P_i}^{max} - Fe_{P_i}^{max})(Fe_{Pi}^{max} - \frac{Fe_{P_i}}{P_i})}{(Fe_{P_i}^{max} - Fe_{P_i}^{min})} + Fe_{P_i}^{max} \right) * L_{light} \quad (14)$$

in which L_{light} is described in Eq. 8. For phytoplankton other than nitrogen fixers and silicifiers the nutrient limitation is given by:

$$L_{nutFe}^{P_i} = \min \left(\frac{PO_4}{PO_4 + K_{PO_4}^{P_i}}, \frac{FER}{FER + K_{FER}^{P_I}}, dinlim \right) \quad (15)$$

in which dinlim is defined in Eq. 10, for silicifiers

$$L_{nutFe}^{DIA} = \min \left(\frac{PO_4}{PO_4 + K_{PO_4}^{DIA}}, \frac{FER}{FER + K_{FER}^{DIA}}, dinlim, \frac{Si}{Si + K_{Si}^{DIA}} \right). \quad (16)$$

and for nitrogen fixers:

$$L_{nutFe}^{FIX} = \min \left(\frac{PO_4}{PO_4 + K_{PO_4}^{FIX}}, \frac{FER}{FER + K_{FER}^{FIX}}, dinlim + R_{FIX}\,(1 - dinlim) \right) \quad (17)$$

2.3 Chlorophyll - DCH, NCH, CCH, PCH, HCH, FCH

The chlorophyll content of each phytoplankton type (DCH for silicifiers, NCH for mixed-phytopla -nkton, CCH for calcifiers and PCH for picophytoplankton, HCH for DMS-producers and FCH for N_2-fixers) is modelled. Chlorophyll evolves in a very similar fashion to phytoplanktonic biomass (see equation 2), as sources and sinks of chlorophyll are of phytoplanktonic origin. The iron-light colimitation model is a dynamical photosynthesis model in which the rate of photosynthesis both controls cellular iron and chlorophyll synthesis and is controlled by their quota [Buitenhuis and Geider, 2010].

$$\begin{aligned} \frac{\partial Chl^{P_i}}{\partial t} &= \underbrace{\rho_{Chl}^{P_i} L_{light} pctnut P_i}_{production} - \underbrace{\mu_0^{P_i} \delta_{P_i} b_{P_i}^T * Chl^{P_i}}_{loss} \\ &- \underbrace{\sum_j g_{P_i}^{Z_j} Z_j \frac{Chl_{P_i}}{P_i}}_{grazing}, \end{aligned} \quad (18)$$

where

$$\rho_{Chl}^{P_i} = \theta_{chl}^{P_i} * pctnut * \frac{L_{light}}{perfrm} \quad (19)$$

$\theta_{chl}^{P_i}$ is the maximum chlorpophyll to carbon ratio for phytoplankton P_i and $perfrm$ and $pctnut$ are defined in equations 6 and 7

Table 2: List of Parameters and variables used to compute the evolution of phytoplankton

Term	**Variable**	**Description**	**Defined in**
δ_{P_i}	rn_resphy	respiration as fraction of growth	namelist.trc.sms
$\mu_{opt}^{P_i}$	rn_mumpft	optimum growth rate	namelist.trc.sms
$\mu^{P_i} P_i$	prophy	productivity of phytoplankton P_i	bgcpro.F90
T_{opt}	rn_mutpft	optimum temperature of growth rate	namelist.trc.sms
ΔT	rn_mudpft	width of temperature response curve	namelist.trc.sms
$f(T)$	tgfunc	temperature dependence of growth rate	bgcpro.F90
α^{P_i}	rn_alpphy	initial slope of photosynthesis vs light intensity curve	namelist.trc.sms
PAR	etot	Photosynthetcally active radiation	bgcpro.F90
Q_{sr}	qsr	surface solar radiation	traqsr.F90
x_g	rn_ekwgrn	absorption coefficient of water for blue-green light	namelist.trc.sms
x_r	rn_ekwred	absorption coefficient of water for red light	namelist.trc.sms
$y_g^{P_i}$	rn_kgrphy	absorption coefficient of chlorophyll for blue-green	namelist.trc.sms
$y_r^{P_i}$	rn_krdphy	absorption coefficient of chlorophyll for red light	namelist.trc.sms
$perfrm$	perfrm	photosynthetic performance	bgcpro.F90
$pctnut$	pctnut	macronutrient and temperature defined growth rate	bgcpro.F90
L_{light}	xlim8	Light limitation for phytoplankton growth	bgcpro.F90
$Fe_{P_i}^{max}$	rn_qmaphy	Maximum Fe quota	namelist.trc.sms
$Fe_{P_i}^{min}$	rn_qmiphy	Minimum Fe quota	namelist.trc.sms
$Fe_{P_i}^{opt}$	rn_qopphy	Optimum Fe quota	namelist.trc.sms
$K_{FER}^{P_i}$	rn_kmfphy	half saturation constant of Fe	namelist.trc.sms
$K_{NH4}^{P_i}$	rn_kmhphy	half-saturation coefficients for $NH4$	namelist.trc.sms
$K_{NO3}^{P_i}$	rn_kmnphy	half-saturation coefficients for $NO3$	namelist.trc.sms
$K_{PO4}^{P_i}$	rn_kmpphy	half-saturation coefficients for $PO4$	namelist.trc.sms
K_{SIL}^{DIA}	rn_sildia	half-saturation coefficient for SIL in diatoms	namelist.trc.sms
$L_{nut}^{P_i}$	xlimpft	macronutrient limitation for phytoplankton growth	bgcpro.F90
$\frac{\rho max}{\rho min}$	rn_rhfphy	ratio between iron starved and iron saturated maximum iron uptake rates	namelist.trc.sms
$\theta_{Chl}^{P_i}$	rn_thmphy	maximum CHL:C ratio	namelist.trc.sms
$\rho_{Chl}^{P_i}$	rhochl	regulation term of chlorophyll synthesis	bgcpro.F90

3 Heterotrophic PFT's

The temporal evolution of zooplankton and the pico-heterotrophs are shown in Figure 3.

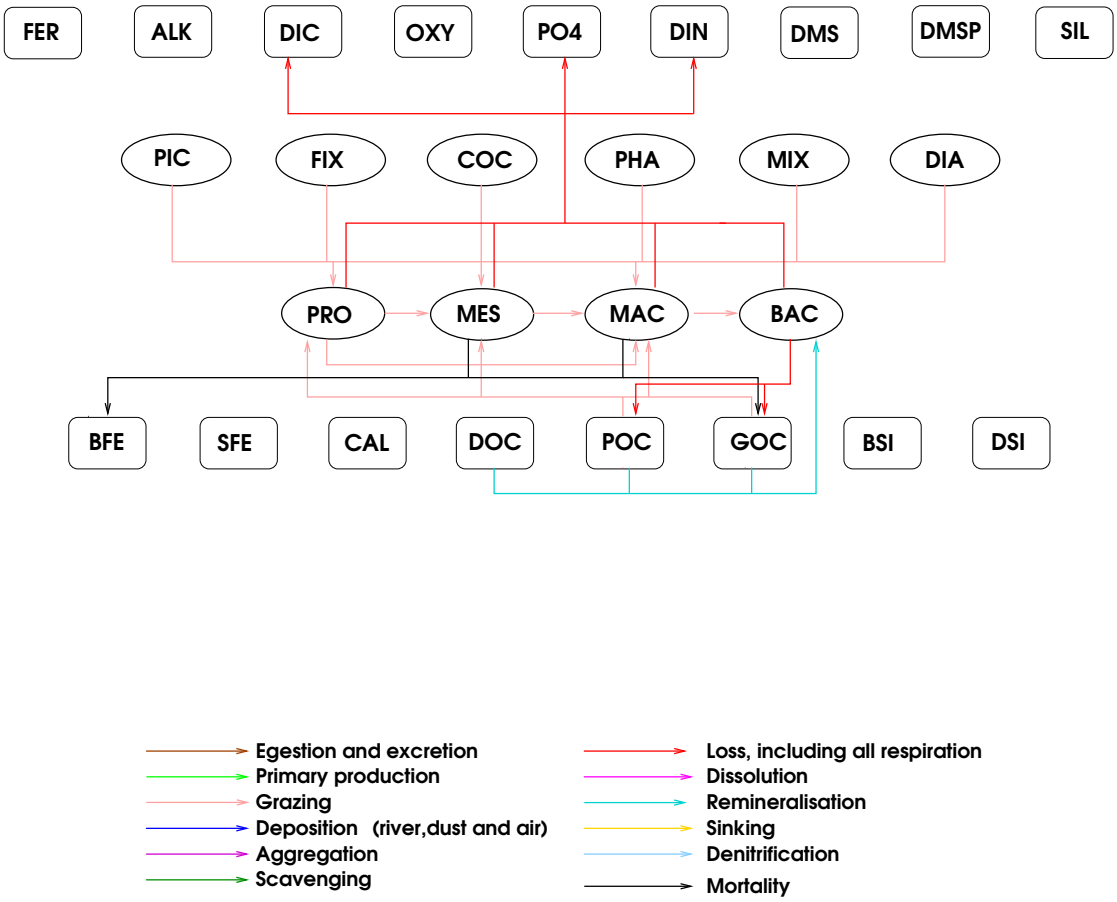

Figure 3: The processes governing the development of the zooplankton and pico-heterortrophs.

3.1 Zooplankton Biomass

The temporal evolution of zooplankton concentrations Z_j in PlankTOM are described as follows [Buitenhuis et al., 2006]:

$$\frac{\partial Z_j}{\partial t} = \underbrace{\sum_{k=1}^{j} g_{F_k}^{Z_j} * F_k * MGE * Z_j}_{growth\ through\ grazing} - \underbrace{\sum_{k=j}^{5} g_{Z_j}^{Z_k} * Z_j * Z_k}_{loss\ through\ grazing} - \underbrace{R_{0^\circ}^{Z_j} * d_{Z_j}^{T} * Z_j}_{basal\ respiration}$$
$$- \underbrace{m_{0^\circ}^{Z_j} * c_{Z_j}^{T} * \frac{Z_j}{K^{Z_j} + Z_j} * \sum_i (Z_j + P_i)}_{mortality\ through\ predation}, \quad (20)$$

where $g_{F_k}^{Z_j}$ is the grazing of zooplankton Z_j on food source F_k and MGE is the growth efficiency. $R_{0^\circ}^{Z_j}$ is the respiration rate at 0°C, d_{Z_j} is the temperature dependence of the respiration ($d^{10} = Q_{10}$). $m_{0^\circ}^{Z_j}$ is the mortality rate at 0°C, c_{Z_j} is the temperature dependence of the mortality ($c^{10} = Q_{10}$). K^{Z_j} is the half saturation constant for mortality and is set to $20 * 10^{-6}$.

The mortality term for jellyfish and macrozooplankton is due to predation by top predators for which the total zooplankton plus phytoplankton biomass is used as a proxy.

In the presence of ice krill are protected from predation so the macrozooplankton mortality is reduced by a factor of .01.

Grazing $g_{F_k}^{Z_j}$, of zooplankton Z_j on food source F_k is dependent on the zooplankton preference, $p_{F_k}^{Z_j}$, the concentration of the food source and the temperature

$$g_{F_k}^{Z_j} = f(T) \frac{p_{F_k}^{Z_j}}{K^{Z_j} + \sum_i p_{F_k}^{Z_j} F_k} \quad (21)$$

in which f(T) is defined in Eq. 4. The food sources F for zooplankton are shown in Table 3.

Table 3: Food sources for zooplankton and pico-heterotrophs

Z_j / Food	Macro-	Jellyfish	Meso-	Pteropods	Proto-zooplankton	Pico-heterotrophs
Macro-zooplankton		*				
Jellyfish	*					
Meso-zooplankton	*	*				
Pteropods	*	*	*			
Proto-zooplankton	*	*	*	*		
Phytoplankton	*	*	*	*	*	
Pico-heterotrophs	*	*	*	*	*	
Large POM	*	*	*	*	*	*
Small POM	*	*	*	*	*	*
Dissolved OM						*

In shallow water (<600m) in the summer months under ice coverage of between .1 and .3 macrozooplankton experience enhanced recruitment [Wiedenmann et al., 2009]. This is included by increasing the growth rate by a factor r_{MAC} when these conditions apply.

The model growth efficiency MGE, a function of gross growth efficiency (GGE), describes the fraction of grazed food incorporated into zooplankton biomass and basal respiration normalised to all material ingested. Equation 39 shows the possible reduction in MGE_{Z_j} when zooplankton graze on phytoplankton with a lower $\frac{Fe}{C}$ ratio than themselves.

Table 4: List of parameters and variables used to calculate the evolution of zooplankton

Term	**Variable**	**Description**	**Defined in**
$g_0^{Z_j}$	rn_grazoo	zooplankton optimum grazing rate	namelist.trc.sms
$g_{max}^{Z_j}$	graze	grazing rate at local T	bgclos.F90
b_{Z_j}	rn_mutpft	Temperature dependence of grazing	namelist.trc.sms
r_{MAC}	rn_icemac	enhanced recruitment factor under ice	namelist.trc.sms
p_F^Z	rn_prfzoo	zooplankton grazing preferences	namelist.trc.sms
K^{Z_j}	rn_grkzoo	half-saturation constant for grazing	namelist.trc.sms
σ^{Z_j}	rn_sigzoo	Fraction of zooplankton excretion as DIC	namelist.trc.sms
ξ^{Z_j}	rn_unazoo	Fraction of unassimilated food	namelist.trc.sms
MGE_{Z_j}	mgezoo	model growth of efficiency	bgcbio.F90
$R_{0^\circ}^{Z_j}$	rn_reszoo	zooplankton respiration at 0°C of	namelist.trc.sms
d_{Z_j}	rn_retzoo	Temperature dependence of zoo. respiration	namelist.trc.sms
$m_{0^\circ}^Z$	rn_mormac	mortality at 0°C of macrozoo.	namelist.trc.sms
c_{Z_j}	rn_motmac	temperature dependence of mortality	namelist.trc.sms
GGE_{Z_j}	rn_ggezoo	Growth efficiency	namelist.trc.sms

3.2 Pico-heterotrophs

The temporal evolution of bacterial concentration is modelled in a similar way to zooplankton:

$$\begin{aligned}\frac{\partial BAC}{\partial t} &= \underbrace{\sum \lambda_{OC}^{*} BGE * BAC}_{growth\ through\ remineralisation} - \underbrace{R_{0^\circ}^{BAC} * d_{BAC}^{T} * BAC}_{respiration} \\ &- \underbrace{\sum_j g_{BAC}^{Z_j} * BAC * Z_j}_{grazing} \end{aligned} \tag{22}$$

where BGE is the bacterial growth efficiency.

The food sources OM for bacteria are DOC, small and large particulate organic carbon and iron (POC, GOC, SFe and BFe).

Mineralisation rate λ^*_{OM} is dependent on the temperature and the available food:

$$\lambda^*_{OM} = M_{opt} f(T) \eta_O \frac{\sum_k p^{BAC}_{OC} OM}{K^{BAC}_{OC} + \sum_k p^{BAC}_{OC} OC}, \tag{23}$$

where M_{opt} is the optimum assimilation rate, f(T) is defined in Eq. 4, bacterial growth is dependent on the available oxygen:

$$\eta_O = \frac{OXY + 3 * 10^{-6}}{OXY + 10 * 10^{-6}}, \tag{24}$$

which leads to a maximum bacterial growth rate in the absence of oxygen that is 0.3 times the maximum growth rate at high oxygen, each food source is associated with a preference p^{BAC}_{OC}, OM in the numerator can be either carbon or iron, while OC in the denominator is always carbon.

K^{BAC}_{OC} is the half-saturation constant for mineralisation of organic matter.

$R^{BAC}_{0^\circ}$ is the respiration rate at 0°C, d_{BAC} is the temperature dependence of the respiration ($d^{10} = Q_{10}$).

Bacterial growth efficiency BGE, which describes the fraction of mineralised food incorporated into bacterial biomass, is a function temperature and iron availability :

$$BGE = min(BGE_{0^\circ} - e * T, \frac{FER_{BAC} + \lambda^*_{SFe} BAC + \lambda^*_{BFe} BAC)}{max((\lambda^*_{DOC} BAC + \lambda^*_{POC} BAC + \lambda^*_{GOC} BAC) * \frac{Fe}{C}_H, 1e-25)}) \tag{25}$$

where BGE_{0° is the bacterial growth efficiency at 0° and e is the temperature dependence of bacteria growth, FER_{BAC} is the uptake of dissolved Fe (see equation 48), and $\lambda^*_{GOC}, \lambda^*_{DOC}, \lambda^*_{POC}$ are the remineralisation rates for DOC, GOC and POC respectively as defined above.

Grazing of bacteria by zooplankton is described in the previous section.

3.2.1 Denitrification

When waters become suboxic, bacteria can also use nitrate in order to gain oxidative power for DOC remineralization. Hence, there is a (bacterial) denitrification term in the model (Eq. 62).

Table 5: List of parameters and variables used to calculate the evolution of pico-heterotrophs

Term	**Variable**	**Description**	**Defined in**
M_{opt}	rn_grabac	Optimum assimilation rate of bacteria	namelist.trc.sms
K_{OC}^{BAC}	rn_kmobac	carbon half saturation constant of bacteria	namelist.trc.sms
p_F^{BAC}	rn_gbadoc	bacterial preference for DOC	namelist.trc.sms
	rn_gbapoc	bacterial preference for POC	namelist.trc.sms
	rn_gbagoc	bacterial preference for GOC	namelist.trc.sms
	rn_gbagon	bacterial preference for GON	namelist.trc.sms
BGE_{0°	rn_ggebac	Bacterial growth efficiency at 0°	namelist.trc.sms
$R_{0^\circ}^{BAC}$	rn_resbac	respiration at 0°C	namelist.trc.sms
d_{BAC}	rn_retbac	Temperature dependence of respiration	namelist.trc.sms
e	rn_ggtbac	Temperature dependence of bacterial growth efficiency	namelist.trc.sms
FER_{BAC}	ubafer	Uptake of dissolved Fe by bacteria	bgcsnk.F90
η_O	$\frac{OXY+3*10^{-6}}{OXY+10*10^{-6}}$	oxygen limitation to bacteria growth	
$\lambda^*_{SFe}BAC$	remsfe	remineralisation of Fe in POC	bgcsnk.F90
$\lambda^*_{BFe}BAC$	rembfe	remineralisation of Fe in GOC	bgcsnk.F90
$\lambda^\star_{DOC}BAC$	remdoc	remineralisation of DOC	bgcnul.F90,bgcsnk.F90
$\lambda^\star_{POC}BAC$	rempoc	remineralisation of POC	bgcnul.F90,bgcsnk.F90
$\lambda^\star_{GOC}BAC$	remgoc	remineralisation of GOC	bgcnul.F90,bgcsnk.F90
$\frac{Fe}{C}_H$	ferat3	Fe:C of heterotrophs	trcini_planktom.F90

4 Organic matter and bacterial Remineralisation

The source and sinks for dissolved organic carbon (DOC) and small (POC) and large (GOC) particulate carbon are shown in Figure 4.

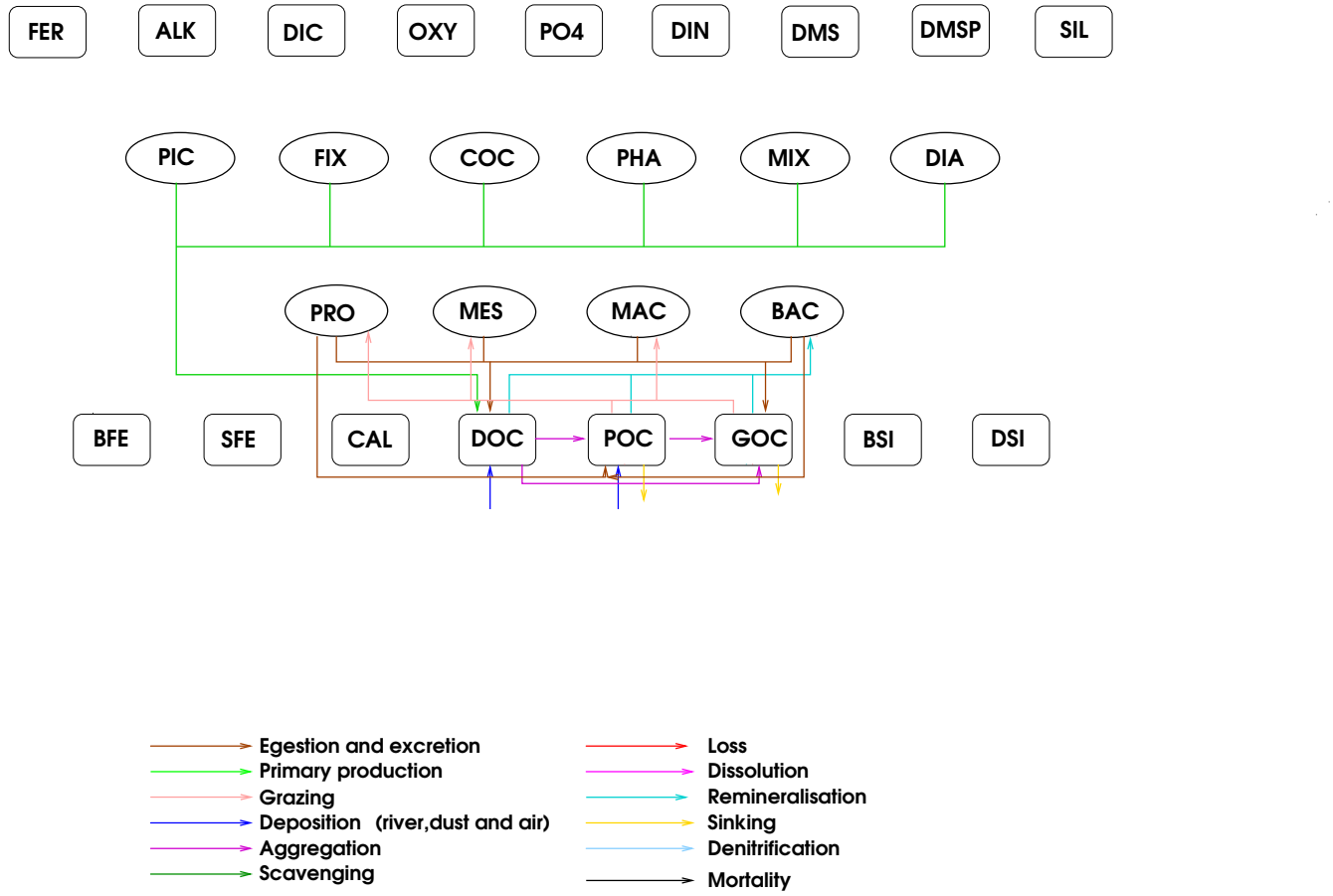

Figure 4: The source and sinks for dissolved organic carbon (DOC) and small (POC) and large (GOC) particulate carbon.

4.1 Dissolved Organic Carbon - DOC

The evolution of DOC is calculated in the following way:

$$\begin{aligned}\frac{\partial DOC}{\partial t} &= \underbrace{\sum \nu_{P_i}^{tot} \mu^{P_i} P_i}_{production} + \underbrace{\sum_j \left[(1-\sigma^{Z_j})(1-\xi^{Z_j} - MGE^{Z_j}) \sum_k g_{F_k}^{Z_j} * F_k * Z_j \right]}_{egestion} \\ &+ \underbrace{.333 R_{0^\circ}^{BAC} d_{BAC}^T BAC}_{excretion} - \underbrace{\lambda_{DOC}^\star BAC}_{remineralisation} - \underbrace{\Phi_{agg}^{DOC \to POC} - \Phi_{agg}^{DOC \to GOC}}_{aggregation} \\ &+ \underbrace{DOC_{riv}}_{river\ input}, \end{aligned} \tag{26}$$

where $\nu_{P_i}^{tot} = \nu_{P_i} + (1 - L_{nut}^{P_i}) \nu_{P_i}^{max}$ is the fraction of phytoplankton growth (Eq. 3) which forms DOC. Bacterial degradation of DOC is given by equation 23.

The aggregation functions $\Phi_{agg}^{X \to Y}$ are described in Section 4.2.

Table 6: List of Parameters used in bacterial remineralisation of DOC

Term	Variable	Description	Defined in
ν_{P_i}	rn_docphy	minimum DOC excretion ratio	namelist.trc.sms
$\nu_{p_i}^{max}$	rn_domphy	maximum DOC excretion ratio	namelist.trc.sms
$g_{F_i}^{Z_j} Z_j$	grazoc	Total grazing by zPFT	bgclos.F90
d_{BAC}	rn_retbac	temperature dependence of bacterial respiration	namelist.trc.sms
DOC_{riv}	depdoc	River input of DOC	trcini

4.2 Particulate aggregation

Particle aggregation through either differential sinking or turbulent coagulation is calculated by:

$$\begin{aligned}\Phi_{agg}^{DOC \to POC} &= \phi_5^{DOC} \epsilon DOC^2 + \phi_7^{DOC} \epsilon DOC\, POC \\ \Phi_{agg}^{DOC \to GOC} &= \phi_6^{DOC} \epsilon\, DOC\, GOC \\ \Phi_{agg}^{POC \to GOC} &= \phi_1^{POC} \epsilon POC^2 + \phi_2^{POC} \epsilon GOC\, POC \\ &\quad + \phi_3^{POC} POC\, GOC + \phi_4^{POC} POC^2 \end{aligned} \tag{27}$$

In which ϵ is the shear rate. The coefficients ϕ were obtained by integrating the standard curvilinear kernels for collisions over the size range of each organic matter pool.

Table 7: List of Parameters used in particulate aggregation

Term	Variable	Description	Defined in
$\Phi_{agg}^{DOC \rightarrow POC}$	xaggdoc	DOC-POC aggregation	bgcsnk.F90
$\Phi_{agg}^{DOC \rightarrow GOC}$	xaggdoc2	DOC-GOC aggregation	bgcsnk.F90
$\Phi_{agg}^{POC \rightarrow GOC}$	xagg	POC-GOC aggregation	bgcsnk.F90
ϕ_5^{DOC}	rn_ag5doc	DOC-POC aggregation	namelist.trc.sms
ϕ_7^{DOC}	rn_ag7doc	DOC-POC aggregation	namelist.trc.sms
ϕ_6^{DOC}	rn_ag6doc	DOC-GOC aggregation	namelist.trc.sms
ϕ_1^{POC}	rn_ag1poc	POC-GOC aggregation	namelist.trc.sms
ϕ_2^{POC}	rn_ag2poc	POC-GOC aggregation	namelist.trc.sms
ϕ_3^{POC}	rn_ag3poc	POC-GOC aggregation	namelist.trc.sms
ϕ_4^{POC}	rn_ag4poc	POC-GOC aggregation	namelist.trc.sms

4.3 Sinking

Using the data in Ploug et al. [2008] and applying the drag equations of Buitenhuis et al. [2001] results in a new function describing the relationship between particle density and sinking speed [Buitenhuis et al., 2013]:

$$V_{sink} = k_{GOC} * MAX(\rho_{particle} - \rho_{seawater}, \rho_{min})^{S_{GOC}}, \tag{28}$$

where, if ρ_{GOC} (=1.08), ρ_{CAL} (=1.34) and ρ_{DSI} (=1.2) are the densities of the organic matter, $CaCO_3$, and SiO_2 respectively, the particle density $\rho_{particle}$ is calculated by:

$$\rho_{particle} = \frac{(GOC * 240. + CAL * 100. + DSI * 60.)}{\max(\frac{GOC*240.}{\rho_{GOC}} + \frac{CAL*100.}{\rho_{CAL}} + \frac{DSI*60.}{\rho_{DSI}}, 10^{-15})} \tag{29}$$

and

$$\rho_{min} = \left(\frac{S_{POC}}{k_{GOC}}\right)^{\frac{1}{S_{GOC}}} \tag{30}$$

4.4 Sediment model

PlankTOM has a very simple sediment model in order to prevent the accumulation of very high particulate matter in the bottom water layer, which led to instabilities in the tracer advection. The sediment model is one layer below the bottom water layer. To facilitate computation, the height of the sediment is the same as the height of the bottom

Table 8: List of Parameters used in sinking

Term	Variable	Description	Defined in
S_{POC}	rn_snkpoc	sinking speed of POC	namelist.trc.sms
S_{GOC}	rn_snkgoc	sinking speed parameter for GOC	namelist.trc.sms
k_{GOC}	rn_singoc	second sinking speed parameter for GOC	namelist.trc.sms
ρ_{min}	dnsmin	density at which GOC sinking speed is rn_snkpoc	trcnam_planktom.F90
$\rho_{seawater}$	rhop	density of sea-water	
$\rho_{particle} - \rho_{seawater}$	xdens	density of particle	bgcsnk.F90
V_{sink}	xvsink	sinking speed of particle	bgcsnk.F90

water layer (fse3t), so that inventories and concentrations may be treated as interchangeable. The sediment layer receives material from sinking fluxes of POC, GOC, GON, CAL, ARA, DSI, SFE and BFE. The remineralisation rates are the same as in the overlying bottom water layer (equations 23, 35, 50). Nutrients are removed from the sediment model to balance river and dust inputs and thus maintain constant inventories.

4.5 Small particulate organic carbon - POC

The temporal evolution of small particulate organic carbon, POC, is calculated as

$$\begin{aligned}
\frac{\partial POC}{\partial t} = & \underbrace{\xi^{PRO} * \sum_{F_i} g_{F_i}^{PRO} PRO}_{proto-zooplankton\ unassimilated\ food} - \underbrace{\sum_{Z_j} g_{POC}^{Z_j} * Z_j * POC}_{grazing\ on\ POC} \\
& + \underbrace{0.333 * R_{0^\circ}^{BAC} * d_{BAC}^{T} * BAC}_{excretion} - \underbrace{\lambda_{POC}^{\star} BAC}_{POC\ remineralisation} - \underbrace{S_{POC} \frac{\partial POC}{\partial z}}_{POC\ sinking} \\
& + \underbrace{\Phi_{agg}^{DOC \to POC}}_{aggregation\ to\ POC} - \underbrace{\Phi_{agg}^{POC \to GOC}}_{aggregation\ to\ GOC} + \underbrace{POC_{riv}}_{river\ input} . \qquad (31)
\end{aligned}$$

Here, ξ^{PRO} is the unassimilated fraction of grazed material, $g_{F_i}^{PRO}$ are the grazing coefficients of proto-zooplankton on food sources F as specified in equation 20, and all others variables are as above.

Table 9: List of parameters and variables used to calculate the evolution of POC

Term	Variable	Description	Defined in
K_{P_i}	rn_snkpoc	sinking speed POC	namelist.trc.sms
POC_{riv}	deppoc	river input of POC	trcini

4.6 Large particulate organic carbon - GOC

The temporal derivative of large particulate organic carbon (GOC) is calculated as

$$\begin{aligned}\frac{\partial GOC}{\partial t} &= \underbrace{\sum_j \xi^{Z_j} \sum_k g_{F_k}^{Z_j} * Z_j * F_k}_{zooplankton\ unassimilated\ food} - \underbrace{\sum_j g_{GOC}^{Z_j} * Z_j * GOC}_{loss\ through\ grazing} + \underbrace{\sum_j m_{0^\circ}^{Z_j} * c^T * Z_j}_{MES,MAC\ mortality} \\ &+ \underbrace{\Phi_{agg}^{DOC\to GOC} + \Phi_{agg}^{POC\to GOC} PHA}_{aggregation\ to\ GOC} - \underbrace{\lambda_{GOC}^{\star} BAC}_{GOC remineralisation} - \underbrace{V_{sink} \frac{\partial GOC}{\partial z}}_{GOC sinking}. \end{aligned} \tag{32}$$

ξ^{Z_j} is unassimilated fraction of material grazed by meso- and macro-zooplankton and m^{Z_j} is meso- and macro-zooplankton mortality as in equation (20). V_{sink} is the sinking rate of GOC and is calculated as equation (28).

5 Carbonate chemistry

5.1 Calcite - CAL and Aragonite - ARA

Calcification in the model is performed by phytoplankton calcifiers, COC, pteropods, PTE, and, in PlankTOM12.0 only, foraminifers, FOR. The sources and sinks for detached $CaCO_3$ (CAL and ARA), dissolved inorganic carbon (DIC) and alkalinity (ALK) are shown in Figure 5

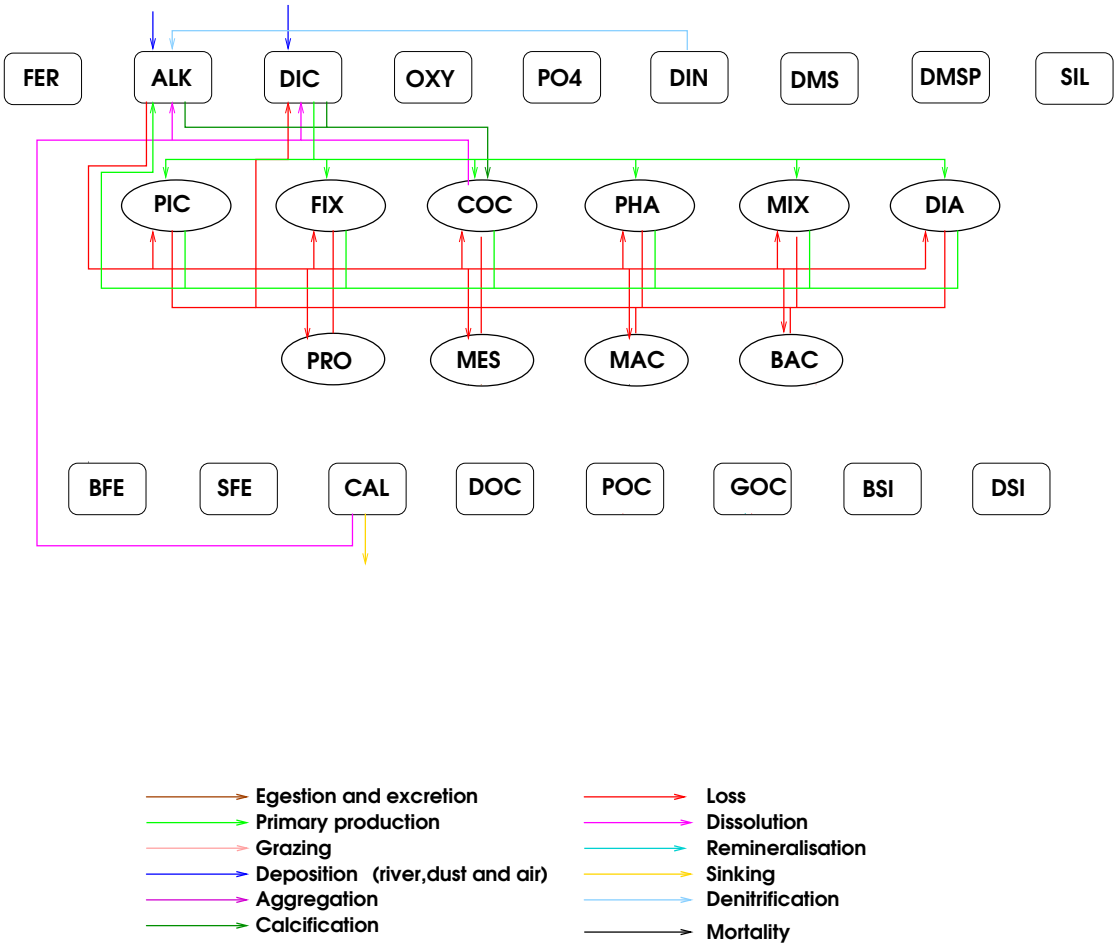

Figure 5: The source and sinks for detached carbonate (CAL), dissolved inorganic carbon (DIC) and alkalinity (ALK).

Attached $CaCO_3$ is produced in a fixed ratio to organic matter and therefore there are no tracers for their concentration. It does, however, reduce alkalinity, ALK, and dissolved inorganic carbon, DIC. Losses of calcifiers result in detached/sinking $CaCO_3$, and enters the tracer CAL (COC and FOR) or ARA (PTE).

$$\frac{\partial CaCO_{3attached}}{\partial t} = R_{CAL} \underbrace{\mu^{COC} COC}_{production\ by\ COC} \tag{33}$$

For detached $CaCO_3$, CAL and ARA:

$$\frac{\partial CAL}{\partial t} = R_{CAL}(1 - R_{diss}) \left(\underbrace{\mu_0^{COC} \delta_{COC} b_{COC}^T COC}_{COC\ loss} + \underbrace{\sum_j g_{COC}^{Z_j} Z_j * COC}_{grazing\ by\ zooplankton} \right) - \underbrace{V_{sink} \frac{\partial CAL}{\partial z}}_{sinking} - \underbrace{\beta_{CO_3} CAL}_{dissolution}, \tag{34}$$

where R_{CAL} is the calcification to calcifier organic carbon production ratio, R_{diss} is the fraction of attached $CaCO_3$ that is dissolved during losses of calcifiers, V_{sink} is the sinking speed of large particles and is described in section 4.3, and β_{CO_3} is the dissolution rate:

$$\beta_{CO_3} = MAX\left(M_{CO_3} * 1 - \Omega_{sat}, 0\right) \tag{35}$$

where Ω_{sat} is the deviation from saturation and M_{CO_3} is the maximum dissolution rate when Ω_{sat} = 0.

CAL and ARA are calculated in bgcbio.F90 and reduced by dissolution in bgclys.F90.

5.2 Dissolved inorganic carbon - DIC

The temporal evolution of dissolved inorganic carbon, DIC, is calculated as:

$$\frac{\partial DIC}{\partial t} = \underbrace{-\sum_i \mu^{P_i} * \left(1 + \nu_{P_i}^{TOT}\right) P_i}_{primary\ production} + \underbrace{consum}_{remineralisation} - \underbrace{R_{CAL} \mu^{COC} COC}_{attached\ CaCO_3} + R_{diss} R_{CAL} \left(\underbrace{\mu_0^{P_I} \delta_{COC} b_{COC}^T COC}_{COC\ loss} + \underbrace{\sum_j g_{COC}^{Z_j} Z_j COC}_{grazing\ by\ zooplankton} \right) + \underbrace{DIC_{riv}}_{river\ input} + \underbrace{\beta_{CO_3} CAL}_{dissolution} + \underbrace{F_{air-sea}^{CO_2}}_{air-sea\ flux}. \tag{36}$$

In addition to the inclusion of grazing by zooplankton remineralistion by bacteria is included as a function of

Table 10: List of parameters and variables used to calculate the evolution of calcite

Term	Variable	Description	Defined in
R_{CAL}	rn_coccal	$CaCO_3$:C_{org} ratio coccolithophores	namelist.trc.sms
	rn_forcal	$CaCO_3$:C_{org} ratio foraminifers	namelist.trc.sms
	rn_pteara	$CaCO_3$:C_{org} ratio pteropods	namelist.trc.sms
$\mu^{COC}COC$	prophy	coccolithophorid productivity	bgcpro.F90
	Eq. 20	PTE and FOR growth	bgclos.F90
R_{diss}	rn_discal	Fraction of $CaCO_3$ dissolved during coccolithophorid death	namelist.trc.sms
	rn_disfor	during foraminifer death	namelist.trc.sms
	rn_disara	during pteropod death	namelist.trc.sms
M_{CO_3}	rn_lyscal	maximum calcite dissolution rate	namelist.trc.sms
	rn_lysara	maximum aragonite dissolution rate	namelist.trc.sms
Ω_{sat}	omecal	calcite saturation state	bgclys.F90
	omeara	aragonite saturation state	bgclys.F90
$\beta_{CO_3}CAL$	remco3	calcite dissolution	bgclys.F90
	remara	aragonite dissolution	bgclys.F90
$V_{sink}CAL$	snkcal	sedimentation rate of calcite	bgcsnk.F90
	snkara	sedimentation rate of aragonite	bgcsnk.F90

their growth efficiency and respiration (in this case subscript j includes the pico-heterotrophs):

$$
\begin{aligned}
consum &= \underbrace{\sum_j \sigma^{Z_j} * (1 - \xi^{Z_j} - MGE^{Z_j}) \sum_k g_{F_k}^{Z_j} * Z_j * F_k}_{foodrespiration} \\
&+ \underbrace{(1 - BGE) * (\lambda^\star_{DOC} BAC + \lambda^\star_{POC} BAC + \lambda^\star_{GOC} BAC)}_{remineralisation} \\
&+ \underbrace{\sum_{j=1}^{3} R_{0^\circ}^{Z_j} d_{Z_j}^T Z_j}_{basal\ respiration} + \underbrace{.333 R_{0^\circ}^{BAC} d_{BAC}^T BAC}_{respiration} + \underbrace{\sum_i \delta_{P_i} b_{P_i}^T \mu_0^{P_i} P_i}_{loss} . \qquad (37)
\end{aligned}
$$

The bacterial growth efficiency, BGE, is given by Equation 25. The terms for attached $CaCO_3$ and production of DIC by dissolution are described in Section 5.1. River deposition DIC_{riv} is the input of DIC from rivers, see Section 8.6. The air-to-sea flux is described in section 7.

Dissolved inorganic carbon is calculated in bgcbio.F90; in bgclys.F90 the $CaCO_3$ dissolution to DIC is included while in bgcflx.F90 the air-sea flux of DIC is added.

Table 11: List of Parameters used in the evolution of DIC and ALK

Term	Variable	Description	Defined in
BGE	bactge	bacteria growth efficiency	bgcbio,bgcsnk.F90
DIC_{riv}	depdic	river input of DIC	river.nc, trcini
$R_{\frac{N}{C}}$	alknut	N+S+P to Carbon ratio	trcini

5.3 Alkalinity - ALK

The temporal evolution of alkalinity is calculated as:

$$\begin{aligned}\frac{\partial ALK}{\partial t} &= R_{\frac{N}{C}}\Big(\underbrace{\sum_i \mu^{P_i} P_i(1+\nu_{P_i}^{tot})}_{production} - \underbrace{consum}_{remineralisation}\Big) - \underbrace{2 * R_{CAL}\mu^{coc}COC}_{calcification} \\ &+ \underbrace{2R_{CAL}R_{diss}\big(\mu_0^{COC}\delta_{coc}b_{COC}^{T}COC + \sum_j g_{coc}^{Z_j}Z_jCOC\big)}_{dissolution} \\ &+ \underbrace{DIC_{riv}}_{river\ input} + \underbrace{N_{denit}}_{denitrification} + \underbrace{2 * \beta_{CO_3}CaCO_3}_{dissolution} \end{aligned} \quad (38)$$

where $R_{\frac{N}{C}} = \frac{N+S+P}{C} = \frac{16+6+1}{122}$ is the effect of nutrient uptake and remineralisation on alkalinity [Wolf-Gladrow et al., 2007]. The terms for the production of attached $CaCO_3$, dissolved COC and dissolved $CaCO_3$ are described in Section 5.1. River deposition, DIC_{riv} is described in Section 8.6 and denitrification, N_{denit} in Section 6.3.

6 Nutrients and gases

The processes governing the evolution of dissolved iron (FER), large (BFE) and small (SFE) particulate iron, dissolved silica (SIL), biogenic silica (BSI) and detrital silica (DSI) are shown in Figure 6.

The processes governing the evolution of phosphate (PO4), dissolved inorganic nitrogen (NO3 and NH4) and gases (OXY and optionally N2S, N2O and DMS) are shown in Figure 7.

6.1 The Iron Cycle

6.1.1 Fe in PFTs

The iron content of phytoplankton is presented in Section 2.2. The Fe/C ratio of zooplankton is fixed. If zooplankton graze on phytoplankton that have a higher Fe:C ratio than themselves, the excess is remineralised to dissolved

iron. If the phytoplankton Fe/C ratio is lower than zooplankton Fe:C, the model growth efficiency (MGE) is decreased:

$$MGE^{Z_j} = MIN\left(1-\xi^{Z_j}, GGE_{Z_j} + \frac{R_{0^\circ}^{Z_j} d_{Z_j}^T Z_j}{\sum_k g_{F_k}^{Z_j}}, \frac{\sum_k g_{F_k}^{Z_j} \frac{Fe_{F_k}}{F_k}(1-\xi^{Z_j})}{MAX\left(\sum_k g_{F_k}^{Z_j}\left(\frac{Fe}{C}\right)_Z, 1e-25\right)}\right) \quad (39)$$

6.1.2 Fe in detrital matter - BFE, SFE

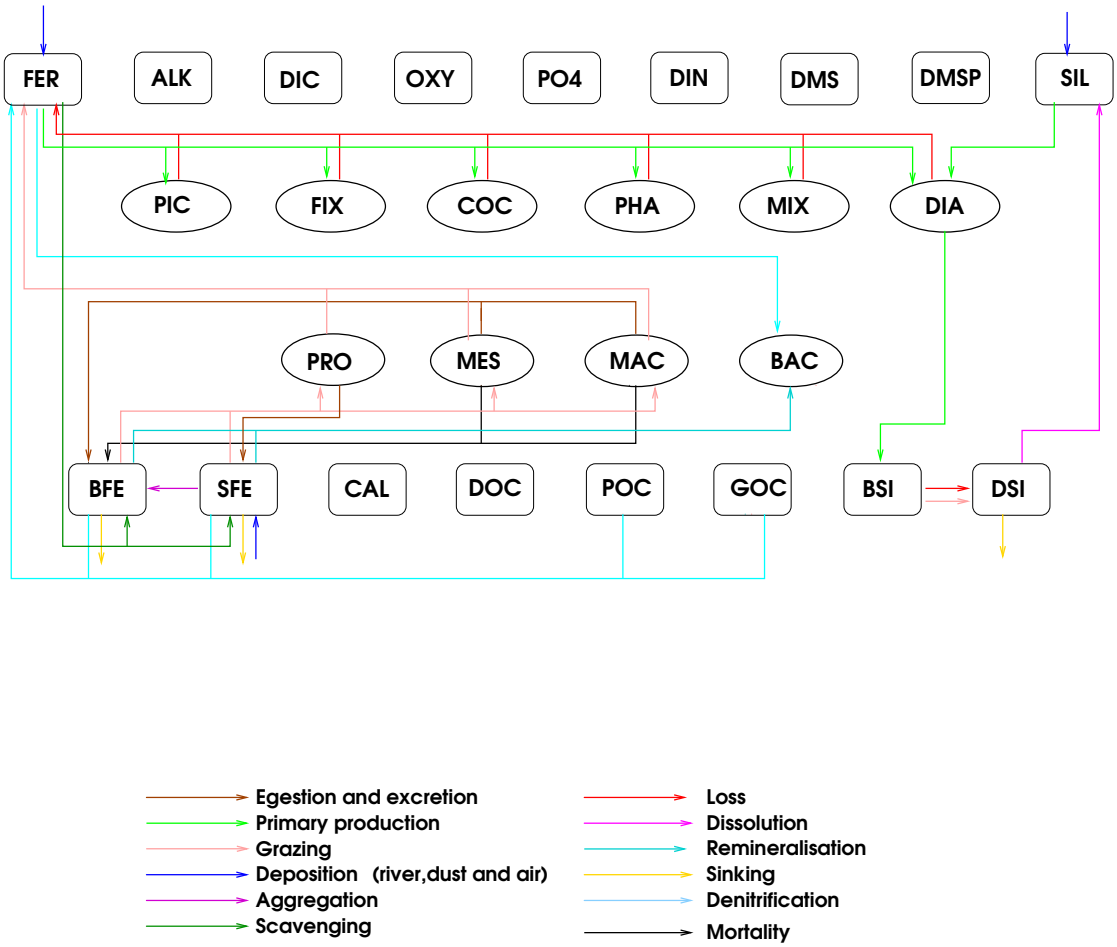

Figure 6: The sources and sinks for dissolved iron (FER), large (BFE) and small (SFE) particulate iron, dissolved silica (SIL), biogenic silica (BSI) and detrital silica (DSI).

Iron in detrital matter is divided into BFE in large organic particles (GOC) and SFE in small organic particles (POC). Production terms of particulate organic iron follow the Fe/C ratio of the source organisms. There is no iron

in DOM, but iron is added from dissolved iron to particulate organic iron during degradation of DOM. Degradation of POM conserves the Fe:C ratio of POM. The bottom correction removes as much carbon from the bottom water layers as is added by rivers (Section 8.6). Because iron is scavenged, the Fe/C ratio of POM sometimes becomes excessive. It is therefore set to a maximum, currently $2 * 10^{-6}$ mol:mol.

$$\begin{aligned}
\frac{\partial BFE}{\partial t} &= \underbrace{Fe_{scave}(POC+GOC+DSI+CAL)GOC}_{scavenging} - \underbrace{\sum_j g_{GOC}^{Z_j} * Z_j * GOC \frac{BFE}{GOC}}_{grazing\ loss} \\
&+ \underbrace{\left(\frac{Fe}{C}\right)_Z \sum_{j=MES,MAC} m_{0^\circ}^{Z_j} c^T z^j}_{mortality} + \underbrace{\sum_{j=MES,MAC} \xi^{Z_j} \sum_k g_{F_k}^{Z_j} * Z_j * F_k \frac{Fe_{F_k}}{F_k}}_{unassimilated\ food} \\
&+ \underbrace{\phi_{agg}^{POC\to GOC} \frac{SFE}{POC}}_{Fe\ aggregation} - \underbrace{\lambda_{GOC}^* Fe}_{remineralisation} - \underbrace{V_{sink} \frac{\partial BFE}{\partial z}}_{sinking\ of\ BFE}
\end{aligned} \tag{40}$$

$$\begin{aligned}
\frac{\partial SFE}{\partial t} &= \underbrace{Fe_{scave} * (POC+GOC+DSI+CAL) * POC}_{scavenging} \\
&- \underbrace{\sum_j g_{POC}^{Z_j} * Z_j * POC \frac{SFE}{POC}}_{grazing\ loss} + \underbrace{\xi^{MIC} \sum_k g_{F_k}^{MIC} * MIC * F_k \frac{Fe_{F_k}}{F_k}}_{unassimilated\ food} \\
&- \underbrace{\phi_{agg}^{POC\to GOC} \frac{SFE}{POC}}_{Fe\ aggregation} - \underbrace{\lambda_{SFe}^* BAC}_{remineralisation} - \underbrace{S_{POC} \frac{\partial SFE}{\partial z}}_{sinking\ of\ SFE} + \underbrace{\left(\frac{Fe}{C}\right)_Z POC_{riv}}_{river\ input}
\end{aligned} \tag{41}$$

The remineralisation λ_{SFe}^* is given by equation 23. Fe_{scav} is described below.

6.1.3 Dissolved Fe - FER

The temporal evolution of dissolved iron, FER, is calculated as follows:

$$\begin{aligned}
\frac{\partial FER}{\partial t} &= \underbrace{-\mu_{opt}^{P_i}(1+\delta^{P_i}) f(T) L_{Q_{Fe}}^{P_i} L_{nutFe}^{P_i} P_i}_{production} + \underbrace{\mu_{opt}^{P_i} \delta_{P_i} f(T) L_{Q_{Fe}}^{P_i} L_{nutFe}^{P_i} P_i}_{loss} \\
&+ \underbrace{\sum_j \left(\sum_k g_{f_k}^{z_j} * Z_j * F_k \frac{Fe_{F_k}}{F_k} (1-\xi^{Z_j}) - \left(\frac{Fe}{C}\right)_Z \sum_k g_{F_k}^{Z_j} * Z_j * F_k * MGE^{Z_j} \right)}_{grazing} \\
&+ \underbrace{FER_{remin_BFE_SFE}}_{mineralisation} - \underbrace{FER_{BAC}}_{bacterial\ uptake} - \underbrace{Fe_{scav}}_{scavenging} + \underbrace{Fe_{dep}}_{dust\ deposition} + \underbrace{Fe_{riv}}_{river\ input}
\end{aligned} \tag{42}$$

Iron is input from rivers, see Section 8.6, and the dissolution of dust from the atmosphere, see Section 8.5. Iron is taken up by phytoplankton during primary production (see above). When iron concentration is above 0.6 nM, it is scavenged by POM: the evolution of scavenged iron, Fe_{scav} is calculated as:

$$\begin{aligned} Fe_{scav} &= k_{scm} + k_{sc} * (POC + GOC + CAL + DSI) * 1e6 \\ &* \frac{-(1 + l_{Fe}k_{eq} - FERk_{eq}) + ((1 + l_{Fe}k_{eq} - FERk_{eq})^2 + 4FERk_{eq})^{0.5}}{2k_{eq}} \end{aligned} \tag{43}$$

where k_{scm} and k_{sc} are scavenging parameters and k_{eq} is given by:

$$k_{eq} = 10^{17.27 - \frac{1565.7}{T-19}}. \tag{44}$$

The iron ligand, l_{Fe} is set to a value of $.6 * 10^-9$ at latitudes North of 30S and below 200m depth, $.3 * 10^-9$ South of 40S and below 200 m, 0 above 100m depth, and linearly interpolated in between. Part of the scavenged iron is added to POM, and part is removed from the model.

Bacterial iron demand is

$$BAC\_Fe\_demand = BGE \left(\frac{Fe}{C}\right)_H * (\lambda^*_{DOC} + \lambda^*_{POC} + \lambda^*_{GOC}) * BAC \tag{45}$$

Bacterial iron supply is

$$BAC\_Fe\_supply = (\lambda^*_{SFe} + \lambda^*_{BFe}) * BAC \tag{46}$$

If supply exceeds demand, the rest contributes to FER:

$$FER_{remin\_BFE\_SFE} = MAX(BAC\_Fe\_supply - BAC\_Fe\_demand, 0.) \tag{47}$$

If demand exceeds supply, it draws on dissolved iron (FER):

$$FER_{BAC} = MAX((BAC\_Fe\_demand - BAC\_Fe\_supply) \frac{FER}{K^{BAC}_{FER} + FER}, 0.) \tag{48}$$

If there is not enough FER to meet this demand, BGE is decreased (Eq. 25).

6.2 The Silicate cycle

Silica is input from rivers and the dissolution of dust from the atmosphere. Growth of diatoms consumes dissolved silica (SIL) from the water to produce hydrated silica (biogenic silica BSI). Loss processes of diatoms produce sinking particulate silica (DSI).

Table 12: List of parameters and variables used to calculate the evolution of iron

Term	Variable	Description	Defined in
$FER_{remin\_BFE\_SFE}$	rbafer	Release of dissolved Fe by bacteria	bgcsnk.F90
Fe_{scav}	xscave	Iron scavenged by particulate organic matter	bgcsnk.F90
Fe_{riv}	depfer	River deposition	trcini
Fe_{dep}	irondep	Dust deposition	bgcbio.F90
k_{sco}	rn_scofer	Scavenging rate for iron by particles	namelist.trc.sms
k_{scm}	rn_scmfer	Minimum scavenging rate for iron	namelist.trc.sms
k_{eq}	xkeq	Scavenging rate parameter	bgcsnk.F90
l_{Fe}	ligfer	iron ligand concentration	bgcsnk.F90

6.2.1 Dissolved SiO_3 - SIL

The temporal evolution of dissolved silica is calculated as:

$$\begin{aligned}\frac{\partial SIL}{\partial t} &= \underbrace{\left(\frac{Si}{C}\right)_{DIA} \mu^{DIA} DIA}_{production} + \underbrace{\beta_{Si} DSI}_{dissolution} \\ &+ \underbrace{SIL_{riv}}_{river\ input} + \underbrace{SIL_{dep}}_{dustdeposition}\end{aligned} \tag{49}$$

where $\mu^{DIA} DIA$ is the primary production, in terms of carbon, of diatoms, β_{Si} is the remineralisation rate of silica which is dependent on temperature, T and oxygen OXY (equation 24):

$$\beta_{Si} = \min\left(rem_{DSI} e^{\frac{ret_{DSI}}{(273.15+T)}}, rem_{max,DSI}\right) \eta_O. \tag{50}$$

$\left(\frac{Si}{C}\right)_{DIA}$ increases with iron stress and silicate availability:

$$\left(\frac{Si}{C}\right)_{DIA} = max(\left(\frac{Si}{C}\right)_{FER}, \left(\frac{Si}{C}\right)_{SIL}) \tag{51}$$

$$\left(\frac{Si}{C}\right)_{FER} = 1. + \left(\frac{BSi}{DIA}\right)_{FER} * min\left(\frac{SIL}{K_{SIL}^{DIA}}, 1\right) * (1 - min\left(\frac{FER}{K_{FER}^{DIA}}, 1\right)). \tag{52}$$

where K_{SIL}^{DIA} and K_{FER}^{DIA} are the half saturation constant for SiO_3 and Fe in diatoms. Observations in the Southern Ocean show a high $\left(\frac{Si}{C}\right)_{DIA}$ ratio in areas with very high Si concentration so $\left(\frac{Si}{C}\right)_{DIA}$ is arbitrarily increased

throughout the ocean to reflect this:

$$\left(\frac{Si}{C}\right)_{SIL} = \left(\frac{BSi}{DIA}\right)_{SIL} * \frac{SIL}{SIL + K_{BSI}}. \tag{53}$$

$\left(\frac{Si}{C}\right)_{DIA}$ is set to the higher of these two ratios. SIL_{dep} is described in 8.5 and SIL_{riv} in 8.6.

Equation (53) is inherited from PISCES [Aumont, 2005] and derived from Equation (8) of Jeandel et al. [1998].

Table 13: List of parameters and variables used to calculate the evolution of silica

Term	**Variable**	**Description**	**Defined in**
β_{Si}	siremin	remineraliation rate of silica (d^{-1})	bgcsnk.F90
$(\frac{BSi}{DIA})_{FER}$	rn_ferbsi	$(\frac{Si}{C})_{DIA}$ increase under Fe limitation	namelist.trc.sms
$(\frac{BSi}{DIA})_{SIL}$	rn_silbsi	$(\frac{Si}{C})_{DIA}$ increase under SiO3 limitation	namelist.trc.sms
$\mu^{DIA}DIA$	prophy	primary production of diatoms (mol (L timestep)$^{-1}$)	bgcpro.F90,bgcnul.F90
$(\frac{Si}{C})_{DIA}$	silfac	Si/C ratio of diatoms	bgcpro.F90
K_{FER}^{DIA}	rn_kmfphy	half saturation constant of Fe	namelist.trc.sms
K_{SIL}^{DIA}	rn_sildia	half saturation constant of SiO3	namelist.trc.sms
K_{BSI}	rn_kmsbsi	half saturation constant for $\left(\frac{Si}{C}\right)$	namelist.trc.sms
rem_{DSI}	rn_remdsi	remineralisation of DSI	namelist.trc.sms
ret_{DSI}	rn_retdsi	temperature depend. remineral. of DSI	namelist.trc.sms
$rem_{max,DSI}$	rn_readsi	max. remineralisation of DSI	namelist.trc.sms
$(\frac{Si}{C})_{min}$	rn_bsidia	minimum $(\frac{Si}{C})_{DIA}$	namelist.trc.sms
SIL_{riv}	depsil	river input of SiO_3	trcini
SIL_{dep}	sidep	input of atmospheric silica to the water column	bgcbio.F90

6.2.2 Biogenic particulate silica - BSI

The temporal evolution of biogenic silica is calculated as:

$$\begin{aligned} \frac{\partial BSI}{\partial t} &= \underbrace{\left(\frac{Si}{C}\right)_{min}\left(\frac{Si}{C}\right)_{DIA}\mu^{DIA}DIA}_{production} \\ &- \underbrace{\sum_j g_{DIA}^{Z_j} * Z_j * DIA\frac{BSI}{DIA}}_{grazing} - \underbrace{\delta_{DIA}\mu_0^{DIA}b^T\frac{BSI}{DIA}}_{loss} \end{aligned} \tag{54}$$

where δ^{DIA} is the fraction of diatom production that is respired/lost, and $\left(\frac{Si}{C}\right)_{DIA}$ is described above.

6.2.3 Sinking particulate silica - DSI

The temporal evolution of sinking particulate silica is calculated as:

$$\begin{aligned}\frac{\partial DSI}{\partial t} &= \underbrace{\delta_{DIA}\mu_0^{DIA}b^T\frac{BSI}{DIA}}_{loss} - \underbrace{\beta_{Si}DSI}_{dissolution} \\ &+ \underbrace{\sum_j g_{DIA}^{Z_j} * Z_j * DIA\frac{BSI}{DIA}}_{grazing} + \underbrace{V_{sink}\frac{\partial DSI}{\partial z}}_{sinking\ DSI}\end{aligned} \tag{55}$$

6.3 Phosphorus and Nitrogen - PO4, NH4 and NO3

Phosphate is input to the ocean by river deposition; it is consumed during phytoplankton growth and produced during respiration.

$$\frac{\partial PO4}{\partial t} = \underbrace{\sum -\mu^{P_i}P_i\left(1+\nu_{P_i}^{tot}\right)\frac{P}{C}}_{production} + \underbrace{consum\frac{P}{C}}_{remineralisation} + \underbrace{PO4_{riv}}_{river\ input} \tag{56}$$

$consum$ is defined in equation 37.

Dissolved ammonium evolves as:

$$\begin{aligned}\frac{\partial NH4}{\partial t} &= \underbrace{\sum -\mu^{P_i}P_i(1+\nu_{p_i}^{tot})\frac{N}{C}DIN_{NH4}}_{production} + \underbrace{consum\frac{N}{C}}_{remineralisation} \\ &- nitrification + \underbrace{NHy_{riv}\frac{N}{C}}_{river\ input} + \underbrace{NHy_{atm}}_{atmosphere\ deposition}\end{aligned} \tag{57}$$

For phytoplankton other than nitrogen fixers:

$$DIN_{NH4} = \frac{NH_4}{(NH_4 + K_{NH4}^{P_i})dinlim} \tag{58}$$

and for nitrogen fixers:

$$DIN_{NH4} = \frac{NH_4}{(NH_4 + K_{NH4}^{P_i})(dinlim + R_{fix}(1-dinlim))} \tag{59}$$

dinlim is defined in Eq. 10.

$$\begin{aligned}nitrification &= r_{nitrif} * max((1 - log(OXY * 1e6) * 0.159)(1 - resp_{BAC}^{NO_3}), 0) \\ &* \frac{NH4}{NH4 + K_{nitrif}} * d_{BAC}^T * NH4\end{aligned} \tag{60}$$

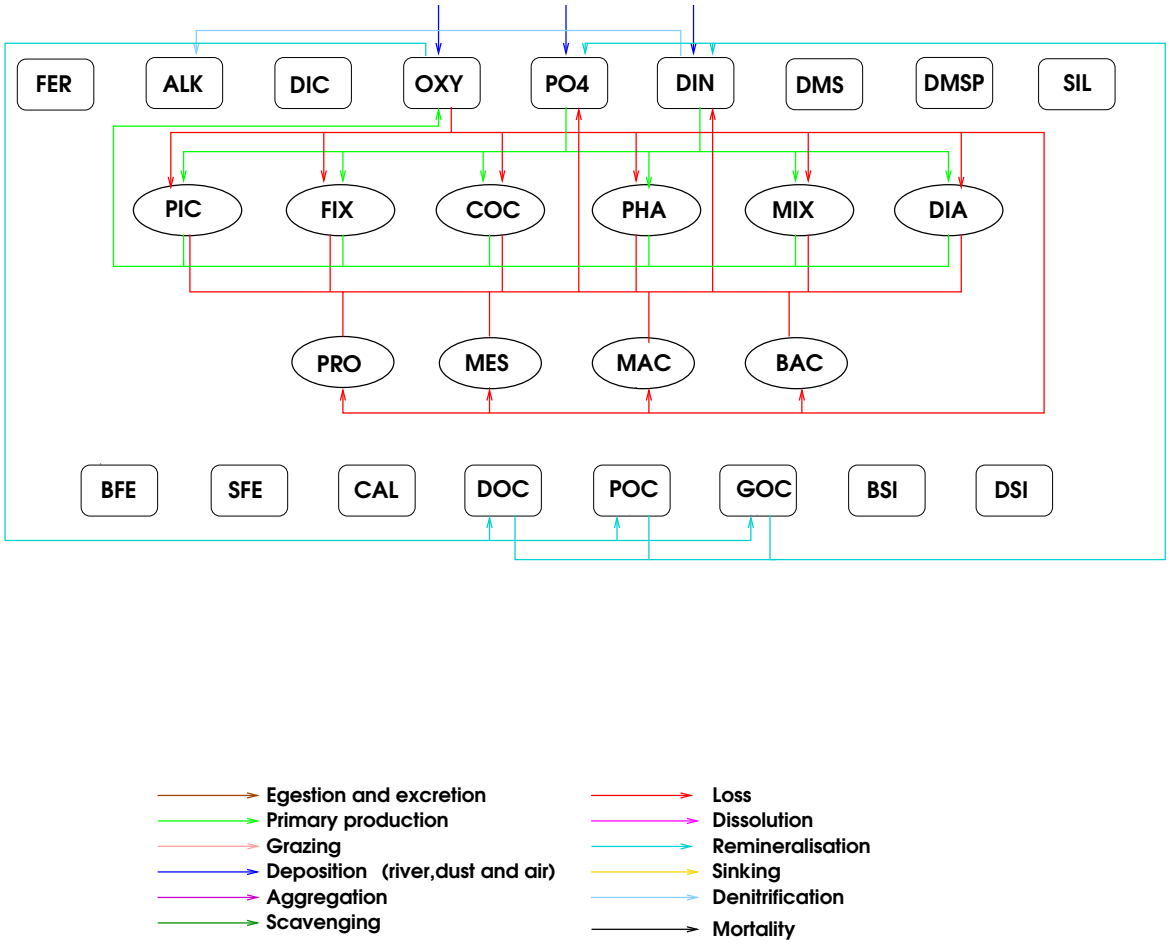

Figure 7: The sources and sinks for phophate (PO4), nitrogen (DIN=NH4+NO3), oxygen (OXY)).

Dissolved nitrate evolves as:

$$\frac{\partial NO3}{\partial t} = \underbrace{\sum -\mu^{P_i} P_i (1+\nu_{p_i}^{tot}) \frac{N}{C} DIN_{NO3}}_{production} - \underbrace{N_{denit}}_{denitrification} + \text{nitrification} + \underbrace{NOx_{riv}\frac{N}{C}}_{river\ input} + \underbrace{NOx_{atm}}_{atmosphere\ deposition} \tag{61}$$

where

$$N_{denit} = 0.8\left(\frac{O}{C} * consum * resp_{BAC}^{NO_3}\right). \tag{62}$$

$\frac{O}{C} = \frac{172}{122}$ and $resp_{BAC}^{NO_3}$ is the fraction of bacterial respiration that uses NO_3 rather than O_2 and is described in Section 6.4. For phytoplankton other than nitrogen fixers:

$$DIN_{NO3} = \frac{NO_3(1-\frac{NH_4}{NH_4+K_{NH4}^{P_i}})}{(NO_3+K_{NO3}^{P_i})dinlim} \tag{63}$$

and for nitrogen fixers:

$$DIN_{NO3} = \frac{NO_3(1-\frac{NH_4}{NH_4+K_{NH4}^{P_i}})}{(NO_3+K_{NO3}^{P_i})(dinlim+R_{fix}(1-dinlim))} \tag{64}$$

6.4 Oxygen - OXY

Oxygen is produced during the growth of phytoplankton. It is consumed during the growth of N_2 fixers on N_2 and during the remineralisation described by the term $consum$ in Section 5.2. There is also an exchange of oxygen with the atmosphere.

$$\frac{\partial OXY}{\partial t} = \underbrace{\frac{O}{C}\sum \mu^{P_i} P_i \left(1+\nu_{P_i}^{tot}\right)}_{phytoplankton\ growth} - \underbrace{\frac{N}{C}\mu^{P_{fix}} P_{fix}\left(1+\nu_{FIX}^{tot}\right)1.25(1-DIN_{nit})}_{growth\ of\ N_2\ fixers\ on N_2} - \underbrace{\frac{O}{C} consum(1-resp_{BAC}^{NO_3})}_{remineralisation} + \underbrace{F_{air-sea}^{O_2}}_{O_2\ flux\ from\ air\ to\ sea} \tag{65}$$

The fraction of bacterial respiration that uses NO_3 rather than O_2, $resp_{BAC}^{NO_3}$ is given by:

$$resp_{BAC}^{NO_3} = \frac{\sin\left(\max\left(-.5, \frac{8.5E-6-OXY}{17E-6+OXY}\right) * \pi\right) + 1}{2} \tag{66}$$

Table 14: List of Parameters used in the evolution of phosphate and nitrogen

Term	Variable	Description	Defined in
DIN_{NH4}	1-dinpft	fraction of phyto growth that is supported by NH4	bgcpro.F90
DIN_{NO3}	dinpft	fraction of phyto growth that is supported by NO3	bgcpro.F90
$K^{P_i}_{NH4}$	rn_kmhphy	NH_4 half saturation constants for phytoplankton	namelist.trc.sms
K_{nitrif}	rn_kmhnit	NH_4 half saturation constant nitrification	namelist.trc.sms
$K^{P_i}_{NO3}$	rn_kmnphy	NO_3 half saturation constants for phytoplankton	namelist.trc.sms
$\frac{N}{C}$	ratn2c	N:C ratio organic matter = 16:122	trcini
N_{denit}	denitr	denitrification	bgcbio.F90
NHy_{atm}	atmamm	Atmosphere input of NH_y	trcini
NHy_{riv}	depamm	River input of NH_y	trcini
NOx_{atm}	atmnit	Atmosphere input of NO_x	trcini
NOx_{riv}	depnit	River input of NO_x	trcini
$PO4_{riv}$	deppo4	River input of phosphate	trcini
R_{FIX}	rn_munfix	Fraction of growth rate during N_2 fixation relative to growth on fixed N	namelist.trc.sms
r_{nitrif}	rn_nitnh4	NH4 saturated nitrification rate at 0 C	namelist.trc.sms
$resp^{NO_3}_{BAC}$	nitrfac	fraction of bacterial respiration using NO_3 rather than O_2	bgcnul.F90

The air-sea exchange of oxygen, $F^{O_2}_{air-sea}$, is given by

$$F^{O_2}_{air-sea} = \left(\frac{O}{N}_{pi} sol_{O_2} \left(1. - e^{20.1050 - 0.0097982 * sstk - 6163.10/sstk} \right) - OXY \right) 0.27 v^2 (1 - \gamma) \quad (67)$$

The terms are described described in Section 7. It is calculated in bgcflx.F90.

6.5 Diagnostic nitrous oxide - N2S

The diagnostic formulation of nitrous oxide production is a function of O_2 consumption, with a yield that depends on the oxygen concentration. Under oxic conditions, there is a constant yield, while under suboxic conditions the yield increases as oxygen decreases :

$$\frac{\partial N2S}{\partial t} = (\alpha_{N_2O} + \beta_{N_2O} * exp(-0.1 * \frac{OXY - 1e-6}{1e-6})) * \frac{O}{C} consum(1 - resp^{NO_3}_{BAC}) \quad (68)$$

6.6 Prognostic nitrous oxide - N2O

The prognostic formulation of nitrous oxide production is a function of redox reactions in the nitrogen cycle.

$$\frac{\partial N2O}{\partial t} = (y_{nitrif} * nitrification + y_{denitr} * N_{denit} - y_{N2Ocons} * N_{N2Ocons} \quad (69)$$

$$N_{N2Ocons} = 0.8 \left(\frac{O}{C} * consum * \frac{\sin\left(\max\left(-.5, \frac{7E-6-OXY}{14E-6+OXY}\right) * \pi\right) + 1}{2} \right) \quad (70)$$

Table 15: List of Parameters used in the evolution of N2S and N2O

Term	Variable	Description	Defined in
α_{N_2O}	rn_aoun2s	yield of oxic N2O production	namelist.trc.sms
β_{N_2O}	rn_betn2s	yield of suboxic N2O production	namelist.trc.sms
$consum$	consum	remineralisation rate	Eq. 37 , bgcnul.F90
N_{denit}	denitr	denitrification	Eq. 62 , bgcbio.F90
$N_{N2Ocons}$	degn2o	N2O consumption rate/$y_{N2Ocons}$	Eq. 70 , bgcbio.F90
$nitrification$	nitrif	nitrification rate	Eq. 60 , bgcbio.F90
$\frac{O}{C}$	rato2c	-O2:C ratio = 172:122	trcini
$resp_{BAC}^{NO_3}$	nitrfac	fraction of bacterial respiration using NO_3 rather than O_2	Eq. 66 , bgcnul.F90
$y_{N2Ocons}$	rn_degn2o	yield of N2O consumption	namelist.trc.sms
y_{denitr}	rn_denn2o	N2O yield of denitrification	namelist.trc.sms
y_{nitrif}	rn_aoun2o	N2O yield of nitrification	namelist.trc.sms

6.7 Methane - CH4

Several formulations of methane cycling were tested: Formulation (1), (4) and (7): production is proportional to metazoan zooplankton fecal pellet production:

$$\frac{\partial CH4}{\partial t} = y_{fecpel} * \underbrace{\sum_j \xi^{Z_j} \sum_k g_{F_k}^{Z_j} * Z_j * F_k}_{zooplankton\ unassimilated\ food} \quad (71)$$

Formulations (1) has a globally invariant y_{fecpel}, in formulation (4) y_{fecpel} = 0 below 2000m, and formulation (7) has a different y_{fecpel} in the open ocean above 2000m and in the coastal ocean.

Formulation (2): production is proportional to O_2 consumption:

$$\frac{\partial CH4}{\partial t} = y_{respir} * \underbrace{\frac{O}{C} consum(1 - resp_{BAC}^{NO_3})}_{remineralisation} \quad (72)$$

Formulation (3):

$$\frac{\partial CH4}{\partial t} = y_{fecpel} * \sum_j \xi^{Z_j} \sum_k g_{F_k}^{Z_j} * Z_j * F_k - y_{respir} * \frac{O}{C} consum(1 - resp_{BAC}^{NO_3}) \quad (73)$$

Formulation (5):

$$\frac{\partial CH4}{\partial t} = y_{fecpel} * \sum_j \xi^{Z_j} \sum_k g_{F_k}^{Z_j} * Z_j * F_k + y_{respir} * \frac{O}{C} consum(1 - resp_{BAC}^{NO_3}) \quad (74)$$

with y_{fecpel} = 0 below 2000m, and y_{respir} = 0 everywhere except the bottom water layer.

Formulation (6):

$$\frac{\partial CH4}{\partial t} = y_{fecpel} * \sum_j \xi^{Z_j} \sum_k g_{F_k}^{Z_j} * Z_j * F_k + y_{hypoxic} * exp(-0.1 * \frac{OXY - 1e-6}{1e-6})) * \frac{O}{C} consum(1 - resp_{BAC}^{NO_3}) \quad (75)$$

7 Air-sea exchange of gases

The air-sea flux of gases (CO_2, O_2, and optionally DMS, N_2O and/or CH_4) is given by the product of gas exchange coefficient and the difference in concentration of the gas across the sea-air interface:

$$F_{air-sea} = k_w * (1 - \gamma) * (pC_{gas}^{air} - pC_{gas}^{sea}) \quad (76)$$

where k_w is the gas exchange coefficient, γ is the fraction of the ocean covered by ice, pC_{gas}^{air} is the concentration of the gas in the air directly above the water, and pC_{gas}^{sea} is the sea surface concentration of the gas.

The gas exchange coefficient is calculated according to Wanninkhof [1992] (eq. 3):

$$k_w = 0.27 * v^2 * \sqrt{660./Schmidt_{gas}} \quad (77)$$

where v is the amplitude of the winds (m/s), sst is the sea surface temperature, and Schmidt$_{gas}$ is the Schmidt number for each gas Wanninkhof [1992].

7.1 CO_2

For the gas exchange coefficient CO_2 Wanninkhof [1992] include a chemical enhancement term:

$$k_w^{CO_2} = 0.27 * v^2 + 2.5 * (0.5246 + 0.016256 * sst + 0.00049946 * sst^2) \quad (78)$$

For CO_2, $pC_{CO_2}^{air}$ is calculated from the measured mixing ratio of CO_2 in the atmosphere ($C_{CO_2}^{air}$, in ppm) times the solubility of CO_2 in sea water and corrected for 100% water vapor Sarmiento et al. [1992]:

$$pC_{CO_2}^{air} = C_{CO_2}^{air} * sol_{CO_2} * (1. - e^{20.1050 - 0.0097982 * sstk - 6163.10/sstk}) \quad (79)$$

where sstk is sea surface temperature in degree Kelvin. The solubility of CO_2 is given by:

$$sol_{CO_2} = e^{c00 + c01/(sstk*.01) + c02*\ln(sstk*.01) + sal*(c03 + c04*qtt + c05*(sstk*.01)^2)} * smicr \quad (80)$$

where sal is the salinity and the coefficents $c00$, $c01$, $c02$, $c03$, $c04$, $c05$ and $smicr$ are given by Wanninkhof [1992]. The Schmidt number for CO_2 is given by:

$$Schmidt_{CO_2} = 2073.1 - 125.62 * sst + 3.6276 * sst^2 - 0.043126 * sst^3 \tag{81}$$

$C^{sea}_{CO_2}$ is the concentration of CO_2 in the model, calculated based on the state variables DIC and TALK.

7.2 O_2

For O_2, $pC^{air}_{O_2}$ is calculated from the measured mixing ratio of O_2 in the atmosphere ($C^{air}_{O_2}$, times the solubility of O_2 in seawater, also corrected for 100% water vapor as for CO_2 Sarmiento et al. [1992]:

$$pC^{air}_{O_2} = C^{air}_{O_2} * sol_{O_2} * (1. - e^{20.1050 - 0.0097982 * sstk - 6163.10/sstk}) \tag{82}$$

The solubility of O_2 is calculated as follows:

$$\begin{aligned} sol_{O_2} &= e^{ox0 + ox1/(sstk*.01) + ox2*\ln(sstk*.01) + sal*(ox3 + ox4*(sstk*.01) + ox5*(sstk*.01)^2)} \\ &* \quad oxyco \end{aligned} \tag{83}$$

The Schmidt number for O_2 is given by:

$$Schmidt_{O_2} = 1953.4 - 128.0 * sst + 3.9918 * sst^2 - 0.050091 * sst^3 \tag{84}$$

where sal is the salinity and the coefficents $ox0$, $ox1$, $ox2$, $ox3$, $ox4$, $ox5$, and $oxyco$ are given by Wanninkhof [1992].

7.3 N_2O

pN_2O uses the same water vapor correction as CO_2.

The solubility of N_2O is calculated as follows (Weiss and Price 1980):

$$\begin{aligned} sol_{N_2O} = e^{(&-62.7062 + 97.3066/(sstk*.01) + 24.1406*\ln(sstk*.01) \\ &+ sal*(-0.058420 + 0.0331983*(sstk*.01) - 0.0051313*(sstk*.01)^2)) \end{aligned} \tag{85}$$

The Schmidt number for N_2O is given by Wanninkhof [1992]:

$$Schmidt_{N_2O} = 2301.1 - 151.1 * sst + 4.7364 * sst^2 - 0.059431 * sst^3 \tag{86}$$

7.4 CH_4

pCH_4 uses the same water vapor correction as CO_2.

The solubility of CH_4 is calculated as follows (Wiesenburg and Guinasso 1979):

$$sol_{CH_4} = e^{(-415.2807+596.8104/(sstk*.01)+379.2599*\ln(sstk*.01)-62.0757*(sstk*.01) \\ +sal*(-0.059160+0.032174*(sstk*.01)-0.0048198*(sstk*.01)^2))} \tag{87}$$

The Schmidt number for CH_4 is given by Wanninkhof [1992]:

$$Schmidt_{CH_4} = 2039.2 - 120.31 * sst + 3.4209 * sst^2 - 0.040437 * sst^3 \tag{88}$$

Table 16: List of parameters and variables used to calculate the evolution of air-sea fluxes

Term	Variable	Description	Defined in
v	wndm	wind speed	
sal	sn(1)	salinity of sea surface layer	
sst	tn(1)	temperature of sea surface (°C)	
$c00$	c00	coefficient in the solubility of CO2	trcini
$Schmidt_{CO_2}$	schmico2	Schmidt number for CO_2	bgcflx.F90
$Schmidt_{O_2}$	schmio2	Schmidt number for O_2	bgcflx.F90
γ	freeze	fraction of ocean covered by ice	ice model Section 8.2
$\frac{O}{N}^{pi}$	atcox	pre-industrial ratio of oxygen to nitrogen	trcini
$F^{O_2}_{air-sea}$	flu16	air-sea oxygen flux	bgcflx.F90

8 Model Setup

8.1 Ocean General Circulation Model

The physical model NEMO v3.1 (Madec [2008],
http://www.nemo-ocean.eu/About-NEMO/Reference-manuals) was developed by the Laboratoire d' Océanographie Dynamique et de Climatologie (LODYC) to study large scale ocean circulation and its interaction with atmosphere and sea-ice. NEMO is based on the Navier-Stokes equations describing the motions of the fluid and on a non-linear equation of state, which couples the two tracers salinity and temperature to the fluid velocity.

8.2 Sea-Ice Model

NEMO is coupled to the Louvain-La-Neuve Sea-Ice Model (LIM, Timmermann et al., 2005), developed by Fichefet and Morales-Maqueda [1999]. LIM has been thoroughly validated for both Arctic and Antarctic conditions, and has been used in a wide range of process studies. Due to the use of an elaborate technique for solving the continuity

equations [Prather, 1986], LIM is particularly suited to describing the ice-edge in coarse grid resolutions, which are typically used for climate modelling studies. The physical fields that are advected in LIM are the ice concentration, the snow volume per unit area, the ice volume per unit area, the snow enthalpy per unit area, the ice enthalpy per unit area, and the brine reservoir per unit area. A full model description and details of the coupling to OPA-ORCA can be found in Timmermann et al. [2005].

8.3 Forcing

8.3.1 Physical Forcing

The model is forced by daily wind stress, cloud cover and precipitation from the NCEP/ NCAR reanalysed fields [Kalnay et al., 1996]. Sensible and latent heat fluxes are calculated with bulk formulae using the differences between the surface temperature calculated by OPA and the observed air temperature, taking into account local humidity. At the end of each year a water balance is calculated and a uniform water flux correction is applied during the following year to conserve the water mass.

8.4 Initialisation

All model simulations are initialized with observations from the World Ocean Atlas 2009 for temperature [Locarnini et al., 2010], salinity [Antonov et al., 2010] PO_4^{3-},NO_3^-, SiO_3^-, [Garcia et al., 2010b] and O_2 [Garcia et al., 2010a]. DIC, alkalinity (GLODAP) observations were from Key et al. [2004]. The biological state variables are initialised with the output from previous model runs.

8.5 Dust input

The model is forced with Fe and Si input from monthly dust fluxes taken from Jickells et al. [2005] and interpolated to daily values in bgcint.F90. The input is total dust rather than in units of Fe. We assume 0.035g Fe per g of dust and either 8.8g Si per g Fe or, the equivalent, 0.308 g Si per g dust. The solubility of Fe in dust is generally taken to be 2 % and may be set in rn_fersol. The solubility of Si in dust is 7.5 %. Using these values the dust is converted to equivalent Fe, Fe_{dep} and Si, Si_{dep} in units of mol/L/timestep in bgcbio.F90.

8.6 River input

Annual fluxes of riverine carbon and nutrient (N, Si, Fe) to the ocean were computed following a global river drainage direction map (DDM30), considering population and basin area [Döll and Lehner, 2002], and river runoff [Kourzoun, 1977, Ludwig and Probst, 1998] at 0.5° increments of latitude and longitude as in da Cunha et al. [2007]. This map represents the drainage directions of surface water on all continents, except Antarctica. Cells of the map are connected by their drainage directions and are thus organized into drainage basins. We use the cells corresponding to basin outlets to the ocean as input data for PlankTOM.

Values for DIC_{riv}, DOC_{riv}, POC_{riv}, NHy_{riv}, NOx_{riv}, $PO4_{riv}$, SIL_{riv} and Fe_{riv} as used in the preceding Sections are obtained by multiplying the input by the relevant parameter in Table 17. Thus all riverine inputs may be switched off by setting their parameter to zero.

In order to close the N, Si, and alkalinity cycles of the ocean, as much POM, DOM, SiO2 and CaCO3 is removed from the bottom water layer as is added by rivers and Si in dust.

8.6.1 Dissolved Inorganic Nitrogen (DIN)

To calculate riverine DIN inputs we used a regression model originally developed by Smith et al. [2003]:

$$\log DIN = 3.99 + 0.35 \log POP + 0.75 \log R \tag{89}$$

where (DIN) is in mol N km^{-2} y^{-1}, (POP) is population density in people km^{-2}, and (R) is runoff in m y^{-1}. The model describes DIN export by the analysis of 165 systems for which DIN flux data is available [Meybeck and A., 1997], S. Smith and F. Wulff (Eds.), LOICZ-Biogeochemical modelling node, 2000, available at http://data.ecology.su.se/MNODE/]. In this model, riverine DIN export to the coastal zone is a function of basin population density and runoff: On the basis of basin area, basin population (for the year 1990) and runoff provided by the DDM30 map, 16.3 Tg DIN y^{-1} (1.16 Tmol N y^{-1}) are transported to the coastal zone by rivers. In the Smith et al. 2003 model, the average N:P ratio of riverine export is 18:1, which is close to the PISCES-T N:P ratio of 16:1. Nitrogen retention in estuarine areas was not included owing to lack of global data.

8.6.2 Dissolved Silica (Si)

Rivers are responsible for 80% of the inputs of Si to the ocean [Treguer et al., 1995]. For an estimate of riverine input of dissolved Si we used the runoff data from the DDM30 map, and applied an average concentration of Si in river waters of 4.2 mg Si/L [Treguer et al., 1995]. Si concentration in river water is variable according to basin geology but regional data is not available. Our estimate leads to a dissolved Si river input of 187 Tg Si y^{-1} to the ocean. This value is comparable to the range of 140 $\pm$ 30 Tg Si y^{-1} for a net riverine dissolved Si input to the ocean proposed by Treguer et al. [1995], considering estuarine retention of Si.

8.6.3 Dissolved Iron (Fe)

Rivers and continental shelf sediments supply Fe to surface waters. Because it is extensively removed from the dissolved phase in estuaries, rivers are thought to be a minor source for the open ocean, but not for coastal zones. We used the runoff data from the DDM30 map and applied an average concentration of dissolved Fe in river waters of 40 mg L^{-1} [Martin and Meybeck, 1979, Martin and Whitfield, 1983]. As for Si, river basin geology influences Fe concentration in river water, but there is no available global database on riverine Fe. Our estimate leads to a gross dissolved Fe input of 1.75 Tg Fe y^{-1}, comparable to the estimate of 1.45 Tg Fe $^{-1}$ by Chester [1990].

During estuarine mixing, flocculation of colloidal Fe and organic matter forms particulate Fe because of the major change in ionic strength upon mixing of fresh water and seawater [de Baar and Jong, 2001]. This removal has been well documented in many estuaries. Literature values show that approximately 80 to 99% of the gross

dissolved Fe input is lost to the particulate phase in estuaries at low salinities [Boyle et al., 1977, Chester, 1990, Dai and Martin, 1995, Lohan and Bruland, 2006, Sholkovitz, 1978].

We apply a removal rate of 99% to our gross Fe flux, and obtained a net input of riverine dissolved Fe to the coastal ocean of 0.02 Tg Fe y^{-1}.

8.6.4 Particulate (POC) and Dissolved Organic (DOC) and Inorganic (DIC) Carbon

The predicted river carbon fluxes are based on models relating river carbon fluxes to their major controlling factors [Ludwig and Probst, 1998, Ludwig et al., 1996b]. For POC, sediment flux is the dominant controlling parameter. For DOC, runoff intensity, basin slope, and the amount of soil OC in the basin are the controlling parameters [Ludwig et al., 1996b]. We applied this model to the DDM30 data set, and we estimate a gross discharge of 148 Tg C y^{-1} and 189 Tg C y^{-1} for POC and DOC, respectively. We assume that DOC has a conservative behavior in estuaries. These values are in agreement with recent modeled values of 170 Tg C y^{-1} as DOC [Harrison et al., 2005], and 197 Tg C y^{-1} as POC [Beusen et al., 2005, Seitzinger et al., 2005]. We used a C:N:P:Fe ratio of 122:16:1:2.44 10^{-4}, thus riverine DOC and POC, when they are remineralized, are also N, P and Fe sources to the ocean. Inorganic carbon is mainly transported by rivers in the dissolved form. For DIC inputs, drainage intensity and river basin lithology are the controlling parameters [Ludwig et al., 1996a]. We applied this model to the DDM30 data set, and we estimate a DIC and alkalinity discharge of 385 Tg C y^{-1} (32.12 Tmol C y^{-1}).

Table 17: List of Parameters used in river input

Variable	**Description**	**Defined in**
rn_rivdic	river input of DIC	namelist.trc.sms
rn_rivdoc	river input of DOC	namelist.trc.sms
rn_rivfer	river input of Fe	namelist.trc.sms
rn_rivpoc	river input of POC	namelist.trc.sms
rn_rivnit	river input of nitrate	namelist.trc.sms
rn_rivpo4	river input of phosphate	namelist.trc.sms
rn_rivsil	river input of silica	namelist.trc.sms
rn_sedfer	coastal release of Fe	namelist.trc.sms

8.7 The namelist.trc.sms file

Values used for the parameters defined in namelist.trc.sms are given in the following tables.

Table 18: List of Parameters defined in namelist.trc.sms

Parameter	(optimised) value (and range)	Units	Description
rn_ag1poc	1.2e4	L s (mol d)$^{-1}$ m^{-2}	small POC (POC$_s$ aggregation
rn_ag2poc	1e4	L s (mol d)$^{-1}$ m^{-2}	POC$_s$ - large POC (POC$_l$) aggregation
rn_ag3poc	140	L (mol d)$^{-1}$	POC$_s$ - POC$_l$ aggregation
rn_ag4poc	150	L (mol d)$^{-1}$	POC$_s$ aggregation
rn_ag5doc	180	L s (mol d)$^{-1}$ m^{-2}	DOC - POC$_s$ aggregation
rn_ag6doc	3.9e3	L s (mol d)$^{-1}$ m^{-2}	DOC - POC$_l$ aggregation
rn_ag7doc	1e3	L s (mol d)$^{-1}$ m^{-2}	DOC - POC$_s$ aggregation
rn_alpphy	1.e-6	mol C m^2 (g Chl mol photons)$^{-1}$	initial slope of photsyntheses vs light intensity curve
rn_aoun2o	1.23e-4 (0.37e-4 - 2.53e-4)	mol N2O (mol NH4)$^{-1}$	N2O yield nitrification
rn_aoun2s	1.06e-5 (0.33e-5 - 2.26e-5)	mol N2O (mol O2)$^{-1}$	oxic N2S yield
rn_betn2s	1.7e-3 (1.7e-3 - 10.18e-3)	mol N2O (mol O2)$^{-1}$	suboxic N2S yield
rn_coccal	0.433	-	ratio of $CaCO_3$ to organic carbon
rn_degn2o	0 (0 - 9.65e-2)	mol N2O (mol NO3)$^{-1}$	yield N2O consumption
rn_denn2o	3.4e-3 (3.4e-3 - 80.8e-3)	mol N2O (mol NO3)$^{-1}$	N2O yield denitrification
rn_domphy	0.45	-	maximum DOC excretion ratio for all phyto
rn_discal	0.75	-	fraction of $CaCO_3$ dissolved during coccolithophore mortality
rn_docphy	0.05	-	excretion ratio for all phyto
rn_ekwgrn	0.0232	m^{-1}	green light absorption coefficient of H_2O
rn_ekwred	0.225	m^{-1}	red light absorption coefficient of H_2O
rn_etomax	80.	W m^{-2}	maximum surface insolation
rn_faco18	0.98	-	bacterial fractionation for O_{18}

Continued on next page

Table 18 – continued from previous page

Parameter	Value	Units	Description
rn_fersol	0.01	-	solubility of iron in dust
rn_gbadoc	0.088	-	relative preference of BAC grazing for DOC
rn_gbagoc	8.76	-	relative preference of BAC grazing for GOC
rn_gbagon	11.42	-	relative preference of BAC grazing for GON
rn_gbapoc	8.76	-	relative preference of BAC grazing for POC
rn_ggebac	0.21	-	growth efficiency BAC
rn_ggezoo	0.3	-	growth efficiency MAC
	0.25	-	growth efficiency MES
	0.29	-	growth efficiency PRO
rn_prfzoo	0.186	-	relative preference of MAC grazing for BAC
	0.186	-	relative preference of MAC grazing for GOC
	1.860	-	relative preference of MAC grazing for MES
	1.860	-	relative preference of MAC grazing for PRO
	1.860	-	relative preference of MAC for DIA
	1.860	-	relative preference of MAC for MIX
	1.860	-	relative preference of MAC for COC
	.930	-	relative preference of MAC for PIC
	1.860	-	relative preference of MAC for PHA
	.186	-	relative preference of MAC for FIX
	0.186	-	relative preference of MES grazing for POC
	.165	-	relative preference of MES grazing for BAC
	0.165	-	relative preference of MES grazing for GOC
	3.302	-	relative preference of MES grazing for PRO
	1.651	-	relative preference of MES for DIA
	1.238	-	relative preference of MES for MIX
	1.238	-	relative preference of MES for COC
	1.238	-	relative preference of MES for PIC
	1.238	-	relative preference of MES for PHA
	0.165	-	relative preference of MES for FIX
	0.165	-	relative preference of MES grazing for POC
	2.480	-	relative preference of PRO grazing for BAC
	0.062	-	relative preference of PRO grazing for GOC
	0.620	-	relative preference of MIC for DIA
	1.240	-	relative preference of MIC for MIX
	1.240	-	relative preference of MIC for COC
	1.240	-	relative preference of MIC for PIC
	1.240	-	relative preference of MIC for PHA
	1.240	-	relative preference of MIC for FIX

Continued on next page

Table 18 – continued from previous page

Parameter	Value	Units	Description
	0.062	-	relative preference of PRO grazing for POC
rn_grabac	3.15	d^{-1}	maximum BAC uptake rate
rn_grazoo	0.106	d^{-1}	maximum MAC grazing rate
	1.22	d^{-1}	maximum MES grazing rate
	1.59	d^{-1}	maximum PRO grazing rate
rn_grkzoo	9.e-6	mol L^{-1}	K_m for MAC grazing
	10.e-6	mol L^{-1}	K_m for MES grazing
	10.e-6	mol L^{-1}	K_m for PRO grazing
rn_icemac	100.0	%	MAC enhanced recruitment under ice
rn_kgrphy	.0118	L (m g Chl)$^{-1}$	light absorption in blue-green for DIA
	.0257	L (m g Chl)$^{-1}$	light absorption in blue-green for MIX
	.0257	L (m g Chl)$^{-1}$	light absorption in blue-green for COC
	.0696	L (m g Chl)$^{-1}$	light absorption in blue-green for PIC
	.0257	L (m g Chl)$^{-1}$	light absorption in blue-green for PHA
	.0657	L (m g Chl)$^{-1}$	light absorption in blue-green for FIX
rn_kmfbac	0.025e-9	mol L^{-1}	K_m for Fe in DOC remineralisation by bacteria
rn_kmfphy	40.e-9	mol L^{-1}	K_m^{Fe} for DIA
	25.e-9	mol L^{-1}	K_m^{Fe} for MIX
	25.e-9	mol L^{-1}	K_m^{Fe} for COC
	10.e-9	mol L^{-1}	K_m^{Fe} for PIC
	25.e-9	mol L^{-1}	K_m^{Fe} for PHA
	40.e-9	mol L^{-1}	K_m^{Fe} for FIX
rn_kmhnit	0.1e-6	mol L^{-1}	K_m^{NH4} nitrification
rn_kmhphy	5.e-6	mol L^{-1}	K_m^{NH4} for DIA
	0.5e-6	mol L^{-1}	K_m^{NH4} for MIX
	0.5e-6	mol L^{-1}	K_m^{NH4} for COC
	0.1e-6	mol L^{-1}	K_m^{NH4} for PIC
	1.5e-6	mol L^{-1}	K_m^{NH4} for PHA
	0.3e-6	mol L^{-1}	K_m^{NH4} for FIX
rn_kmnphy	2.e-6	mol L^{-1}	K_m^{NO3} for DIA
	2.0e-6	mol L^{-1}	K_m^{NO3} for MIX
	2.0e-6	mol L^{-1}	K_m^{NO3} for COC
	2.0e-6	mol L^{-1}	K_m^{NO3} for PIC
	3.0e-6	mol L^{-1}	K_m^{NO3} for PHA
	13.0e-6	mol L^{-1}	K_m^{NO3} for FIX
rn_kmobac	1e-7	mol L^{-1}	K_m for DOC in DOC remineralisation by bacteria
rn_kmpbac	1e-7	mol L^{-1}	K_m for PO_4
rn_kmpphy	7.6e-6	mol L^{-1}	$K_m^{PO_4}$ for DIA

Continued on next page

Table 18 – continued from previous page

Parameter	Value	Units	Description
	12.2e-6	mol L^{-1}	$K_m^{PO_4}$ for MIX
	15.9e-6	mol L^{-1}	$K_m^{PO_4}$ for COC
	15.9e-6	mol L^{-1}	$K_m^{PO_4}$ for PIC
	97.6e-6	mol L^{-1}	$K_m^{PO_4}$ for PHA
	24.4e-6	mol L^{-1}	$K_m^{PO_4}$ for FIX
rn_kmsbsi	20e-6	mol L^{-1}	K_m for the Si/C ratio of DIA
rn_krdphy	.0056	L (m g Chl)$^{-1}$	light absorption in red for DIA
	.0098	L (m g Chl)$^{-1}$	light absorption in red for MIX
	.0098	L (m g Chl)$^{-1}$	light absorption in red for COC
	.0197	L (m g Chl)$^{-1}$	light absorption in red for PIC
	.0098	L (m g Chl)$^{-1}$	light absorption in red for PHA
	.0181	L (m g Chl)$^{-1}$	light absorption in red for FIX
rn_lyscal	10e-5	mol L^{-1}	inertia conc. for $CaCO_3$ dissolution
rn_mormac	0.020	d^{-1}	MAC mortality rate
rn_motmac	1.0481	-	temp. dependence of MAC mortality
rn_mumpft	0.44	d^{-1}	maximum growth rate DIA
	0.35	d^{-1}	maximum growth rate MIX
	0.70	d^{-1}	maximum growth rate COC
	0.26	d^{-1}	maximum growth rate PIC
	0.68	d^{-1}	maximum growth rate PHA
	0.046	d^{-1}	maximum growth rate FIX
rn_munfix	0.56	-	fraction of growth rate during N2fix relative to growth on NO3
rn_mutpft	1.0379	-	temp. dependence of BAC
	1.0400	-	temp. dependence of proto-zooplankton
	1.0242	-	temp. dependence of meso-zooplankton
	1.1165	-	temp. dependence of macro-zooplankton
	1.0680	-	temp. dependence of DIA
	1.0461	-	temp. dependence of MIX
	1.0132	-	temp. dependence of COC
	1.0611	-	temp. dependence of PIC
	1.0520	-	temp. dependence of PHA
	1.0623	-	temp. dependence of FIX
rn_nitnh4	0.79	d^{-1}	maximum nitrification rate
rn_qmaphy	2.e-7	-	maximum quota for Fe for all phyto
rn_qmiphy	4.0e-6	-	minimum quota for Fe for all phyto
rn_qopphy	8.6e-6	-	optimal quota for Fe for all phyto
rn_readsi	0.1	d^{-1}	max. DSi remin.

Continued on next page

Table 18 – continued from previous page

Parameter	Value	Units	Description
rn_remdsi	179831	d^{-1}	DSi remin.
rn_retdsi	-4366	d^{-1}	T. depend. DSi remin.
rn_resbac	0.10	d^{-1}	BAC respiration at 0°C
rn_reszoo	0.018	d^{-1}	MAC respiration at 0°C
	0.028	d^{-1}	MES respiration at 0°C
	0.010	d^{-1}	PRO respiration at 0°C
rn_resphy	0.012	-	fractional phytoplankton loss rate: DIA
	0.15	-	fractional phytoplankton loss rate: MIX
	0.15	-	fractional phytoplankton loss rate: COC
	0.15	-	fractional phytoplankton loss rate: PIC
	0.15	-	fractional phytoplankton loss rate: PHA
	0.15	-	fractional phytoplankton loss rate: FIX
rn_retbac	1.0494	-	temp. dependence of BAC respiration
rn_retzoo	1.0942	-	temp. dependence of MAC respiration
	1.0887	-	temp. dependence of MES respiration
	1.0897	-	temp. dependence of PRO respiration
rn_rhfphy	29.	-	maximum/minimum Fe uptake rate
rn_rivdic	1.	-	(1 - estuarine retention fraction) of river DIC
rn_rivdoc	1.	-	(1 - estuarine retention fraction) of river DOC
rn_rivpoc	0.55	-	(1 - estuarine retention fraction) of river POC
rn_rivpo4	1.	-	(1 - estuarine retention fraction) of river PO_4
rn_rivsil	1.	-	(1 - estuarine retention fraction) of river SIL
rn_rivfer	0.25	-	(1 - estuarine retention fraction) of river FER
rn_scofer	1.e-3	$(\text{mol L}^{-1})^{-0.6}\ \text{d}^{-1}$	scavenging of Fe
rn_scmfer	1.e-3	$(\text{mol L}^{-1})^{-0.6}\ \text{d}^{-1}$	minimum scavenging of Fe
rn_sedfer	1e-11	mol L^{-1}	coastal release of Fe
rn_sigzoo	0.70	-	fraction of MAC excretion as PO_4
	0.68	-	fraction of MES excretion as PO_4
	0.66	-	fraction of PRO excretion as DOM
rn_sildia	0.42e-6	mol L^{-1}	$K_m^{SiO_3}$ for diatoms
rn_singoc	0.0303	$\text{m}^2\ (\text{kg d})^{-1}$	Sinking rate parameter of POC_l, $CaCO_3$ and DSi
rn_snkgoc	0.6923	-	sinking rate parameter of POC_l,$CaCO_3$ and SiO_2
rn_snkpoc	3.0	m d^{-1}	sinking speed of POC_s
rn_thmphy	0.7	g mol^{-1}	maximum CHL:C ratio for DIA
	0.4	g mol^{-1}	maximum CHL:C ratio for MIX
	0.4	g mol^{-1}	maximum CHL:C ratio for COC
	0.4	g mol^{-1}	maximum CHL:C ratio for PIC
	0.5	g mol^{-1}	maximum CHL:C ratio for PHA

Continued on next page

Table 18 – continued from previous page

Parameter	Value	Units	Description
	0.3	g mol^{-1}	maximum CHL:C ratio for FIX
rn_unazoo	0.18	-	unassimilated fraction of phyto during MAC grazing
	0.3	-	unassimilated fraction of phyto during MES grazing
	0.13	-	unassimilated fraction of phyto during PRO grazing

References

J. I. Antonov, D. Seidov, T. Boyer, R. Locarnini, A. Mishonov, H. Garcia, O. Baranova, M. Zweng, and D. Johnson. *World Ocean Atlas 2009, Volume 2: Salinity*. NOAA Atlas NESDIS 69. U.S. Government Printing Office, Washington, D.C., 2010.

Olivier Aumont. Pisces biogeochemical model. Unpublished report, 2005. URL `http://ftp.legos.obs-mip.fr/pub/romsagrif/DATA`$_R OMS/papers/manuel_p isces.pdf$.

A. Beusen, A. Dekkers, A. Bouwman, W. Ludwig, and J. Harrison. Estimation of global river transport of sediments and associated particulate c, n, and p. *Global Biogeochemical Cycles*, 19(4), 2005.

E. Boyle, J. Edmond, and E. Sholkovitz. Mechanism of iron removal in estuaries. *Geochimica et Cosmochimica Acta*, 41(9):1313–1324, 1977.

E. Buitenhuis, P. van der Wal, and H. J. de Baar. Blooms of emiliana huxleyi are sinks of atmospheric carbon dioxide: a field and mesocosm study derived simulation. *Global Biogeochemical Cycles*, 15:577–587, 2001.

E. Buitenhuis, C. Le Quere, O. Aumont, G. Beaugrand, A. Bunker, A. Hirst, T. Ikeda, T. O'Brien, S. Piontkovski, and D. Straile. Biogeochemical fluxes through mesozooplankton. *Global Biogeochemical Cycles*, 20:GB2003, 2006. doi: 10.1029/2005GB002511.

E. Buitenhuis, T. Hashioka, and L. Quéré. Combined constraints on ocean primary production and phytoplankton biomass from observations and a model. *Global Biogeochemical Cycles*, 27:847–858, 2013.

E. T. Buitenhuis and R. Geider. A model of phytoplankton acclimation to iron-light colimitation. *Limnol. Oceanogr*, 55(2):714–724, 2010.

R. Chester. *Marine Geochemistry*. Unwin Hyman, 1990.

L. da Cunha, E. T. Buitenhuis, C. Le Quéré, X. Giraud, and W. Ludwig. Potential impact of changes in river nutrient supply on global ocean biogeochemistry. *Global Biogeochemical Cycles*, 21:GB4007, 2007. doi: 10.1029/2006GB002718.

M. Dai and J. Martin. First data on trace-metal level and behavior in 2 major arctic river-estuarine systems (ob and yenisey) and in the adjacent kara sea, russia. *Earth And Planetary Science Letters*, 131(3-4):127–141, 1995.

H. J. W. de Baar and J. T. M. D. Jong. Distributions, sources and sinks of iron in seawater. In *The Biogeochemistry of Iron in Seawater*, pages 123–153. John Wiley, 2001.

P. Döll and B. Lehner. Validation of a new global 30-min drainage direction map. *Journal Of Hydrology*, 258(1-4): 214–231, 2002.

T. Fichefet and M. A. Morales-Maqueda. Modelling the influence of snow accumulation and snow-ice formation on the seasonal cycle of the antarctic sea-ice cover. *Climate Dynamics*, 15(4):251–268, 1999.

H. E. Garcia, R. Locarnini, T. Boyer, J. Antonov, O. Baranova, M. Zweng, and D. Johnson. *World Ocean Atlas 2009, Volume 3: Dissolved Oxygen, Apparent Oxygen Utilization, and Oxygen Saturation*. NOAA Atlas NESDIS 70. U.S. Government Printing Office, Washington, D.C., 2010a.

H. E. Garcia, R. Locarnini, T. Boyer, J. Antonov, M. Zweng, O. Baranova, and D. Johnson. *World Ocean Atlas 2009, Volume 4: Nutrients (phosphate, nitrate, silicate)*. NOAA Atlas NESDIS 71. U.S. Government Printing Office, Washington, D.C., 2010b.

J. Harrison, N. Caraco, and S. Seitzinger. Global patterns and sources of dissolved organic matter export to the coastal zone: Results from a spatially explicit, global model. *Global Biogeochemical Cycles*, 19(4), 2005.

C. Jeandel, D. Ruiz-Pino, E. Gjata, A. Poisson, C. Brunet, E. Charriaud, F. Dehairs, D. Delille, M. Fiala, C. Fravalo, and J.C. Miquel. Kerfix, a time-series station in the southern ocean: a presentation. *Journal of Marine Systems*, 17(1-4):555–569, 1998.

T. D. Jickells, Z. S. An, K. K. Andersen, A. R. Baker, G. Bergametti, N. Brooks, J. J. Cao, P. W. Boyd, R. A. Duce, K. A. Hunter, H. Kawahata, N. Kubilay, J. laRoche, P. Liss, N. Mahowald, J. M. Prospero, A. J. Ridgwell, I. Tegen, and R. Torres. Global iron connections betwen desert dust, ocean biogechemistry, and climate. *Science*, 308:67–71, 2005.

E. Kalnay, M. Kanamitsu, R. Kistler, W. Collins, D. Deaven, L. Gandin, M. Iredell, S. Saha, G. White, J. Woollen, Y. Zhu, M. Chelliah, W. Ebisuzaki, W. Higgins, J. Janowiak, K. C. Mo, C. Ropelewski, J. Wang, A. Leetmaa, R. Reynolds, R. Jenne, and D. Joseph. The ncep/ncar 40-year reanalysis project. *Bulletin of the American Meteorological Society*, 77(3):437–471, 1996.

R. Key, A. Kozyr, C. Sabine, K. Lee, R. Wanninkhof, J. Bullister, R. Feely, F. Millero, C. Mordy, and T.-H. Peng. A global ocean carbon climatology: Results from glodap. *Global Biogeochemical Cycles*, 18:GB4031, 2004.

V. I. Kourzoun. *Atlas of World Water Balance*. UNESCO, 1977.

R. A. Locarnini, A. Mishonov, J. Antonov, T. Boyer, H. Garcia, O. Baranova, M. Zweng, and D. Johnson. *World Ocean Atlas 2009, Volume 1: Temperature*. NOAA Atlas NESDIS 68. U.S. Government Printing Office, Washington, D.C., 2010.

M. Lohan and K. Bruland. Importance of vertical mixing for additional sources of nitrate and iron to surface waters of the columbia river plume: Implications for biology. *Marine Chemistry*, 98(2-4):260–273, 2006.

W. Ludwig and J. L. Probst. River sediment discharge to the oceans: Present-day controls and global budgets. *American Journal of Science*, 298:265–295, 1998.

W. Ludwig, J. Probst, and S. Kempe. Predicting the oceanic input of organic carbon by continental erosion. *Global Biogeochemical Cycles*, 10(1):23–41, 1996a.

W. Ludwig et al. River discharges of carbon to the world's oceans: Determining local inputs of alkalinity and of dissolved and particulate organic carbon. *Comptes Rendus de l'Academie des Sciences - Serie IIA Sci. Terres Planetes*, 323(12):1007–1014, 1996b.

G. Madec. *NEMO ocean engine Note du pole de modélisation*, volume 27. Institut Pierre-Simon Laplace, Paris, 2008.

J.-M. Martin and M. Meybeck. Elemental mass-balance of material carried by major world rivers. *Marine Chemistry*, 7(3):173–206, 1979.

J.-M. Martin and M. Whitfield. The significance of the river input of chemical elements to the ocean. In *Trace Metals in Sea Water*, pages 265–296. Plenum, 1983.

M. Meybeck and R. A. River discharges to the oceans: An assessment of suspended solids, major ions, and nutrients. Technical report, U.N. Environ. Programme, 1997.

H. Ploug, M. Iversen, M. Koski, and E. Buitenhuis. Production, oxygen respiration rates and sinking velocity of copepod fecal pellets: Direct measurements of ballasting by opal and calcite. *Limnol. Oceanogr.*, 53:469–476, 2008.

M. C. Prather. Numerical advection by conservation of second-order moments. *Journal of Geophysical Research*, 91(D6):6671–6681, 1986.

J. L. Sarmiento, J. C. Orr, and U. Siegenthaler. A perturbation simulation of co_2 uptake in an ocean general-circulation model. *Journal of Geophysical Research-Oceans*, 97(C3):3621–3645, 1992.

S. Seitzinger, J. Harrison, E. Dumont, A. Beusen, and A. Bouwman. Sources and delivery of carbon, nitrogen, and phosphorus to the coastal zone: An overview of global nutrient export from watersheds (news) models and their application. *Global Biogeochemical Cycles*, 19(4), 2005.

E. Sholkovitz. Flocculation of dissolved fe, mn, al, cu, ni, co and cd during estuarine mixing. *Earth And Planetary Science Letters*, 41(1):77–86, 1978.

S. Smith, D. Swaney, L. Talaue-McManus, J. Bartley, P. Sandhei, C. McLaughlin, V. Dupra, C. Crossland, R. Buddemeier, B. Maxwell, and F. Wulff. Humans, hydrology, and the distribution of inorganic nutrient loading to the ocean. *Bioscience*, 53(3):235–245, 2003.

R. Timmermann, H. Goosse, G. Madec, T. Fichefet, C. Ethe, and V. Duliere. On the representation of high latitude processes in the orca-lim global coupled sea ice-ocean model. *Ocean Modelling*, 8(1-2):175–201, 2005.

P. Treguer, D. Nelson, A. Vanbennekom, D. Demaster, A. Leynaert, and B. Queguiner. The silica balance in the world ocean - a reestimate. *Science*, 268(5209):375–379, 1995.

R. Wanninkhof. Relationship between wind-speed and gas-exchange over the ocean. *Journal of Geophysical Research-Oceans*, 97(C5):7373–7382, 1992.

J. Wiedenmann, K. Creswell, and M. Mangel. Connecting recruitment of antarctic krill and sea ice. *Limnol. Oceanogr.*, 54(3):799–810, 2009.

D. A. Wolf-Gladrow, R. E. Zeebe, C. Klaas, A. Koertzinger, and A. Dickson. Total alkalinity: the explicit conservative expression and its application to biogeochmical processes. *Marine chemistry*, 106:287–300, 2007.

Supplementary Material B

A global ocean opal ballasting–silicate relationship

B. B. Cael[1], C. Mark Moore[2], Joe Guest[3], Tereza Jarníková[3], Colleen B. Mouw[4], Chris Bowler[5,6], Edward Mawji[1], Stephanie A. Henson[1], and Corinne Le Quéré[3]

[1]National Oceanography Centre, Southampton, UK
[2]School of Ocean and Earth Science, University of Southampton, UK
[3]School of Environmental Sciences, University of East Anglia, Norwich, NR4 7TJ, UK
[4]University of Rhode Island, Graduate School of Oceanography, Narragansett, RI, USA
[5]Institut de Biologie de l'Ecole Normale Supérieure (IBENS), Ecole Normale Supérieure, CNRS, INSERM, Université PSL, 75005 Paris, France
[6]Stazione Zoologica Anton Dohrn, Naples, Italy

Key Points:

- Opal ballasting varies by more than a factor of six across ocean regions; calcium carbonate ballasting is uniform.
- Silicate concentration predicts opal ballasting which suggests that the latter varies with diatom frustule thickness.
- This emergent relationship's absence from a sophisticated biogeochemical model indicates it holds useful information for constraining models.

Corresponding author: B. B. Cael, `cael@noc.ac.uk`

Abstract

Opal and calcium carbonate are thought to regulate the biological pump's transfer of organic carbon to the deep ocean. A global sediment trap database exhibits large regional variations in the organic carbon flux associated with opal flux. These variations are well-explained by upper ocean silicate concentrations, with high opal 'ballasting' in the silicate-deplete tropical Atlantic Ocean, and low ballasting in the silicate-rich Southern Ocean. A plausible, testable hypothesis is that opal ballasting varies because diatoms grow thicker frustules where silicate concentrations are higher, carrying less organic carbon per unit opal. The observed pattern does not fully emerge in an advanced ocean biogeochemical model when diatom silicification is represented using a single global parameterization as a function of silicate and iron. Our results suggest a need for improving understanding of currently modeled processes and/or considering additional parameterizations to capture the links between elemental cycles and future biological pump changes.

Plain Language Summary

Opal, or hydrated silica, is taken up in the surface ocean by diatoms to construct their protective frustules. Another plankton type, coccolithophores, generate protective platelets from calcium carbonate. These two minerals, and thereby plankton types, play major roles in the global carbon cycle. The 'biological carbon pump' transfers carbon from the upper ocean to the ocean's depths, where it can stay for millenia. This process has influenced past atmospheric carbon dioxide concentrations and could also do so in the future. The transfer of carbon to the deep ocean is partially regulated by the amount of 'ballast' minerals in sinking particles, especially opal and calcium carbonate, which are denser and cause particles to sink faster and/or protect organic carbon from microbial consumption. We show that unlike calcium carbonate, opal's ballasting effect varies a great deal between different regions of the ocean. The variation in opal ballasting is well-explained by the upper-ocean concentration of silicate between these regions. This suggests a simple explanation: when silicate concentrations are high, diatoms grow thick frustules which actually results in lower carbon sinking per unit opal. Capturing this ballasting–silicate relationship in carbon cycle models may improve their ability to predict future biogeochemical cycles and climate.

1 Introduction

The biological carbon pump (BCP) entails the uptake, processing, and transfer of organic carbon to the deep ocean by biological processes. Particulate organic carbon (POC) and associated nutrients sinking out of the ocean's upper layer are gradually remineralized by grazing processes and microbial activity. The depth at which POC is remineralized determines the water mass that the resulting inorganic carbon enters, and thus the timescales of potential (re-)exposure to the atmosphere (DeVries et al., 2012; Boyd et al., 2019). Generally, the deeper POC penetrates into the ocean, the longer it is stored (Siegel et al., 2021; Baker et al., 2022). However, the mechanistic processes that underlie the considerable spatial and temporal variability in POC flux and remineralization (Cram et al., 2018; Bol et al., 2018) are still debated (Henson et al., 2022). One hypothesis posits that a portion of sinking POC is associated with 'ballast minerals', i.e. calcium carbonate and biogenic silica generated by calcifying organisms and diatoms, respectively (Armstrong et al., 2001; Klaas & Archer, 2002). These minerals are thought to deepen the remineralization depth of POC either through protection of the POC, or by increasing the particles' excess density and thus sinking speed. Although the presence of ballast minerals has a strong statistical relationship with remineralization depth, a lack of mechanistic understanding introduces challenges for parameterizing ballasting in Earth system models, despite its potential to be an important component of carbon cycle-climate feedbacks (Barker et al., 2003; Petrou et al., 2019; Heinze et al., 2019).

Our objectives here are to diagnose i) the ballast effects of opal and calcium carbonate (in terms of the POC flux at a reference depth associated with a unit of opal or calcium carbonate flux), ii) the extent to which the ballasting effects vary among ocean regions, iii) the drivers of regional variations, and iv) whether variations in ballasting effects might be helpful for constraining global ocean biogeochemical models. To achieve these objectives, we apply a statistical model based on the robust log-normality of ocean particle fluxes (Cael et al., 2018, 2021) to a global sediment trap database (Mouw et al., 2016). We find that, while the majority of parameters of the statistical model remain relatively constant, the ballasting by opal varies by almost an order of magnitude between different regions. We discuss various possible mechanisms to explain this regional difference but identify one that is parsimonious, plausible, and experimentally testable: diatom frustule thickness varies with upper ocean silicate availability. We find that this relationship does not occur in a state-of-the-art ocean biogeochemical model (Buitenhuis et al., 2019), underscoring that the opal ballasting pattern that we uncover here is not produced ecosystem and particle processes as currently parameterized, and therefore that this relationship holds useful information for constraining ocean biogeochemical models.

2 Methods

2.1 Statistical Model

Following (Cael et al., 2018, 2021), our statistical model is derived from the log-normality of POC/PIC/PSi fluxes. This statistical model is based on the empirically validated (Cael et al., 2018, 2021; Cael, 2021) argument that i) net primary production varies log-normally because multiple conditions need to be met in order for production to occur, and production cannot occur if any one of these conditions is met, such that the 'law of necessary conditions' applies (Montroll & Shlesinger, 1982), ii) the export ratio of export production over net primary production is a variable quantity, and particle export out of the euphotic layer is equal to net primary production times this export ratio by definition, and iii) particle flux at a given depth is equal to particle export times the transfer efficiency to that depth, which is also a variable quantity. If the fluxes of particulate organic carbon ($\mathcal{F}_{\mathrm{POC}}$ (mgC m^{-2} d^{-1} – though all fluxes are implicitly non-dimensionalized in Eq. 1 by dividing by 1 mg m^{-2} d^{-1}), particulate inorganic carbon ($\mathcal{F}_{\mathrm{PIC}}$ (mgC m^{-2} d^{-1}, i.e. calcium carbonate in units of C mass), and particulate silica ($\mathcal{F}_{\mathrm{PSi}}$ (mgSi m^{-2} d^{-1}, i.e. opal in units of Si mass), are log-normally distributed (Cael et al., 2021), and the latter both act in concert as ballasting minerals (i.e. organic carbon flux to a given depth can be facilitated by either or both minerals and does not necessarily require both), then they should approximately be related by an equation of the form (Cael et al., 2021)

$$\mathcal{F}_{\mathrm{POC}} = (\alpha_{\mathrm{PIC}}\mathcal{F}_{\mathrm{PIC}} + \alpha_{\mathrm{PSi}}\mathcal{F}_{\mathrm{PSi}})^{\gamma} z^{\Delta b}. \tag{1}$$

In Eq. 1 α_{PIC} (dimensionless) is the organic carbon flux associated with a unit of inorganic carbon flux, α_{PSi} (gC/gSi) is the organic carbon flux associated with a unit of opal flux, and γ (dimensionless) is the degree of sub-/super-linearity in the scaling relationship between organic carbon fluxes and ballast mineral fluxes. The difference in flux attenuation between POC and ballast minerals is captured by $\Delta b = b - b_{bal}$, which is the difference between the exponents of the power-law profiles ((Martin et al., 1987)) of fluxes of POC and mineral ballasts. Eq. 1 implicitly assumes that the PSi and PIC fluxes are attenuated with the same exponent. Eq. (1) also does not account for POC flux not associated with mineral ballast, because these fluxes are implicitly assumed to be negligible at the deep measurement depths of interest here; this relationship is therefore likely invalid at shallow depths such as the base of the euphotic layer (though note we find no systematic depth dependency of the residuals in our analysis; see §3.1). Here z is normalized to a given reference depth z_0, for which we use 1km. Our results are not affected

by this choice. γ can be interpreted as the extent to which the effect of ballast minerals have 'diminishing returns' because if $\gamma < 1$ and increasingly so as $\gamma \to 0$, particles with e.g. twice the ballast mineral loading will have less than twice the organic carbon content (γ can in principle be > 1 but this is mechanistically implausible and is not seen in the observations). α_{PIC} and α_{PSi} can be interpreted as the organic carbon flux per unit of each ballast mineral flux at the reference depth; strictly speaking this is only true when $\gamma = 1$, but regardless of the value of γ the ratio of the α values captures the relative ballast effect per unit mass of each mineral. (Note that Equation 1 is equivalent to the one given in (Cael et al., 2021), with Δb used here in replacement of b to make it explicit that this parameter captures the *difference* in vertical attenuation of organic carbon versus ballast mineral fluxes, $\alpha_{\mathrm{PIC}} = \kappa^{1/\gamma}$ and $\alpha_{\mathrm{PSi}} = \beta\kappa^{1/\gamma}$ used in replacement of κ and β to make the ballast effect of each mineral explicit parameters, and a reference depth of 1km used rather than 3500m because measurements of the full water column are considered rather than just near-bottom sediment traps.)

2.2 Sediment Trap Data

We utilized a global dataset of POC, PIC, and particulate silica (PSi) flux estimated from POC, PIC, and PSi concentration observations from sediment traps (Mouw et al., 2016). We only analyze coincident POC, PIC, and PSi flux measurements from sediment traps. Data were compiled from public repositories and directly from the literature. PIC fluxes are sometimes reported in $CaCO_3$ flux units, and PSi fluxes are sometimes reported in SiO_2 and $Si(OH)_4$ flux units; we converted these to PIC and PSi fluxes respectively using the ratio of their molar masses. The data set contains 15,792 individual POC flux estimates, measured on timescales of days to weeks, at 674 unique locations collected between 1976 and 2012; see Figure 1 in (Mouw et al., 2016). Most of the dataset (71%) was measured at $\geq$500m, with the most common deployment depths between 1000–1500 m. 85% of the observations are concentrated in the Northern Hemisphere. (For the two tropical regions spanning both hemispheres, 45% of the Tropical Atlantic data are from the Northern Hemisphere, whereas 87% of the Tropical Pacific data are from the Northern Hemisphere; thus the latter can essentially be considered representative of the Northern Tropical Pacific. Excluding the 258 (of 2286) Southern Hemisphere data points from the Tropical Pacific region does not meaningfully affect our results.)

These data are split into five broad geographic regions. The Southern Ocean (SO) is defined here as south of 30°S, the North Pacific (NP) and Atlantic (NA) as north of 30°N, and the Tropical Pacific (TP) and Atlantic (TA) aas all data equatorward of 30°. (There are few measurements in the Indian Ocean and these are included as part of the Pacific measurements; the Tropical Pacific regions is technically therefore the Tropical Indo-Pacific, though we refer to it as the Tropical Pacific because the measurements are predominantly from the Pacific Ocean.) The data from major time-series sites were excluded from our analyses, as the database is unavoidably very spatially biased, even without including these sites, and these locations would be vastly over-represented if included, such that our global analysis would be largely dictated by the behavior of a few locations (the majority with low silicate concentrations, furthermore). Excluding these locations, the database includes 768/2274/2286/1327/504 co-located measurements of $\mathcal{F}_{\mathrm{POC}}$, $\mathcal{F}_{\mathrm{PIC}}$, and $\mathcal{F}_{\mathrm{PSi}}$ in the SO/NP/TP/NA/TA respectively.

2.3 Statistical Analysis

Equation 1 is fit to the data from each region following the regression procedure in (Cael et al., 2021). The ($\alpha_{\mathrm{PSi}}/\alpha_{\mathrm{PIC}}$,$\Delta b$) that yields the best fit, using a scaling relationship of the form $y \propto x^{\gamma}$, between $\mathcal{F}_{\mathrm{POC}} z^{\Delta b}$ and $\mathcal{F}_{\mathrm{PIC}} + \frac{\alpha_{\mathrm{PSi}}}{\alpha_{\mathrm{PIC}}}\mathcal{F}_{\mathrm{PSi}}$ is identified. Major axis type II regression is used to account for the fact that uncertainties exist on both the x- and y-axis. Multiplicative (i.e., relative rather than absolute) errors are assumed, given that particle fluxes scale with one another and are log-normally distributed. Pa-

rameter uncertainties are calculated via bootstrap resampling (Efron & Tibshirani, 1986) with 1,000 bootstrap reiterations and reported as the median absolute deviation amongst bootstrap ensemble members.

To estimate the opal ballasting for each individual measurement, Eq. (1) is recast into

$$\alpha_{\mathrm{PSi}} = \frac{1}{\mathcal{F}_{\mathrm{PSi}}}\Big((\mathcal{F}_{\mathrm{POC}} z^{-\Delta b})^{1/\gamma} - \alpha_{\mathrm{PIC}}\mathcal{F}_{\mathrm{PIC}}\Big). \tag{2}$$

The measured fluxes of POC, PIC, and PSi, and the measurement depth, along with a representative global value for γ, Δb, and α_{PIC} (here we use the mean across regions as these other parameters are fairly constant between regions, see §3) are then used in Eq. (2) to estimate α_{PSi}. This estimate of α_{PSi} is then compared to co-located upper ocean silicate concentrations ([Si], (µmol/kg)) to test the hypothesis that higher [Si] values are associated with lower α_{PSi} values. [Si] values were taken from the World Ocean Atlas 2018 (Garcia et al., 2019). The 80m depth at which [Si] is considered here was selected as the depth at which the Spearman rank correlation between [Si] at that depth and the inferred α_{PSi} at the same latitude and longitude is a maximum. For 80m, the correlation is 0.68. Our results are not sensitive to this choice; the correlation for all depths 0-500m is ≥ 0.65. The logarithm of α_{PSi} is then regressed against the logarithm of [Si] (at 80m) using the second-order polynomial of the form $y = p_2x^2 + p_0$, which approximately captures the nonlinear relationship between $\log(\alpha_{\mathrm{PSi}})$ and $\log([\mathrm{Si}])$ in §3.3. Including a p_1x term made no difference.

2.4 Numerical Model

A global ocean biogeochemical model is used to test if the properties inferred using the database emerge in the current generation of models. We use the NEMO-PlankTOM12 model which represents explicitly twelve Plankton Functional Types (PFTs), six phytoplankton types (picophytoplankton, N_2-fixers, diatoms, *Phaeocystis*, and other mixed-phytoplankton), five zooplankton (protozooplankton, mesozooplankton, crustacean and gelatinous macrozooplankton, and pteropods) and bacteria (Buitenhuis et al., 2023, 2019; Le Quéré et al., 2016; Wright et al., 2021). All PFTs are represented using vital parameters of growth and loss rates based on available observations, and interact with each other using food preferences generally based on size. Growth rates depend on temperature and nutrient availability.

The model includes a full silicon cycle, with its dissolved, biogenic and detrital pools. The Si:C ratio within diatoms increases with iron stress and silicate availability as in (Aumont et al., 2015). Loss processes of diatoms produce sinking particulate silica, therefore the PSi:POC ratio is dependent on both iron and silica availability, as well as diatom concentration, grazing, and dissolution rates. Sinking of organic matter is a function of the ballasting density of the particles. A full description of the equations and parameters is provided in the PlankTOM12 manual (Buitenhuis et al., 2023). The model is embedded in the NEMOv3.6 general ocean circulation model, and is forced with NCEP reanalysis data (Saha et al., 2010). The model includes an optimization of global parameters to reproduce the size and vertical profiles of the observed organic carbon, opal and calcium carbonate fluxes presented here. This optimization was conducted by modifying the remineralization rate of silica, the dissolution rate of calcite, and the remineralisation rate of POC, until the global model POC, PSi and PIC fluxes reproduced the global median of the observations as a function of depth. We conducted sensitivity simulations with the variable Si:C ratio to test the effect on PSi:POC of modifying model parameters. In addition to the optimized baseline simulation, we present two extremes, one where the Si:C ratio is fixed by removing its dependence on silicate and iron concentrations, and one where the maximum Si:C is doubled from optimal model value (the range be-

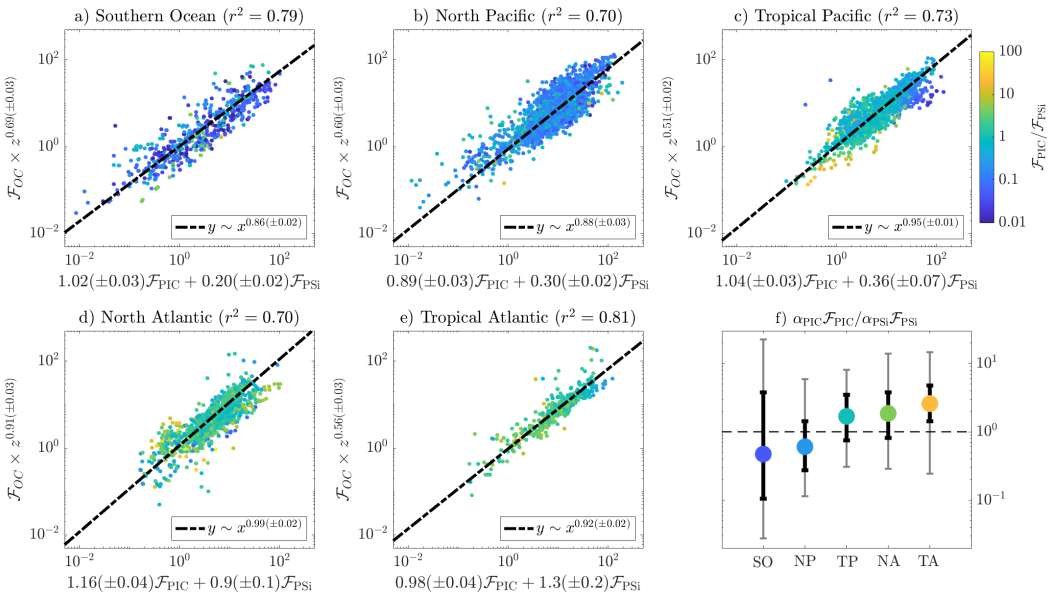

Figure 1. a-e) Scaling relationships corresponding to Equation 1 between organic carbon and ballast fluxes for the five regions considered here. Color indicates the PIC:PSi flux ratio. Parameter estimates are given on x- and y-axis labels. Units on both axes are mgC m^{-2} d^{-1}. Parameter values and uncertainties are estimated as described in the Methods. f) Median, interquartile range, and 95% range of ratio of POC flux at 1km estimated to be associated with inorganic carbon vs. opal (i.e. $\alpha_{PIC}\mathcal{F}_{PIC}/\alpha_{PSi}\mathcal{F}_{PSi}$) for each region. Dashed black line corresponds to equal organic carbon flux associated with each ballast mineral.

tween maximum and minimum Si:C is increased from 6 to 12) and the half-saturation concentration regulating the Si concentration at which this effect takes place is halved (from 20 to 10 µmol/L). Those ranges are chosen to encompass possible extremes based on the existing model parameterisation.

3 Results & Discussion

3.1 Regional Scaling Relationships

Figure 1 shows the fit of Equation 1 to the sediment trap data in each region. In each case, $\mathcal{F}_{POC}$ is well-predicted from ballast fluxes, with r^2 = 0.70-0.81. The ballast effect of opal, α_{PSi}, has a coefficient of variation of 77%, and varies by more than a factor of six between 1.3±0.2 gC/gSi in the Tropical Atlantic to 0.20±0.02 gC/gSi in the Southern Ocean (Table 1). In other words, in the Tropical Atlantic 1 mgSi m^{-2} d^{-1} of opal flux carries more than six times more organic carbon flux at 1km than 1 mgSi m^{-2} d^{-1} of opal flux in the Southern Ocean. The highest α_{PSi} values are found in the Atlantic, then the Pacific and then the Southern Ocean. Within the Atlantic and Pacific Oceans, the tropical regions have larger α_{PSi} values than the Northern regions (Figure 1f). Altogether there appears to be a very large difference in the Si associated mineral ballasting between different ocean regions, with potentially large implications for ocean biogeochemical cycling. By comparison, the parameters α_{PIC} and γ, and Δb vary less between regions, with coefficients of variation of 10%, 6%, and 24% respectively (these parameters are discussed below).

Table 1. Parameter estimates and uncertainties (median absolute deviation) for each region. These are calculated from the regression method visualized in Figure 1a-e.

Region	α_{PIC}	α_{PSi}	γ	Δb
Southern Ocean	1.02 ± 0.03	0.20 ± 0.02	0.86 ± 0.02	0.69 ± 0.03
North Pacific	0.89 ± 0.03	0.30 ± 0.02	0.88 ± 0.03	0.60 ± 0.03
Tropical Pacific	1.04 ± 0.03	0.36 ± 0.07	0.95 ± 0.01	0.51 ± 0.02
North Atlantic	1.16 ± 0.04	0.9 ± 0.1	0.99 ± 0.02	0.91 ± 0.03
Tropical Atlantic	0.98 ± 0.04	1.3 ± 0.2	0.92 ± 0.02	0.56 ± 0.03

Despite the much smaller α_{PSi} values in the Southern Ocean and North Pacific, the far larger $\mathcal{F}_{\mathrm{PSi}}$ fluxes in these regions mean that opal carries more POC flux at 1km than PIC for a majority of measurements in those regions (Figure 1f), as quantified by a $\alpha_{\mathrm{PIC}}\mathcal{F}_{\mathrm{PIC}}/\alpha_{\mathrm{PSi}}\mathcal{F}_{\mathrm{PSi}}$ ratio of < 1. In the other three regions, calcium carbonate carries more POC flux at 1km, i.e. there is a $\alpha_{\mathrm{PIC}}\mathcal{F}_{\mathrm{PIC}}/\alpha_{\mathrm{PSi}}\mathcal{F}_{\mathrm{PSi}}$ ratio >1, for a majority of measurements, as has often been reported in the literature (Klaas & Archer, 2002; Francois et al., 2002; Armstrong et al., 2001; Wilson et al., 2012). The large variability of this ratio between measurements in all regions underscores that both ballast minerals play important roles; the interquartile range of $\alpha_{\mathrm{PIC}}\mathcal{F}_{\mathrm{PIC}}/\alpha_{\mathrm{PSi}}\mathcal{F}_{\mathrm{PSi}}$ spans values below and above 1 for all regions besides the tropical Pacific.

Parameters other than α_{PSi} are fairly uniform across regions and change in plausible ways in light of the processes controlling the biological pump. α_{PIC} is nearly constant between regions, consistent with PIC either increasing particles' excess density or protecting POC similarly between regions. γ is slightly <1 in all regions except the North Atlantic, but only slightly so, indicating some degree of 'diminishing returns' on the effect of ballast minerals, but not enough to make as large a difference to POC fluxes as variations in α_{PSi}. Δb is higher at higher latitudes. If one assumes that regional variations in Δb are predominantly due to variations in the attenuation of $\mathcal{F}_{\mathrm{POC}}$, i.e. that the spatial variations in the vertical attenuation of ballast fluxes are negligible compared to those of organic carbon fluxes, this observation is consistent with some sediment-trap derived patterns for b (Henson et al., 2012). These regional variations in Δb are enough to make an appreciable difference in $\mathcal{F}_{\mathrm{POC}}$ fluxes at the seafloor – e.g. for the mean ocean depth of $z = 3682$m (Charette & Smith, 2010), the smallest Δb yields a value of $(z/z_0)^{\Delta b} = 1.9$, whereas the largest Δb value yields 3.3. However, because the spatial variations in flux attenuation are highly uncertain and sometimes contrasting between studies (Henson et al., 2012; Marsay et al., 2015), we do not interpret these variations here; we instead focus on the larger variations in α_{PSi}.

Note that we do not find systematic behavior with depth in the residuals, which suggests that a power-law approximation of flux attenuation with depth is suitable for our analysis. We do not consider the variations in these parameters further.

3.2 Possible Mechanisms

A simple and arguably parsimonious explanation for the regional variations in α_{PSi} is that variations in α_{PSi} are determined by upper ocean silicate concentrations ([Si], μmol/kg). Indeed, [Si] is lowest in the surface waters of the Atlantic and highest in the Southern Ocean, due to the interaction of the meridional overturning circulation with both the temperature dependent long remineralization length scale of Si and high Si:N uptake ratios in the surface Southern Ocean (Sarmiento et al., 2007, 2004; Holzer et al., 2014; Gnanadesikan, 1999). Globally Si is largely trapped in the Southern Ocean (Holzer et al., 2014) because of high production and export of PSi, which is largely regenerated at depths be-

low the northward flowing Antarctic intermediate and sub-Antarctic mode waters (AAIW/SAMW) (Sarmiento et al., 2007). Outside the Southern Ocean, the Atlantic is partly filled with preformed Si carried by the upper branch of the overturning circulation, which is ventilated by AAIW/SAMW formed within the relatively Si-depleted lower latitudes of the Southern Ocean (Sarmiento et al., 2004), and the Pacific is partly filled by the lower branch, which is ventilated by the relatively Si-rich higher latitudes in the Southern Ocean. Furthermore, tropical regions in the Atlantic and Pacific are more Si-depleted than regions higher to the north because some ventilation of deep waters occurs at high latitudes, even in the Pacific (Qiu & Huang, 1995). As a result, Atlantic diatoms grow in the most Si-depleted conditions and Southern Ocean diatoms grow in the most Si-replete conditions, with tropical diatoms growing in intermediate Si concentations. The more Si-deplete the conditions in which diatoms grow, the less opportunity diatoms have to meet or exceed their minimum quota of silica. This will tend to lead to lower Si:C stoichiometry for diatoms in more Si-deplete conditions, meaning thinner-frustuled diatoms of a given size and/or larger diatoms. This is because opal is predominantly contained in diatoms' frustules, whereas carbon is predominantly contained in diatoms' interiors. Thus for two diatoms of the same size, the one with the thicker frustule will carry less organic C per unit Si as it sinks; similarly for two diatoms with the same frustule thickness, the smaller one will carry less organic C per unit Si as it sinks. If opal ballasting is due to intact diatom frustules carrying organic carbon downwards as they sink, then thinner frustules, and/or larger diatoms, will correspond to more organic carbon carried per unit opal, and hence larger α_{PSi}. Diatoms in the Southern Ocean, and to a lesser extent in the (North) Subarctic Pacific, will thus be expected to have more ability to make thicker frustules in order to protect themselves from grazers, as observed (Assmy et al., 2013; Pančić et al., 2019), which results in higher Si:C ratios and lower α_{PSi} values. We thus hypothesize that there should be a negative relationship between α_{PSi} and [Si] (see §3.3).

Several other factors may complicate this simple explanation for regional variation in α_{PSi}. Different diatom taxa are characterized by different morphologies, with widely varying sizes and opal frustule pattern variations (Round et al., 1990). Different diatom species also exhibit specific biogeographies, inhabiting different ocean regions (Tréguer et al., 2018; Malviya et al., 2016). Sporulation of diatoms, especially of those abundant in the Southern Ocean such as *Chaetoceros*, may also influence the Si:C of organic material sinking into the deep sea (Armand et al., 2008). The different compositions of diatom communities in different oceanic regions may therefore impact opal ballasting, but may also in turn be influenced by the global availability of Si (§3.3). Furthermore, the Si content of diatom frustules can be impacted by environmental conditions other than [Si]. Silicification of diatoms is tightly linked to the cell cycle of growth, with Si uptake primarily occurring during the G2 interphase (Martin-Jézéquel et al., 2000). If the availability of other nutrients needed for cell growth (nitrate, phosphate, or iron) or other external growth conditions slow or prolong the G2 phase of the cell cycle in diatoms, silicification and diatom ballast increases. It has also been reported that increased grazing pressure may also lead to more heavily silicified diatoms (Pondaven et al., 2007) presumably as a mechanism for organisms to enhance their protection from grazing losses. In contrast, Si deficiency is the only condition that acts to reliably lower the silica content of the diatom cell wall (Brzezinski et al., 1990). All these factors are likely to impact the formation and degradation of particles. Fecal pellets can also contribute appreciably to POC fluxes and their stoichoimetry is necessarily reflective of their prey (Ducklow et al., 2001), so the selective grazing of diatoms of different frustule thicknesses (Ryderheim et al., 2022) and the relative balance of fecal pellets and aggregates in total POC fluxes will also play a role. Additionally, dust deposition is known to vary between regions and may further affect particles directly by being incorporated as lithogenic ballast (n.b. these are not collated in the (Mouw et al., 2016) database) or indirectly by supplying nutrients such as iron and thereby influencing phytoplankton communities.

Of these additional factors, there has been particular previous focus on the observed enhanced silicification of diatoms in response to iron limitation (Takeda, 1998; Hutchins & Bruland, 1998; Franck et al., 2000; Brzezinski et al., 2003). This mechanism has been invoked to explain higher organic carbon export out of the upper ocean in iron-depleted (Brzezinski et al., 2015) and silicate-rich waters (Arteaga et al., 2019), as well as higher silicate burial in iron-depleted waters (Pichevin et al., 2014), alongside contributing to the higher Si:N export ratios observed in the SO (Sarmiento et al., 2004). Iron limitation dependent enhanced silicification could potentially produce α_{PSi} variations, because iron limitation would lead to thick diatom frustules, hence potentially lowering organic carbon per unit Si and hence α_{PSi}. At global scales, surface silicate concentrations will generally be anticorrelated with iron limitation (Browning & Moore, 2023), although the high latitude North Atlantic represents a possible exception (see below). Consequently we cannot currently discount some iron dependence contribution to the observed global scale patterns in α_{PSi}, however, we consider a direct silicate availability based mechanism more plausible and parsimonious for several reasons. Firstly, although iron limitation likely promotes enhanced silicification in diatoms, high silicate would still be necessary to supply the silicate uptake required for such increased silicification. Second, even in the absence of iron limitation, there are potential ecological advantages to enhanced silicification when silicate is abundant, e.g. as a protection against grazing (). Third, the North Atlantic is known to be iron-limited to some degree (Browning & Moore, 2023), but we find a high α_{PSi} for that region, associated with the low silicate concentrations there (§3.3). Fourth, the model we analyze in §3.4 includes a parameterisation for the iron dependence mechanism but does not reproduce the observed α_{PSi}-[Si] relationship.

3.3 Silicate–Opal Ballasting Relationship

To test for a relationship between α_{PSi} and [Si] more quantitatively, we use Equation 2 to estimate α_{PSi} for each sediment trap measurement. For (α_{PIC}, Δb and γ) we use the means over the five regions (= 1.02, 0.65, 0.92 respectively). Our results are not sensitive to these parameter values. We then compare these estimates to the co-located [Si] (at 80m depth). Figure 2a shows that the estimated α_{PSi} decreased from a value of $\sim$1.8 when [Si]$\rightarrow$0, to small values as [Si] becomes large. This relationship is approximately described by the function $\alpha_{\mathrm{PSi}} = 1.8e^{-0.2(\log[\mathrm{Si}])^2}$ ($r^2 = 0.49$, $p \ll 0.01$). Decreasing α_{PSi} with increasing [Si] is consistent with the direct Si dependence hypothesis presented above, as low-[Si] regions would be expected to result in thinner diatom frustules and hence diatoms with more organic carbon per unit Si, with the opposite being the case for high-[Si] regions.

Note that it has also been shown that lower silicate concentrations are associated with higher export ratios (export production over net primary production) in the Southern Ocean (Britten et al., 2017; Arteaga et al., 2018), which has been attributed to opal ballasting. These results are consistent with but distinct from the α_{PSi}-[Si] relationship we present here, because they concern the ratio of organic carbon export out of the upper ocean to net primary production rather than organic carbon flux to silica flux below the upper ocean. Taken together these findings suggest that silicate-enriched waters have lower export ratios and lower organic carbon fluxes carried to depth per silica flux, both due to less effective opal ballasting.

3.4 Model Simulation

To test for the capacity of the NEMO-PlankTOM12 model to reproduce the observed [Si]-α_{PSi}, we sample the model analogously to how the real ocean has been sampled and repeat the same analysis on the pseudo-observations. Note that this exercise can provide evidence as to whether or not the observed relationship is caused by ecosystem and particle proesses as currently parameterized, but cannot validate our frustule thickness hypothesis. Specifically, we draw $\mathcal{F}_{POC/PIC/PSi}$ values at the 1000m reference

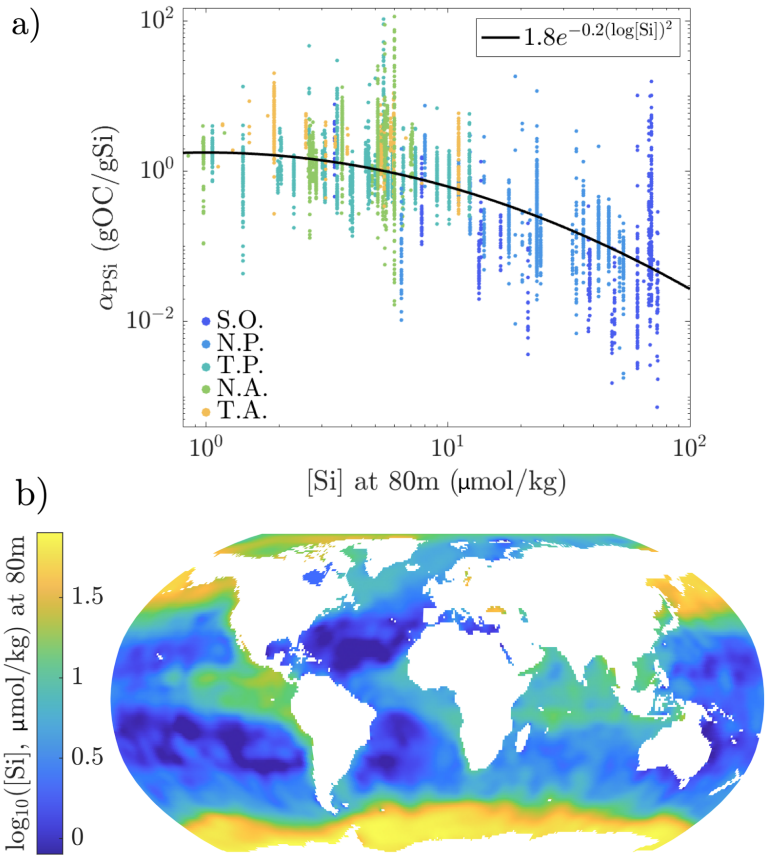

Figure 2. a) Opal ballasting coefficient as estimated by Equation 2 (Methods) versus silicate concentration at 80m. Black line indicates empirical fit. b) Annual mean logarithmic silicate concentration at 80m in the World Ocean Atlas.

depth at the same latitudes, longitudes, and months for which we have sediment trap measurements from monthly model output, using a randomly selected model year, 2000. Neither sub-monthly nor interannual variations should affect the relationship we investigate here. We also draw corresponding [Si] values at 80m depth. We then repeat the analysis from §2.3 on these data.

When Si:C sensitivity to nutrient concentrations is turned off in the model, we find a weak relationship between model [Si] and inferred α_{PSi}, with a correlation coefficient of -0.13 (compared to -0.68 for the observations). When the standard Si:C sensitivity is used, we find a slightly stronger relationship (correlation of -0.14), but still much weaker than in the observations. Even the enhanced Si:C sensitivity returns a relationship that is still below the observations (correlation of -0.22). Thus the observed strong negative [Si]-α_{PSi} relationship is not found in the model. A full range of model sensitivity has not been performed, and modeled ecosystem composition, and in particular the relative concentration of diatoms, could affect those results. The weak dependence of α_{PSi} on [Si] may be explained by other factors discussed above that the model resolves, such as the balance of fluxes by fecal pellets versus aggregates or dust deposition. However, the absence of a clear strong relationship between [Si] and α_{PSi} in the model pseudo-observations suggests that the observed α_{PSi}-[Si] relationship may not be caused by ecosystem and particle processes as currently parameterized, and that the observed relationship therefore includes useful novel information for constraining and improving ocean biogeochemical models. As α_{PSi} quantifies the organic carbon fluxes carried by silica fluxes, the large observed variation in α_{PSi} suggests that correctly parameterizing the processes that produce the observed α_{PSi}-[Si] relationship could substantially improve models' ability to simulate the present-day biological pump and to predict its future changes. The observed α_{PSi}-[Si] relationship is in this sense a novel piece of evidence to constrain models' representation of ecosystem – carbon export relationship. This constraint is particularly valuable as ecosystem complexity is currently becoming increasingly well-represented within carbon cycle models. Validation of models using such emergent relationships can help improve the representation of the biological carbon pump, which should help reduce the large model spread in projections of biological pump changes.

3.5 Conclusion

Altogether these results suggest that the ballasting effect by opal varies a great deal in different parts of the ocean, and that much of this variation can be explained by local surface ocean silicate concentrations. We argue that the most parsimonious explanation of this pattern is that diatom communities in silicate-rich regions have more frustrule mass per unit interior mass than those in silicate-depleted regions. If diatom frustules carry the organic carbon inside them as they sink, such a silicate concentration–opal ballasting relationship may occur irrespective of whether this is due to physiological plasticity or ecological selection, differences in diatom size or morphology, and whether the change in thickness is in response to metabolic constraints linked with availability of other nutrients or top-down effects linked to grazing pressure from zooplankton.

One important aspect to demonstrated here is that variable stoichiometry alone may not be sufficient to parameterize the frustule thickness mechanism that we hypothesize to cause the relationship between α_{PSi} and [Si]. Diatoms' silicate uptake ratio relative to other elements is dependent on silicate concentrations (Jin et al., 2006; Marchetti et al., 2010; Brzezinski et al., 2011), meaning higher [Si] can lead to higher diatom Si:C ratios and hence lower α_{PSi}. Some models also incorporate the effect of iron concentrations on silicate uptake (Pasquier & Holzer, 2017; Matsumoto et al., 2013), and some models such as the one we analyze here (Wright et al., 2021) and (Pasquier & Holzer, 2017) incorporate both Si and Fe effects simultaneously. The model we analyze here incorporates stoichiometric variations but still does not reproduce the observed α_{PSi}-[Si] relationship. This suggests that this observed relationship is not only due to variations in

diatom stoichiometry, but also how diatom Si and C are incorporated into particles and remineralized as particles sink. This could be explained, as described in §3.2, by intact diatom frustules within sinking particles carrying organic carbon within them as they sink. In any case, the results in §3.4 suggest that not only the variations in diatom stoichiometry and frustule thickness, but also the effect of these variations on particle sinking and/or remineralization dynamics, need to be better parameterized to capture the observed α_{PSi}-[Si] relationship.

As mentioned above, other factors may also play a role, such as the grazing protection provided by thicker frustules (Assmy et al., 2013; Ryderheim et al., 2022), which could also in principle be parameterized. The very large gradients in silicate concentration in the upper ocean (Figure 2b) suggest that the inclusion of this phenomenon could generate large changes for historical estimates and future projections of carbon export, particularly if this phenomenon substantially influences the distribution of Si (Matsumoto et al., 2002; Matsumoto & Sarmiento, 2008; Griffiths et al., 2013). Note however that the relationship in Figure 2a also includes a great deal of variability, which would have to be accounted for in such a parameterization e.g. by a transformation bias correction (Beauchamp & Olson, 1973). This variability is not surprising in light of the known variability in POC fluxes, the characteristics of which inform our statistical model (Cael et al., 2018, 2021). Such a parameterization also constitutes a hypothesis which could be tested experimentally and further refined with measurements of diatoms' stoichiometry, frustule thickness, and size, in different regions and/or across silicate concentration gradients.

Acknowledgments

We thank Angelicque White, Thomas Kiørboe, and Ken Andersen for useful discussions, and Benoît Pasquier and an anonymous reviewer for their constructive feedback. Cael, Henson and Jarníková acknowledge support by the National Environmental Resarch Council (NERC) Grant NE/T010622/1 CELOS (Constraining the EvoLution of the southern Ocean carbon Sink). Cael, Guest, Henson, and Le Quéré acknowledge support from the Schmidt Futures Virtual Earth System Research Institute project CALIPSO. Le Quéré acknowledges support from the NERC Grant NE/V011103/1 Marine Frontiers. Guest acknowledges support from the Royal Society Grant RP.R1.191063. Bowler acknowldges support from the European Research Council (ERC) under the European Union's Horizon 2020 research and innovation programme (Diatomic; grant agreement No. 835067).

Open Research

The data used for this study are available from `https://doi.pangaea.de/10.1594/PANGAEA.855600` and `https://ncei.noaa.gov/access/world-ocean-atlas-2018/` and the code for their analysis is available for review purposes at `https://www.github.com/bbcael/opal` and will be deposited to a FAIR compliant repository if this article is eventually accepted. Numerical model documentation and output are available at `https://www.uea.ac.uk/web/groups-and-centres/green-ocean/model`.

References

Armand, L. K., Cornet-Barthaux, V., Mosseri, J., & Queguiner, B. (2008). Late summer diatom biomass and community structure on and around the naturally iron-fertilised kerguelen plateau in the southern ocean. *Deep Sea Research Part II: Topical Studies in Oceanography*, *55*(5-7), 653–676.

Armstrong, R. A., Lee, C., Hedges, J. I., Honjo, S., & Wakeham, S. G. (2001). A new, mechanistic model for organic carbon fluxes in the ocean based on the

quantitative association of poc with ballast minerals. *Deep Sea Research Part II: Topical Studies in Oceanography*, *49*(1-3), 219–236.

Arteaga, L. A., Haetjens, N., Boss, E., Johnson, K. S., & Sarmiento, J. L. (2018). Assessment of export efficiency equations in the southern ocean applied to satellite-based net primary production. *Journal of Geophysical Research: Oceans*, *123*(4), 2945–2964.

Arteaga, L. A., Pahlow, M., Bushinsky, S. M., & Sarmiento, J. L. (2019). Nutrient controls on export production in the southern ocean. *Global biogeochemical cycles*, *33*(8), 942–956.

Assmy, P., Smetacek, V., Montresor, M., Klaas, C., Henjes, J., Strass, V. H., ... others (2013). Thick-shelled, grazer-protected diatoms decouple ocean carbon and silicon cycles in the iron-limited antarctic circumpolar current. *Proceedings of the National Academy of Sciences*, *110*(51), 20633–20638.

Aumont, O., Ethé, C., Tagliabue, A., Bopp, L., & Gehlen, M. (2015, August). Pisces-v2: an ocean biogeochemical model for carbon and ecosystem studies. *Geoscientific Model Development*, *8*(8), 2465–2513. Retrieved from `http://dx.doi.org/10.5194/gmd-8-2465-2015` doi: 10.5194/gmd-8-2465-2015

Baker, C. A., Martin, A. P., Yool, A., & Popova, E. (2022). Biological carbon pump sequestration efficiency in the north atlantic: a leaky or a long-term sink? *Global Biogeochemical Cycles*, *36*(6), e2021GB007286.

Barker, S., Higgins, J. A., & Elderfield, H. (2003). The future of the carbon cycle: review, calcification response, ballast and feedback on atmospheric co2. *Philosophical Transactions of the Royal Society of London. Series A: Mathematical, Physical and Engineering Sciences*, *361*(1810), 1977–1999.

Beauchamp, J. J., & Olson, J. S. (1973). Corrections for bias in regression estimates after logarithmic transformation. *Ecology*, *54*(6), 1403–1407.

Bol, R., Henson, S. A., Rumyantseva, A., & Briggs, N. (2018). High-frequency variability of small-particle carbon export flux in the northeast atlantic. *Global Biogeochemical Cycles*, *32*(12), 1803–1814.

Boyd, P. W., Claustre, H., Levy, M., Siegel, D. A., & Weber, T. (2019). Multi-faceted particle pumps drive carbon sequestration in the ocean. *Nature*, *568*(7752), 327–335.

Britten, G. L., Wakamatsu, L., & Primeau, F. W. (2017). The temperature-ballast hypothesis explains carbon export efficiency observations in the southern ocean. *Geophysical Research Letters*, *44*(4), 1831–1838.

Browning, T. J., & Moore, C. M. (2023). Global analysis of ocean phytoplankton nutrient limitation reveals high prevalence of co-limitation. *Nature Communications*, *14*(1), 5014.

Brzezinski, M. A., Baines, S. B., Balch, W. M., Beucher, C. P., Chai, F., Dugdale, R. C., ... others (2011). Co-limitation of diatoms by iron and silicic acid in the equatorial pacific. *Deep Sea Research Part II: Topical Studies in Oceanography*, *58*(3-4), 493–511.

Brzezinski, M. A., Dickson, M.-L., Nelson, D. M., & Sambrotto, R. (2003). Ratios of si, c and n uptake by microplankton in the southern ocean. *Deep Sea Research Part II: Topical Studies in Oceanography*, *50*(3-4), 619–633.

Brzezinski, M. A., Krause, J. W., Bundy, R. M., Barbeau, K. A., Franks, P., Goericke, R., ... Stukel, M. R. (2015). Enhanced silica ballasting from iron stress sustains carbon export in a frontal zone within the c alifornia c urrent. *Journal of Geophysical Research: Oceans*, *120*(7), 4654–4669.

Brzezinski, M. A., Olson, R. J., & Chisholm, S. W. (1990). Silicon availability and cell-cycle progression in marine diatoms. *Marine ecology progress series*, 83–96.

Buitenhuis, E. T., Guest, J. K., Wright, R., Townsend, P., & Le Quéré, C. (2023). *Description of the planktom equations.* Zenodo. Retrieved from `https://zenodo.org/doi/10.5281/zenodo.8388158` doi: 10.5281/ZENODO.8388158

Buitenhuis, E. T., Le Quere, C., Bednaršek, N., & Schiebel, R. (2019). Large contribution of pteropods to shallow caco3 export. *Global Biogeochemical Cycles*, *33*(3), 458–468.

Cael, B. (2021). Variability-based constraint on ocean primary production models. *Limnology and Oceanography Letters*, *6*(5), 262–269.

Cael, B., Bisson, K., Conte, M., Duret, M. T., Follett, C. L., Henson, S. A., ... others (2021). Open ocean particle flux variability from surface to seafloor. *Geophysical Research Letters*, *48*(9), e2021GL092895.

Cael, B., Bisson, K., & Follett, C. L. (2018). Can rates of ocean primary production and biological carbon export be related through their probability distributions? *Global biogeochemical cycles*, *32*(6), 954–970.

Charette, M. A., & Smith, W. H. (2010). The volume of earth's ocean. *Oceanography*, *23*(2), 112–114.

Cram, J. A., Weber, T., Leung, S. W., McDonnell, A. M., Liang, J.-H., & Deutsch, C. (2018). The role of particle size, ballast, temperature, and oxygen in the sinking flux to the deep sea. *Global Biogeochemical Cycles*, *32*(5), 858–876.

DeVries, T., Primeau, F., & Deutsch, C. (2012). The sequestration efficiency of the biological pump. *Geophysical Research Letters*, *39*(13).

Ducklow, H. W., Steinberg, D. K., & Buesseler, K. O. (2001). Upper ocean carbon export and the biological pump. *Oceanography*, *14*(4), 50–58.

Efron, B., & Tibshirani, R. (1986). Bootstrap methods for standard errors, confidence intervals, and other measures of statistical accuracy. *Statistical science*, 54–75.

Franck, V. M., Brzezinski, M. A., Coale, K. H., & Nelson, D. M. (2000). Iron and silicic acid concentrations regulate si uptake north and south of the polar frontal zone in the pacific sector of the southern ocean. *Deep Sea Research Part II: Topical Studies in Oceanography*, *47*(15-16), 3315–3338.

Francois, R., Honjo, S., Krishfield, R., & Manganini, S. (2002). Factors controlling the flux of organic carbon to the bathypelagic zone of the ocean. *Global Biogeochemical Cycles*, *16*(4), 34–1.

Garcia, H., Weathers, K., Paver, C., Smolyar, I., Boyer, T., Locarnini, M., ... others (2019). World ocean atlas 2018. vol. 4: Dissolved inorganic nutrients (phosphate, nitrate and nitrate+ nitrite, silicate).

Gnanadesikan, A. (1999). A global model of silicon cycling: Sensitivity to eddy parameterization and dissolution. *Global Biogeochemical Cycles*, *13*(1), 199–220.

Griffiths, J. D., Barker, S., Hendry, K. R., Thornalley, D. J., Van De Flierdt, T., Hall, I. R., & Anderson, R. F. (2013). Evidence of silicic acid leakage to the tropical atlantic via antarctic intermediate water during marine isotope stage 4. *Paleoceanography*, *28*(2), 307–318.

Heinze, C., Eyring, V., Friedlingstein, P., Jones, C., Balkanski, Y., Collins, W., ... others (2019). Esd reviews: Climate feedbacks in the earth system and prospects for their evaluation. *Earth System Dynamics*, *10*(3), 379–452.

Henson, S. A., Laufkötter, C., Leung, S., Giering, S. L., Palevsky, H. I., & Cavan, E. L. (2022). Uncertain response of ocean biological carbon export in a changing world. *Nature Geoscience*, *15*(4), 248–254.

Henson, S. A., Sanders, R., & Madsen, E. (2012). Global patterns in efficiency of particulate organic carbon export and transfer to the deep ocean. *Global Biogeochemical Cycles*, *26*(1).

Holzer, M., Primeau, F. W., DeVries, T., & Matear, R. (2014). The southern ocean silicon trap: Data-constrained estimates of regenerated silicic acid, trapping efficiencies, and global transport paths. *Journal of Geophysical Research: Oceans*, *119*(1), 313–331.

Hutchins, D. A., & Bruland, K. W. (1998). Iron-limited diatom growth and si: N uptake ratios in a coastal upwelling regime. *Nature*, *393*(6685), 561–564.

Jin, X., Gruber, N., Dunne, J., Sarmiento, J. L., & Armstrong, R. (2006). Diagnos-

ing the contribution of phytoplankton functional groups to the production and export of particulate organic carbon, caco3, and opal from global nutrient and alkalinity distributions. *Global Biogeochemical Cycles*, *20*(2).

Klaas, C., & Archer, D. E. (2002). Association of sinking organic matter with various types of mineral ballast in the deep sea: Implications for the rain ratio. *Global biogeochemical cycles*, *16*(4), 63–1.

Le Quéré, C., Buitenhuis, E. T., Moriarty, R., Alvain, S., Aumont, O., Bopp, L., ... others (2016). Role of zooplankton dynamics for southern ocean phytoplankton biomass and global biogeochemical cycles. *Biogeosciences*, *13*(14), 4111–4133.

Malviya, S., Scalco, E., Audic, S., Vincent, F., Veluchamy, A., Poulain, J., ... others (2016). Insights into global diatom distribution and diversity in the world's ocean. *Proceedings of the National Academy of Sciences*, *113*(11), E1516–E1525.

Marchetti, A., Varela, D. E., Lance, V. P., Lance, V. P., Palmucci, M., Giordano, M., & Virginia Armbrust, E. (2010). Iron and silicic acid effects on phytoplankton productivity, diversity, and chemical composition in the central equatorial pacific ocean. *Limnology and Oceanography*, *55*(1), 11–29.

Marsay, C. M., Sanders, R. J., Henson, S. A., Pabortsava, K., Achterberg, E. P., & Lampitt, R. S. (2015). Attenuation of sinking particulate organic carbon flux through the mesopelagic ocean. *Proceedings of the National Academy of Sciences*, *112*(4), 1089–1094.

Martin, J. H., Knauer, G. A., Karl, D. M., & Broenkow, W. W. (1987). Vertex: carbon cycling in the northeast pacific. *Deep Sea Research Part A. Oceanographic Research Papers*, *34*(2), 267–285.

Martin-Jézéquel, V., Hildebrand, M., & Brzezinski, M. A. (2000). Silicon metabolism in diatoms: implications for growth. *Journal of phycology*, *36*(5), 821–840.

Matsumoto, K., & Sarmiento, J. L. (2008). A corollary to the silicic acid leakage hypothesis. *Paleoceanography*, *23*(2).

Matsumoto, K., Sarmiento, J. L., & Brzezinski, M. A. (2002). Silicic acid leakage from the southern ocean: A possible explanation for glacial atmospheric pco2. *Global Biogeochemical Cycles*, *16*(3), 5–1.

Matsumoto, K., Tokos, K., Huston, A., & Joy-Warren, H. (2013). Mesmo 2: A mechanistic marine silica cycle and coupling to a simple terrestrial scheme. *Geoscientific Model Development*, *6*(2), 477–494.

Montroll, E. W., & Shlesinger, M. F. (1982). On 1/f noise and other distributions with long tails. *proceedings of the National Academy of Sciences*, *79*(10), 3380–3383.

Mouw, C. B., Barnett, A., McKinley, G. A., Gloege, L., & Pilcher, D. (2016). Global ocean particulate organic carbon flux merged with satellite parameters. *Earth System Science Data*, *8*(2), 531–541.

Pančić, M., Torres, R. R., Almeda, R., & Kiørboe, T. (2019). Silicified cell walls as a defensive trait in diatoms. *Proceedings of the Royal Society B*, *286*(1901), 20190184.

Pasquier, B., & Holzer, M. (2017). Inverse-model estimates of the ocean's coupled phosphorus, silicon, and iron cycles. *Biogeosciences*, *14*(18), 4125–4159.

Petrou, K., Baker, K. G., Nielsen, D. A., Hancock, A. M., Schulz, K. G., & Davidson, A. T. (2019). Acidification diminishes diatom silica production in the southern ocean. *Nature Climate Change*, *9*(10), 781–786.

Pichevin, L., Ganeshram, R., Geibert, W., Thunell, R., & Hinton, R. (2014). Silica burial enhanced by iron limitation in oceanic upwelling margins. *Nature Geoscience*, *7*(7), 541–546.

Pondaven, P., Gallinari, M., Chollet, S., Bucciarelli, E., Sarthou, G., Schultes, S., & Jean, F. (2007). Grazing-induced changes in cell wall silicification in a marine diatom. *Protist*, *158*(1), 21–28.

Qiu, B., & Huang, R. X. (1995). Ventilation of the north atlantic and north pacific: subduction versus obduction. *Journal of Physical Oceanography*, *25*(10), 2374–2390.

Round, F. E., Crawford, R. M., & Mann, D. G. (1990). *Diatoms: biology and morphology of the genera*. Cambridge university press.

Ryderheim, F., Grønning, J., & Kiørboe, T. (2022). Thicker shells reduce copepod grazing on diatoms. *Limnology and Oceanography Letters*.

Saha, S., Moorthi, S., Pan, H.-L., Wu, X., Wang, J., Nadiga, S., ... others (2010). The ncep climate forecast system reanalysis. *Bulletin of the American Meteorological Society*, *91*(8), 1015–1058.

Sarmiento, J. L., Gruber, N., Brzezinski, M., & Dunne, J. (2004). High-latitude controls of thermocline nutrients and low latitude biological productivity. *Nature*, *427*(6969), 56–60.

Sarmiento, J. L., Simeon, J., Gnanadesikan, A., Gruber, N., Key, R., & Schlitzer, R. (2007). Deep ocean biogeochemistry of silicic acid and nitrate. *Global Biogeochemical Cycles*, *21*(1).

Siegel, D., DeVries, T., Doney, S., & Bell, T. (2021). Assessing the sequestration time scales of some ocean-based carbon dioxide reduction strategies. *Environmental Research Letters*, *16*(10), 104003.

Takeda, S. (1998). Influence of iron availability on nutrient consumption ratio of diatoms in oceanic waters. *Nature*, *393*(6687), 774–777.

Tréguer, P., Bowler, C., Moriceau, B., Dutkiewicz, S., Gehlen, M., Aumont, O., ... others (2018). Influence of diatom diversity on the ocean biological carbon pump. *Nature Geoscience*, *11*(1), 27–37.

Wilson, J. D., Barker, S., & Ridgwell, A. (2012). Assessment of the spatial variability in particulate organic matter and mineral sinking fluxes in the ocean interior: Implications for the ballast hypothesis. *Global Biogeochemical Cycles*, *26*(4).

Wright, R. M., Le Quéré, C., Buitenhuis, E., Pitois, S., & Gibbons, M. J. (2021). Role of jellyfish in the plankton ecosystem revealed using a global ocean biogeochemical model. *Biogeosciences*, *18*(4), 1291–1320.